AN EXPERIMENTAL ANALYSIS OF CRITICAL FACTORS
INVOLVED IN THE BREAKDOWN PROCESS
OF LEADING EDGE VORTEX FLOWS

by

Kenneth D. Visser

directed by

Robert C. Nelson

14961

P. 285

FOREWORD

The following report is submitted to the NASA Langley Research Center in fufillment of grant NAG-1-1156. This research report is the doctoral dissertation of Kenneth. D. Visser and summarizes the results of the effort. The research was directed by Robert C. Nelson.

AN EXPERIMENTAL ANALYSIS OF CRITICAL FACTORS INVOLVED IN THE BREAKDOWN PROCESS OF LEADING EDGE VORTEX FLOWS

Abstract

by

Kenneth D. Visser

Experimental crosswire measurements of the flowfield above a 70° and 75° flat plate delta wing were performed at a Reynolds number of 250,000. Survey grids were taken normal to the planform at a series of chordwise locations for angles of attack of 20° and 30°. Axial and azimuthal vorticity distributions were derived from the velocity fields. The dependence of circulation on distance from the vortex core as well as on chordwise location was examined. The effects of nondimensionalization in comparison with other experimental data was made.

The circulation distribution scales with the local semispan and grows approximately linearly in the chordwise direction. For regions of the flow outside of the vortex subcore, the circulation at any chordwise station was observed to vary logarithmically with distance from the vortex axis. The circulation was also found to increase linearly with angle of incidence at a given chordwise station.

A reduction in the local circulation about the vortex axis occurred at breakdown. The spanwise distribution of axial vorticity was severely altered through

the breakdown region and the spanwise distribution of axial vorticity present appeared to reach a maximum immediately preceding breakdown. The local concentration of axial vorticity about the vortex axis was reduced while the magnitude of the azimuthal vorticity decreased throughout the breakdown zone. The axial vorticity components with a negative sense, found in the secondary vortex, remained unaffected by changes in wing sweep or angle of attack, in direct contrast to the positive components. The inclusion of the local wing geometry into a previously derived correlation parameter indicated the circulation of growing leading edge vortex flows to be similar at corresponding radii from the vortex axis.

It was concluded that the flow over a delta wing, upstream of the breakdown regions and away from the apex and trailing edge regions, is conical. In addition, the dominating factors leading to the onset of breakdown are felt to be the local circulation of the vortex and the accompanying pressure field.

TABLE OF CONTENTS

LIST OF FIGURES

LIST OF SYMBOLS

c	chord
C_{pt}	total pressure $P_t - P_{static_\infty} / q$
k_1	tangential cooling coefficient
k_2	cooling coefficient normal to plane of hot wire sensors
M	Mach number
P	pressure
q	dynamic pressure
r	radial direction
r_c	vortex core radius
R_e	Reynolds number
s	semispan
s*	local semispan
u	velocity in the x direction
U_B	velocity normal to plane of hot wire sensors
U_N	velocity normal to hot wire sensor
U_T	velocity tangent to hot wire sensor
U_∞	freestream velocity
v	velocity in the y direction
V	velocity vector
V_i	velocity in the i direction
w	velocity in the z direction
x	chordwise direction
y	spanwise direction
z	direction normal to the surface of the model
α	angle of attack
ε	apex half angle
Γ	circulation
Λ	sweep angle
ϕ	azimuthal direction
ρ	freestream air density
Ω_i	vorticity in the i direction

ACKNOWLEDGEMENTS

CHAPTER I

INTRODUCTION AND BACKGROUND

1.1 Synopsis

A vortex structure is a truly fascinating physical phenomenon. The ability of a rotating fluid to maintain a cohesive structure that would surely seem to tear itself apart at a moments notice is of itself worth noting. Yet, vortices are present in many situations, from giant funnel clouds to the stirring of coffee in a cup. They can persist in a regular fashion in the wake of a flat plate or may form and disperse quickly behind blunt bodies. Common to all of these structures, however, is that their behavior can be generalized to that of a mass of fluid rotating about a common center.

Certain types of vortex structures will exhibit a transition in their state from a coherent, relatively high rotational speed flow to a much slower form. Almost instantly, a rapid change will occur in the flowfield including an expansion of the central core region and an associated rise in pressure along the vortex axis, which drastically alters the downstream characteristics. Leading edge vortex flows, such as that generated by delta wing planforms, also experience a severe decrease in the core's axial and circumferential velocity and large scale turbulent dissipation as a direct result of this 'vortex breakdown' or 'bursting'. The underlying physics of this apparently stable flowfield combined with an seemingly unpredictable disruptive process has interested aerodynamic researchers for over 35 years.

More specifically, the process by which breakdown occurs above a delta wing planform is of great concern from a flight performance point of view. The nature of a typical delta wing vortex

is illustrated in Figure 1.1. At high angles of attack, the boundary layer on the lower surface of the delta wing flows outboard. The fluid separates at the sharp leading edge, forming a free shear layer which curves upward and rolls into a core of high vorticity above the top side of the wing. Each of the two counter-rotating vortices also contain axial flow components in the central core regions, around and along which the fluid spirals.
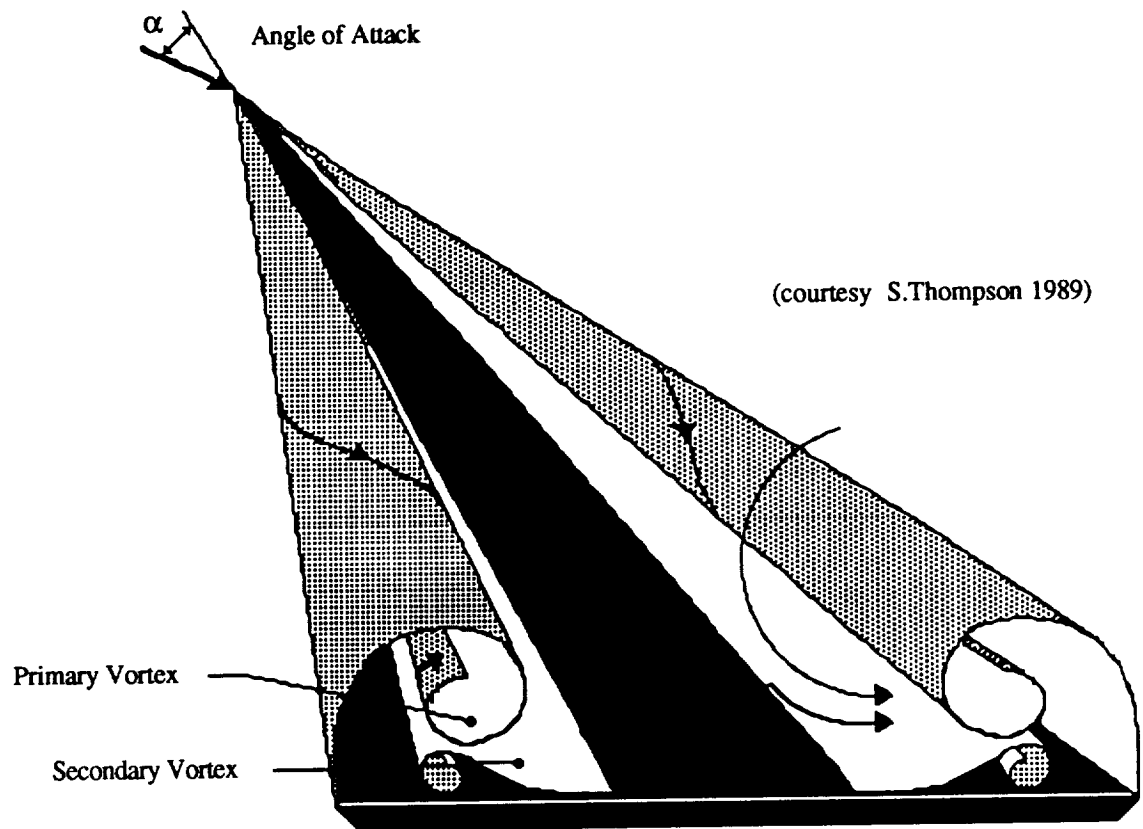
Figure 1.1 Delta Wing Vortex Flow Schematic

Additional spanwise outflow is induced on the upper surface beneath the coiled vortex sheet. This spanwise flow over the surface separates as it approaches the leading edge to form the secondary vortex structures which have an opposite sense of rotation. The main effect of the secondary vortex is to displace the primary vortex upwards and inwards. The size and strength of the

primary vortex increases with angle of incidence. It becomes the dominant steady flow feature through a wide range of practical flight attitudes. The pressure field in these vortices results in an incremental lift termed the "vortex" or "nonlinear" lift.

Delta wing performance is limited by vortex breakdown. As the angle of incidence is increased, breakdown moves toward the apex. The large suction pressures created by the leading edge vortices are reduced, aft of the breakdown region. This increase in surface pressure results in a lower lift contribution by the vortex behind the breakdown region. Upon reaching the apex, a further increase in the angle of attack causes total separation of the leeward flow or stall. The effect of breakdown on the gross features of the flow can be seen in Figure 2a. A laser light sheet is used to visualize planes normal to the wing surface. The vortex on the far side of this delta wing has broken down, in contrast to the unburst vortex in the foreground. A photograph of the 'spiral' type of breakdown is presented in Figure 1.2b. Smoke used to trace the flow is placed into the central core of the vortex and vividly demonstrates the abruptness of this transition phenomena.
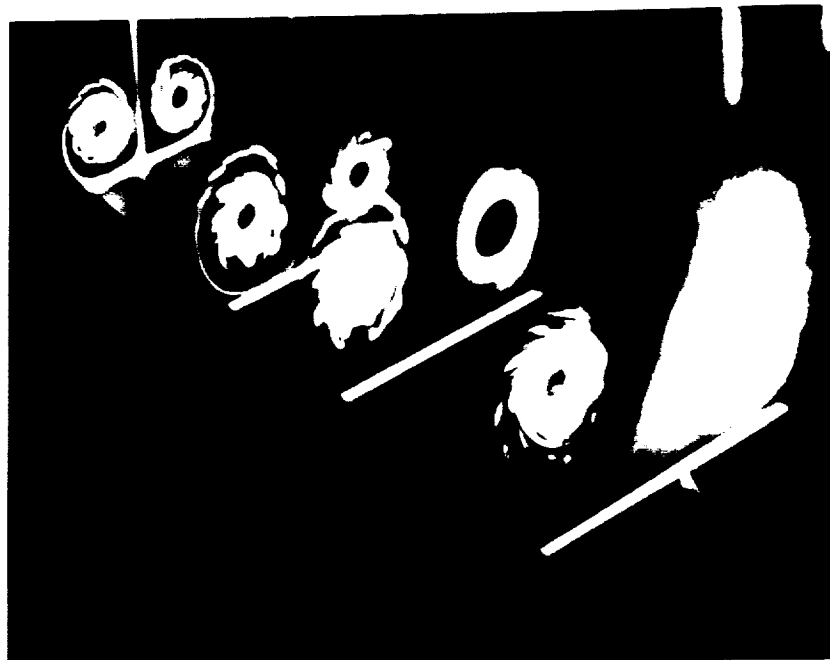
Figure 1.2a Vortex Breakdown, Laser Sheet (Payne, 1987)
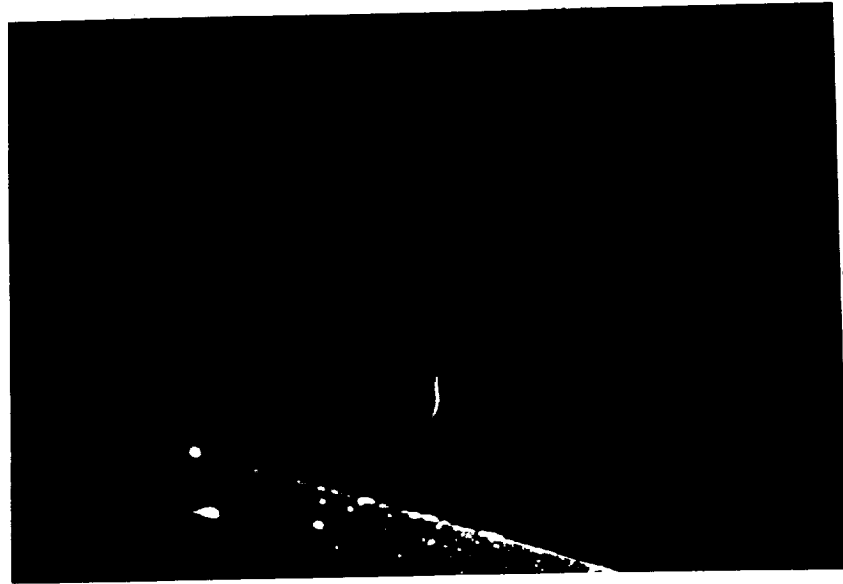
Figure 1.2b Vortex Breakdown, Spiral Breakdown

As a further example of the significant effects of breakdown on the the vortex flowfield the total pressure distributions above a 70° sweep wing (Payne, 1987) at a chordwise station of x/c = 0.5 are depicted in Figure 1.3. At an angle of attack of 30°, the breakdown is aft of this station, while at α = 40° the breakdown region has moved forward of this location. The post-breakdown

a)   b)
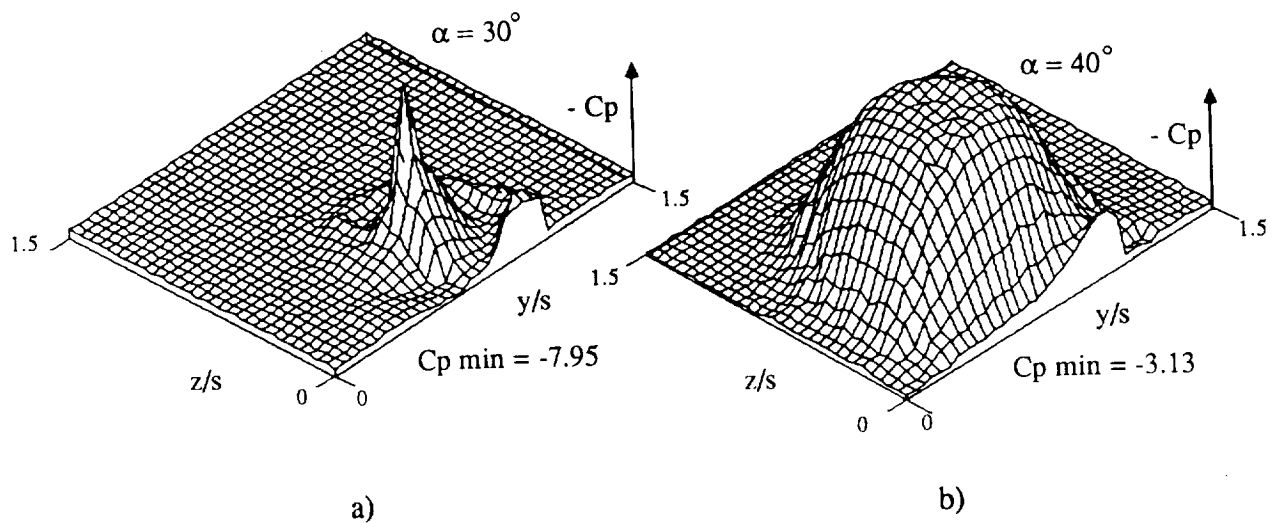
Figure 1.3 Total Pressure Distributions a) Pre-breakdown b) Post-breakdown

flow in Figure 1.3b has the scale of the pressure axis expanded to illustrate the local features. The pressure increase in the core, aft of breakdown, is substantial, and the expansion of the pre-breakdown, narrow core region is also evident.

Early investigators observed the onset of breakdown in wind and water tunnels under various test conditions. Others immediately began theoretical and numerical investigations in an effort to not only understand what is occurring, but to predict the onset of this drastic change in the flowfield. Efforts have included variation of all manner of possible parameters, including wing geometry, angle of attack, and Reynolds numbers. Most investigators approach the study of delta wing vortical flows by asking such questions as: "Why does vortex breakdown occur?" and "What factors influence breakdown?" A different perspective on the problem can be gained by posing the inverse question: "Why does the vortex manage to maintain a cohesive flow structure upstream of the transition/breakdown region?", especially in light of rotational rates on the order of 50,000 rpm.

It is important to understand the physics of the vortex flowfield, both in general and that specific to delta wings. The following section describes the behavior of vortex flows, including an early model, and the characteristics of the specific case of the delta wing planform are overviewed. The remaining portion of the chapter is devoted to presentation of possible mechanisms for vortex breakdown. These are examined separately in light of the past theoretical, numerical and experimental explanations, which then leads to the present experimental study.

1.2 Phenomenological Aspects of the Vortex Flowfield

In order to gain a better understanding of the delta wing flowfield and its important characteristics, an overview of some basic concepts is given. This is followed by a review of an

analytic model derived by Stewartson and Hall in the early 1960's which uses simplifying assumptions on the flowfield behavior as a means for obtaining a solution. Finally, additional concepts used to describe the vortex flow will be presented

1.2.1 Fundamental Vortex Behavior

The vast majority of vortex structures resemble the classical two dimensional Rankine vortex as shown in Figure 1.4. A strongly rotational central core region is surrounded by an irrotational region. The central region possesses a tangential velocity distribution which grows with increasing radius, such as $V_\emptyset = \omega r$. This is termed a rotational or 'forced' vortex. At a specified radius, the velocity begins to decrease with increasing distance from the vortex axis in the form of a $V_\emptyset \sim 1/r$ distribution and the irrotational or 'free' vortex flow continues to infinity.
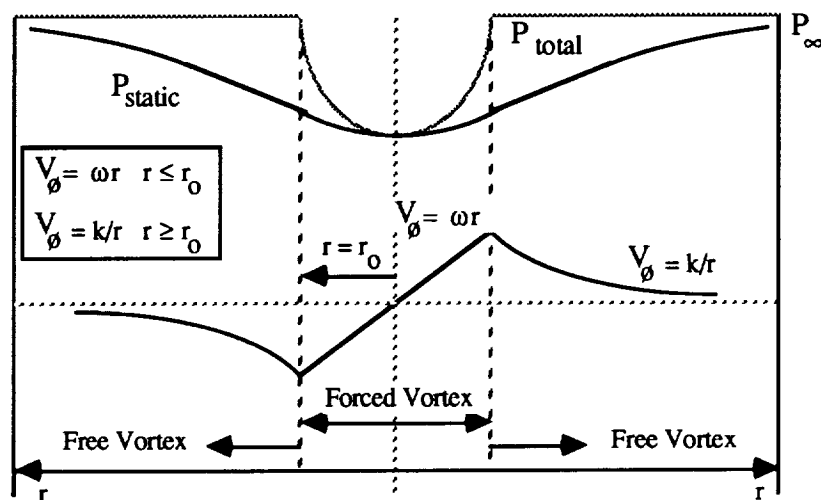
Figure 1.4 Two Dimensional Rankine Vortex Structure

 The presence of viscosity, however, tends to merge these regions such that a region exists between the purely irrotational flow and that of the core region. This region possesses rotational properties, and is described by a profile that combines aspects of both. An exact solution to the Navier Stokes equations for the decay of a vortex under the action of viscosity is presented by Batchelor (1967) with a tangential profile of the form

$$V_{\emptyset}(r,t) \; = \; v \; = \; \frac{\Gamma_o}{2\Pi r} \; (\, 1 - \; e^{-r^2/4vt} \,) \qquad\qquad (1.1)$$

This profile is presented in Figure 1.5 along with $V_{\emptyset}(0,0)$ which remains undefined at $r = 0$. For $t > 0$, the vortex takes the form of an external irrotational flow matched to an inner core through an annular rotational, viscous region. Since vt is greater than zero for a timescale, t, based on the ratio of the root chord of the model to a freestream velocity, the resulting profile can be scaled to resemble that measured in real fluids.
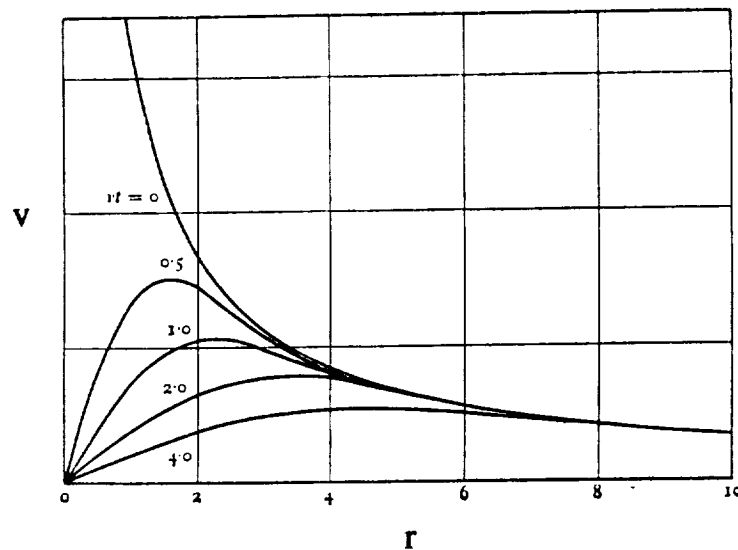
Figure 1.5 Viscous Vortex Structure (Batchelor, 1967)

Actual vortex structures occurring in nature are seen to be more complex than their two dimensional counterparts. Tornadoes possess large updraft velocities along their axis. The addition of some rotation to a fluid draining through a hole at the bottom of a container causes it to drain much more quickly leading to the conclusion that the interaction of the tangential and axial velocity component in a vortex is very significant.

The primary vortex structure above a delta wing, as well as that found in swirling tube flows, exhibit an additional velocity component. An axial, jetting type of profile exists normal to the plane of the vortex, reaching a maximum along the core axis as illustrated in Figure 1.6. Axial velocities have been measured in the vortex cores of delta wings to over three times that of the freestream. The core region also exhibits large tangential velocity gradients near its center. For the sake of a reasonable analysis, however, simplifying assumptions are generally made as will be shown.
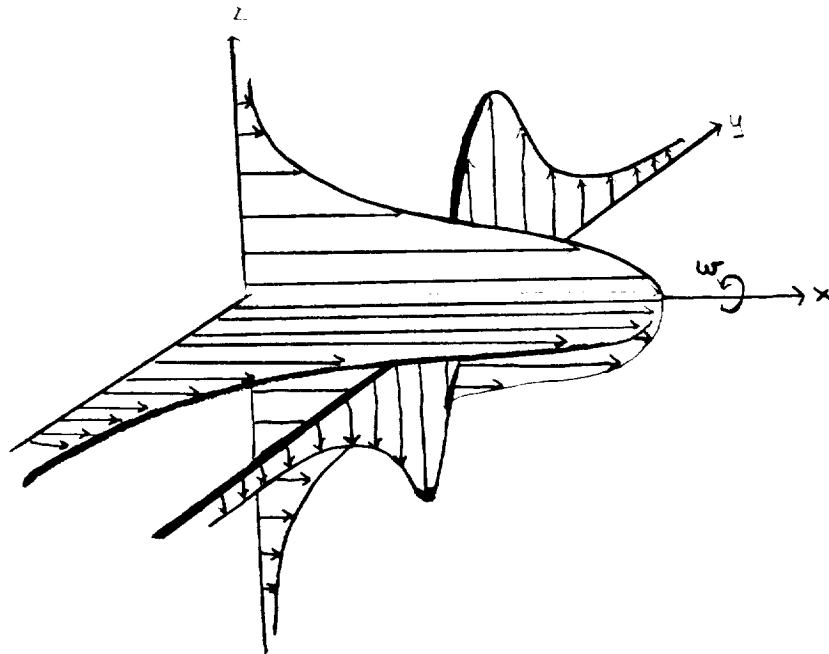
Figure 1.6 Vortex Velocity Field with Axial Component

Delta wing vortices are not symmetric and the influence of the wing surface can not be simply neglected. Leibovich (1984) summarized several aspects regarded as common to delta wing flows. The flow separating from the leading edge of a delta wing is generally regarded as a sheet of vorticity that spirals inward as it progresses down the wing. A core region is formed near the center part of this spiral. Vorticity is continually fed into the vortex structure from the boundary layer on the underside of the wing at the leading edge. The core region continues to enlarge in a conical fashion in the chordwise direction, as does the entire field, which results in an almost linear increase in the circulation with downstream distance. The axial velocity increases as a direct result of the drop in centerline pressure with distance from the apex.

The definition of the core region is usually taken to be the axisymmetric center of the vortex which behaves in a rotational fashion. Five hole probe measurements by Earnshaw (1961) above a unity aspect ratio delta wing at $\alpha = 14.9°$ led to his division of the vortex core into three regions. He estimated the core to be approximately 30% of the local semispan in diameter and essentially conical in nature. Along the axis of this vortex core is the 'viscous subcore', which measured about 5% local semispan in diameter and contains high velocity and large pressure gradients. The subcore exhibits the appearance of an axisymmetric rotating flow, rather than conical, along with some solid body rotation properties. Outside of the core lies a region containing the trace of the vortex sheet. A schematic in Figure 1.7 depicts these defined flow regions. It will be shown later that the subcore contains the majority of the axial vorticity. Leibovich (1984) noted that the Reynolds number has no effect on the size of this vortex core region and only serves to decrease the size of the subcore region as the Reynolds number increases. The axis of the vortex is generally located on the order of a core diameter above the wing. The vertical core locations, as measured by Payne (1987) for a wing sweep of 75° at $\alpha = 10°$ to 40° are presented in Figure 1.8. The core position maintains an approximately constant height, relative to the local span, above the wing at all chord stations for a given angle of incidence. This indicates, at the very least, that the vortex trajectory reflects a conical behavior
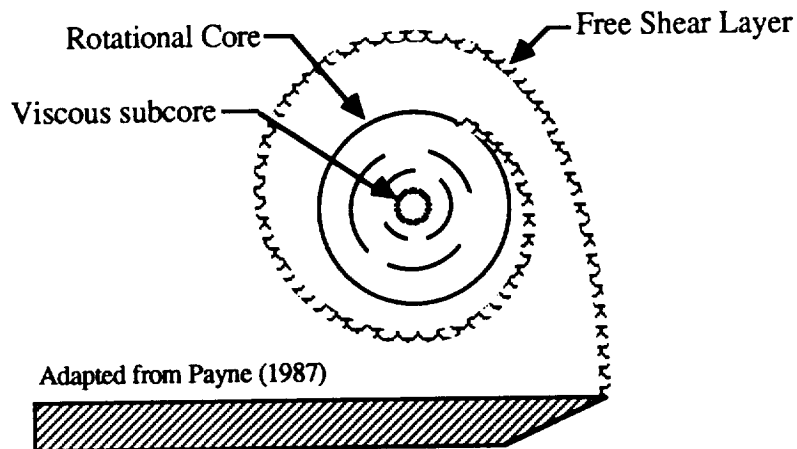
Figure 1.7 Three Regions of a Delta Wing Vortex Structure

in the flow. In addition, the angle between the vortex trajectory and the planform surface can be seen to increase in an approximately linear fashion with angle of attack at the lower values of α.
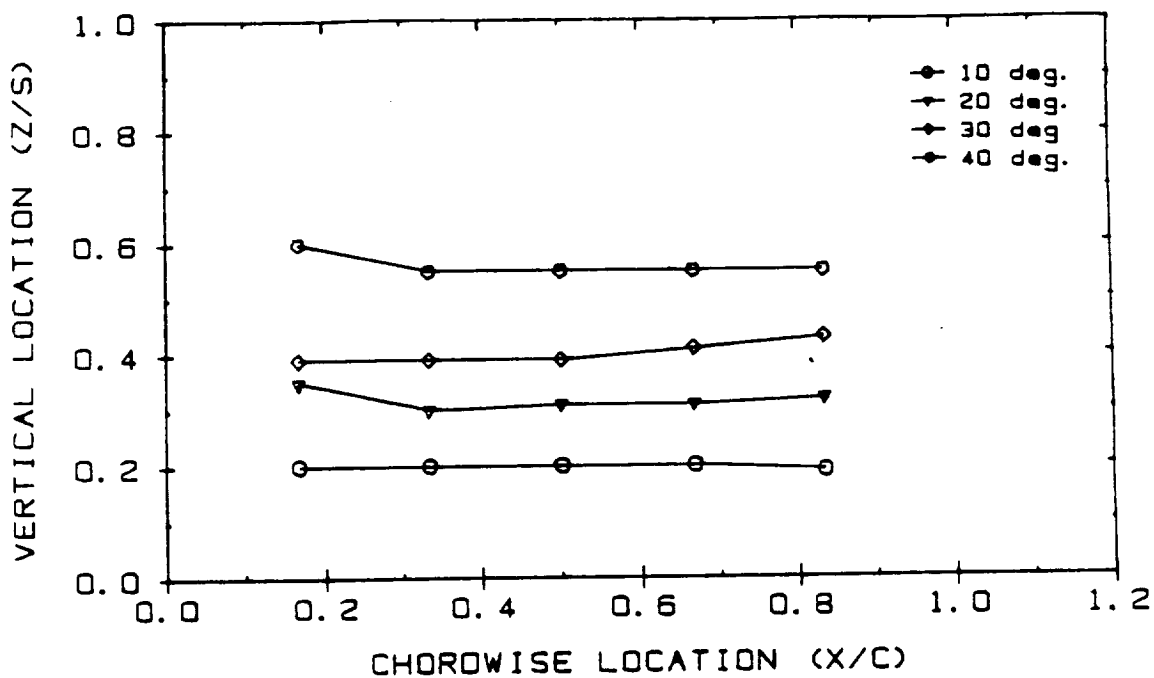
Figure 1.8 Vortex Core Locations (Payne 1987)

Erickson (1981) mentions a core position variation for laminar versus turbulent boundary layer flows on the wing surface. The primary core moves upward and inward for the laminar case, relative to the turbulent one, because of secondary vortex displacement effects. Higher suction pressure peaks are evident in the turbulent case, but the integrated pressures are the same. He discusses in detail the effect of Reynolds number on vortex flow development. At higher Reynolds numbers, based on the chord, c, the ratio of scales of the transport process of diffusion to convection is on the order of

$$\frac{1}{Re^{0.5}}$$

which is also a measure of the boundary layer thickness. It appears that large scale vortex structures are determined primarily by convective transport mechanisms, implying an independence of Reynolds number. Vortex core axial velocities, however, have been shown to be Reynolds number dependent. Erickson concludes that the majority of the phenomena observed in the delta wing flow field is dominated by potential flow effects associated with the external field, that is the external pressure gradient.

1.2.2 An Analytic Delta Wing Vortex Model

One of the earliest analytical explanations for the flow observed in the primary vortex of a delta wing was the incompressible solution proposed by Stewartson and Hall (1963) based on a simplified model introduced by Hall (1961). This model has been found to compare quite favorably with experimental data by several researchers. The flow was approximated to follow a steady, axisymmetric behavior which simplified the cylindrical Navier-Stokes equations to the form below utilizing the geometry of Figure 1.9.

$$V_r \frac{\partial V_r}{\partial r} + V_x \frac{\partial V_r}{\partial x} - \frac{V_\phi^2}{r} = -\frac{1}{\rho}\frac{\partial P}{\partial r} + \nu \left(\frac{1}{r}\frac{\partial}{\partial r}\left(r\frac{\partial V_r}{\partial r}\right) + \frac{\partial^2 V_r}{\partial x^2} - \frac{V_r}{r^2}\right) \qquad (1.2a)$$

$$V_r \frac{\partial V_\phi}{\partial r} + V_x \frac{\partial V_\phi}{\partial x} + \frac{V_r V_\phi}{r} = \nu \left(\frac{1}{r}\frac{\partial}{\partial r}\left(r\frac{\partial V_\phi}{\partial r}\right) + \frac{\partial^2 V_\phi}{\partial x^2} - \frac{V_\phi}{r^2}\right) \qquad (1.2b)$$

$$V_r \frac{\partial V_x}{\partial r} + V_x \frac{\partial V_x}{\partial x} = -\frac{1}{\rho}\frac{\partial P}{\partial x} + \nu \left(\frac{1}{r}\frac{\partial}{\partial r}\left(r\frac{\partial V_x}{\partial r}\right) + \frac{\partial^2 V_x}{\partial x^2}\right) \qquad (1.2c)$$

$$\frac{1}{r}\frac{\partial}{\partial r}(rV_r) + \frac{\partial}{\partial x}(V_x) = 0 \qquad (1.2d)$$
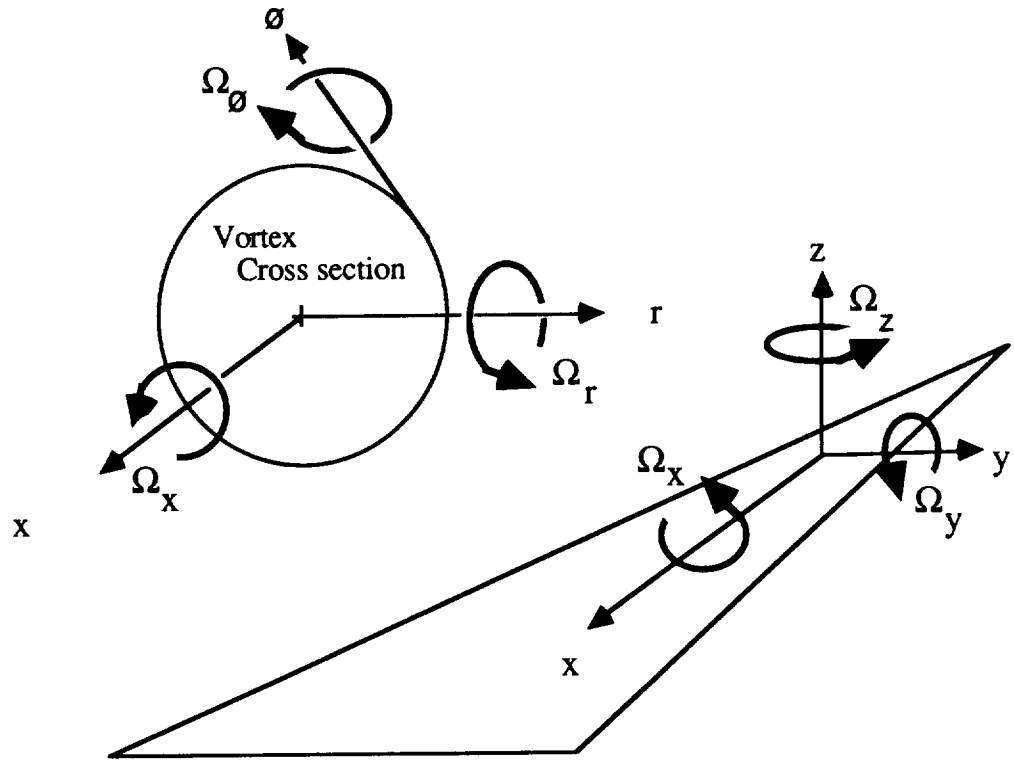
Figure 1.9 Vortex Geometry

Stewartson and Hall assume the diffusion of vorticity is confined to a geometrically slender core. The direct result of this simplification is the elimination of the terms $V_r \frac{\partial V_r}{\partial r}$ and $V_x \frac{\partial V_r}{\partial x}$. The flow contains no vortex sheets, and thus must be continuous and rotational to allow vorticity convection. The outer core pressure and velocity fields are considered to be conical, that is, maintaining constant values along rays emanating from the apex. An inviscid outer core solution is determined to specify the boundary conditions for the viscous inner core solution. The resulting solution for the inviscid flow regime is

$$\frac{V_x}{\mathbf{V_x}} = 1 - \alpha \ln\left(\frac{r}{ax}\right) \qquad\qquad \frac{V_r}{\mathbf{V_x}} = -\frac{r\,\alpha}{2\,x} \qquad\qquad (1.3a)\,,(1.3b)$$

and

$$\frac{V_\phi}{\mathbf{V_x}} = \left(\frac{\mathbf{V_\phi}^2}{\mathbf{V_x}^2} - \alpha^2 \ln\left(\frac{r}{ax}\right)\right)^{0.5} \qquad\qquad (1.4)$$

where

$$\alpha = \left(1 + \frac{2\mathbf{V_\phi}^2}{\mathbf{V_x}^2}\right)^{0.5} - 1 \;>\; 0 \qquad\qquad (1.5)$$

The outer radius of the core is defined by $r = ax$. The boldface type in the equations above denote the values of the flow velocities at the outer radius of the core. As $r \rightarrow 0$ this solution breaks down because the ignored viscous terms become important. An order of magnitude analysis was then performed by Stewartson and Hall, similar to that of a boundary layer approximation. For a sufficiently small value of ν, the viscous core will be slender and changes in the radial direction will be much greater than those axially. The original NS equations thus become

$$\frac{V_\phi^2}{r} = \frac{1}{\rho}\frac{\partial P}{\partial r} \qquad\qquad (1.6a)$$

$$V_r\frac{\partial V_\phi}{\partial r} + V_x\frac{\partial V_\phi}{\partial x} + \frac{V_r V_\phi}{r} = v\left(\frac{1}{r}\frac{\partial}{\partial r}\left(r\frac{\partial V_\phi}{\partial r}\right) - \frac{V_\phi}{r^2}\right)$$ (1.6b)

$$V_r\frac{\partial V_x}{\partial r} + V_x\frac{\partial V_x}{\partial x} = -\frac{1}{\rho}\frac{\partial P}{\partial x} + v\left(\frac{1}{r}\frac{\partial}{\partial r}\left(r\frac{\partial V_x}{\partial r}\right)\right)$$ (1.6c)

$$\frac{1}{r}\frac{\partial}{\partial r}(rV_r) + \frac{\partial}{\partial x}(V_x) = 0$$ (1.6d)

The introduction of suitable independent variables and asymptotic expansions are used to arrive at a set of ordinary differential equations solved by the Runge Kutta method. Interestingly, it was found that for suitably small values of the kinematic viscosity, the axial velocity component was nearly constant across the viscous region. The solution is presented in Figure 1.10a from Stewartson and Hall (1963).
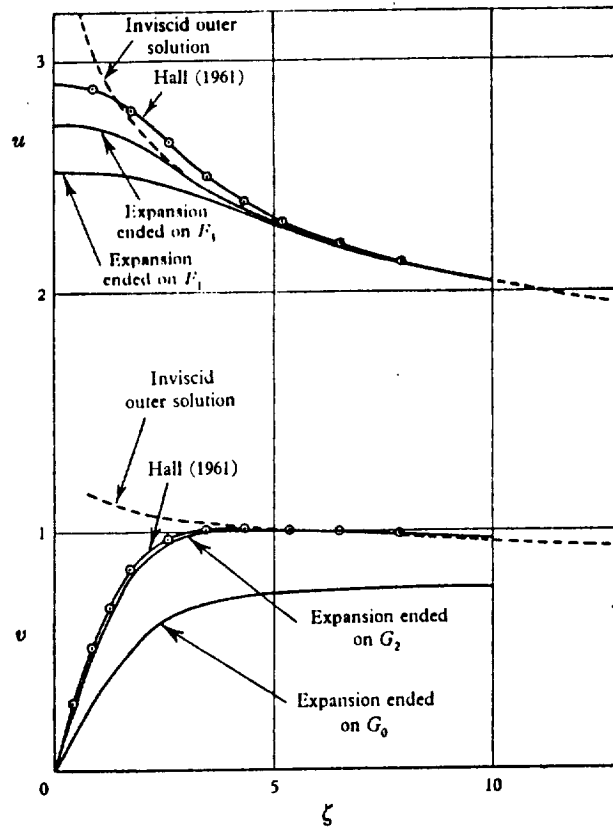
Figure 1.10a   Vortex Model, Analytical Results (Stewartson and Hall, 1963)

Laser Doppler Velocimetry (LDV) measurements by Pagan and Solignac (1986) on a vortex in the wake of a 75° sweep delta wing at α = 19.3° are compared with Hall and Stewartson (1963) in Figure 1.10b. Good agreement is demonstrated, although the experimental subcore region is seen to be larger. The profiles of Pagan and Solignac also indicate three distinct vortex regions

i) an internal, viscous, solid body rotation motion

ii) an external, irrotational area with a potential velocity law of the 1/r form

iii) in intermediate "Euler" region where the flow is inviscid and rotational.
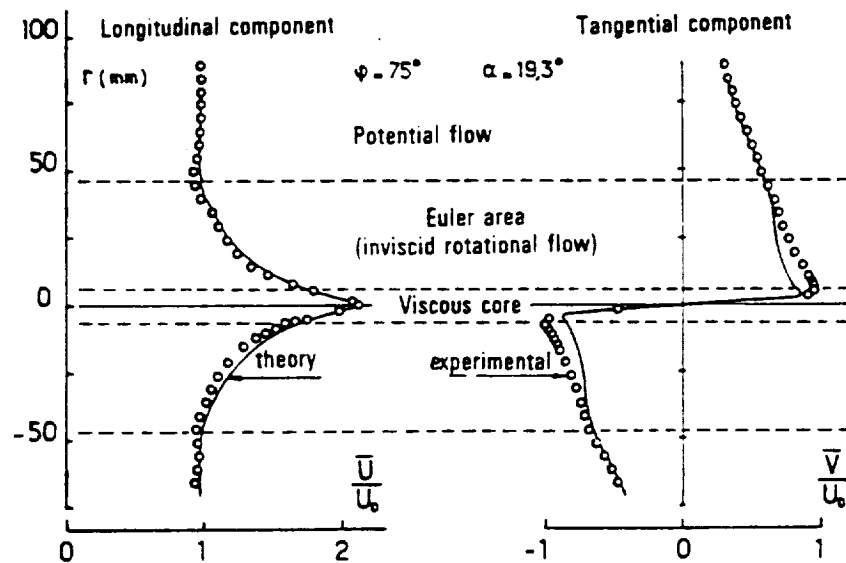
Figure 1.10b   Vortex Model, Experimental comparison (Pagan and Solignac, 1986)

Verhaagen and van Ransbeeck (1990) have compared their data to Stewartson and Hall by matching the numerical inner core solution at each chordwise location to the edge of their local rotational core. This was based on pressure and velocity measurements above a 76° sweep half span model. Verhaagen and van Ransbeeck defined their rotational core to be the region inside of which the vorticity is continuously distributed and no shear layer can be detected as shown in Figure 1.11a. They found the velocity and pressure distributions along the core axis to be strongly over estimated by the theory and attributed this largely to the fact that the subcore size

and axial velocity variations were much greater than that assumed in the theoretical derivation. Correlation with the theory improved with chordwise distance from the apex. The distribution of the circumferential velocity in the inviscid region matched quite well. The core total pressure, however, was found to be much lower in the experiment than what the theory predicted.

Overall , the theory agreed reasonably well with the experimental data in the range of x/c = 0.3 to 0.7. An example of the axial velocity is given in Figure 1.11b at a chordwise station of x/c = 0.5. The good agreement should not come as a surprise. Stewartson and Hall constructed a theory using an isolated axisymmetric vortex. In the wind tunnel, as the vortex moves rearward on the wing, and subsequently away from the planform surface, the influence of the wall decreases. In addition, near the apex, the wing span is on the order of the thickness of the model, resembling more of a blunt body than a slender wing. The vortex core size is also on the

a)   b)
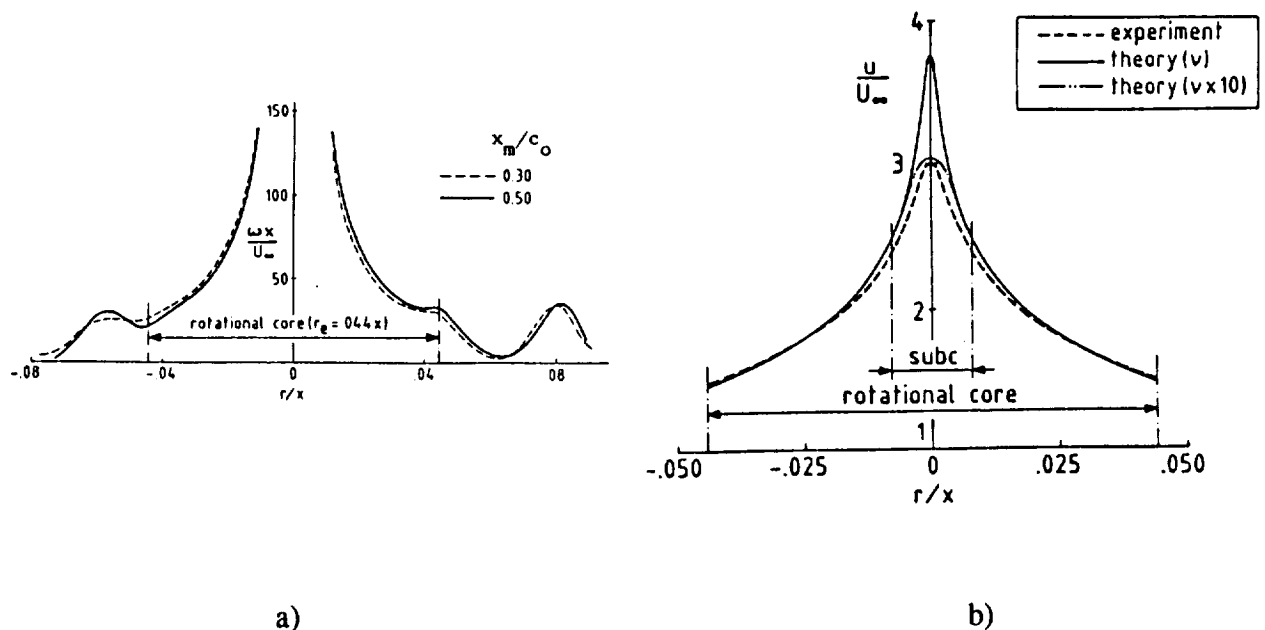
Figure 1.11 Validation of Flow Conicality (Verhaagen and van Ransbeeck, 1990)

a) Rotational Core b) Axial Velocity

order of the wing thickness in this region which would invalidate the assumptions of a slender wing approach. Hence, it would be expected that the experimental data would correspond more closely to the predicted theory away from the apex and the trailing edge regions.

The model outlined above represents one type of approximation used to predict vortex flows, that being an axially symmetric core with a continuously distributed vorticity. The other type of flow model employs a sheet of vorticity, emanating from the leading edge and rolling into a spiral as it winds into the center of the vortex. Mangler and Weber (1967) present a conical analysis using this type of reasoning. Experimental observations have indicated that the vorticity is confined to this sheet during the initial phase of roll up. Viscous effects are ignored by Mangler and Weber and the vorticity is assumed to be concentrated on a thin sheet, the flow between the sheets being irrotational. They also state that that the total head for the core region remains constant, which seems questionable in light of the total pressure drop at the vortex center. Yet the leading terms of their asymptotic solution indicate that their solution for a potential flow with sheets of vorticity is identical to the solution by Hall (1961) of an axisymmetric flow with distributed vorticity.

1.2.3 Further Concepts on Leading Edge Flows

The analysis of the leading edge vortex flow and its effect on a delta wing planform has also been undertaken from an aerodynamic force point of view, as an alternate approach to predicting the physics of the fluid interactions using the equations of fluid motion. Polhamus(1971) devised a method, referred to as the leading edge suction analogy, to predict the lift on a delta wing by separating the normal force into potential lift and vortex lift components. This can be written as

$$C_L = K_p \sin\alpha\cos^2\alpha + K_v \sin^2\alpha\cos\alpha = C_{Lp} + C_{Lv} \qquad (1.7)$$

and is illustrated in Figure 1.12. The potential term is based on lifting surface theory where K_p is the potential lift coefficient slope at zero angle of attack. The lift due to the vortex term results from the suction generated by the equivalent attached flow about the edge and K_v is estimated from the potential flow leading edge suction calculations.
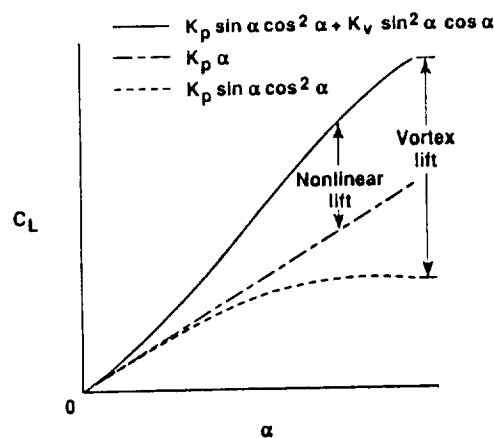
Figure 1.12 Vortex Lift Definitions (Hemsch, 1990)

No knowledge of the shape, strength or position of the vortex is required. Lift measurements by Wentz and Kohlman (1971) on 70° and 75° delta wings are in excellent agreement with this analogy up to breakdown as shown in Figure 1.13. Surface pressure measurements by Er-El and Yitzhak (1988) on a 60 and 75 degree sweep delta wings also indicate that the analogy provided good predictions of normal force, potential and vortical components and normal force loadings up to $\alpha = 20°$.
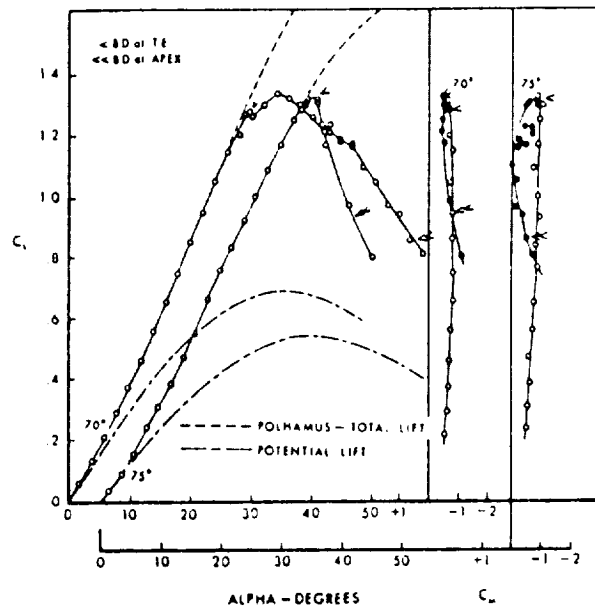
Figure 1.13 Vortex Lift Distribution (Wentz and Kohlman,1971)

Hemsch (1990) makes a relevant point that can easily be overlooked when examining the resulting lift on a delta wing. The vortex lift increment is often referred to as the nonlinear lift increment, $C_{L_{nl}}$, when in fact the nonlinear increment is defined as

$$C_{L_{nl}} = C_L - K_p \alpha \qquad (1.8)$$

and illustrated in Figure 1.12. His analysis has shown that although the nonlinear lift component increases with increasing sweep, the vortex lift component decreases as does the vortex strength as noted in Figure 1.14.
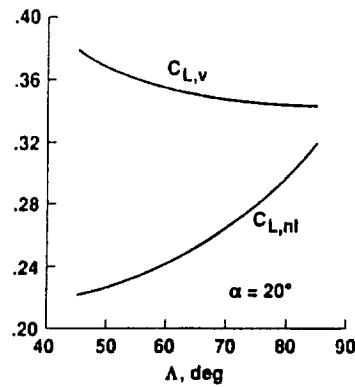
Figure 1.14 Vortex Lift Coefficient Behavior (Hemsch, 1990)

The correlation of experimental data about highly swept delta wings, using similarity parameters, is an additional means of gaining insight into the behavior of the leading edge flow. Sychev (1960) introduced parameters for hypersonic flows about slender bodies which were extended by Barnwell (1987) to the inner region of subsonic/transonic flow. The flow is implied to have smooth, small axial gradients at high angles of attack. Sychev analyzed the Euler equations using a geometrical slenderness assumption

$$\delta = \frac{\text{maximum semispan}}{\text{body length or wing chord}} \ll 1$$

His results involved only the parameter $k_1 = \delta \cot\alpha$. Hemsch (1988,1989) has utilized this in the form below which exhibits a more appropriate asymptotic behavior for small α,

$$k_3 = \frac{\tan\alpha}{\text{Aspect Ratio}} = \frac{\text{constant}}{k_1} \tag{1.9}$$

to correlate data accumulated over a range of thin delta wings. Supersonic flows over sharp-edged wings were found to correlate very well for a wide range of flows, up to aspect ratios of four, thus extending the similarities proposed by Sychev. Normal force coefficients and circulation values generated numerically on a series of thin gothic wings and delta wings with sweeps of $65°$ to $85°$ were found to correlate well when scaled in this manner. Pitching moments correlated less well, indicating a dependency on aspect ratio with subsonic Mach numbers. Interestingly, Earnshaw and Lawford (1964) found the positions of the primary attachment line and the secondary separation line to correlate well with $\alpha\tan\Lambda$, similar in form to $1/k_1$, implying the flow is roughly conical. The present study examines extensions of these concepts in Section 5.2.

It is worth noting that the final word on the effects of the leading edge vortex with regards to the flow above a delta wing, excluding the breakdown process for the moment, is still not definite. Some interesting discussions are put forth by Dixon (1989) on the physics of leading edge vortex lift. He suggests that the primary contribution to vortex lift is due to the shear layer and that the vortex which results from the rollup of this shear layer has only small, indirect effects on the lifting surface. His major conclusions indicate that total lift is not strongly sensitive to the position or strength as long as the vortex is near the leading edge. In addition, the drag depends on the amount of flow entrained by the free vortex, which in turn is a function of the free vortex circulation, its rate of growth, and the distance along the vortex axis. The following discussion on the mechanisms associated with breakdown will further serve to illustrate the diversity of thought on this subject.

1.3 Breakdown Mechanisms and Criteria

The occurrence of vortex breakdown is not a random event. Certain physical conditions must be present in a flow that will eventually exhibit breakdown. First, the flow must be of a highly swirling nature. The amount of swirl present in a flow can be determined by the value of the swirl angle = $\tan^{-1}$ (V_ϕ/V_x), determined from the local values of the axial, V_x, and tangential, V_ϕ, velocity components. Generally speaking, this value is determined in the vortex core and found to be greater than 40° for the flow directly upstream of breakdown. Secondly, it appears that for breakdown to occur there must also be an adverse axial pressure gradient. The occurrence, as well as the position, of the breakdown region can be severely influenced by the pressure gradient outside of the immediate vortex flow, such as a convergence of the tunnel walls or an object placed in the downstream wake. The removal or reduction of an adverse, axial gradient can delay breakdown. Finally, all breakdown phenomena show a divergence of the vortex core region directly upstream of breakdown. This can be attributed to the axial adverse pressure gradient, however as Hall (1972) mentions, any divergence of the outer streamtubes, even if the external adverse gradient is not sufficient to induce breakdown, can produce an adverse gradient in the interior of the vortex core because of continuity.

The breakdown region appears to follow one of two forms: the axisymmetric bubble breakdown, where the rearward part of the bubble is open ended and irregular, as if it were shedding from some imaginary blunt body of revolution, and the spiral type, typified by an abrupt kink in the subcore which proceeds to spiral about the original axis for up to several revolutions before dispersing (Figure 1.2b). The axial component of the flow in the core, measured at up to three times freestream, decelerates and stagnates in the space of one or two core diameters. This is accompanied by a substantial rise in the core pressure. Expansion of the cores, as presented by Leibovich (1978), range from 1.5 to 3 times the diameter present in the upstream flow, the bubble form showing significantly greater expansion. Reversed flow is typically noted in bubble

breakdown forms. This condition of reversed flow is not specifically required in order that the 'breakdown process' occur, however, as has been pointed out by Cutler, Naaseri, and Bradshaw (1989) and Faler and Leibovich (1977).

The breakdown phenomena is not solely a delta wing phenomena. Swirling tube flows also exhibit breakdown characteristics similar to delta wing vortical flows. Another phenomenon which has shown evidence of breakdown is the tornado. This, again is different from either a delta wing or a confined tube flow in that there are no solid boundaries parallel to the vortex axis. The complexities of these vortical flows are such that a complete analytical solution is difficult to obtain. Theories do exist that partially predict the occurrence of certain flow phenomena, such as breakdown or the sensitivity of the region to the severity of external parameters, such as pressure gradients.

Excellent reviews of research dealing with vortex structures and breakdown, both theoretical and experimental, have been written by Hall (1972), Parker (1976), Erickson (1981), Wedemeyer (1982), Hall (1985), Leibovich (1984), Lee and Ho (1989), and Ng (1989). These deal with all aspects of vortex flows, including tube vortex flows and delta wing vortices, and range from stability/breakdown observations to analysis of theoretical models. Information pertinent to the present study is summarized below. The following explanations are detailed according to their theoretical, numerical and experimental nature.

1.3.1 Theoretical Suppositions

Several theories have been proposed to explain the occurrence of breakdown. Hall (1972) groups these theories into three categories which will also be used here for the purpose of discussion.

1. Vortex breakdown is similar to the separation of a two dimensional boundary layer. (Gartshore 1962, Stewartson and Hall 1966)

2. Hydrodynamic instability results in the transition to post breakdown flow. (Ludweig 1962,1965)

3. An existence of a critical state occurs which causes breakdown to occur. (Squire 1960, Benjamin 1962, 1967 Bossel 1967,1969)

These will be considered in detail below and a more extensive analysis can be found in Hall (1972).

The quasi-cylindrical approximation for describing the vortex field, using boundary layer simplifications, was detailed previously with the theory of Stewartson and Hall (1966). The idea behind using this approximation as a means for predicting breakdown is the same as that of determining separation points in a boundary layer flow. If the calculation shows that a separation of the flow may occur in a boundary layer, the corresponding real flow has been shown to actually separate at or near that location even though the equations themselves fail to model the flow at that point. In the same manner, one might expect that a quasi-cylindrical vortex core calculation which began to indicate appreciable axial gradients, or a failure of the equations at that point, would in the physical flow correspond to vortex breakdown. Gartshore (1962) and Bossel (1971) introduced other assumptions on velocity profiles and even included reversed flow regions. Unfortunately, the differences between failure of the quasi-cylindrical approximations and the limit of the velocity distributions to describe the flow are difficult to interpret. Gartshore concluded that breakdown occurred because of a viscous diffusion of vorticity from the core of the vortex to the outer flow. Mager (1972) associated a singularity in the incompressible quasi-cylindrical momentum-integral solution with breakdown.

The concept of a critical state of the flow serves as a basis for several theories, all of which interpret this concept in a slightly different fashion. The ability of the flow to sustain an infinitesimal stationary sinusoidal disturbance, referred to as subcritical flow, or an infinite set of disturbances, supercritical, is the criterion used for breakdown. If the flow is at the point where it can just support a disturbance, it is termed critical. Squire (1960) interpreted this critical state in general terms stating that if standing waves can exist, disturbances downstream will propagate upstream and cause breakdown. Randall & Leibovich (1973) contend that this wave is in fact a finite amplitude wave.

Benjamin (1962, 1967) proposed that the critical state had an important but not exclusive role stating that breakdown was 'a transition between two states of axisymmetric swirling flow, being much the same in principle as a hydraulic jump...'. Upstream of breakdown the flow is supercritical and cannot support standing waves, while downstream the flow is subcritical and can support standing waves. He showed that the subcritical flow could be represented as a small but finite perturbation of the supercritical flow. In this way he countered Squire by proposing that the existence of these waves do not lead to breakdown, but that the leading standing wave is the breakdown phenomenon. Benjamin demonstrated that increasing the swirl of the flow causes the supercritical flow to approach the critical state and if increased enough, the flow will go subcritical.

Theoretical extensions of Squire and Benjamin based mainly on linear and nonlinear wave models were carried out by many investigators including: Leibovich (1970), Landahl(1972), Bilanin (1973), Leibovich and Randall (1973), Randall and Leibovich (1973). This critical approach was also exploited by Bossel (1969) who constrained the flow to a state of rigid rotation. He then imposed boundary conditions such that a stagnation point existed and found the flow to diverge and form a bubble. Larger upstream swirl formed a bubble easier and the form of the theoretical streamlines were similar to experimental observations. Bossel used the

ideas of Hall to estimate that a swirl angle, defined as $\tan^{-1}(V_z / V_x)$, of 54.8° anywhere in the

vortex would cause flow stagnation. Escudier (1983) goes a step further by proposing a two

stage, supercritical - supercritical / supercritical - subcritical, transition based on swirling tube

flows. The first stage of the transition is isentropic. The flow changes state from an initial

supercritical condition to a state that is also supercritical and can revert back to the upstream

flow. The second stage of the transition is non-isentropic, much like a hydraulic jump or a

shock wave, in which the flow transitions to the post breakdown sub-critical state. In addition,

his analysis suggests breakdown occurs for a unique swirl number, $\Gamma / \pi\, r_c U_\infty$, which is

equal to $\sqrt{2}$ for a Rankine vortex with an infinitesimally small core radius, r_c. He does

conclude, however, that a free breakdown must have a different character than tube flow

breakdowns.

Stability arguments for breakdown were proposed as early as 1916 by Lord Rayleigh. His

analysis indicated that a cylindrical flow with no axial motion was stable provided that the

derivative of the square of the circulation was positive,

$$\frac{1}{r^3} \frac{\partial(\Gamma^2)}{\partial r} > 0 \tag{1.10}$$

Extensions to this concept were proposed by Howard and Gupta (1962) in the form of

$$\frac{\frac{1}{r^3} \frac{\partial \Gamma^2}{\partial r}}{\frac{\partial V_x}{\partial r}} > \frac{1}{4} \tag{1.11}$$

to maintain stability to axial disturbances for cylindrical flows with axial shear components.

Leibovich and Stewartson (1983) introduced a criterion based on Rayleigh's arguments with

axial flow permitted for the centrifugal instability of columnar vortices in the form

$$V_{\phi} \frac{\partial \Omega}{\partial r}\left(\frac{\partial \Omega}{\partial r}\frac{\partial \Gamma}{\partial r} + \left(\frac{\partial V_x}{\partial r}\right)^2\right) < 0 \qquad (1.12)$$

where $\Omega = \Gamma D \Pi / 4Q$ is a dimensionless parameter introduced by Sarpkaya (1971) using the volume flow rate Q. This inequality is suggested to indicate massive instability and transition to turbulence at large Reynolds numbers if exceeded.

The hydrodynamic instability ideas put forth by Ludweig (1962, 1967) were based on a stability boundary he determined for inviscid flow in a narrow annulus. Accordingly he suggested that the vortex flow will be unstable to spiral disturbances if

$$\left(\frac{5}{3} - \frac{r}{V_\phi}\frac{\partial V_\phi}{\partial r}\right)\left(\frac{r}{V_\phi}\frac{\partial V_x}{\partial r}\right)^2 - \left(1 - \frac{r}{V_\phi}\frac{\partial V_\phi}{\partial r}\right)\left(1 - \left(\frac{r}{V_\phi}\frac{\partial V_\phi}{\partial r}\right)^2\right) > 0 \qquad (1.13)$$

Once the flow became unstable amplification of the spiral disturbances might occur which would induce an asymmetry on the core, leading to stagnation and breakdown. The explanations for a breakdown process involving spiral disturbances are not strong, however. No evidence points to the ability of weak spiral disturbances to cause asymmetry of the stable, axisymmetric, upstream core. Leibovich (1984) notes that the expansion of the vortex core after breakdown is a direct result of the mixing associated with the instabilities and turbulence. Therefore, whether these spiral instabilities are responsible for breakdown or not, they do play a role on the post breakdown flowfield.

The stability of the axial vortex structure has even been examined in light of tornado structures by Davies-Jones (1982). He comments on the ability of the vortex to sustain inertial wave motions because of its 'rotational stiffness', unlike a non-rotating, homogeneous, incompressible flow. Davies-Jones considers a flow where the centrifugal forces are balanced

by the radial pressure gradient and the angular momentum increases in absolute value away from the rotation center. If a fluid particle displaced radially outward, while conserving its angular momentum, it will experience a net force that will restore it to its original position. He notes that such a displaced fluid particle will actually oscillate about its equilibrium position until damped by viscous forces.

It has been observed that, when compared with experimental data, both Benjamin's criticality theory and Hall's quasi-cylindrical approach do predict the occurrence of vortex breakdown accurately in some cases. Neither is complete, however, in describing all the breakdown phenomena occurring in vortex tube experiments and aspects of both theories may be required, as well as instability arguments, for a complete model.

A recent study on the physical mechanisms governing vortex breakdown in confined cylindrical flows by Brown and Lopez (1988) introduces some interesting possibilities on the breakdown of delta wing vortices. Several extensive theoretical and numerical discussions on the aspects of this type of flow have been given by Turner (1966), Bode, Leslie, and Smith (1975), Rotunno (1979), and Wilson and Rotunno (1986). They deal more specifically with tornado flows and the insights on the behavior of vorticity are very valuable. The discussion of Brown and Lopez (1988), outlined below, presents a unique criterion based on the relation of the angle of the velocity vector to the vorticity vector on a stream surface upstream of breakdown. Variation of the problem parameters, especially the Reynolds number, has resulted in an axial flow deceleration great enough to sustain a stagnant flow region containing recirculating fluid and termed a vortex breakdown bubble. This phenomena is very similar in character to that seen in cylindrical tubes and over delta wings and so will be detailed below.

Brown and Lopez regard the breakdown region as a transition region from a concentrated vortical flow to a solid body rotation. Their basic argument is that the physical mechanisms involved rely on the production of negative azimuthal vorticity, that is

$$\eta = \frac{\partial V_r}{\partial z} - \frac{\partial V_z}{\partial r} \tag{1.14}$$

which results from a tilting and stretching of the predominantly axial vorticity vector, ζ. They further state that steady, inviscid, axisymmetric swirling flow can be viewed in three ways: an interaction between the total head and angular momentum of the fluid (both conserved on a stream surface), a balance between the radial pressure gradient and the centrifugal force, or in terms of the generation of azimuthal vorticity.

They addressed the question of why the strong vortical core diverges by considering the Euler equation of the radial momentum:

$$V_r \frac{\partial V_r}{\partial r} + V_z \frac{\partial V_r}{\partial z} = \frac{V_\phi^2}{r} - \frac{1}{\rho} \frac{\partial P}{\partial r} \tag{1.15}$$

Downstream from the point where the flow is cylindrical, $V_r = 0$, a divergence of the flowfield, $\frac{\partial V_r}{\partial z} > 0$, will occur only if the centrifugal force exceeds the pressure gradient (in the absence of viscous stresses). This process can be examined further from a vorticity point of view. Using circulation (angular momentum) and the total head respectively:

$$\Gamma = r \, V_\phi \qquad\qquad H = \frac{P}{\rho} + \frac{(V_r^2 + V_z^2 + V_\phi^2)}{2}$$

and substituting into the above equation of motion gives:

$$V_z \frac{\partial V_r}{\partial r} = \frac{\Gamma}{r^2} \frac{\partial \Gamma}{\partial r} - \frac{\partial H}{\partial r} + V_z \frac{\partial V_z}{\partial r} \qquad (1.16)$$

Employing the azimuthal vorticity, η, defined earlier yields:

$$V_z \eta = \frac{\Gamma}{r^2} \frac{\partial \Gamma}{\partial r} - \frac{\partial H}{\partial r} \qquad (1.17)$$

Rewriting this in terms of the stream functions:

$$V_r = \frac{1}{r} \frac{\partial \psi}{\partial z} \qquad\qquad V_z = -\frac{1}{r} \frac{\partial \psi}{\partial r}$$

keeping in mind that Γ and H are constant on ψ yields:

$$\eta = \frac{\Gamma}{r} \frac{\partial \Gamma}{\partial \psi} - r \frac{\partial H}{\partial \psi} \qquad (1.18)$$

Further manipulation leads to:

$$\frac{\eta}{\eta_0} = \frac{\sigma_0}{\sigma} \left(\frac{\alpha_0}{\beta_0} \right) - \frac{\sigma}{\sigma_0} \left(\frac{\alpha_0}{\beta_0} - 1 \right) \qquad (1.19)$$

where σ is the radius of the stream surface $r = \sigma(z)$ for a curve on which the stream function is a constant (i.e. $\psi(r,z) = \psi_1$). The terms α_0 and β_0 are defined as:

$$\alpha_0 = \frac{V_{\phi_0}}{V_{z_0}} \qquad \beta_0 = \frac{\eta_0}{\zeta_0}$$

and represent the tangents of the helix angle for the velocity and vorticity vectors respectively. The term ζ is the axial vorticity and the $_0$ subscript denotes a station upstream of the breakdown.

The essence of the above derivation is that η is dependent on the ratio of α_0 to β_0 and σ to σ_0. Brown and Lopez suggest that if an inviscid mechanism is the dominant factor, then a negative value of η is required to bring the axial velocity, V_z, to zero. The value of η only becomes negative for $\alpha_0 > \beta_0$ as the ratio of σ to σ_0 increases from unity, that is on a diverging stream surface. This negative η will induce a negative axial velocity leading to a further increase in σ and consequently a more negative value of η. It is this 'positive feedback' which may be responsible for the rapid spatial divergence of the core. Diverging of the core will continue until the negative η grows large enough to actually turn the flow back towards the axis.

Brown and Lopez then comment on how this type of mechanism would apply to pipe flows possibly to freestream swirling flows like delta wing flowfields. They state that upstream of the breakdown the flow is of a cylindrical nature and hence:

$$\frac{V_\emptyset^2}{r} = \frac{1}{\rho}\frac{\partial P}{\partial r} \tag{1.20}$$

To address the question of how breakdown is initiated, they assume $V_r = 0$ and distributions for $V_\emptyset$ and V_z based rimental data from the literature. expressions for η, ζ, and the ratio of α_0 to β_0 a n determined however the esence viscosity is required to allow the to evolve numerical is an flow would not change w based on the bound con e the ed swirling y state that it is the diffusion of axial which ay leads to

$$\frac{V_\emptyset^2}{r} - \frac{1}{\rho}\frac{\partial P}{\partial r} > 0 \tag{1.21}$$

They further anticipate it is this vorticity diffusion which leads to a radial redistribution of Γ and a stretching and tilting of vortex lines due to an increase of V_ϕ. This is followed by a reduction in the initially positive azimuthal component of vorticity with axial distance and the subsequent beginning of an 'inviscid breakdown' process. Leibovich (1984) also supports the concept of breakdown being essentially an inviscid process. A criterion for this breakdown process is that $\alpha_0 > \beta_0$ and although viscosity is required to initiate a reduction of η and V_ϕ and the initial divergence of the stream lines, the breakdown can be considered an inviscid process driven by the feedback mechanism described earlier. On delta wings, the radial and axial velocity distributions will establish a characteristic α_0 / β_0 for each angle of attack and be critical to the occurrence, location and strength of breakdown.

Although Brown and Lopez postulate that the breakdown processes is inviscid, the viscous interactions of the process can not be completely dismissed. Krause has performed an order of magnitude analysis that indicates that the increase in pressure in the axial direction, as the axial core flow stagnates, is a direct result of the viscous as well as inertial forces present in the core. Provided that the radial velocity components are small, this becomes a solely viscous process. He further shows that the outer portion of the vortex cannot support a pressure gradient along the axis if the radial distribution of the azimuthal (tangential) velocity component is equal to that of a potential vortex (i.e. a 1/r distribution).

A final remark is included here on studies performed in the area of tornado research, which has developed virtually independently from the research on delta wings. Similarities exist between these type of flows and those above a delta wing. Vortex breakdown phenomena have been observed, under laboratory conditions, in tornado vortex chambers (TVC) capable of simulating atmospheric tornados. These type of flowfields are generally characterized by a swirl parameter defined as

$$S = \frac{r_0 \Gamma}{2Q} \tag{1.22}$$

where r_0 and Q represent the inlet opening and flow rate of the tornado apparatus (Davies-Jones (1973)). The circulation, Γ, is determined in a plane normal to the vortex axis. Depending on the geometry of the apparatus, this can then be simplified further to the swirl ratio, V_φ/V_z mentioned earlier. An analysis by Walko and Gall (1986) indicates that breakdown of a tornado in a TVC is a direct result of viscous diffusion. They note that the axial pressure gradient is zero for highly swirling flows, but is strongly influenced by diffusion at lower swirls. In addition, the flow is strongly sensitive to the condition of the axial velocity component. Staley (1985) proposes that the principal source of kinetic energy for amplifying non-axisymmetric perturbations on a tornado flow is the radial shear of the axial flow, which, as noted previously, is the principal component of azimuthal vorticity for these types of flows. The axial vorticity term, which is related directly to the radial shear of the rotating fluid, then extracts energy from these perturbations. Further reviews of these studies can be found by Rotunno (1977), Howells, Rotunno, and Smith (1988), Pauley (1989). An extensive discussion on the physical phenomena associated with tornado morphology is given by Davies-Jones (1982).

1.3.2 Numerical Approaches

The advent of super computers have enabled researchers to extensively investigate numerical models of the three dimensional flows above a delta wing. The majority of numerical codes, excluding Navier-Stokes models, may be classified as either potential or Euler codes, using either a continuous vorticity distribution in the field or a vortex sheet method, as outlined by Hoeijmakers and Rizzi (1985). The former uses vortex sheets with a discontinuous velocity potential across them to model the free shear layers. Isolated line vortices are used for the cores.

The topology of the flow must be known quite well in advance as the rotational flow regions must be "fitted". The method is well established and the results for flows without breakdown are in reasonable agreement with experiments. Euler solutions are based on the Euler equations, allowing rotational flow everywhere, and capturing implicitly the vortical parts of the flow as the solution evolves. Two schools of thought exist with respect to the validity of utilizing these inviscid codes. A comparison of the results from various Euler solvers by Williams, Kordulla, Borsi, and Hoeijmakers (1990) with experimental data concluded that Euler methods are unsatisfactory in representing the flow due to their failure to represent secondary separation. Wagner, B., Hitzel, S. M., Schmatz, M.A.,Schwarz, W., Hilgenstock, A., and Scherr, S. (1988) reported, however, that reasonable agreement for overall pressure and force distributions between experiment and Euler code simulation is possible.

Predicting breakdown using Euler codes does appear to be possible, however. O'Neil, Barnett, and Louie (1989) have demonstrated a vortex breakdown effect above semispan models of 60° and 70° delta wings at Mach = 0.2 that closely follows experimental trends. They conclude breakdown is primarily governed by inviscid factors. Hitzel (1988) concludes that the Euler calculations indicate breakdown to be triggered by adverse pressure gradients and is independent of viscous effects. Further discussions on Euler simulations can be found in Hitzel, Wagner and Leicher (1986).

Navier-Stokes (NS) codes allow calculations to be performed in a less restricted way than the Euler equations. Liu and Hsu (1987) give a review of NASA contributions to three dimensional, incompressible, NS simulations of slender wing vortices. Krist, Thomas, Sellers, and Kjelgaard, for example used a thin layer approximation of the 3-D, time-dependent, compressible, laminar NS equations to compare with LDA measurements by Kjelgaard and Sellers (1990) about a 75° delta wing at an angle of attack of 20.5°, Re = 500000 and Mach = 0.3 . Even though the equations modeled a laminar flow, comparisons at a chordwise station of

70% were quite favorable. The maximum predicted velocity, however, was still found to be less than that determined experimentally.

Numerical breakdown results have been presented by Grabowski and Berger (1976) on an unconfined viscous vortex, using solutions of the full, steady, axisymmetric Navier-Stokes equations. They concurred with Hall (1972) in that breakdown is the result of a critical retardation of the flow. As well, the results showed that a vortex with sufficient swirl can be reduced to the critical breakdown state by diffusion of vorticity, a non-linear coupling of the axial and swirl velocities, flow divergence and pressure forces.

Ekaterinaris and Schiff (1990) used a Navier-Stokes code on a 75° sweep delta wing for $32° \leq \alpha \leq 40°$ to predict breakdown. Bubble type breakdown was observed on fine and coarse grids with no trace of unsteadiness. Indicators of breakdown, such as reversed axial flow and increases in surface pressure, along with diverging and coiling streamlines substantiated their arguments. Other NS studies which have predicted bubble and spiral breakdowns can be found in Fujii and Schiff (1989), Thomas, Taylor and Anderson (1987) and Hartwich, Hsu, Luckring, and Liu (1988). Axisymmetric vortex filament methods by Nakamura, Leonard and Spalart (1985,1986), employing experimental data for upstream conditions, have also been used to simulate both bubble and spiral forms of breakdown such as that observed by Faler and Leibovich (1978)

The use of non-dimensional parameters, in conjunction with Navier Stokes codes, has been shown to be very useful in predicting flow conditions and vortex breakdown. A reduced form of the steady, incompressible NS equations utilizing the Sychev (1960) parameter discussed previous, was computed by Dagan and Almosino (1989). Very good agreement with experimental data on delta wings with aspect ratios of 0.25 to 0.7 and α up to 30° was obtained provided the basic slenderness constraint on both the wing and the vortex was met. The major

assumption used a viscous, inner region dominated by the vorticity equation that was subsequently matched to an outer potential region.

Numerical experiments by Powell and Murman (1988) found that the level of the total pressure loss predicted in the vortex core was independent of the Reynolds number using a similarity Navier-Stokes solution. Their results matched the analytical results of Hall (1961) quite well, not all that surprising considering they restricted the flow to an incompressible, axisymmetric, conical, high Reynolds number flow with a slender core. Experimental comparison with Earnshaw (1961) showed an overprediction of the axial and tangential velocities as well as the radial total pressure distribution.

The effects of Reynolds and Rossby number parameters were investigated by Spall and Gatski to evaluate the NS equations formulated in terms of velocity and vorticity. The Rossby number is important in the study of the Coriolis force and inertial forces in large scale atmospheric fluid motions (Bode, Leslie and Smith (1975)). Although the Coriolis force is regarded as a restoring force, it can cause fluid particles to overshoot their initial locations and even set up waves in the resulting fluid motion termed 'inertial waves'. The Rossby number is defined as

$$R_O = \frac{U^*}{r^* \, \Omega} \tag{1.23}$$

where r^* is the radius of maximum swirl, U^* is the axial velocity at r^*, and Ω is the vortex rotation rate as $r \rightarrow 0$. If this is applied as a stability criterion to the theory of Squire (1960), R_O must be less than 0.56 theoretically to permit the existence of axisymmetric standing waves. Spall and Gatski found that since the local Rossby number should decrease near breakdown, and that the numerical tests reveal viscous diffusion increases R_O, it is necessary to impose an

external adverse pressure gradient to decrease R_0 with downstream distance, in order for breakdown to occur.

A parametric numerical study by Delery, Pagan and Solignac (1987) of the NS equations using velocity profiles of the form

$$V_x = 1 + (V_{x_{axis}} - 1) \, e^{(-Br^2)} \qquad V_\phi = \frac{\Gamma_0 (1 - e^{-Br^2})}{r} \qquad (1.24), (1.25)$$

indicated that there is a maximum value of the circulation, Γ_0, which will cause the flow to transition to breakdown denoted by a negative value of V_x in the computational domain. Breakdown was concluded to be an inviscid process and only a function of the strength of the vortex, provided the Reynolds number is large enough and the other parameters of the flow are held constant. A large sensitivity of the onset of breakdown to the axial velocity on the vortex centerline was also noticed.

Presently, it seems that none of these ideas are sufficient to accurately predict vortex breakdown on a delta wing over a wide range of conditions. Computational results have been seen to correspond to experimental data, however no theory exists which can yield the flow detail in the breakdown zone nor universally predict breakdown locations which consistently compare with experimental results. In addition, the experimental data is not always completely consistent across different investigations. Thus it is essential that further studies be conducted in an effort to uncover information which may shed light on this problem.

1.3.3 Experimental Studies

Researchers have conducted a wide variety of investigations to measure the vortex flowfield and to observe the onset of breakdown. A summary of relevant studies and contributions is presented here. Discussion of results directly comparable to the present study will be made, where applicable, in Chapter 5. A list of specific measurements on delta wings and their associated geometries can be found in Appendix A.

Vortex breakdown was first detected by Peckham and Atkinson (1957) over a highly swept delta wing at large angles of incidence. This phenomena was also seen to occur elsewhere as noted by Smith and Bessemer (1959) in aircraft trailing vortices. Since parameter variation and flow control could be defined much easier in confined flows, a great majority of tests have been conducted in swirling pipe flows. The asymmetries present in delta wing flows are removed and the numerical results are more comparable. The results of these studies will be detailed first.

1.3.3.1 Tube Flows

Some of the first experiments on swirling pipe flows were conducted by Harvey (1962) using flow drawn radially inward through a set of vanes and into a tube. He observed that variation of the swirl of the flow indicated breakdown to be an intermediate stage between two types of flow: those that exhibit axial velocity reversal and those that do not. Harvey also concluded that, because the observed breakdown could revert back to the upstream conditions via the introduction of a favorable pressure gradient, the reversible breakdown process represents a division between subcritical and supercritical regimes and is not an instability process. An instability would grow unchecked and lead to an irreversible process.

Analytical profiles of the form,

$$V_x = V_{x1} + V_{x2} \, e^{(-\alpha r^2)} \qquad\qquad V_\emptyset = \frac{\lambda(1 - e^{-\alpha r^2})}{r} \qquad\qquad (1.26)\,,\,(1.27)$$

equivalent to that presented by Batchelor (1967) above, fit Harvey's (1962) data quite well, as noted by Leibovich (1984). Recall that this is the same analytical profile as that in Figure 1.5. The major difference between these types of flow and that above a delta wing, apart from the physical wall boundary, is that the core size is a function of the boundary layer shed by the centerbody of the apparatus. Hence, both the flow rate (Reynolds number) and the vane angle contribute to the amount of vorticity in the core, unlike sharp-edged delta wings, where Reynolds number effects appear to play a negligible role above a critical value.

The effect of instabilities on stationary breakdown was investigated by Sarpkaya (1971) in a series of experiments in a conical tube apparatus. He noted from motion pictures that a toroidal vortex ring, with an axis gyrating at a regular frequency about the bubble axis, appears to empty and replenish fluid in the breakdown bubble. Variation of swirl and Reynolds number produced spiral and bubble forms, including a double helix form with no stagnation point. Sarpkaya (1971) felt breakdown did not depend on a single mechanism, but resulted from hydrodynamic instabilities, depending on the combination of Reynolds number and circulation of the flow. He concluded (1971) that his observations are in perfect accord with Benjamin's theory, and no other theory can account for this itself. Further experiments on the effects of adverse pressure gradients by Sarpkaya (1974) indicate that the effect of increasing this parameter has the same result as increasing the circulation or the mean flow rate.

Six distinct types of vortex tube breakdown modes were isolated by Faler and Leibovich (1977), including those categorized by Sarpkaya (1971,1974). A schematic of these forms of

breakdown is given in Figure 1.15. For all the breakdown cases observed, the flow was laminar upstream of breakdown and turbulent shortly downstream of the breakdown region. Increasing the Reynolds number, based on tube diameter, or the swirl angle, caused each type of breakdown to be seen in a repeatable succession. The highest Reynolds number (about 8000 based on the tube diameter) and swirl angle gave rise to the bubble form of breakdown. Type 0 refers to the so-called axisymmetric mode. A stagnation point on the axis is followed by an abrupt expansion around a bubble of recirculating fluid. For low circulation rates and higher Reynolds number, the type 0 form alternated with the type 1, which has a slight asymmetric, ragged nature that tends to break up into a turbulent wake. Four others types representing a variation on the spiral structure. The spiral type of breakdown, type 2, occurred at lower Reynolds numbers and is marked by an abrupt kink of the fluid along the vortex axis. At the lowest values of swirl and Reynolds number, the type 6 form appeared. The vortex filament was moved gently off the axis, expanding in radius, until it nearly reached the tube wall. The filament would also, at times, shear into a tape as it moved off axis. The type 5 form evolves directly from the type 6 when another shearing branch forms and they wind around each other in a double helix fashion. The type 6 could also evolve into a type 4 where the filament or tape would roll back onto itself up to the point of deflection. After a time fluid would be ejected from this recirculating zone and the type 4 flattened bubble form would be fully developed. Type 3 was a combination of 4 and 2. It should be noted that types 4, 5 and 6 only occurred at relatively low tube Reynolds numbers of about 2500. Faler and Leibovich (1977) draw several strong conclusions from this study. First, all flows that exhibit axisymmetric, type 0 and 1, or spiral, type 2, breakdown are supercritical upstream in the sense of Benjamin (1962). Secondly, flows that subsequently undergo breakdown are all stable to infinitesimal, inviscid disturbances, including axisymmetric and non-axisymmetric perturbations. Finally, no axisymmetric disturbance patterns exist in these flows.

Type 0 not closed, asymmetric exit

Type 1 large scale turbulence

Axisymmetric forms

Type 2 spiral in same sense as base flow rotation

Type 3

Type 4 flattened bubble

Type 5 double helix

Type 6 large amplitude, off axis displacement
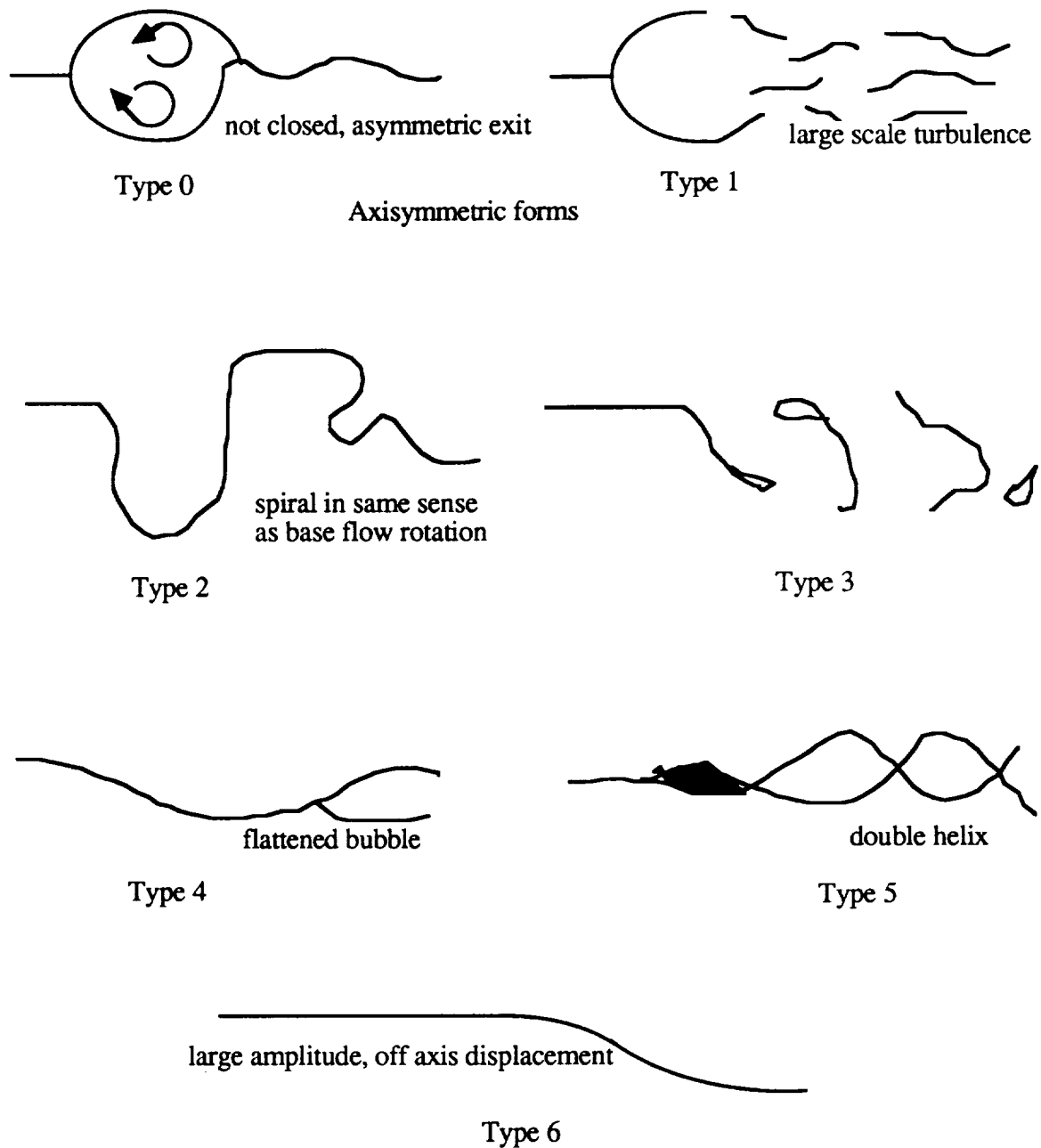
Figure 1.15 States of Tube Breakdown

Laser Doppler anemometry experiments provided, for the first time, precise data on the velocity field of the vortex and the accompanying breakdown region. Initial investigations were carried out by Faler (1976), Faler and Leibovich (1977,1978), Garg (1977), and Escudier et al. (1980). Analysis of this data enabled Leibovich (1983) to determine the vortex status at any

point as subcritical or supercritical and the results agreed reasonably well with vortex tube experiments. Leibovich (1984) argues that these two, visually different forms of breakdown, spiral and bubble, are indeed different because of their different expansion ratios and the imposed upstream conditions. Sarpkaya (1971) has shown in his conical tube apparatus that increasing swirl from zero causes the spiral form to occur first at a particular mean location. At some larger value of swirl, the form will switch to the bubble form, several core diameters upstream of the previous location. This discontinuity is proposed by Leibovich to be a strong reason for considering these two types of breakdown to be truly distinct. He also concludes from stability arguments (1984) that the bubble breakdown contains less stable wake and approach flows than the spiral form.

Laboratory experiments have also been carried out in cylindrical tanks having a jet issuing fluid tangent to the outside wall to simulate vortex behavior. Velocity profiles measured by Escudier, Bornstein and Maxworthy (1982) were found to be qualitatively similar to those measured above delta wings. A profile of the form

$$V_\phi = \frac{\Gamma_c}{2\Pi r} (1 - e^{-r^2/r_o^2}) + \frac{\omega r}{2} \qquad (1.28)$$

was found to fit the data satisfactorily. It was noted that there was no flattening of the axial profile. The implication of this is that since $\partial V_x/\partial r$ still existed, so did the azimuthal vorticity component and, thus, there was no external irrotational flow present anywhere.

Further tests by Escudier and Zehnder (1982) with their tangential jet entry device have shown that a simple parameter, $Re\Omega^3 R =$ constant, R being a dimensionless parameter based on the geometry, correlates the conditions for breakdown at a fixed axial location in their apparatus. In the swirl vane generators, this becomes $Re\Omega^2 =$ constant. This formulation breaks down, as

pointed out by Leibovich (1984) since bubble and swirl breakdowns have different locations as a function of Re and ω in swirl vane devices. The most interesting aspect of the results of Escudier and Zehnder is that they noted an opposite sense of rotation of the spiral rotation to the rotation of the base flow. As mentioned previously, the spiral form of the breakdown continues to wrap about the core axis for several revolutions. Experiments in swirl vane generators have shown the sense of rotation of the tracers in the flow to be the same as that in the upstream flow. Spiral breakdown of leading edge flows, as shown by Lambourne and Bryer (1961), have a sense of rotation of the core filament, in the same manner as the tangential jet entry device, that is, opposite to that of the upstream swirling flow.

1.3.3.2 Delta Wing Flows

Many studies have been performed on delta wing planforms. Their empirical behavior is well documented under a range of various conditions. Based on research cited in the literature, Payne (1987) has reviewed the major factors which can influence the breakdown of vortices above delta wings. This is summarized below followed by a brief discussion on particular studies relevant to the present efforts

The actual position of this breakdown is a strong function of the pressure gradient along the vortex, the initial axial core velocity, and the angle of sideslip, or yaw angle. Increasing the sweep angle or decreasing the angle of attack causes the location of the breakdown to move aft. The breakdown position will move forward during flow acceleration and remain so until the steady speed condition is reached, whereupon it returns to its normal breakdown position as noted by Lambourne and Bryer (1961). The reverse is true for deceleration. An increase in the swirl of the flow or a larger adverse pressure gradient tends to promote the onset of breakdown. Thicker wings, rounded leading edges, lower Reynolds numbers, and of course more complex

geometries can also substantially influenced the location of breakdown. Comparison of the seven hole probe and LDV data acquired by Payne (1986,1987) with the present study will be made on an individual basis in Chapter 5.

Payne also summarized the effects reported to have a minimal effect on breakdown. Reynolds number effects on the flow are small at higher Reynolds numbers, but the effects on position and strength of the leading edge vortices become more pronounced at low Reynolds numbers, that being below $Re_c \approx 100,000$. This applies to sharp edged, thin delta wings at moderate angles of attack. A study using a flat, 63° sweep delta wing by Schrader, Reynolds, and Novak (1988) revealed the major influence of Reynolds number to be in the viscous secondary separation region and that the overall aerodynamic forces were influenced only slightly. Wing stall characteristics were weakly dependent on Reynolds number, but strongly affected by Mach number. A slight lift decrease was noted at the higher Reynolds numbers, but the slope of the lift curves remained unchanged. Extensive water tunnel tests by Erickson (1981) have shown vortex generation, sheet and core location, as well as vortex strength are accurately reflected in a water tunnel due to the insensitivity of the separation point location to Reynolds number changes. Erickson (1982) notes, however, that correlations are best at high angles of attack.

The geometry of the wing can play a key role in determining the resulting delta wing field. A thickening of the delta wing has been seen to reduce the strength of the leading edge vortices and the non-linear lift components as noted by Peckham (1958) and Squire (1967). The loss of lift is associated with a decrease in $dC_L/d\alpha$ resulting from a weaker vortex system. The angle of incidence for a certain lift therefore increases and a smaller lift to drag ratio results. Squire (1967) did note an increase in the stability as the loss of lift occurred over the forward part of the wing.

Hummel and Srinivasan (1967) found that increasing the aspect ratio of delta wings causes the effects of breakdown on the lift and moment to occur at lower angles of incidence and that these effects are decreased as the aspect ratio increases. They also feel the cross sectional shape of even thin wings has a considerable influence on the breakdown position. Zohar and Er-El (1988) note that the effect of breakdown on the suction induced by the leading edge vortices is lower for higher aspect ratio (lower sweeps), while the lift to drag ratio is seen to increase. This was deduced from surface pressure measurements on delta wings of 55°-75° sweep. Earnshaw and Lawford (1964) noted a gain in the lift with a convex surface on the suction side of the wing. Lambourne and Bryer (1961) demonstrated how longitudinal camber can delay breakdown, presumably because of the beneficial pressure gradients induced .

Conversely, Wentz and Kohlman (1971) observed that variation of the trailing edge geometry of 70° sweep delta, diamond and arrow planforms, had a negligible effect on vortex breakdown location. Previously (1969), they noted that the vortex breakdown region crossed the trailing edge at the same angle of attack for all these trailing edge configurations. Thompson (1975) noted the effect of cropping a 75° sweep delta by 40% resulted in breakdown location differences of ± 2.5% x/c in a water tunnel.

The leading edge shape of the delta wing has also been seen to have a considerable effect on the position of the vortex breakdown region. As early as 1955, Bartlett and Vidal determined that bevelled edge wings produced a higher value of C_{L_α} than rounded edges. Squire (1967) determined that a blunter leading edge causes a decrease in the lift curve slope on sharp edged delta wings with an aspect ratio of 4/3 ($\Lambda = 71.6°$). He found the loss of lift was large and occurred near the apex as indicated by the change in pitching moment. Squire also comments that the scale of the vortex flow at the apex is on the order of the wing thickness and that the blunting retards the initial vortex development, whereas further aft the vortex is too large to be influenced by leading edge details. Kegelman and Roos (1989) investigated leading edge

geometries, ranging from blunt rounded edges to leeward and windward bevels, and found the breakdown location to be strongly affected by these geometric variations. Sharp edged wings with a positive leading edge camber were seen to give the greatest vortex lift and the strongest post stall behavior. The breakdown position does seem to be independent of the turbulent breakdown of the shear layer near the leading edge. Attempts at altering the leading edge by Lambourne and Bryer (1961), including a trip wire on the upper surface had no significant effect.

This breakdown of the vortex structure is seen to occur not so much at a point, but over a region. Lambourne and Bryer (1962) describe three stages of vortex breakdown: flow deceleration, spiral deflection, and breakdown to full scale turbulence. Measurements by Payne, Ng, and Nelson (1987) and others have found the vortex core region to indeed transform from a jet-like to a wake-like flow over a spatial region when breakdown occurs. The actual location of the breakdown region also tends to vary, within 5% of the chord. Faler and Leibovich (1977), in vortex tube experiments, describe the location of the breakdown as only quasi-steady in the axial location. The breakdown almost continually drifted back and forth along the core axis. The axial extent and velocity of the drift was seen to increase with increasing Reynolds and circulation numbers.

The pressure field above the delta wing and the external pressure gradients imposed by the test section have been an area of extensive testing. Pressure measurements in the vortex core by Lambourne and Bryer (1961) for the 65° sweep wing at $\alpha = 15$ indicated that while both the static and total pressure fell as distance aft of the apex was increased, and most sharply at the apex, the total pressure was seen to have a nearly constant value along the length of the vortex at roughly $C_{pt} = -5.0$. Lambourne and Bryer state that the pressure distribution along the axis depends on three factors

i)   increasing vortex strength tends to provide a falling axial pressure

ii) diffusion of vorticity in the viscous core provides a rising pressure

iii) deceleration of the longitudinal velocity component in the irrotational flow region tends to cause a rise in the axial pressure. The trailing edge can cause such an effect because of the pressure recovery experienced at the trailing edge. They suggest the pressure changes sensed in the core are amplified above what is experienced in the outer flow.

In contrast to the data of Lambourne and Bryer (1961), Naarding and Verhaagen (1988) reported a drop in the axial total pressure with increasing x/c as well as a sharp drop near the apex. They comment that the difference is because their probe was on the order of the viscous core size and Lambourne and Bryer's probe was an order of magnitude smaller, due to the larger wing used by Lambourne and Bryer. The better resolution of Lambourne and Bryer would explain their lower pressure values, but does not explain the reduction of values as Naarding and Verhaagen move closer to the apex. Smearing of the pressure profile due to a locally large probe size, would result in higher pressures, not lower.

Kegelman and Roos (1990) noted the total pressure loss in the core of 60° and 70° flat plate delta wings with a 25° bevelled windward edge to be the same at all chordwise locations for a constant angle of attack. The peak loss value was seen to increase with angle of attack and the 60° vortex structure was concluded to be stronger than the 70° because of a higher peak vorticity. Surface pressure measurements also indicated a stronger suction peak for the 60° wing until the occurrence of breakdown. The effect of Reynolds number was examined and found to have almost no effect on core trajectory, breakdown location or aerodynamic loading. At high α, C_{Lmax} is seen to decrease slightly. Below this, the net loading does not change for increasing Reynolds number despite an outboard shift in the secondary separation point.

LDA measurements were made by Pagan and Solignac (1986) on a vortex generated by a 75° sweep delta wing at $\alpha = 19.3°$ and allowed to enter a two dimensional variable pressure

duct. They noted large amplitude low frequency oscillation in the region of flow just in front of the breakdown bubble. They also determined that the flow behaves in an Euler form outside and inside the recirculation bubble by computing the difference between the pressure gradient and the cross product of the velocity and the vorticity vectors, the only terms in the Euler approximation of the equations of motion. A difference of zero indicated the flow to be behaving in an Eulerian sense. This condition was not verified, however, along the relatively thin interface layer at the outer boundary of the recirculation zone. This interface boundary also exhibited very high axial velocity fluctuations. Further tests to examine adverse pressure gradient effects were made by Delery, Pagan and Solignac (1987) with the same apparatus at α = 27.5°. A close correspondence was found between the pressure gradient and the vortex strength as given by the local swirl velocity in Figure 1.16.
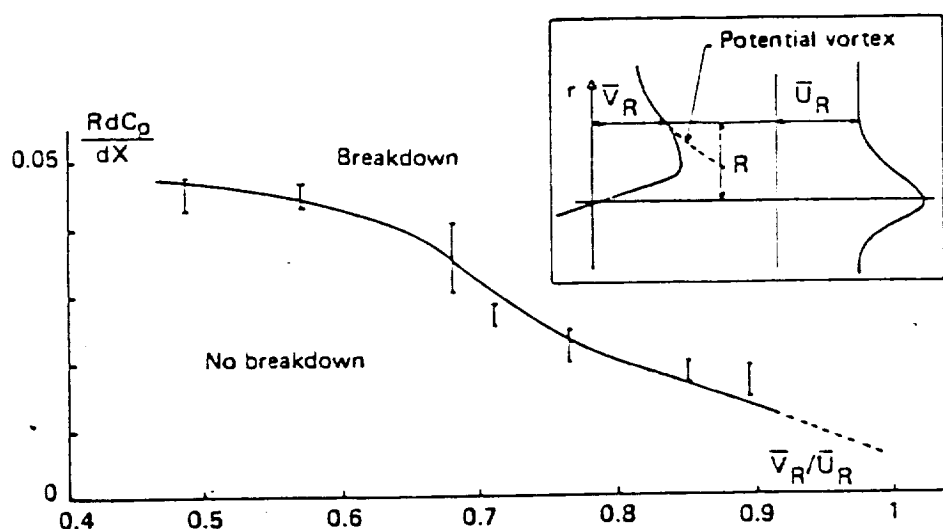
Figure 1.16 Effect of Adverse Pressure Gradient and Swirl on Breakdown

(Delery, Pagan and Solignac, 1987)

A limit to the vortex strength was found, beyond which breakdown occurred even in the absence of an adverse gradient. Further analysis of the data at 19.3° revealed a breakdown oscillation of about 8 Hz. Earnshaw and Lawford (1964) observed low frequency force fluctuations for sweep angles less than 65° at low angles of incidence. Higher sweep angles

reduced these fluctuations and if $65° < \Lambda < 76°$ no fluctuations were seen until maximum lift was achieved.

The stability concepts put forth by Ludweig (1961) were concluded to be experimentally supported by Engler (1988). He states that Ludweig's stability theory is correct based on an opto-acoustic technique of measuring the stability parameter in the flow field above a 68° sweep delta wing. Flow visualization by Lowson (1988) on 70° and 80° sweep wings at Reynolds numbers of 3000 to 20,000 points to quasi-two dimensional instabilities existing in the shear layer leaving the leading edge. A second local streamwise instability was also seen to be present and both instabilities were inhibited by the vortex stretching and wrapping process. The frequency of this leading edge shedding followed a $Re^{0.5}$ law in the same form observed by Gad-el-Hak and Blackwelder (1985). Ng (1989) points out, however, that the boundary layer thickness is varying continuously along the leading edge. Since the shear layer thickness is dependent on the boundary layer thickness just prior to separation, and the characteristic velocity is constant along the leading edge, any shedding frequency should vary according to position.

Studies concerning the secondary vortex have not been nearly as extensive as those centered on the primary structure. The influence of the secondary vortex structure and its separation location on the overall flow has been investigated by Hummel (1979), who carried out extensive tests on an aspect ratio 1 (sweep = 76°) flat plate delta wing including balance, pressure and boundary layer measurements. He reported that the presence of the secondary causes a displacement of the primary vortex inwards and upwards and that the presence of the secondary vortex locally increases suction on the surface below it. These effects are small for turbulent boundary layers, but large for laminar. Also, Hummel noted that the trailing vortex forms in a rotation sense opposite to the leading edge vortex.

Kjelgaard and Sellers (1990) obtained a series of measurements above a 75° sweep wing, including LDV, five hole probe and surface visualization. They confirmed the transition of the boundary layer to occur at a Reynolds number

$$Re_t = \frac{x_t U_\infty}{\nu} \qquad (1.29)$$

where x_t is the streamwise distance from the apex to the transition point, of Hummel (1979) as being approximately 800,000 - 900,000. The transition of the boundary layer from laminar to turbulent shifts the secondary separation point outboard. Naarding and Verhaagen (1988) found this transition Reynolds number limit to extend to about 2 million for their biconvex wing at lower incidences. Carcaillet, Manie, Pagan and Solignac (1986) noted the beginning and end of the transition region which, from their tests lies roughly between that of Hummel and Naarding and Verhaagen. Naarding and Verhaagen note that for wings of aspect ratio 1 ($\Lambda = 76°$), if the Reynolds number based on the root chord is below 500,000 the entire boundary layer on the upper wing surface can be expected to remain laminar.

Increasing the Reynolds number was seen to move the mean boundary layer transition point towards the apex as reported by Carcaillet, Pagan and Solignac (1986) from tests on a 75° sweep flat plate delta. They comment on the non-conical nature of the flow, this being much more evident in the core pressures than the velocities. Measurements with a 3-D LDV indicated large turbulence levels in the primary, the feeding sheet, and large shear stresses in the region between the feeding sheet and the secondary vortex.

Breakdown correlations are continually being offered as a means for prediction of breakdown. The swirl angle was one such parameter mentioned previous. Hawk, Barnett, and O'Neil (1990) further analyzed the data acquired by Kegelman and Roos (1990). They point

out that conventional models of the fields would give swirl angle distribution contours as concentric rings, growing in magnitude away from the vortex model, and reaching a maximum at the outer edge of the core. No such pattern was evident. They observe most local swirl angle values are greater than 45° in the vortex burst region. These maximum swirl angles tend to occur in the shear layer and not the rotational core, maintaining constant values along the wing, even though the vortex strength is increasing. In addition they appear to be independent of the wing sweep, angle of attack, or loading.

Cornelius (1990) has examined the effect of the Rossby number and a second Rossby parameter, defined as

$$R_\Omega = \frac{U_c}{\Omega \; r_v} \qquad\qquad R_{mr} = \frac{\int_{A_\xi} U^2 \; dy \; dz}{\int_{A_\xi} V_v{}^2 + W_v{}^2 \; dy \; dz} \qquad (1.30)\,,(1.31)$$

respectively, where r_v is the radius of the core vorticity $= \sqrt{A_\xi /\pi}$ where Ω is the rotation rate defined from the integrated axial vorticity, U_c is the axial velocity, A_ξ is the area encompassing the axial vorticity, and V_v and W_v are the mean velocities in vortex coordinates. He concludes that $R_\Omega \geq 0.55$ and $R_{mr} > 1.0$ will lead to a growth of spiral instabilities while for $R_\Omega \geq 0.55$ and $R_{mr} \leq 1.0$ the bubble form is imminent. Note the difference in Cornelius' definition of this parameter from that of Spall and Gatski. The Rossby number has also been defined for atmospheric vortex structures as

$$\text{Rossby Number} = \frac{V_{\phi max}}{\Omega \; r_c} = \frac{\text{maximum tangential velocity}}{\text{average vorticity * core radius for } V_{\phi max}}$$

where values of 10^4 for tornados and 10^2 for mesocyclones have been reported by Davies-Jones (1982). The implications of the Rossby parameter will be examined further in Chapter 2.

Lambourne and Bryer (1961) have conducted tests in wind and water tunnels using various flat and cambered plate geometries and noted a correlation of the breakdown position with the parameter involving the wing sweep and the angle of attack, defined as $\gamma = \cos^{-1}(\cos\alpha\ \sin\Lambda)$. This parameter indicated a correlation of the data taken on their swept wings of $55°$ to $70°$. They suggested, on the basis of their tests, that breakdown is not based on the amplification of small upstream disturbances. They also determined that the total pressure in the core and the adverse pressure gradient along the axis, which can be altered by the geometry of the wing or externally to the field, are essential factors in causing breakdown to occur. Although no measurements were made, the proportionality of the core radius to $\sqrt{vc/U}$ was proposed. Earnshaw and Lawford (1964) noted that at moderate incidences, the location of the surface flow separation and attachment lines were seen to correlate in a linear fashion with $\alpha\tan\Lambda$, indicating the flow behaves in a roughly conical fashion.

Finally, a swirl type correlation for experimental data based on the parameter

$$S = \frac{(dw/dr)_{r=0}\ ^r w_{max}}{u_o U} = \frac{1.994}{\lambda u_o}\sqrt{\frac{k}{P}} \tag{1.32}$$

which is defined on conditions in the core, was presented by Wilson (1977). The parameters k and λ were supplied by a subsonic potential flow panel method. The dependence of this parameter on the angle between the wing leading edge and the freestream, $\emptyset = \cos^{-1}(\cos\alpha\ \sin\Lambda)$ was seen to follow a bounded linear distribution.

Many efforts have been aimed at uncovering the physics behind the vortex breakdown phenomena. The ability to predict the location of vortex breakdown, theoretically, numerically or from experimental data with a high degree of proficiency is very desirable. As can be inferred

from the above discussion, investigative results, both experimental and numerical, are not always conclusive and have even led to contention on particular aspects of the problem. There are certain aspects, however, upon which every one agrees.

The flow upstream of breakdown on a delta wing can be modeled well by a number of different methods, both analytically and numerically. Comparison with experimental data away from the apex and trailing edge regions indicates very good agreement. The tangential velocity profile, for example, can be approximated quite well with a simple exponentially declining $1/r$ distribution. Aerodynamic forces can also be predicted very well within a certain angle of attack regime. Overall, investigators agree the delta wing vortex flow follows a conical fashion. The subcore, however, is often assumed to be cylindrical when used in computational schemes, but this assumption has yet to be suitably quantified empirically.

The prediction of the breakdown phenomena and the resulting changes in the flowfield structure does not compare consistently with empirical data. As can be expected, breakdown prediction is the area where the most disagreement arises with respect to what is physically occurring. Numerical results are typically qualitative both in location and flow features. It would appear that the use of any flow approximation short of a full Navier-Stokes code is insufficient to model the physics of the flow behavior at breakdown. Euler codes can not account for diffusion, boundary layers or transition phenomena and appear capable of only predicting pre-breakdown flows with a high degree of confidence. The breakdown itself may behave in an inviscid manner, but some type of viscous interaction to approach the state needed to breakdown seems to be required.

Understanding a fluid phenomena, such as vortex breakdown, demands a strong understanding of what is physically occurring. The relation of the strength of the vortex to the associated axial flow, for instance, is critical to the state of the vortex. The axial velocity is in turn

is affected by the external flow conditions which are not always documented in experimental studies. Anything that alters the local pressure gradient along the axis and therefore affects the axial velocity can have profound effects on breakdown. This ranges from the local planform camber to the tunnel pressure gradient. Most of the concepts on the flow state prior to breakdown are theoretical in form and have not been verified experimentally, but investigators agree that the flow must reach some critical form which then transitions to a state that will initiate breakdown. Certain physical features of the breakdown have only been addressed only at an empirical level, such as the types of breakdown, but these features may have a minimal effect on the overall flow. Bubble and spiral forms are seen on a delta wing, yet the post breakdown flow behaves in the same manner far enough downstream of the breakdown zone. On the other hand, there could be more substantial physics involved. The sense of the spiral breakdown, for instance, is opposite to the rotation of the primary vortex on a delta wing, but carries the same sense for a breakdown in a tube.

No standards for theoretical or experimental parameters exist that describe the flow state in a manner consistent enough to indicate the onset of breakdown, except for perhaps the swirl angle. Even this value is subject to dispute, varying from as much as 42 to 52° in the flow measured directly preceding breakdown. In addition, the swirl angle does not account for any local pressure field and is a point property as opposed to an integrated field effect, which may not be truly representative of the flow. If the combination of certain measured flow features, perhaps in the form of some parameter, could indicate the state of the flow at a particular chordwise station, and if their values changed in such a way in a downstream direction to approach a limit, breakdown could also be predicted. The following chapter outlines this line of reasoning.

CHAPTER II

A PATH FOR THIS STUDY

2.1 Characterizing the Onset of Breakdown

The motivation for the majority of delta wing research is to determine why the leading edge vortex structure breaks down. The present study falls under this umbrella as well and poses several questions as a more concrete basis for direction. What is occurring in the flow that prevents the vortex structure from remaining in its pre-breakdown state? For that matter, what keeps the vortex in its pre-breakdown state in the first place? Is it possible to define the conditions on the flowfield in such a way as to tell when the breakdown process will occur? Are there physical quantities that can be measured that will indicate the state of the vortex?

The following discussion examines these concepts. First, some general comments on the use of particular parameters to evaluate the vortex flowfield are made. A specific look is then taken at the nature of the vorticity field above a delta wing and what light may be shed on the nature of breakdown by a more in depth study of this property. Finally, the specific goals and objectives of this study are outlined.

In broadest terms, the vortex flowfield can be regarded as a transition from one flow state to another which may occur as a result of a combination of certain flow parameters reaching a critical or unstable state. One can attempt to quantify such critical breakdown parameters in two forms: as a function of either the independent or the dependent variables. The former would involve factors such as angle of attack, sweep angle of the wing, and sideslip. An indication

parameter involving dependent variables would be based upon flow conditions resulting from the geometry of the problem such as the local condition of the adverse pressure gradient or the local vorticity.

From the review in Chapter 1, the determination of such breakdown indication parameters could be based on several forms including

    i.   A local balance of the pressure forces with the acceleration of the fluid.

    ii.   A local balance between the generation and convection of vorticity.

    iii. The size of the local length scale compared to the wing geometry.

    iv. A relation based on external pressure gradient, wing geometry, angle of attack, etc.

The conditions at breakdown can also be used to establish an empirical criterion for the onset of this phenomenon. Then, given the relevant parameters of the flow, either from a geometrical standpoint (alpha,sweep angle) or a consideration of the flowfield (vorticity, circulation, local pressure distribution), the position of breakdown could be determined. Any of these factors can also be examined in a chordwise progression to see how they vary up to, and beyond, breakdown. The swirl angle criteria is an example of one such a consideration.

This development of a parameter can also be approached using similarity arguments. A function can be generated by considering the variables which are important to the flow field and then constructing a non-dimensional parameter (or set of parameters) which would indicate more precisely the conditions leading to breakdown. This more rigorous means has been demonstrated by Sychev (1960) and then Hemsch (1988) as noted earlier.

The delta wing flowfield also contains factors which are difficult to quantify. The complete role of the secondary vortex, which is a direct result of the viscous nature of the flow, is not well

understood. Both the primary and secondary port side vortex structures are illustrated in Figure 2.1 using a titanium tetrachloride vapor method for marking vortical flows by Visser, Nelson, and Ng (1988).
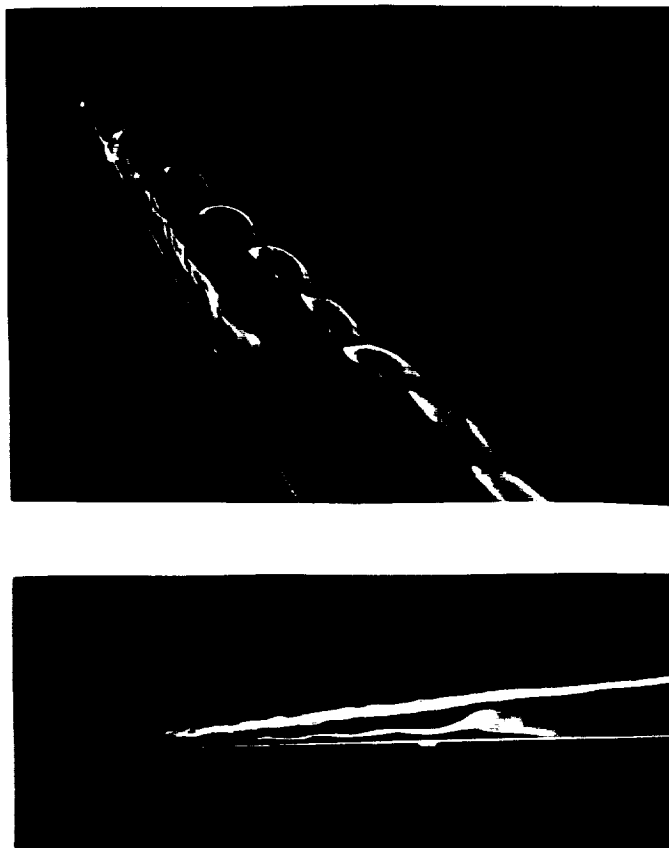
Figure 2.1 Visualization of the Secondary Vortex on a 70° Delta Wing

The coherent behavior of the primary vortex in Figure 2.1 is reflected in the secondary, but with an opposite sense of rotation. It appears that the secondary vortex undergoes a change, visually resembling the breakdown phenomena of the primary vortex, well before any such occurrence in the primary vortex. The secondary does, however, retain a vortical flow behavior aft of this point, as will be detailed in the present measurements. Reported characteristics of the secondary vortex also include displacing the primary vortex inwards and upwards. Its behavior is also dependent on the Reynolds number, especially for transition to a turbulent boundary layer. Questions still

remain, though, as to the effect, if any, of the secondary vortices on the magnitude of the primary vortex pressure peaks when compared to an Euler type solution. Even more nebulous concepts, such as the effect of the secondary vortices on the vorticity distribution above the wing, remain to be investigated.

Although the data base of delta wing flowfield information is growing, most experimenters are constrained to a specific configuration at a fixed angle of attack or chord location. This information, helpful for the sake of comparison, provides little or no information on the changing flow field state in the chordwise direction. Aspects such as rate of vorticity generation or circulation distribution in the streamwise direction are impossible to address.

Other subtler reasons also exist which make comparison difficult. Data compiled from several different investigators (Kjelgaard and Sellers (1988), Verhaagen (1990), Carcaillet, Manie, Pagan, and Solignac (1986), Pagan and Solignac (1986)) are compared in Table 1. The sweep angles and the angles of attack are roughly the same. The values of vorticity presented are the maximum values found in the flow field and coincide with the core axis. Typically, investigators use the model root chord, c, and the freestream velocity, U_∞, as nondimensionalizing scales for the flow. The results are seen to vary quite substantially. The local semispan, s* could also be considered a viable length scale, since flow visualization indicates the vortex structures scale with the wing geometry. Use of the local semispan would account for local geometric changes due to sweep angle and allow for comparison of data taken at different chord stations. The data of Kjelgaard and Sellers (1988), for example, indicates a lower value of vorticity than that of Payne for a location 20% farther from the apex. If s* is used as a scaling factor, the magnitude of the axial vorticity component is seen to exceed that of Payne. It is also noted that identical geometries, such as that of Payne and the current investigation, have produced different values of the axial vorticity component. These differences indicate there are other factors which have not been taken into account and add to the difficulty in obtaining a clear picture of the physics involved. A closer

examination of the grid resolution of each investigation, indicated in the last column of Table 1,

provides some insight. The highest derived vorticity values correspond to the finest grid resolution

Investigator	Angle of Attack (°)	Sweep Angle (°)	Chord (mm)	Freestream Velocity U_∞ (m/s)	Chordwise Station x/c	Maximum Vorticity Ω_x (1/s)	$\dfrac{\Omega_x c}{U_\infty}$	$\dfrac{\Omega_x s^*}{U_\infty}$	Measurement Grid Resolution (y/s)
Payne	20.0	75	406.4	10	0.5	8,383	341	46	0.04166
Kjelgaard and Sellers	20.5	75	568.8	12.8	0.7	7,113	316	59	0.0323
Visser and Nelson	20.0	75	406.4	9.7	0.5	12,340	517	69	0.030
	20.0	75	406.4	10.0	0.5	22,774	925	124	0.015
Verhaagen	20.4	76	2220.0	25	0.5	17,400	1545	193	0.0145
Carcaillet	20.0	75	500	20.3	0.6	23,061	568	91	*
	20.0	75	500	119	0.6	114,144	480	77	*
	20.0	75	1450	40	0.8	11,034	400	86	*
Pagan and Solignac	19.3	75	560	14.5	1.4 (wake)	6,732	260	70	*

* unavailable

Table 1 Comparison of Maximum Axial Vorticity Data

and vice versa. Since vorticity is a measure of the smallest scales of the flow, it would only make

sense that a finer measurement grid would be able to 'capture' the high gradients of velocity

present in the field. The behavior of the vorticity field is now examined in more detail and

arguments for the use of this property as an indicator of the onset of breakdown are given

Previously obtained experimental data is also presented to illustrate the potential viability of such

arguments.

2.2 The Delta Wing Vorticity Field

The aspects of the vorticity field would seem to be of utmost importance in gaining a better understanding of the flowfield behavior. The vorticity or rotationality of the fluid could well be the decisive factor in the mechanism of vortex breakdown. Both the generation of vorticity, which is transported into the vortex, and the convection rate downstream of this vorticity could play a crucial role in determining where the breakdown of the primary vortex occurs. Lee and Ho (1989) state that ' a stationary leading edge vortex is achieved only when the convection of vorticity along the core axis balances the vorticity generation from the boundary layer of the leading edge'. They further conclude that a reduction in the axial convection, via the adverse pressure gradient at the trailing edge of the planform, results in vortex breakdown and that the swirl angle will indicate the vorticity balance. A similar argument, postulated by Ng (1989), is that a critical vorticity concentration occurs, above which the aerodynamic forces cannot maintain a stable vortex over the airfoil. If this concentration is exceeded the vortex transitions to another state, such as post breakdown, to redistribute the excess vorticity. An increase in the angle of attack leads to a higher rate of generation of the axial vorticity component without an accompanying increase in the axial velocity. The subsequent increase in the vortex strength leads to vortex breakdown .

Ashenberg (1987) attempted to model the flow about a slender wing to avoid the limitation of using a suction analogy, since this analogy is not capable of predicting the flow near the surface of the wing. He assumed the type of breakdown does not affect the aerodynamic properties of the wing and that conical flow is assumed near the apex which is used as an upstream condition for the solution. Downstream of breakdown, two dimensional sources were distributed along the vortex axis. Although the lift was found to be overpredicted and pressure peaks were displaced laterally outboard, he noted from his mathematical expressions that the expansion of the bubble caused a reduction of the vorticity shed from the leading edge.

Consider the state of the vorticity field as an indicator of the onset of breakdown. Perhaps the vortex structure may be unable to exist in the cohesive pre-breakdown state if, say, a maximum local value of vorticity in the vortex is reached or if, perhaps, an upper limit exists on the total amount of distributed vorticity in the vortex being convected at a given time. The first proposal reflects the point type property of vorticity. Determining Ω_x and Ω_y, or in polar notation, the radial, Ω_r, and the azimuthal, Ω_{theta}, vorticity components, over various wings at a series of chordwise locations, and suitable nondimensionalization of the data might point to a critical maximum in the flowfield. The supposition of Lopez (1988) that a change in sign of Ω_{theta} causes breakdown could also be verified experimentally.

The second hypothesis arises from the reasoning that the vortex may have a limit on the maximum amount of vorticity per unit area or volume. If one continues to feed vorticity into the system, it can only 'hold' so much before it must revert to a more stable configuration in order to contain or transport the increase in vorticity . Extending this further, since the breakdown position maintains an average mean location, it could be assumed that the vorticity being generated is balanced by the vorticity being convected downstream for some given set of fixed conditions, such as sweep angle and angle of attack. If the flow conditions are then in some way altered, so as to add more vorticity upstream of the breakdown without a corresponding increase in the convection rate downstream, the breakdown would be seen to move upstream. This would indicate that some sort of critical condition, based on a maximum vorticity distribution, exists causing the initial vortex structure to transition to the post breakdown state. An increase in the angle of attack or a decrease in sweep angle would momentarily cause the relative vorticity generation rate to become higher than the convective rate. Hence, the critical vorticity distribution would be reached earlier (i.e. upstream of the initial breakdown location) and the breakdown would move towards the apex until a stable situation is again reached. For this reason it may be advantageous to consider the relation of the vorticity generation to convection terms.

The argument of a critical vorticity distribution can be substantiated in light of the work by Pagan and Solignac (1987) mentioned previously in 1.2.2. Their results indicate that a maximum vortex strength, as given by the maximum swirl velocity ratio, is strongly dependent on the local freestream pressure gradient, controlled by moveable flaps in their tunnel section. This can also be interpreted as the maximum amount of vorticity at a given station, or circulation/vortex strength, is limited by the ability of the flow to move downstream, regulated by the pressure gradient. Thus, the state of the vortex, with regards to its breakdown potential, can be described by a ratio of strength generation conditions to flow transport conditions. Specific ratios could include flowfield properties such as the circulation at a station to convective velocity, or geometrical variables, such as a function of α and Λ to imposed tunnel gradient.

Empirical verification of such proposals can best be investigated by utilizing parameters based on the state of the flow as revealed by the ratios of the relevant variables. Several examples of this were outlined in Chapter 1. Interestingly, if the swirl parameter

$$S = \frac{r_0 \Gamma}{2Q} \tag{1.22}$$

mentioned previously in the use of tornado studies and reduced to the form of V_ϕ / V_x for delta wings, is examined further, several possibilities are revealed which may be useful in correlating delta wing flows. Rewriting the parameter in terms of the average axial velocity component, $V_{x_{avg}}$

$$S = \frac{r_0 \Gamma}{2\Pi r_0^2 V_{x_{avg}}} = \frac{\Gamma}{2\Pi r_0 V_{x_{avg}}} \tag{2.1}$$

the relation can also be seen to indicate the transport of circulation in the axial direction. The parameter can also be expressed in terms of the average vorticity over the area normal to that bounded by r_0

$$S = \frac{r_0 \, \Omega_x}{2V_{x_{avg}}} \qquad (2.2)$$

This is simply the inverse of the Rossby number and can be interpreted as a measure of the convection of the vorticity. If the radius r_0 is defined to be that of the subcore of the delta wing vortex, which will be shown later to contain the majority of positive axial vorticity, the streamwise behavior of this parameter could provide an indication of whether or not breakdown was imminent.

The flowfield can be examined on a point by point basis, using the local axial values of vorticity and velocity and some length scale, such as the chord or the local span, s^*,

$$S = \frac{\Omega_x \, s^*}{V_x} \qquad (2.3)$$

to observe any type of local effect. Since a comparison of the data using a point property analysis is susceptible to effects such as the grid resolution, an integrated approach can also be used. The radius of the subcore could be the length scale,

$$S = \frac{\Omega_x \, r_0}{V_x} \qquad (2.4)$$

and averaging the axial vorticity and velocity components over the region of the subcore could help in alleviating potential resolution discrepancies.

As can be seen, different variables can be incorporated into these nondimensional parameters. If the velocity in the numerator above was V_{ϕ} instead of V_x, then perhaps this would provide the 'critical condition parameter'. This may be so. This type of guessing can continue ad

infinitum and therefore the parameters in this study are limited to those based on strong physical arguments.

The suppositions presented above were based on a examination of some existing data and theories in the literature. This data and the conclusions drawn from its examination are now presented below as a basis for the discussion of the objectives of the present study.

Axial vorticity was calculated from LDV velocity data taken by Payne (1987) and Anders (1982) is shown in Figure 2.2. The axial vorticity, based on polar coordinates is given below:

$$\Omega_x = \frac{1}{r}\frac{\partial(rV_\phi)}{\partial r} - \frac{1}{r}\frac{\partial V_r}{\partial \phi} \qquad (2.5)$$

Under the assumption that the azimuthal gradient of the radial velocity is negligible, axisymmetric flow and a negligible radial velocity , the relation becomes

$$\Omega_x = \frac{V_\phi}{r} + \frac{\partial V_\phi}{\partial r} = \frac{w}{r} + \frac{\partial w}{\partial r} \qquad (2.6)$$

This is applied to data acquired along a traverse directly through the vortex core. The angles of attack of Payne and Anders were 20° and 19.3° respectively and the corresponding sweep angles were 70° and 68.2°. No breakdown is occurring over the wing. Both core traversals were taken near mid-chord (x/c = 0.5 and 0.67). The Reynolds numbers are comparable (425,000 and 170,000) for this type of flow. Payne has a chord length of 406.4 mm while Anders has 137.5 mm. If the spanwise variation in the vorticity (calculated using central differencing in polar coordinates) is nondimensionalized using the local span length and the freestream velocity, the results are comparable.
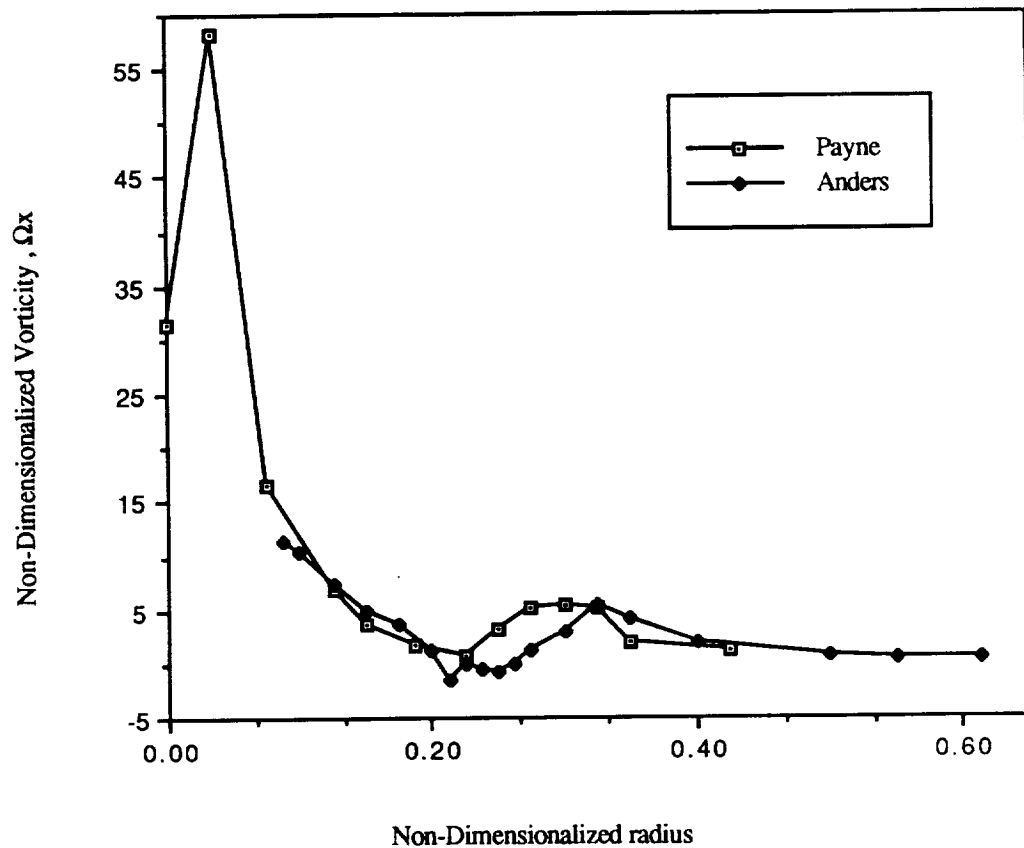
Figure 2.2 Axial Vorticity Data of Payne and Anders

Axial vorticity was also calculated from LDA velocity data acquired by Iwanski (1988) over a one inch thick, 70° sweep, flat plate delta at $\alpha = 30°$. The vorticity can be nondimensionalized in two ways: by the local half span, s*, to account for the increase in the vortex length scale, or by the root chord, as is generally done in the literature. Figure 2.3 illustrates how the velocity data from Iwanski can be used to observe the spanwise variation in vorticity at different chord stations. The axial vorticity profiles are seen to increase in magnitude and narrow in width in the downstream direction up to x/c = .411 (Figure 2.3a). Further downstream, Figure 2.3b, the magnitude of the values drop off and the peaks broaden as the breakdown region is traversed.
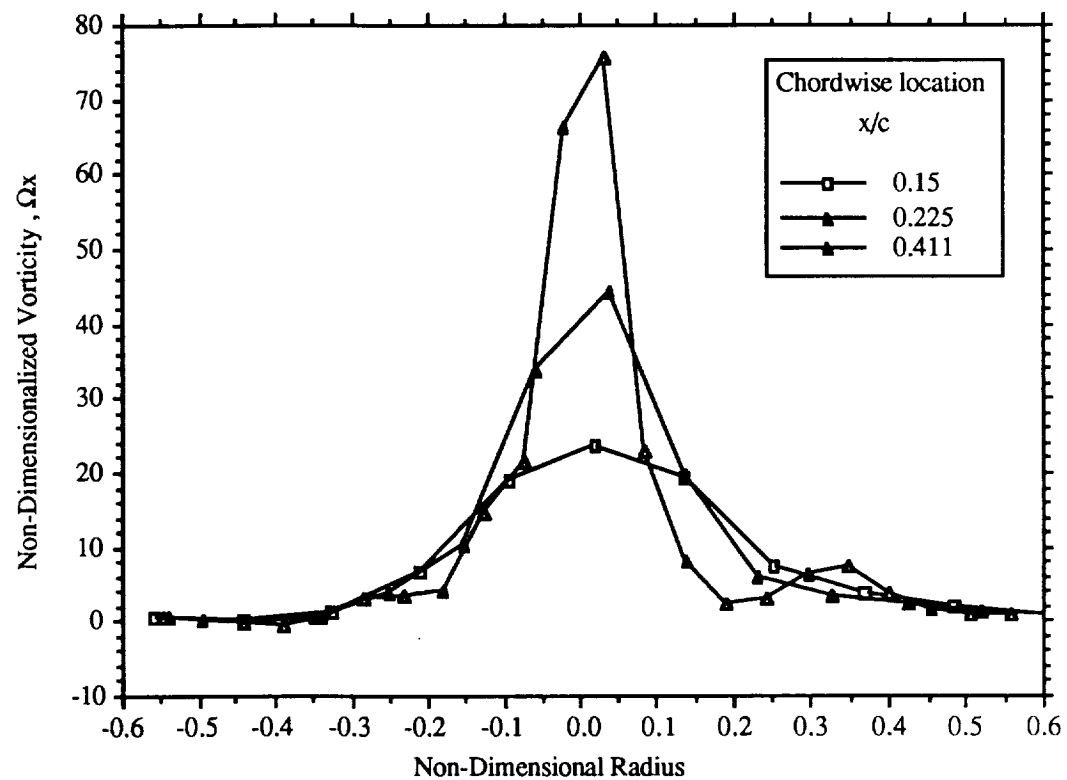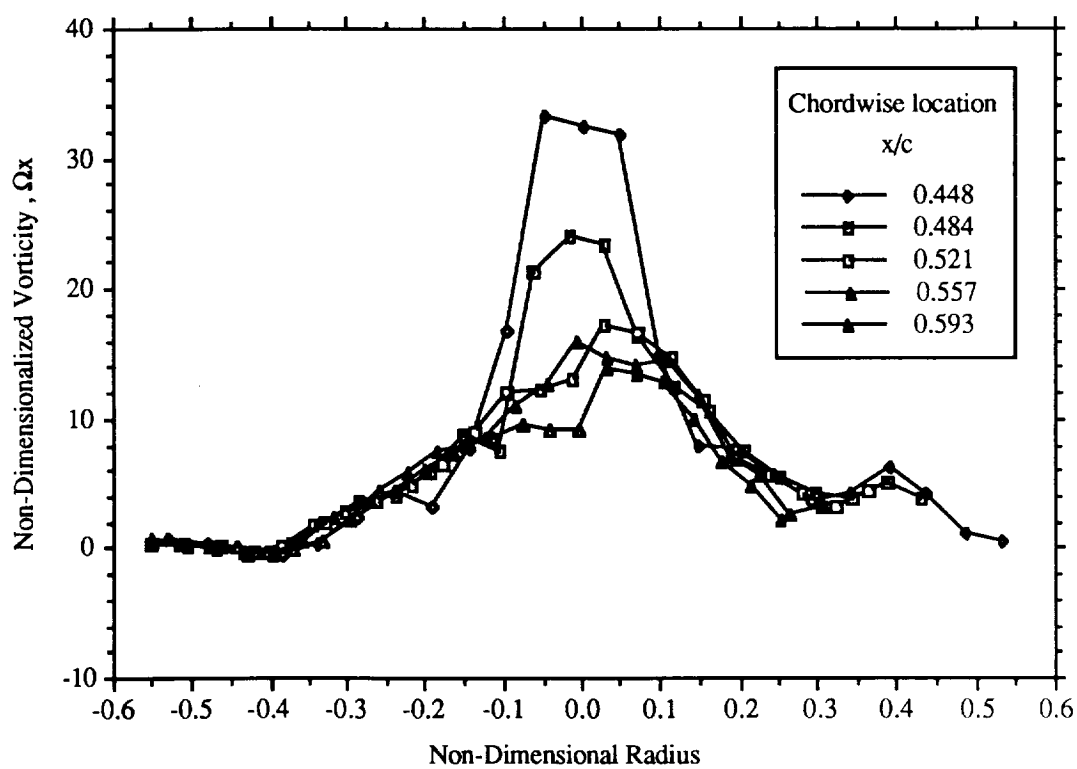
Figure 2.3 Iwanski LDV Breakdown Data a) Upstream b) Downstream

From the above discussion, it is evident that the vorticity field undergoes large changes in the axial vorticity distribution as the breakdown region is encountered. Thus, the measurement and subsequent analysis of vorticity was regarded as an important aspect of this investigation. Before the objectives and goals of this study are laid out, however, a hypothesis is presented in the next section which deals with another aspect of the flowfield that could indicate the state of the vortex relative to breakdown, in terms of the tangential velocity component and the pressure field.

2.3   A Heuristic Proposal

A proposal is outlined below which would allow the state of the delta wing vortex, relative to its condition at breakdown, to be evaluated in terms of measurable flow quantities at a given chordwise station. The region referred to as the viscous subcore in the vortex is suggested to act as a solid body downstream of the apex generation region, where the wing geometry is thin compared to the local flow. This being so, the cross sectional flow can be treated as if the radial pressure gradient supplies the required centripetal acceleration to maintain a pre or post breakdown vortex.

The flow is assumed to follow a steady, axisymmetric, incompressible behavior, as was proposed by Hall (1961), with the appropriate equations (1) repeated here

Momentum:

$$r: \quad V_r\frac{\partial V_r}{\partial r}+V_x\frac{\partial V_r}{\partial x}-\frac{V_\phi^2}{r}=-\frac{1}{\rho}\frac{\partial P}{\partial r}+\nu\left(\frac{1}{r}\frac{\partial}{\partial r}\left(r\frac{\partial V_r}{\partial r}\right)+\frac{\partial^2 V_r}{\partial x^2}-\frac{V_r}{r^2}\right) \qquad (2.7a)$$

$$\phi: \quad V_r \frac{\partial V_\phi}{\partial r} + V_x \frac{\partial V_\phi}{\partial x} + \frac{V_r V_\phi}{r} = \nu \left(\frac{1}{r} \frac{\partial}{\partial r} \left(r \frac{\partial V_\phi}{\partial r} \right) + \frac{\partial^2 V_\phi}{\partial x^2} - \frac{V_\phi}{r^2} \right) \qquad (2.7b)$$

$$x: \quad V_r \frac{\partial V_x}{\partial r} + V_x \frac{\partial V_x}{\partial x} = -\frac{1}{\rho} \frac{\partial P}{\partial x} + \nu \left(\frac{1}{r} \frac{\partial}{\partial r} \left(r \frac{\partial V_x}{\partial r} \right) + \frac{\partial^2 V_x}{\partial x^2} \right) \qquad (2.7c)$$

Continuity:
$$\frac{1}{r} \frac{\partial}{\partial r} (r V_r) + \frac{\partial}{\partial x} (V_x) = 0 \qquad (2.7d)$$

The analysis now deviates form that of Stewartson and Hall (1963) in the core region as described earlier by introducing a limiting assumption. Restricting attention to the viscous subcore region, a further simplification is introduced based on observations in the wind tunnel using flow visualization and measurements performed with x-wires and 5 hole probes. This simplification is also the basis for many solid body theory models, that being:

The radial velocity, V_r, is negligible in the viscous subcore upstream of breakdown.

Although this assumption is incorporated by many of the studies mentioned earlier, further substantiation of this premise is now given based on the observations of this study and a previous study by Visser (1988). The negligible radial velocity appears to be confirmed experimentally using flow visualization. No tracer particles are seen to spiral into the subcore region when released either upstream of the wind tunnel test section or locally about the model, excluding the apex. Interestingly, Davies-Jones (1982) reports that no entrainment into the core region is seen for tornado structures in the flowfield away from ground level. It also appears that tracers placed into the subcore region remain in the 'core' and are neither transported to the outer vortex flow region nor 'spun out' to some particular radius within the subcore region. Laser light sections have shown a tracer filled cross section for the entire chordwise length of the vortex as reported by Visser, Nelson, Ng (1988). Any radial velocity gradients would 'spin out' the particles and cause

a)
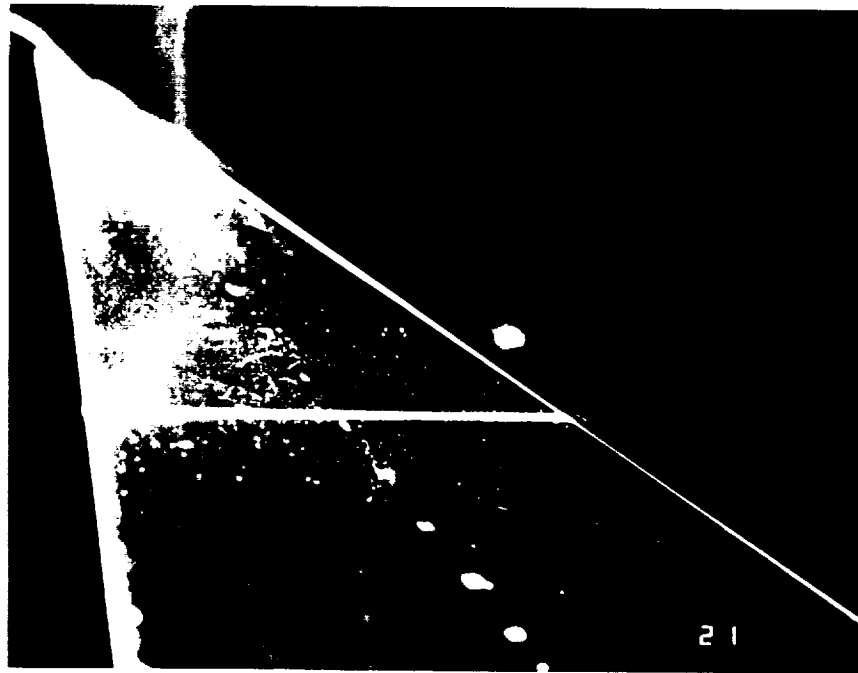
b)

Figure 2.4 Vortex Visualization a) Sub - Core b) Laser Light Sheet

a dark center hole to appear at some point down the length of the vortex, creating in essence a ring of smoke at the outer edge of the subcore. No such phenomena is observed. Measurements performed using an x-wire and a five hole probe indicate that this core, based on the distance between the maximum tangential velocity components, remains approximately constant in diameter upstream of breakdown. Flow visualization by Visser, Nelson, Ng (1988) and Payne (1987), in Figure 2.4a and b respectively, indicates a core size that appears to be of a cylindrical nature rather than conical. It is quite obvious that near the breakdown region, as the core stagnates and begins to expand, radial velocity components can not be neglected. However if this analysis is restricted to the pre-breakdown state, neglecting V_r is not an unreasonable approximation.

Introducing this radial velocity approximation further simplifies the above equations to the form:

$$\frac{V_\phi^2}{r} = -\frac{1}{\rho}\frac{\partial P}{\partial r} \tag{2.8a}$$

$$V_x\frac{\partial V_\phi}{\partial x} = \nu\left(\frac{1}{r}\frac{\partial}{\partial r}\left(r\frac{\partial V_\phi}{\partial r}\right) + \frac{\partial^2 V_\phi}{\partial x^2} - \frac{V_\phi}{r^2}\right) \tag{2.8b}$$

$$V_x\frac{\partial V_x}{\partial x} = -\frac{1}{\rho}\frac{\partial P}{\partial x} + \nu\left(\frac{1}{r}\frac{\partial}{\partial r}\left(r\frac{\partial V_x}{\partial r}\right) + \frac{\partial^2 V_x}{\partial x^2}\right) \tag{2.8c}$$

$$\frac{\partial V_x}{\partial x} = 0 \tag{2.8d}$$

and substituting the resulting continuity condition into the x direction momentum yields

$$\frac{1}{\rho}\frac{\partial P}{\partial x} = \frac{\nu}{r}\frac{\partial}{\partial r}\left(r\frac{\partial V_x}{\partial r}\right) \tag{2.9}$$

Recall that these equations are being used for the region of flowfield up to the outer boundary of the subcore or the inside of what is referred to as the inviscid Euler rotational region.

Several aspects of the flowfield become immediately apparent. The change in the axial velocity component, $\partial V_x/\partial x$, is zero from continuity. Leibovich (1983) stated that the axial velocity continues to increase along the axis and Verhaagen and van Ransbeeck (1990) have measured the axial velocity and found it to increase with axial direction up to a certain downstream distance. The theory of Stewartson and Hall (1963) also indicate an axial component of velocity that increases with axial distance, again up to a point, whereupon it becomes constant as shown by Verhaagen and van Ransbeeck . Stewartson and Hall (1963) include a radial velocity term in their model, directed inwards to accommodate the increase in axial velocity. This radial term depends on distance and as x increases, the magnitude of the radial velocity component decreases to a negligible amount.

The constant axial velocity component that results from the present derivation is because of the zero radial velocity constraint imposed. Yet both from the theory and measurements noted above, the axial velocity seems to reach a constant value at some distance downstream of the apex. It is known that the axial velocity stagnates at breakdown and even exhibits reversed flow. Hence one could presume at the very least that the axial velocity would reach a maximum and then begin to decrease to the breakdown point. The deceleration of the flow occurs over a very short distance, on the order of 2 or 3 core diameters. Thus it may be that for a distance directly upstream of the breakdown zone, the axial velocity reaches and maintains a maximum value, similar to that shown by the above investigators. This being so, a zero radial velocity would be reasonable and the above assumptions justified on more than just the basis of flow visualization.

It should also be noted from the x-momentum equation that the axial pressure gradient is not zero. Since

$$\frac{\partial V_x}{\partial r} < 0 \qquad (2.10)$$

due to the jet like nature of the axial flow, the pressure gradient in the axial direction is also required to be negative for $\partial V_x/\partial x = 0$. This pressure gradient has been verified experimentally by Verhaagen and van Ransbeeck (1990) and by Lambourne and Bryer (1961). Present measurements will be discussed later. As mentioned earlier, Stewartson and Hall (1963) found that $\partial V_x/\partial r = 0$ for a low enough value of the kinematic viscosity (see Batchelor (1967)), which would suggest a constant pressure along and across the core.

The zero radial velocity also implies a solid body type of rotational flow. As noted earlier, flow visualization has indicated a viscous subcore diameter that does not appear to vary in a conical fashion, but rather maintains a cylindrical form. This implies $V_{\varnothing}$ to be a constant at a specified radius for any axial direction, that is no dependence on x. Using this with the the $\varnothing$ momentum equation gives

$$\frac{\partial}{\partial r}\left(r \frac{\partial V_{\varnothing}}{\partial r}\right) = \frac{V_{\varnothing}}{r} \qquad (2.11)$$

and a solution of $V_{\varnothing} = \omega r$ which agrees with the solid body implication.

This is not to say that this solid body rotation behavior actually occurs. Indeed there may be shear occurring in the fluid at different radii from the core center. If the rotational rates of the subcore region is approximated by the above

$$\omega = \frac{V_{\varnothing}}{r} \qquad (2.12)$$

with $V_{\varnothing}$ typically on the order of 1.3 - 1.5 V_{∞} and d $\cong$ 6-10 E-03 m, ω values up to 5000 rad/s or almost 800 rps (48,000 rpm) for the tests presented later in this study. Higher tunnel speed

would increase this rate substantially. Data from Payne (1987) based on LDV data gives rotational speeds approaching 60,000 rpm.

Nonetheless, the particles appear to maintain their respective distances from the core, indicative of a solid body rotating flow. In addition measurements of the velocity field through the core indicate a linear variation with radius, also a property of a field undergoing solid body rotation. The total pressure drop, which has been measured at the core center, is seen to accompany such flows and so for the moment this assumption will still be maintained.

The radial momentum equation provides the most interesting possibilities as to insight on the physics of the flowfield. It is interesting to note that the reduced radial momentum equation derived above by assuming a zero radial velocity is identical to that presented by Stewartson and Hall (1963) who had imposed a slenderness condition.

$$\frac{V_\phi^2}{r} = \frac{1}{\rho}\frac{dP}{dr} \tag{2.13}$$

This relation can be interpreted as a balance between the radial pressure gradient and the centripetal forces. A better explanation is that the radial pressure gradient is such to exert a large enough centripetal force to keep the vortex together. Alternatively it can be said that for a given pressure gradient, there is a maximum centripetal acceleration that can occur and hence a maximum tangential velocity. This type of flow is also referred to as 'cyclostrophic flow' (Davies-Jones, 1973).

It could be surmised from the above that if an initially balanced system was to be upset such that the radial pressure gradient became less than the required acceleration (i.e. a local pressure rise along the axis), the particles would no longer be held to their orbital paths and would

attempt to travel in straight lines, i.e.. the core would expand or diverge. Conversely, if V_ϕ was reduced it could be expected that the pressure gradient would drive the core to a smaller radius with a subsequent radial inflow opposite to the outflow seen in the breakdown region. Or, extending this concept, if the centripetal acceleration (tangential velocity) was modified to remain smaller in magnitude than the local radial pressure gradient, breakdown could possibly be delayed.

This argument is consistent with experimental observations of the swirl angle parameter defined as:

$$\text{swirl angle} = \tan^{-1}\left(\frac{V_\phi}{V_x}\right) \qquad (2.14)$$

where V_x is the axial velocity component and V_ϕ the tangential component. Typically the swirl angle increases in a chordwise direction to a value of between 40° to 50° whereupon breakdown of the vortex is observed. Larger magnitudes of V_ϕ relative to V_x would seem to indicate breakdown was imminent. Since the increase of the acceleration term in the radial momentum equation is dependent on the square of this tangential velocity, V_ϕ, both of the above arguments point to a reduction of the local tangential velocity as a means to delay the breakdown process. A further implication is that the circulation or strength of the vortex, defined as the line integral in a plane normal to the vortex axis:

$$\Gamma = \int \mathbf{V} \cdot d\mathbf{l} \qquad (2.15)$$
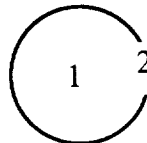
would have to be reduced. That is, the vortex would have to be weakened in order to delay breakdown and possibly enough weakening could move or maintain the breakdown region in the wake.

It would be helpful if equation (2.13) could be used in direct conjunction with properties that are measurable in the core region. Equation (2.13) could then be utilized to indicate the current status of a given vortex with respect to breakdown. Two approaches can be taken to using this relation. First, equation (2.13) can be simply interpreted as: 'What pressure gradient is required to maintain the maximum centripetal acceleration?'. Thus the relation can be evaluated at any point in the vortex using experimental data and without resorting to integration or any assumption on the behavior of V_{ϕ}. The most interesting spatial locations would occur where the tangential velocity is the largest. Thus equation (2.13) can be stated as

$$\rho \, \frac{V_{\phi max}^{2}}{r_{V_{\phi max}}} = \left(\frac{\partial P}{\partial r}\right)_{@r_{V_{\phi max}}} \tag{2.16}$$

The value of $V_{\phi max}$ is is generally taken to be the edge of the subcore region. The pressure data at this location must also be available to obtain the local gradient. The local ratio of the pressure gradient term to the acceleration could then then be compared.

As an alternative approximation, equation (2.13) can be integrated from the vortex center, denoted as 1 below, to the radius of the subcore region, 2, using a $V_{\phi} = \omega r$, solid body distribution

$$\int_{1}^{2} \frac{dP}{\rho} = \int_{1}^{2} \frac{(\omega r)^{2}}{r} \, dr$$

yielding:

$$P_{2} - P_{1} = \frac{\rho \omega^{2}}{2} \, (r_{2}^{2} - r_{1}^{2}) \tag{2.17}$$

Denoting P_{1} as the pressure at the core axis P_{axis} and setting $r_{1} = 0$ gives:

$$P_2 - P_{axis} = \frac{\rho \, \omega^2 \, r_2^2}{2} = \frac{\rho \, V_{\emptyset 2}^2}{2}$$

or

$$\frac{2 \, (P_2 - P_{axis})}{\rho V_{\emptyset 2}^2} = 1 \tag{2.18}$$

A further implication is that the pressure gradient required is dependent on the square of the local swirl ratio at r_2

$$\frac{2 \, (P_2 - P_{axis})}{\rho U_2^2 \, \tan(swirl_2)^2} = 1 \tag{2.19}$$

What remains is to define where $V_{\emptyset 2}$ is to be measured, that is, where the boundary 2 is located. If the value $V_{\emptyset 2}$ is taken as the largest tangential velocity in the flow field, as in approach 1, the value of P_2 is also required at this point. Four cases can be examined, the first three of which are based on the ratio

$$\frac{2 \, (P_2 - P_{axis})}{\rho V_{\emptyset 2}^2} = \frac{2 \, (\Delta P)}{\rho V_{\emptyset 2}^2}$$

and are listed as follows:

i) Use the static pressure difference, $\Delta P = P_\infty - P_{axis_\infty}$, noting that

$$P_\infty = P_{\infty total} - \rho U_\infty/2 \quad \text{and} \quad P_{axis_\infty} = P_{axis \, total} - \rho U_{axis}/2$$

ii) Use the total pressures, $\Delta P = P_{t_\infty} - P_{t \, axis}$.

iii) Use the pressure at $r_{V_{\emptyset max}}$, $\Delta P = P_{V_{\emptyset 2}} - P_{axis}$. This requires all the velocity components at to be known at $r_{V_{\emptyset max}}$ to obtain the static pressure from the total pressure.

iv) Use two values of pressure to either side of $r_{V\phi 2}$. These values can be used in conjunction with the ratio above, but also with the approach to equation (2.16). This is the most correct evaluation, as the closest approximation to the local pressure gradient is obtained.

The question now arises as to what this represents? Can this parameter be simply be interpreted as the ratio of the radial pressure to the centripetal acceleration of the fluid? That is, in order to maintain the centripetal acceleration necessary to keep the fluid on the circular trajectory defined by the vortex, a certain pressure gradient must be required? If the ratio is > 1, is the pressure gradient is large enough to maintain the coherent structure? If it is < 1, are the required centripetal forces are too large and the vortex diverges? Could this possibly be used as some kind of breakdown criterion? Available data and the present tests will be used to examine the above conjectures in Chapter 5.

Although the above derivations did not assume an inviscid behavior, viscous effects do not appear explicitly in the the reduced radial momentum equation, which formed the basis for the above arguments. The effect of viscosity should not be overlooked, however, as its effects are seen quite readily if the entire flow field above a delta wing is considered. The existence of the secondary vortex is a direct result of viscous interaction at the wing surface. Consider, for a moment the possible effects of this secondary vortex using the idealized situation below:
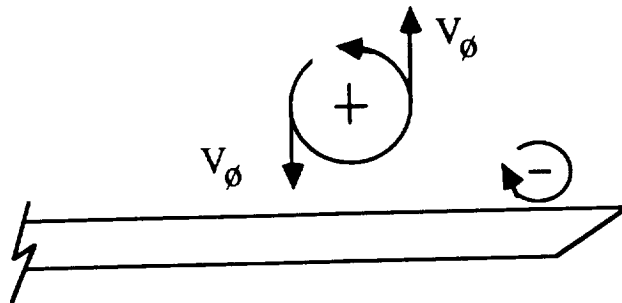
Figure 2.5 Ideal Delta Wing Flow Vortex Representation

It would be expected that the secondary vortex induces a velocity field on the primary vortex. This would tend to cause the value of the tangential velocity, V_ϕ, in the primary to be larger in magnitude on the side nearer to the secondary than on that closer to the wing centerline. This is observed experimentally. Thus it may be that it is the effect of the secondary which causes V_ϕ to increase to the point where

$$\frac{V_\phi^2}{r} > \frac{1}{\rho}\frac{dP}{dr}$$

and thereby initiate breakdown.

The rotation of the secondary vortex would also cause the distance between the core of the primary vortex and the wing to be greater than if the secondary were not there. This would have the effect of reducing the measured suction peak value at the surface of the wing. The implications of this concept could be far reaching if it could be substantiated. Reduction or removal of the secondary might not only delay breakdown, but also increase the lift by moving the primary vortex nearer to the wing surface, possibly to the maximums calculated by current Euler codes. Earlier preliminary tests using small angular tabs as vortex generators were conducted by the author to investigate the possibility of altering the breakdown location by manipulating the flow near the surface. Tabs were placed near the apex, both on the upper surface and the bevelled leading edge. The breakdown location was found to move further aft for certain tab orientations. The effect these generators had quantitatively on the actual vorticity distribution of the secondary, or even the primary vortex, was not determined, however.

2.4   Goals and Objectives of Present Study

The above research summary and that of the previous chapter can be summarized as three important conclusions, pointing the way for the study described hereafter and for further investigations. First, it is quite apparent that the external conditions which can be imposed on the vortex field to initiate or delay breakdown are well known and documented. These include the pressure field, the local swirl of the flow, based on either circulation or vorticity, and the axial velocity field, regardless if the vortex is confined or free. Additionally, from an experimental point of view, variation of a particular parameter has shown that the onset of breakdown is not caused foremost by a change in the swirl of the local flow, which subsequently leads to stagnation of the axial velocity and on through the breakdown process. Breakdown can just as easily be caused by an external change in the adverse pressure gradient which may then lead to a stagnation and then a change in swirl followed by core expansion and breakdown. Depending on the flow conditions, a combination of these factors may be required.

Secondly, flowfield measurements taken to verify theoretical postulations are needed. Much research has been undertaken to determine aerodynamic behavior and verify existing codes for delta wing flows, but data acquired for the purpose of examining the flow state as it approaches breakdown in order to observe any significant changes is not extensive. In general, flowfield surveys, using pressure or LDV techniques are expensive and time consuming and thus relatively sparse.

Finally, it is very important to accurately document the external conditions imposed on the experiment when obtaining a set of measurements. This is naturally assumed to be done by investigators and is most often the case. However other aspects, generally not accounted for, may exert appreciable influence on the results. One of the these aspects is grid resolution. This is,

naturally, a serious point of contention for numerical computations of a flow domain, but how often is it addressed by experimenters when conducting a series of flowfield measurements? Measurements conducted in flows with strong gradients, as is certainly the case here, are dependent on grid resolution as much as the associated numerical simulations.

Based on these conclusions, a direction for the present study was derived. The lack of data on the chordwise progression of a vortex above a delta wing prompted a systematic investigation to measure the delta wing flowfield at a set of various stations. The flowfield properties including circulation and vorticity were felt to be of interest as it has been demonstrated that an increase the circulation will initiate breakdown. Angle of attack and geometrical variation, including sweep and chord length were varied in an attempt to determine if the flow reaches some measurable critical state, particularly involving aspects of the vorticity components, that would then initiate a flow transition to the post breakdown state.

Specifically, the variations in flowfield characteristics were derived from velocity field data acquired at a series of chordwise stations using a hot wire technique presented in the following chapter. Acquisition of the data was performed using different grid sizes to examine questions on resolution. Single wire spectral data was obtained in the core upstream of breakdown to observe any dominating frequencies for interests sake. Additional measurements were taken in the form of surface pressures and total pressures to try and correlate these quantities with the flowfield velocities. Flow visualization, including on and off surface, was used to aid in interpretation of the flow.

An indication of the state of the vortex based on these measured properties was the basis for examining the data. If a measured or derived property did not indicate changes suggesting breakdown was forthcoming or had occurred, then it could be regarded as a minimal factor in terms of a parameter analysis. Initially, each flowfield station could be analyzed in terms of their

local and overall properties, including derivative and integrated characteristics. Comparison with theoretical criterion presented previously could then be made. Scaling the data in various ways would hopefully enable better comparisons at a local scale and/or a global scale of the flow properties at each measured station, especially with respect to other data in the literature. Finally, the flow can be examined with the aid of the relevant parameters described previously to attempt to quantify the flow state at each chordwise station.

CHAPTER III

CROSSED HOT WIRE ANEMOMETRY

3.1 A Brief Overview of Current Techniques

Many researchers have used two hot wire anemometers in an X-wire configuration to determine velocity fields and an extensive list of references can be found in Freymuth (1982). The measurement of X-wire voltages and their conversion to velocity can be divided into two categories: the table lookup method and the effective velocity method.

The table lookup method requires that the probe be rotated through a series of angles and the velocity varied at each position. In this way a table of wire voltages versus angle and velocity is generated. Curves fitted through these points can be generated in such a way that, given a pair of measured voltages in an unknown flowfield, a velocity and angle can be found and the subsequent velocities along specific axis can be determined. Lueptow, Breuer, and Haritonidis (1988) give a description of this technique. This can be used for both X-wire and triple wire probes. The major drawback is that it is time consuming , especially if temperature compensation is required, and a rotatable apparatus is required. The benefits, however, include no assumptions on the probe geometry or variable cooling rate estimations for velocity components not normal to the wire.

The effective velocity approach is the more widely used method. This technique centers on the concept that the wire senses an effective velocity comprised of velocity vectors normal and

C-2

tangential to the wire and thus cool it at different rates. Jørgensen (1971) has expressed the most general form of this equation as:

$$U_{eff}^2 = U_N^2 + k_1^2 U_T^2 + k_2^2 U_B^2 \qquad (3.1)$$

for an X-wire lying in the NT plane as depicted in Figure 3.1.
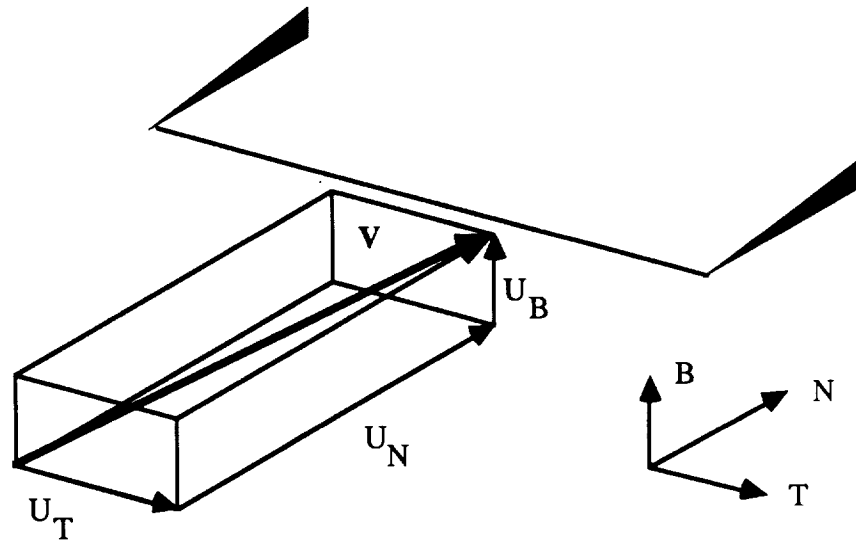
Figure 3.1 Single Wire Geometry

The k values are the yaw and pitch factors which are functions of the wire and even the yaw and pitch angles to an extent. Typical values taken are $k_1 = .2$ to $.3$ and $k_2 = 1.08$ to 1.12 although a complete study by Jørgensen (1971) demonstrates this variation. Expressions for the velocity components are then derived based on the probe geometry and/or the particular flowfield geometry.

To illustrate the extension of this measurement technique to an X-wire configuration, consider the geometry of two wires in Figure 3.2.
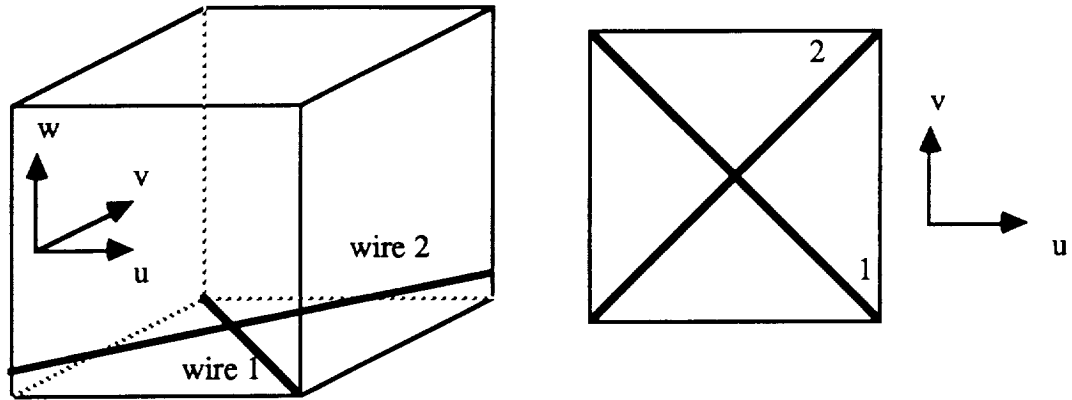
Figure 3.2 Cross-wire Geometry

An unknown velocity vector **V**, comprised of u and v (w = 0) and at some angle α, is to be measured by wires 2 and 1 at angles β + α and 90° to β + α respectively as illustrated in Figure 3.3a. It is assumed that only the normal components of the velocity on each wire are required. This is equivalent to a reduction of the Jørgensen equations to the form

$$U_{eff} = U_N \tag{3.2}$$

The measured voltages are V_1 and V_2 and are assumed to act at 90° to the direction of the wire. That is, the velocities seen by wires 1 and 2 to are derived from V_1 and V_2.
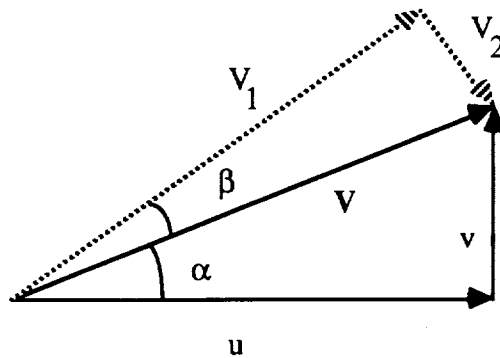
Figure 3.3a Unknown Velocity Vector with u > v.

Thus, from geometry,

$$\cos (\alpha + \beta) = \cos\alpha\cos\beta - \sin\alpha\sin\beta = \frac{u}{V}\frac{V_1}{V} - \frac{v}{V}\frac{V_2}{V} = \frac{1}{V^2} (uV_1 - vV_2)$$

or solving for u,

$$u = \frac{V^2 \cos (\alpha + \beta) + vV_2}{V_1} \qquad (3.3a)$$

Similarly, from sin $(\alpha + \beta)$,

$$u = \frac{V^2 \sin (\alpha + \beta) + vV_1}{V_2} \qquad (3.3b)$$

Equating these two expressions for u and solving for v yields,

$$v = V_1\sin (\alpha + \beta) - V_2\cos (\alpha + \beta) \qquad (3.4)$$

If, from geometry, $\alpha + \beta = 45°$ then

$$v = \frac{\sqrt{2}}{2} (V_1 - V_2) \qquad (3.5a)$$

and subsequently

$$u = \frac{\sqrt{2}}{2} (V_1 + V_2) \qquad (3.5b)$$

Hence the u velocity component would be proportional to the sum of the measured voltages (velocities), while the value of v would be proportional to the difference.

Now, consider Figure 3.3b below where the value of v > u.
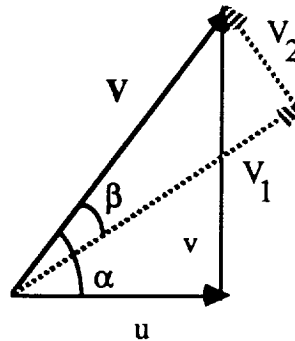
Figure 3.3b Unknown Velocity Vector with v > u.

In order to resolve the velocity into the known wire angles, the expression

$$\cos (\alpha - \beta) = \cos\alpha\cos\beta + \sin\alpha\sin\beta$$

is required. The resulting expressions for u and v become

$$u = \frac{\sqrt{2}}{2} (V_1 - V_2) \qquad\qquad v = \frac{\sqrt{2}}{2} (V_1 + V_2) \qquad\qquad (3.6a), (3.6b)$$

which are the inverse of the initial derivations.

It is readily seen that this type of derivation is useful only if the general flow direction is known in order that the probe may be oriented correctly. In addition, the w (out of plane) component must be negligible and the effects of tangential cooling on the wire are ignored. Many investigators choose to use this approach, because general inclusion of all the terms proposed by

Jørgensen (1971) leads to a series of equations with multiple solutions which are difficult to solve uniquely. Flowfields are simplified or terms are ignored to accommodate simpler forms of the Jorgensen equations. Further derivations illustrating the increased complexity of inclusion of these terms in a general form can be found in Appendix D.

The inherent complexity of these equations is evident. It appears that no one has used an X-wire to measure an unknown constant velocity flowfield, that being three magnitudes and three directions, even with successive rotations. The measurements that are taken, are performed in a flow where either the flow directions are known (Löfdahl (1986), Pailhas and Cousteix (1990)), or where there is a strongly preferred direction of mean motion in the three-dimensional shear flow (Mojola (1974)). Löfdahl (1986) fails to address the problem by disregarding the tangential cooling component effect. Browne, Antonia, and Chua (1989) in their discussion of calibration methods for yaw response in x-wire probes state that as with angle methods, the effect of the velocity component normal to the wire must be neglected. Klatt (1969) and Andreas (1978) also take this approach.

Other hot-wire methods have been employed in an effort to measure the flow field and include configurations using up to nine wires. Janjua, McLaughlin, Jackson and Lilley (1982) have used a six-orientation single wire method in the axisymmetric flow of a gas turbine engine combustor to determine an unknown velocity field. Comparisons of the results with independent data have demonstrated the reliability of this method. The largest uncertainties were found to exist in the measurement of the turbulent shear stresses. Further tests by Jackson and Lilley (1986) indicate that this technique adequately measures the properties of the flowfield independent of the dominant flow direction except if it is aligned with the probe axis. In addition the time-mean velocity in the probe direction is inadequately deduced. It was also reported by He (1988) that this technique has the same precision as a muti-hole Pitot tube with the advantages of hot wire anemometry.

Triple wire probes are available commercially and contain a third wire which is oriented such to provide a means for obtaining the entire velocity vector in a single measurement. Both DISA and TSI manufacture triple wire probes capable of measuring all three velocity components and their respective directions. There is a constraint on the use of these probes, however. The velocity velocity being measured must lie in an acceptance cone of 70° about the axis of the probe as shown below in Figure 3.4 Thus the flow direction must be approximately known, as noted by Gaulier (1977), and depending on the derivation the resulting equations become fourth order transcendental, requiring interpretation of the roots for validity, as detailed by Lekakis, Adrian, and Jones (1989).

(a)   (b)
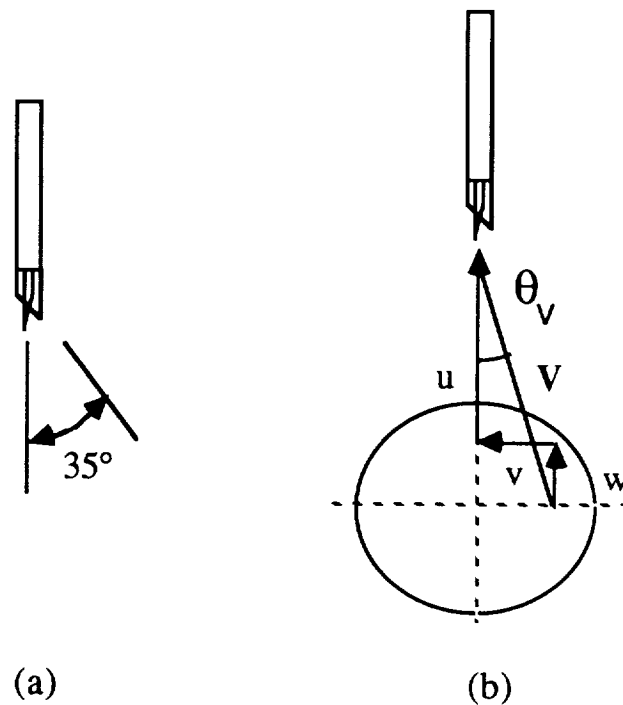
Figure 3.4 Triple Wire Acceptance Cone

This restriction on the direction of the velocity vector, which again implies a known velocity direction, is too severe for the measurements required in the present study. Consider the velocity vector shown in Figure 3.4b, consisting of the components u, v, w, and scaled by the freestream velocity U_∞. If, for the moment, w is set to zero and the angle between the axial component of the velocity and that of the lateral velocity component is defined as

$$\theta_v = \tan^{-1}(\frac{v}{u}) \tag{3.7}$$

For an axial velocity of $u/U_\infty = 1$ and the maximum allowable value of θ_v constrained to 35°, v_{max}/U_∞ can not be greater than 0.7. As illustrated in Figure 3.5, should w/U_∞ attain a value greater than zero, as is certainly the case in the present flowfield, the velocity would lie outside of the cone of acceptance.
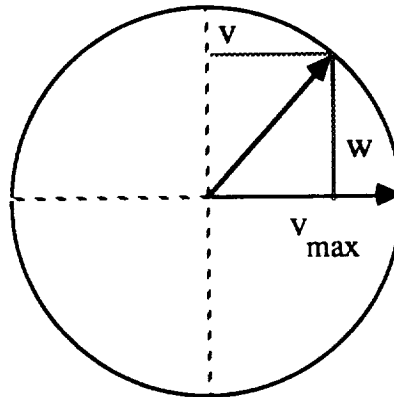
Figure 3.5 Constraint circle

Since the angle v_{max}/U_∞ makes with u must be $\leq 35°$, and for any point on the circle in Figure 3.5 above

$$v_{max}^2 = v^2 + w^2$$

it can be seen that

$$\theta_{v_{max}} = \tan^{-1}\left(\frac{v_{max}}{u}\right) = \tan^{-1}\left(\frac{\sqrt{v^2 + w^2}}{u}\right) \leq 35° \qquad (3.8)$$

Hence, a value of $u = 1.3$ requires $v^2 + w^2 = 0.83$. Seven hole probe data from a core traverse by Payne (1987) in Figure 3.6 indicates regions of the flow, such as $u = 1.3$, $w = 1$, and $v = 0.25$, which violates this constraint. Thus the use of commercial triple wire probes was deemed unacceptable for the present study using conventional data processing procedures.
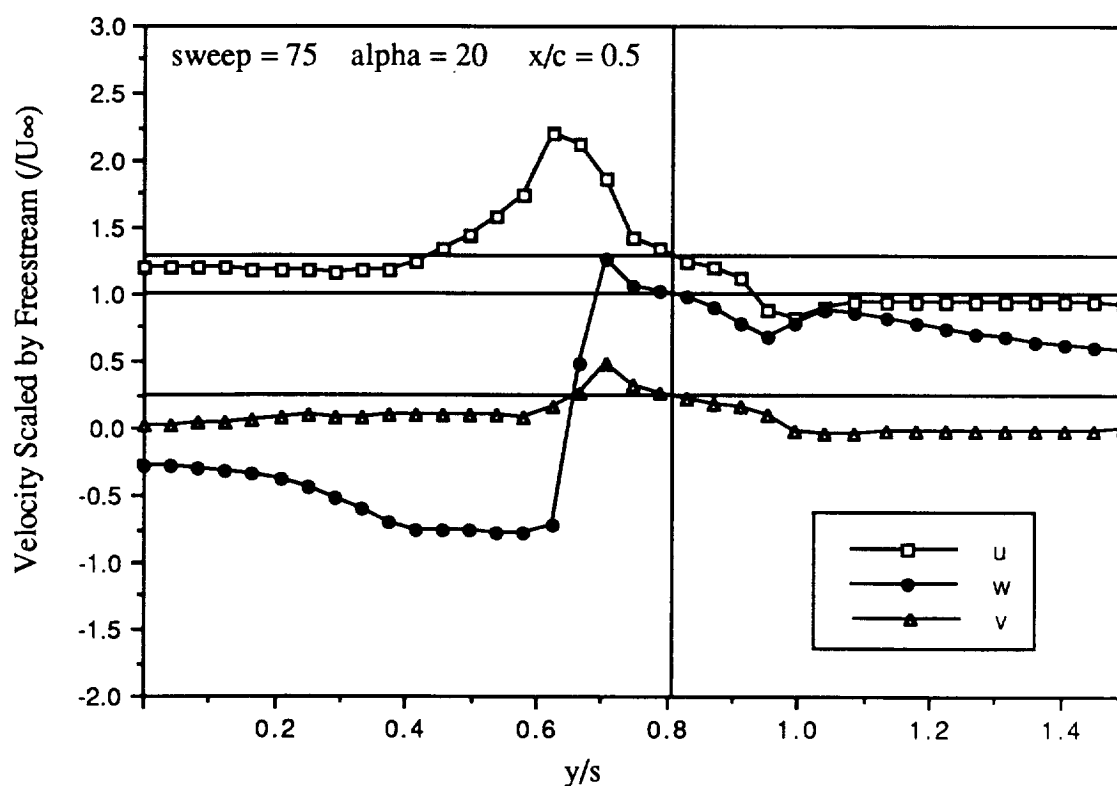
Figure 3.6 Seven Hole Probe Traverse Data

This triple wire constraint has been overcome, as reported by Jacobsen (1977), for flight data acquired in the tip vortex wake of a T-33 aircraft. A three wire probe was mounted on the

nose boom of a Gates Learjet such that the probe axis was parallel to the longitudinal axis of the aircraft. The axial component of the jet is thus added to the tip vortex axial component and therefore keep the velocity vector in the cone of acceptance.

The use of hot wire probes with more than three wires to measure instantaneous vorticity values has been proposed by Kovasznay in the early 1950's. The Kovasznay type probe, Figure 3.7a, consists of four prongs supporting four wires to form a Wheatstone bridge, when operated by a constant current anemometer.
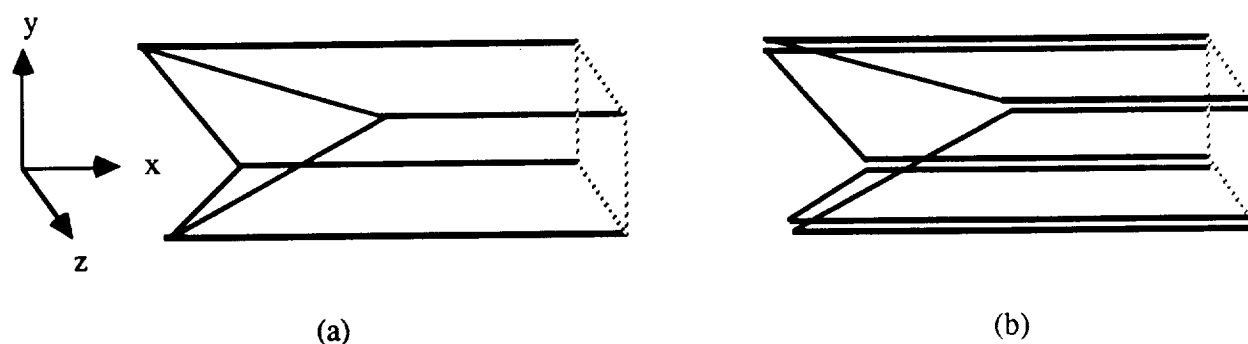
Figure 3.7 Kovasznay Type Four Wire Probes

Kastrinakis, Eckelmann, and Willmarth (1979) found it was not possible to measure instantaneous vorticity values or rms values with a Kovasznay type probe in flows with large cross-stream velocity components. They suggested that each wire be supported by its own set of prongs as in Figure 3.7b. Vukoslavevic and Wallace (1981) have built and tested this type of probe, but tests in a low speed boundary layer indicated errors occurred if the cross-stream velocity components were accounted for as they themselves could be in error by as much as 80%. They concluded that this four wire probe does not provide enough information to determine the instantaneous streamwise vorticity or cross-stream velocities. A review by Foss and Wallace (1988) discusses efforts and ensuing complications based on other configurational four wire

probes, as well more complicated five and nine wire probes, to obtain instantaneous values of vorticity.

Swirl angles larger than 45° exist in the present flowfield which eliminates the use of commercially available triple wire probes. Due to the amount of data required to examine useful trends in the flow, the six-orientation technique was eliminated in deference to a procedure involving multiple x-wires. In addition, because v, and w are on the order of u, the flow will exert appreciable tangential cooling and cooling by velocity components normal to the plane of the X-wire. It would thus be incorrect to disregard these terms of Jørgensen's equation. The nature of the flow under investigation precludes any assumptions concerning flow direction or relative magnitudes, apart from the fact that the axial velocity maintains a streamwise sense for the flow upstream of the breakdown region. Due to the inherent non-linearity of the associated equations and the resulting multiple solutions, it became apparent that several measurements at each spatial location are required using different x-wire configurations. A summary of the technique used in this study follows.

3.2 A Method for Unknown Three Dimensional Flows

Minimization of the number of spatial measurements required to obtain the mean velocity field was felt to be essential to providing the most accurate data possible. For this reason, the table lookup method, detailed by Lueptow, Breuer, and Haritonidis (1988), was initially examined. The required probe uses a sensor plane parallel to the probe axis, such as the DISA 55P61 in Figure 3.8b.

a. DISA 55P62   b. DISA 55P61
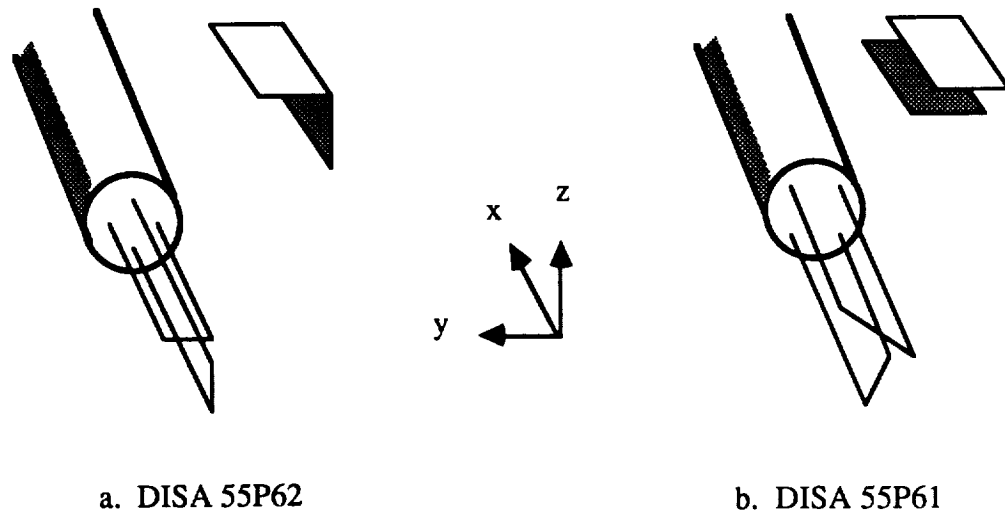
Figure 3.8 Cross-wire Probe Configuration

Calibration involved positioning the probe axis parallel to the freestream and varying the velocity while recording both wire voltages. The probe was then rotated to keep the plane of the wires parallel to the oncoming stream and the procedure repeated. In such a way, a calibration relation of the wire voltage pairs as a function of the speed and position was created. By suitable inversion, the velocity and direction could then be determined from a measured pair of voltages in the unknown field.

Although the normal and tangential effects were thus included, this method fails to account for velocities normal to the plane of the wire. Thus two grid sweeps of the field were required with the probe rotated 90° for the second sweep. In this way it was hoped that u and v would be measured on the first pass and u and w on the second. The results of a u - v pass for the vortex on the right side of the delta wing can be compared to data acquired by Payne (1987) in Figure 3.9. The survey plane was taken normal to the planform surface and normal to the x direction. Each axis has been scaled by the local semispan. Thus a y/s = 1.0 corresponds to the leading edge of the planform.
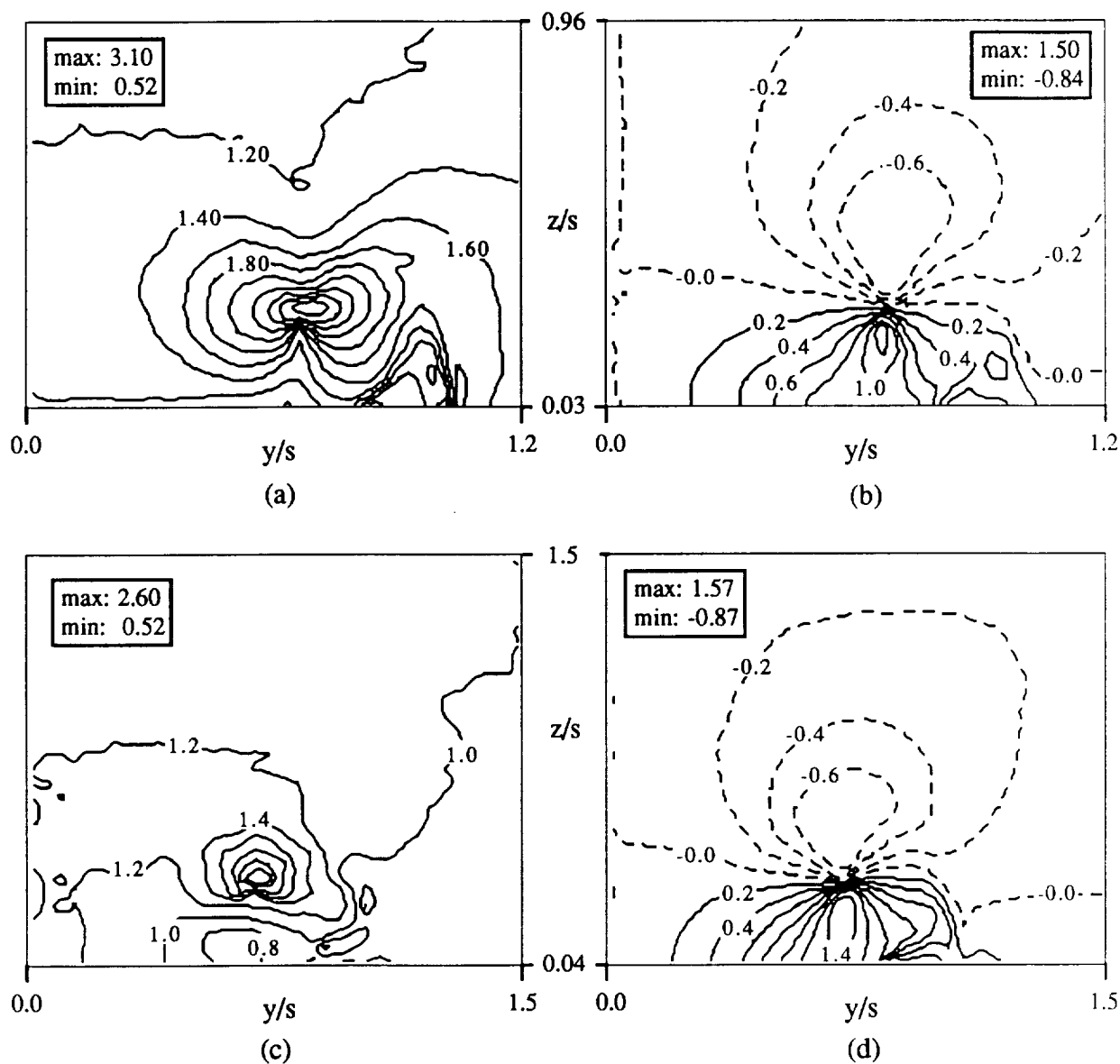
Figure 3.9 Table Lookup Method Results for sweep = 70° alpha = 20° x/c = 0.5

a) u/U∞ b) v/U∞ c)u/U∞, Payne d) v/U∞, Payne

The velocity component normal to the plane of the wires was found to contaminate the measured velocities. The axial component reflects the influence of the w component, that being normal to the wing surface, in the presence of two lobes to the left and right of the vortex center.

The presence of the normal component in these regions causes the measured axial velocity to appear larger than it actually is. The effect on the transverse component is much less pronounced and can be seen from the displacement of the zero velocity contour. In a similar manner, the axial velocity obtained in the second sweep was contaminated with the transverse, v, component.

Several schemes were employed to isolate the unwanted effects including iterative schemes. No procedure was completely successful as the resulting field would contain unresolved regions. As a final resort, the use of a physical shield on the probe during acquisition of the data was investigated. It was felt that this would possibly eliminate the unwanted effects of the velocity component normal to the plane of the wires. Although this concept has not been utilized on x-wire configurations, it has been employed in conjunction with a single wire. Günkel, Patel, and Weber (1971) affixed a disk-like shield around a single wire to minimize the effects of lateral velocity components in measuring reversing flows from 0.3 - 10 m/s. Their conclusions indicate drastic improvements. A shield of the type shown in Figure 3.10 was therefore constructed. The topside is removed for clarity.
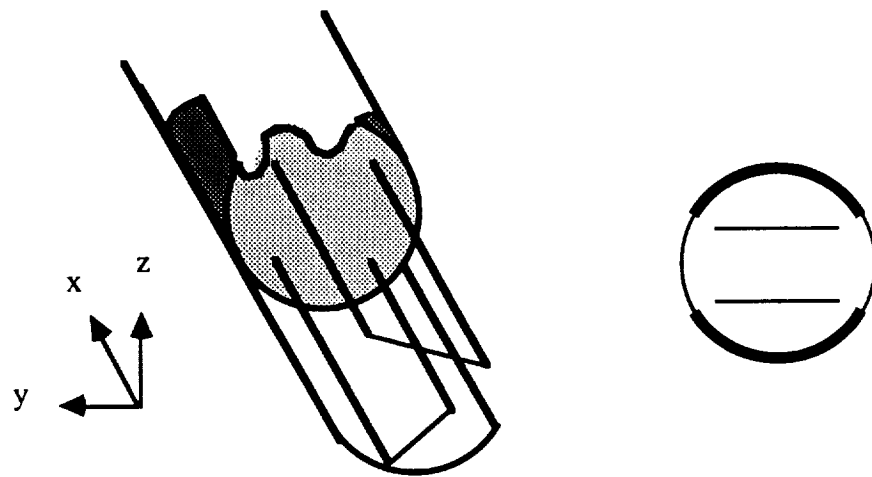
Figure 3.10 Cross-wire Probe Shield

Essentially, the concept behind the shield is that it would allow only the velocity components in the plane of the wires to be detected. After several iterative designs, a configuration was reached that gave a qualitative comparison with the data of Payne, as is shown in Figure 3.11.
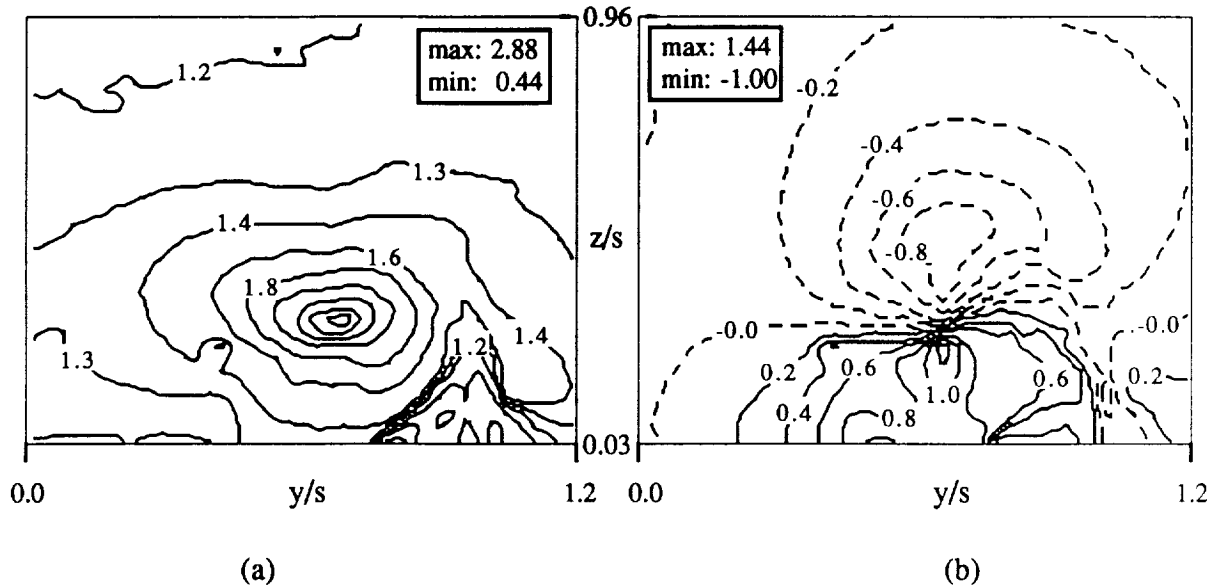
Figure 3.11 Shielded Probe Method Results for sweep = 70° alpha = 20° x/c = 0.5

a) u/U_∞ b) v/U_∞

Quantitatively, however, the shielded probe data still reflected an increase in the velocity components and the influence of such a device on the local flow is questionable. This line of investigation was therefore terminated in favor of a method utilizing the effective velocity concept. This is not to say, however, that this indicates a shielded probe technique to be invalid. Optimization of the shield design may yield data that represents the two desired components of the flow being measured.

Since the component of velocity normal to the plane of the x-wire cannot be neglected in parts of the field, it would seem mandatory that the Jørgensen equation incorporating all the

cooling terms be employed. With two different configurational measurements, it is possible to obtain a series of four non-linear equations in four unknowns. Thus, it could be surmised that a solution exists, possibly in an explicit form. Depending on the configuration used, however, the equations will only yield information on some of the quantities, such as u,v,w with unknown directions. All the attempts so far at solving these equations without some type of knowledge of the field, such as directions or relative magnitudes of one velocity component much larger than another, or simplification, such as ignoring the effect of tangential cooling, have led to solutions which possess regions in the measured field where singularities were seen to occur.

The method adopted for the present study is outlined by Sherif and Pletcher (1987). It is based on the effective velocity measurement method, and uses an X-wire array with the wires in a plane perpendicular to the probe axis. This configuration is depicted in Figure 3.8a. Their procedure requires two rotations of the x-wire and the resulting equations are solved explicitly in terms of u, v, and w. In addition, they state that the flow being measured should be of a three dimensional nature. Initial tests indicated it was possible to determine magnitudes of the velocity comparable with that obtained by other investigations to $u \pm 2.3\%$. Topographically, this procedure also seemed to give the best result, with no serious gross errors in the field. Unfortunately, there is no way to determine the sign of v and w without further information, their technique only revealing three of the six unknowns for the field.

Since the present field has five unknowns, the direction of u being known if data is taken upstream of breakdown, these equations were rewritten for the probe configuration of the two wires parallel to the oncoming stream and at $\pm 45°$, according to the geometry of Figure 3.8b. Details can be found in Appendix D. The resulting equations are similar to that obtained by Sherif and Pletcher. They are also a set of three nonlinear equations with three unknowns plus a fourth equation. The direction of v and w could also be derived from this geometry as will be shown shortly. The intent, as noted previously, was to minimize the number of surveys required.

Unfortunately singularity problems occurred when the values of v and w approached each other in magnitude, as noted in Appendix D, and resulted in areas of the flowfield which were grossly in error. In addition, the values of u were not topographically representative of the field, although the maximum magnitudes were comparable. A Newton iteration scheme relived the problem somewhat, however artificial constraints were required to get rid of the singularities and the side effects of these were unknown.

It was therefore decided to return to the method of Sherif and Pletcher. In order to fully determine the three velocity components and their associated directions, however, it was necessary to take four grid sweeps above the wing at each chordwise location. Probe 1, a DISA 55P62, had wires lying in a plane perpendicular to the probe axis, while the wires of probe 2, a DISA 55P61, were lying in a plane parallel to the probe axis, as depicted in Figure 3.8a and 3.8b respectively. The initial two grid sweeps used probe 1 with wire 1 at the reference of zero degrees and wire 2 at negative 90 degrees using the geometry in Figure 3.8 and in accordance with that of Sherif and Pletcher (1987). The probe was then rotated $45° \pm 0.5°$ about its axis and a second sweep initiated.This provided enough information for the velocity magnitudes to be determined. The second probe was used to take two sweeps with the plane of the wires parallel to the wing and perpendicular to it respectively. This second set of sweeps determined the direction of the transverse (v) and normal (w) velocity components. The direction of u was always assumed to be in the positive direction, as the probe was kept in the flow forward of the breakdown region.

The complete derivation of the equations describing the velocity components in terms of the measured voltages can be found in Sherif and Pletcher (1987). The major equations will be noted below. In addition the expressions used to determine the directions of the v and w components based on the probe geometry used for the third and fourth spatial passes will be detailed. The

geometry in Figure 3.12 will be referred to and corresponds to that of Sherif and Pletcher, however the notation is in accordance with the convention present here.
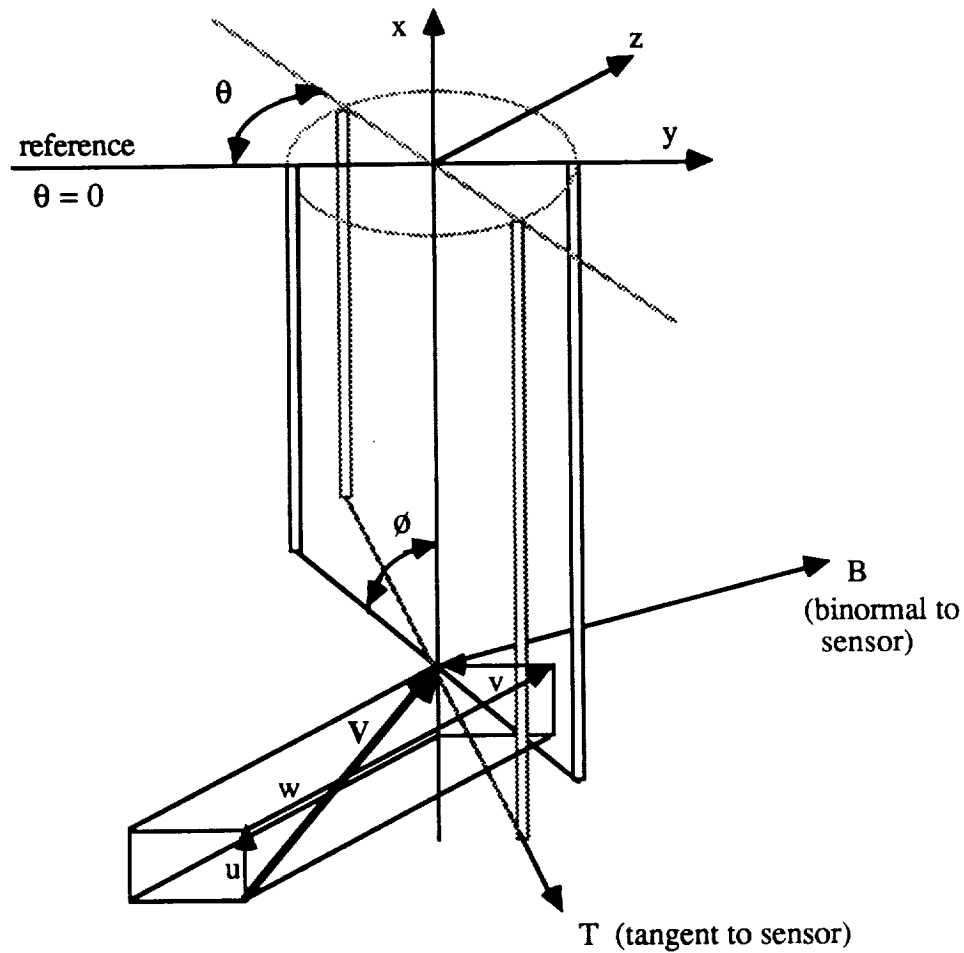
Figure 3.12 Slanted Hot-wire Geometry

The terms present in Jørgensen's equation can be represented as follows

$$U_N = u \sin\emptyset - v \cos\theta \cos\emptyset + w \sin\theta \cos\emptyset \qquad (3.9a)$$

$$U_T = - u \cos\emptyset - v \cos\theta \sin\emptyset - w \sin\theta \sin\emptyset \qquad (3.9b)$$

$$U_B = - v \sin\theta + w \cos\theta \qquad (3.9c)$$

At $\phi = 90°$ and the following reduced forms of equations (3.9 a - c) are derived,

$$U_N = u \tag{3.10a}$$

$$U_T = -v\cos\theta - w\sin\theta \tag{3.10b}$$

$$U_B = -v\sin\theta + w\cos\theta \tag{3.10c}$$

If these are substituted into Jørgensen's equation, a general expression for the measured effective velocity can be obtained.

$$U_e^2 = v^2(k_1^2\cos^2\theta + k_2^2\sin^2\theta) + w^2(k_1^2\sin^2\theta + k_2^2\cos^2\theta) + u^2$$
$$+ v\,w\,(\sin2\theta(k_2^2 - k_1^2)) \tag{3.11}$$

Substituting in for values of θ corresponding to rotation angles of $0°$, $90°$, and $45°$ gives

$$U_e^2\,(\theta = 0°) = v^2\,k_1^2 + w^2\,k_2^2 + u^2 \tag{3.12a}$$

$$U_e^2\,(\theta = 90°) = v^2\,k_2^2 + w^2\,k_1^2 + u^2 \tag{3.12b}$$

$$U_e^2\,(\theta = 45°) = \frac{1}{2}v^2(k_1^2 + k_2^2) + \frac{1}{2}w^2(k_1^2 + k_2^2) + u^2 + v\,w\,(k_2^2 - k_1^2) \tag{3.12c}$$

These equations can now be solved for u, v and w,

$$v = \frac{(\{U_e^2(90°) - U_e^2(0°)\} + [\{U_e^2(90°) - U_e^2(0°)\}^2 + \{U_e^2(90°) + U_e^2(0°) - 2U_e^2(45°)\}^2]^{0.5})}{2(k_2^2 - k_1^2)} \tag{3.13a}$$

$$w = \frac{(U_e^2(90°) + U_e^2(0°) - 2U_e^2(45°))}{2(k_2^2 - k_1^2)\,v} \tag{3.13a}$$

$$u = \sqrt{U_e^2(90°) - w\,k_1^2 - v\,k_2^2} \qquad\qquad (3.13a)$$

In order to determine the directional sign on the v and w velocity components, two additional spatial sweeps were required using the Figure 3.8b probe configuration. This probe was rotated about its axis 90° to obtain position 2 from position 1 as depicted in Figure 3.13.
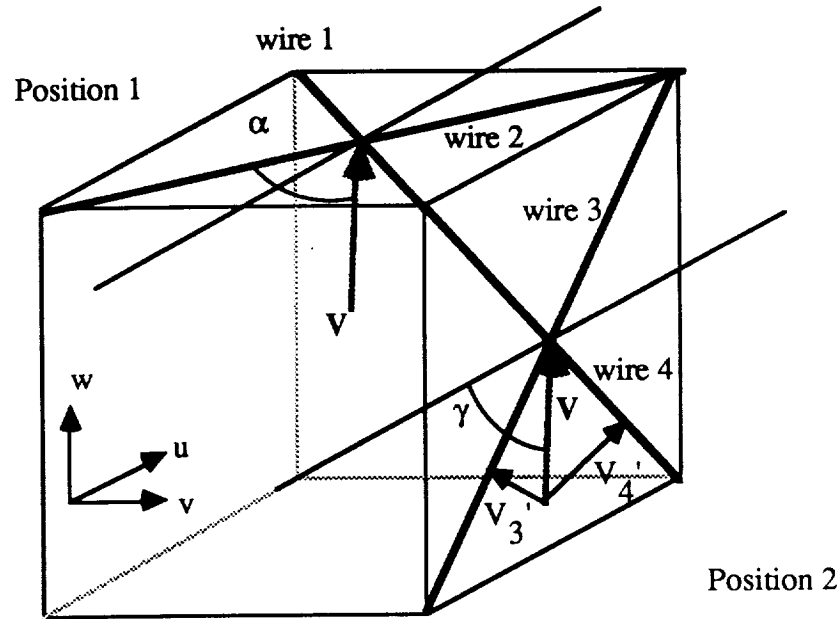
Figure 3.13 Directional Determination Geometry

From the above geometry, the value of γ, corresponding to the angle between the projection of the velocity vector on the u-w plane and the x axis, can be seen to vary $\pm 90°$, positive being defined as the particular angle shown. It can be seen that if the projected vector lies anywhere in this region, the effective velocity sensed by wire 4 will be greater than that of wire 3. Actually, a unique value can only be determined for $0° < \gamma < 45°$. If γ is equal to say 55°, this would give the same readings on wires 3 and 4 as at $\gamma = 35°$. Nonetheless, a greater effective velocity on wire 4 than wire 3 would indicate than there is a positive w velocity component and that is what is

required. Similarly, a greater effective velocity on wire 3 than wire 4 indicates a negative w velocity. Mathematically, this can be represented as,

$$\gamma = 45° - \tan^{-1}\left(\frac{U_{eff_3}}{U_{eff_4}}\right)$$

The sign of γ thus determines the sign of the w velocity component. In a similar manner, a relation for then sign of v can be determined

$$\alpha = 45° - \tan^{-1}\left(\frac{U_{eff_1}}{U_{eff_2}}\right)$$

A positive value of α indicates a positive value of v, using the coordinate system shown. As an example of the effectiveness of this directional determination, an α map and a γ map of the field above a 75° delta wing at 20° angle of attack are given in Figure 3.14.
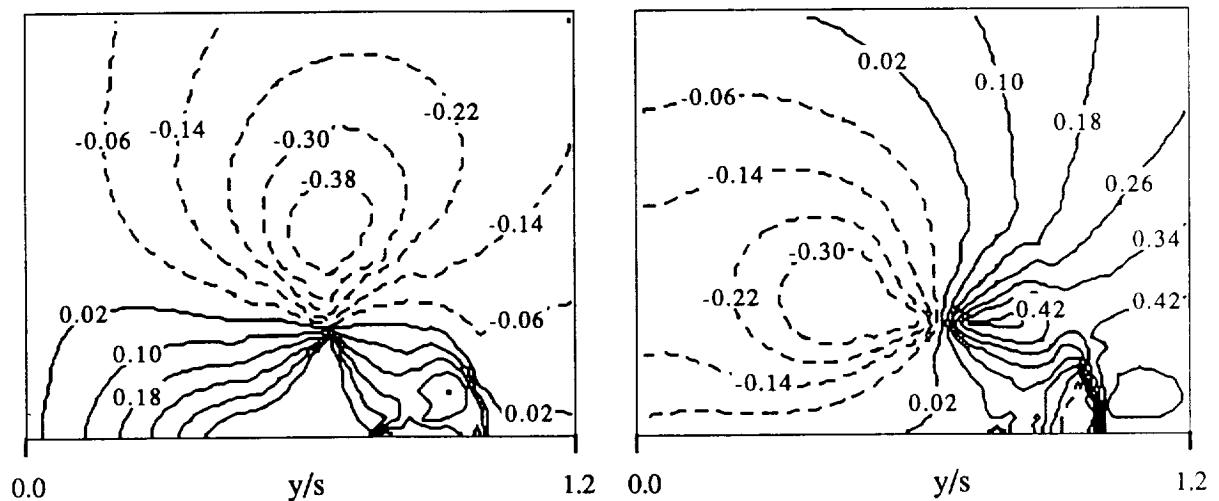
Figure 3.14 Directional Maps a) α b) γ

The complete procedure for acquiring a field of data therefore combines Sherif and Pletchers technique with two additional grid sweeps for direction. In order to check the validity of this method, outside of comparing data acquired over a delta wing with published data, the probe was tested in a known set of flowstreams. The probe was oriented to arrive at six different sets of velocity components listed below:

1. $u = U_\infty$, $v = w = 0$

2. $u = v = \dfrac{U_\infty}{\sqrt{2}}$, $w = 0$

3. $u = w = 0$, $v = U_\infty$

4. $u = 0$, $v = w = \dfrac{U_\infty}{\sqrt{2}}$

5. $u = w = \dfrac{U_\infty}{\sqrt{2}}$, $v = U_\infty$

6. $u = v = w = \dfrac{U_\infty}{\sqrt{3}}$

The difference between what the velocity values, scaled by U_∞, should be and what the procedure outlined above resulted in, is shown in Figure 3.15.
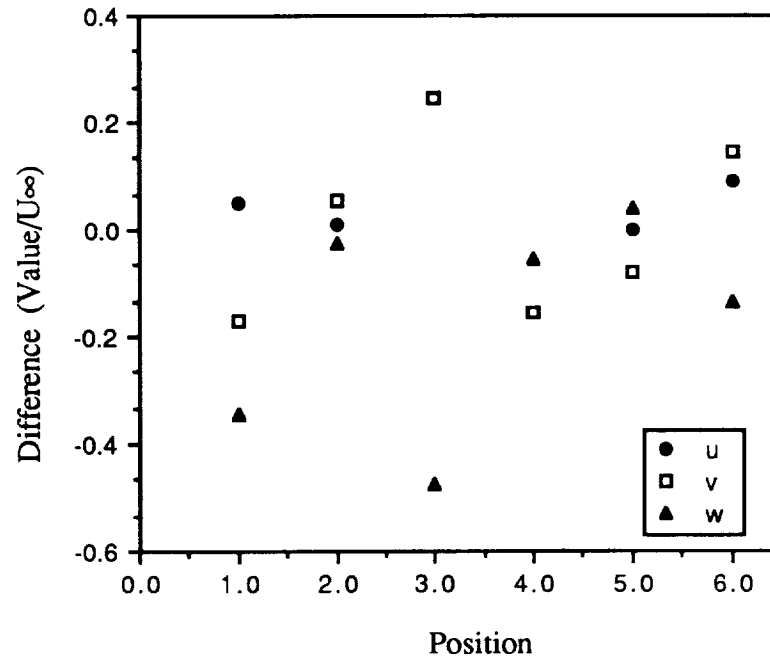
Figure 3.15 Cross Wire Positional Response

Obvious differences existed between the measured and actual values. The largest discrepancies for the w component at position 3. Sherif and Pletcher note that this method is suitable for three dimensional flows and position 3 contains two component which should be zero. Hence, one would expect the largest error to occur there. Conversely, the condition where all the components are of equal value would be expected to yield the lowest error. This is not the case, for position 6 indicates errors approaching 0.2. The lowest errors occur in positions 2 and 5. Position 5 contains values of roughly equal magnitude, but position 2 has w = 0. Note that the values of u and v in position 2 are equal. For positions where u = 0, that being positions 3 and 4, a negative square root arose from the equations given previously and therefore the points are not displayed. If such a condition is used to denote a value of u ≤ 0, that is, simply a conditional check, then the error difference would be zero. Although only one test was performed at each orientation, it is evident that as the flow departs from three dimensionality, where all three components are of the same order, the error increases dramatically. The equations (3.13 a - c) were further examined for their output sensitivity to changes in the measured input voltages. Since this was done using data obtained from the measurement surveys, discussion will be deferred until Chapter 5. A listing of the sensitivity inputs and outputs is provided in Appendix C.

It should be noted that the important matter of temperature calibration of the wires has been circumvented. This is a very important consideration, as a calibration of a wire is not independent of the ambient temperature. To avoid the necessity of temperature compensation due to ambient changes, the wires were calibrated individually prior to and during each run. The ambient was constantly monitored and did not vary by more than ± 1°C which has a negligible effect on the measured voltages during the course of any one run. For information on temperature compensation techniques the reader is referred to Bearman(1971), Drubka, Tan-atichat, and Nagib (1977), Machen (1986), and Manca, Mastrullo, and Mazzei (1988).

CHAPTER IV

EXPERIMENTAL APPARATUS AND PROCEDURES

4.1 The Wind Tunnel

The experiments in this study were performed in the University of Notre Dame subsonic wind tunnel facilities. The tunnel is of the indraft, open circuit type and consists of the 24:1 contraction inlet, a test section, and the diffuser section as depicted in Figure 4.1.
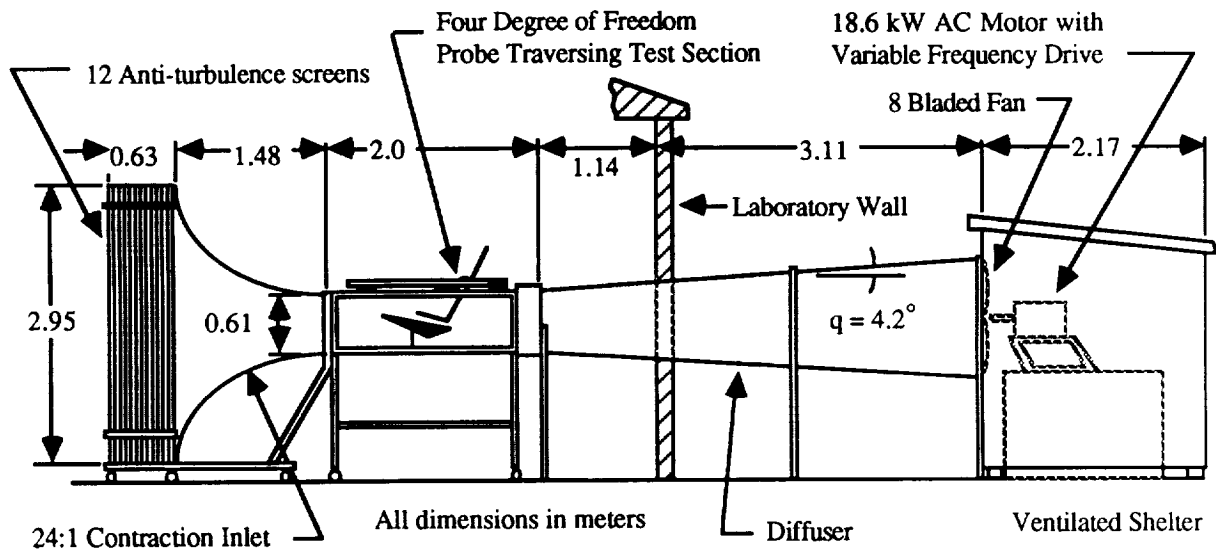
Figure 4.1 Notre Dame Wind Tunnel

The test sections are interchangeable and are typically 610 mm by 610 mm (24 in. by 24 in.) cross-section with a length of 1820 mm (72 in.). The diffuser section expands the flow downstream of the test section through a 4.2 meter (13.8 foot) length at an included angle of 4.2°.

The tunnel is powered by an 18.6 kw AC induction motor which drives an 8 bladed 1.2 meter (4 foot) fan located in the diffuser outlet . Twelve "anti-turbulence" screens are mounted across the entrance to the contraction inlet to reduce the flow irregularities to a scale where they rapidly dissipate.

The primary benefit of such a design is that it allows for flow visualization using a wide variety of tracer materials without contamination of the flow as would occur in a closed circuit design. The major disadvantage is susceptibility to atmospheric disturbances. Any variation of the pressure outside causes the tunnel velocity to vary with time. To reduce the amount of unsteadiness in the flow due to outside gusting, a flow restricter constructed of 5 mm (0.2 in.) diameter plastic tubes, 200 mm (7.9 in.) long and mounted in a frame, can be inserted between the test section and the diffuser. Due to the required flow speeds for calibration during this investigation, the flow restricters were not employed. The turbulence intensity in this particular wind tunnel configuration has been determined by Brendel and Huber (1984) using a single wire hot wire anemometer to be below 0.5% for all speeds and configurations and less than 0.1% at all clean section flow speeds for disturbances with frequencies greater than 10 Hz.

4.2 The Test Section

The test section utilized for the majority of tests was previously designed and used by Payne (1987). The section dimensions were 610 mm by 610 mm by 1820 mm (24 by 24 by 76 inches). The four degree of freedom probe traversing mechanism was integrated with the roof of the test section as illustrated in Figure 4.2.
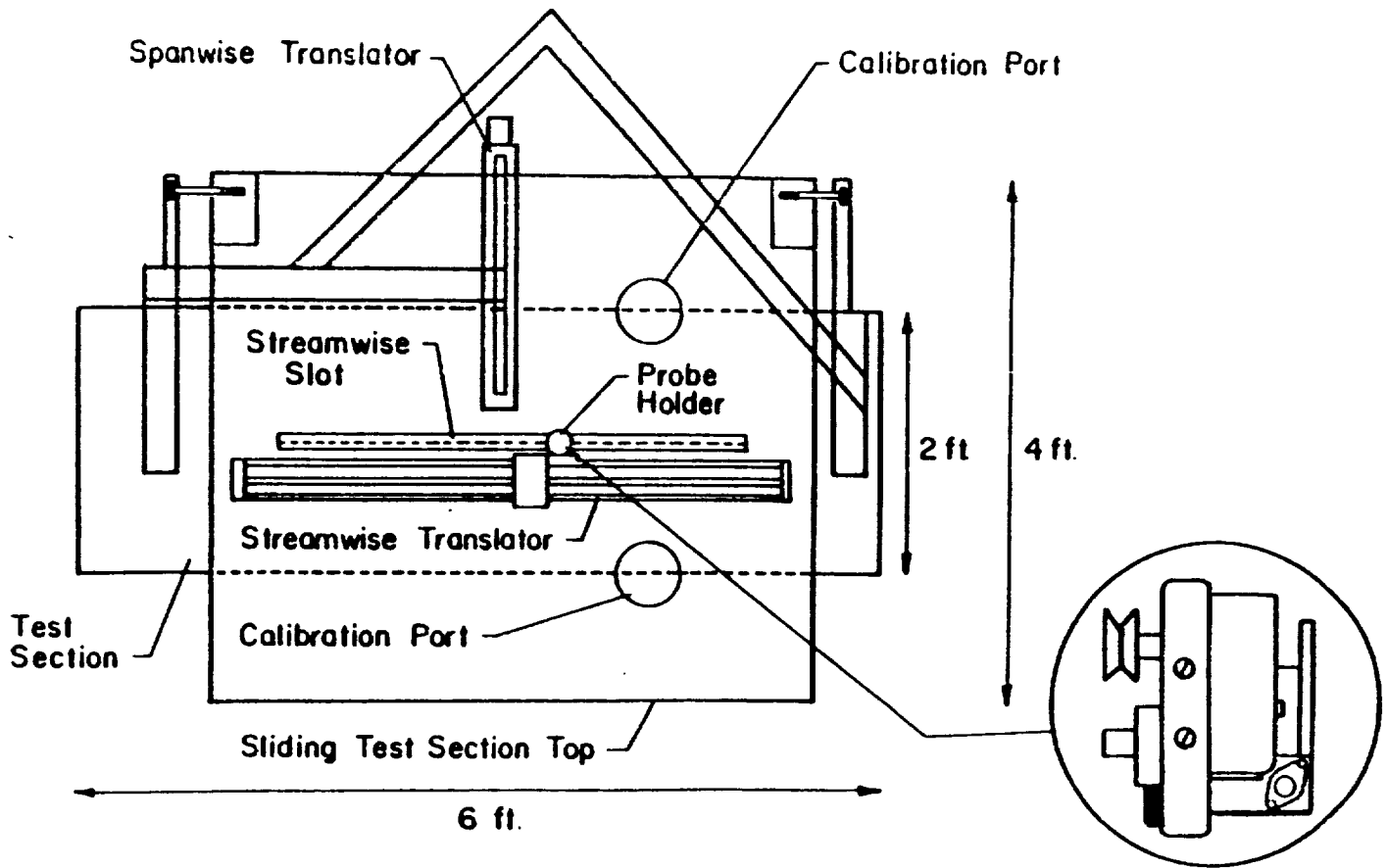
Figure 4.2 Three Dimensional Traversing Test Section (top view by Payne, 1987)

The system was computer controlled in the spanwise, streamwise and vertical directions. The probe position could also be rotated about the pitch axis manually. The streamwise and spanwise translator motions were driven with Slo-Syn MO623-FD08 stepper motors powered by a Velmex amplifier/controller model 8202M1. Directional control in the vertical utilized a DISA 52B01 Sweep Drive Unit in conjunction with a 52C01 stepper motor. The amplifiers themselves were controlled by a Macintosh II computer equipped with a National Instruments MIO-16 12 bit data acquisition board. Code was developed utilizing LABView software to maneuver the probe to any relative position given the desired distances. The particular setup required the use of all 8 digital I/O 0-5 volt lines for control. Further technical details can be found in Visser (1989). The minimum step sizes possible in the streamwise, spanwise, and normal directions as noted by Payne (1987) were 0.0064 mm, 0.0254 mm, and 0.0208 mm respectively with an overall positional accuracy of ± 1 mm.

4.3 Models

All the models used for testing were flat plate delta wings having a windward 25° bevelled edge. The flowfield velocity measurement models were made of aluminum, having a centerline chord of 406.4 mm (16 inches) and a thickness of 6.35 mm (0.25 inches). The sweep angles were 70° and 75°. A schematic of the coordinate system and the associated geometric details is illustrated in Figure 4.3.
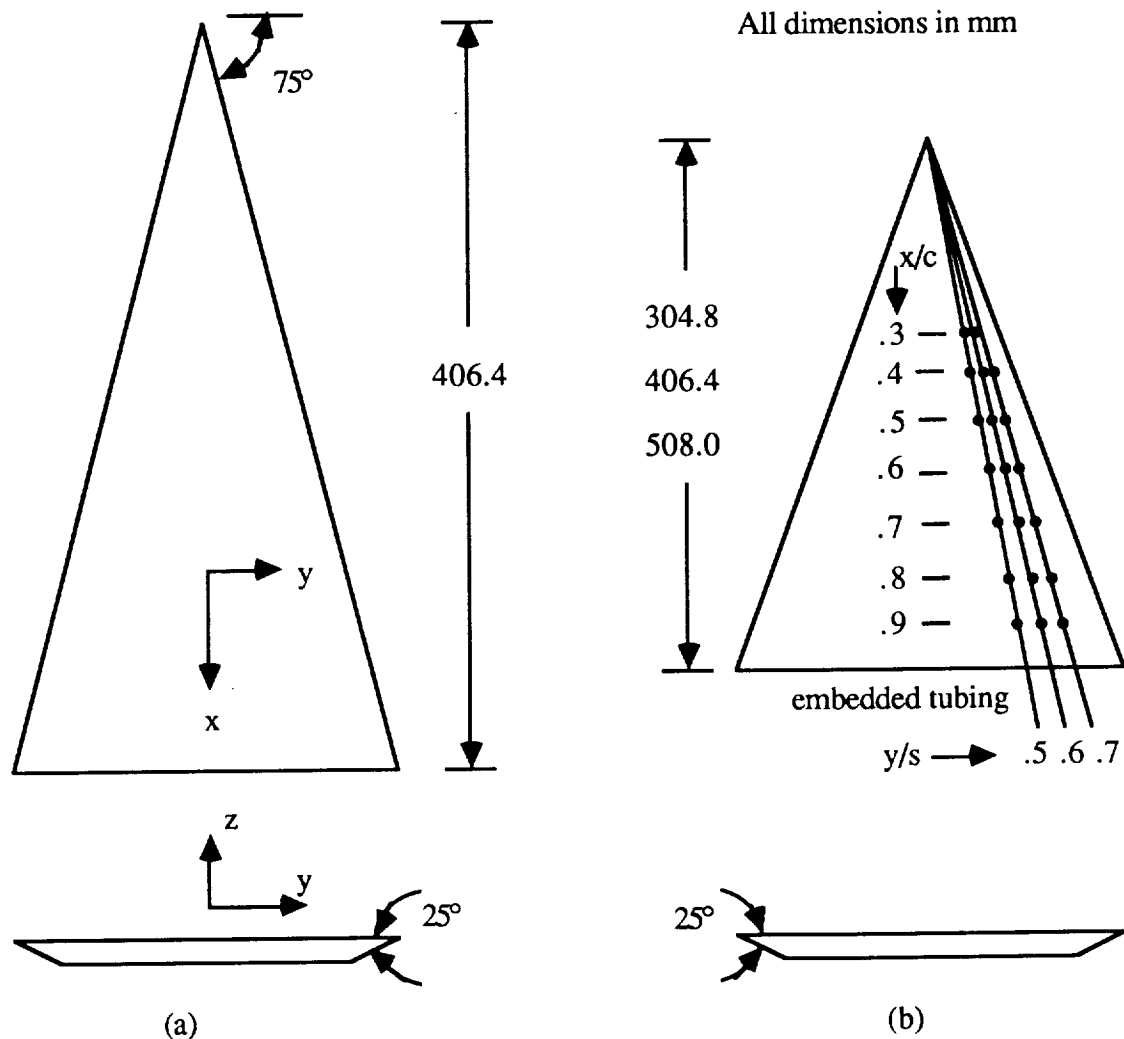
Figure 4.3 Delta Wing Model Geometries a) Aluminum Full Span b) Acrylic Full Span

The surface pressure measurements were taken using 0.25 inch thick, 70° sweep acrylic delta wing planforms. Three chord lengths of 304.8 mm, 406.4 mm, and 508.0 mm (12, 16, and 20 inch) were investigated. Channels were milled into the surface, allowing 1.37 mm ID / 1.83 mm OD (0.054 / 0.072 inch) stainless steel tubing to be embedded along rays of $y/s = 0.5, 0.6$, and 0.7 on each of the models. Pressure tap holes of an outer diameter of 1.07 mm (0.042 inch) were then drilled at chord stations ranging from 0.2 to 0.9 as shown in Figure 4.3b. When measuring the surface pressure, all the taps were covered by a piece of transparent tape, save the station being measured.

Additional velocity measurements were made using a half span aluminum model of the same sweep and bevel as the full span aluminum models, but a root chord of 26.95 inches. This enabled the effect of a finer grid resolution to be examined in conjunction with a smaller relative probe size. A splitter plate was employed during these tests.

4.4 Flow Visualization Techniques

Three types of flow visualization were applied during the course of this investigation. Kerosene and titanium tetrachloride were used to mark the flow externally. Visualization of the planform surface was accomplished using a mixture of kerosene, oleic acid and titanium dioxide.

Kerosene was vaporized on electric resistance heater strips to produce a white "smoke" which, in conjunction with the correct lighting, visualized the flow. Four of these systems were combined to form a smoke generator. A squirrel cage blower forced the smoke through a series of cooling pipes to reduce possible buoyancy effects. The smoke was exhausted through the rake of tubes and entered the tunnel upstream of the contraction section. An extensive review on the

subject, both past and present, is given by Mueller (1978) and pertinent schematics can be found in Visser (1988).

Titanium tetrachloride ($TiCl_4$) is a colorless liquid that, upon exposure to water vapor, reacts to form a dense white smoke composed of hydrochloric gas and titanium dioxide particles. This smoke can be introduced into the flow field to locally visualize certain aspects of the fluid motion. Other applications have included dripping or painting the liquid onto a model enabling brief periods of visualization before the supply had to be replenished (Freymuth, Bank, and Palmer (1985)). In the present tests, titanium tetrachloride was contained in a specially constructed glass flask under an inert nitrogen atmosphere. The low vapor pressure of the $TiCl_4$ allows the region above the liquid to saturate with the vapor component and thus the gaseous space inside the container contains a mixture of the nitrogen and the $TiCl_4$ vapor. Nitrogen was fed into the container, displacing the vapor in the bottle out to the test section where it exited at the model. The tunnel probe acts in a similar manner to a water tunnel dye marker in that the vapor was immediately visible, marking a particular streakline. Further details are described by Visser (1988) and Visser, Nelson, and Ng (1988).

Surface visualization was conducted on the 70° and 75° degree models. Each was fitted with a mounting pin at the trailing edge to facilitate removal and subsequent record on film. A mixture of 15 parts of kerosene, 5 parts of titanium dioxide and 1 part oleic acid provided an oil based slurry which was spread uniformly on the model at zero tunnel velocity. The tunnel was then run at the test condition until the liquid evaporated leaving the skin friction lines visible. The models were subsequently removed from the tunnel, photographed and cleaned prior to the next test. Tests were conducted at a Reynolds number of 250,000 while the angle of attack was varied from 25° to 45°. Both the leeward and windward surfaces were documented. Tests with the models reversed, such that the bevel was on the leeward side, were also performed.

Still and moving visual recordings were made of the flow over the models to help in analyzing the data. Photographs were taken using a Nikon FM2 35mm SLR camera. These were used to record the various surface visualization patterns at different angles of attack. Kodak Tri - X Pan 400 ASA black and white print film was used for the photographs. Video taping was accomplished using a Panasonic Digital 5000 System Camera capable of an effective frame rate of 1/1000 of a second. A Panasonic NV - 8950 VHS recorder was used to document the events. Lighting was in the form of high intensity 1000 Watt lamps placed so as to maximize tracer visibility.

4.5 Pressure Measurements

Surface pressure measurements were made on the 0.25 inch thick, 70° swept acrylic delta wings of 12, 16, and 20 inch chord length. Transparent tape was used to cover the all the pressure tap holes save the one which was being measured. The Reynolds number was held to 250,000 and the sting location was also varied. Angles of attack ranged from 25 to 45 degrees.

Total pressure measurements were made in the core of the vortex above the 75° swept delta wing at angles of 20° and 30° degrees angle of attack. Various chord stations were examined, all at a Reynolds number of 250,000. A stainless steel tube probe of 1.07 mm ID / 1.47 mm OD (0.042 / 0.058 inch) used to measure the total pressure and is shown in Figure 4.4. To obtain the total pressure, the probe was maneuvered to the core center, based on the value of the maximum axial velocity obtained from the hotwire measurements. The probe location was then manually adjusted in the y/s and z/s directions until a minimum value of of the total pressure was observed.
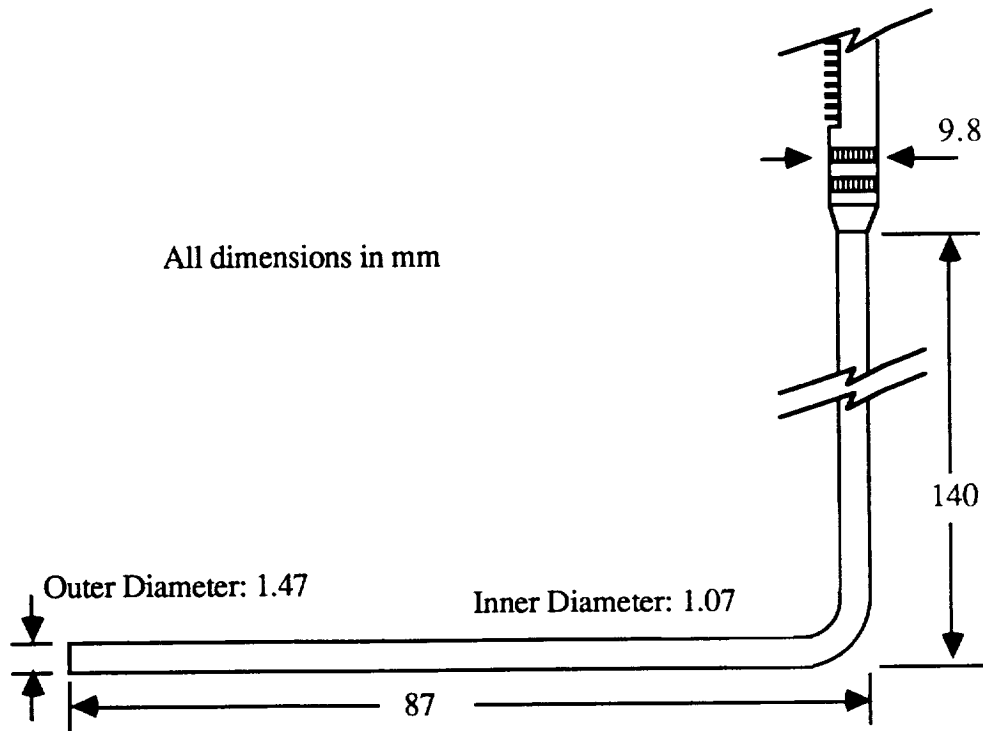
Figure 4.4 Total Pressure Probe

All dimensions in mm

9.8

140

Outer Diameter: 1.47

Inner Diameter: 1.07

87

4.6 Cross-wire Equipment

The majority of velocity field data was accumulated over a 75° sweep delta wing at 20° angle of attack. Measurements were made at various chordwise stations in grid planes normal to the upper surface. The angle of attack was then increased to 30° and chordwise stations were measured upstream of the probe induced breakdown of approximately x/c = 0.5. Experiments by Payne, Ng, and Nelson (1987) comparing LDV and seven hole probe data have shown that the effect of introducing a probe into the flowfield does not greatly distort the flowfield provided the measurements are taken upstream of the breakdown zone. Flow visualization confirmed that positions measured were kept upstream of the breakdown region. A 70° sweep configuration was utilized at 20° angle of attack in an effort to observe the effect of sweep. A final set of tests were

taken with the larger half span model to observe the relative effects of grid resolution changes .
Unless specifically noted, all the data presented reflects a Reynolds number of 250,000.

The geometry of the probe used for acquiring the hot wire data is shown in Figure 4.5. A
DISA geared probe holder held the probe extensions out to the actual cross wire probe. As detailed
earlier, two x-wire probe configurations were utilized and were illustrated in Figure 3.8. Probe 1,
a DISA 55P62, had wires lying in a plane perpendicular to the probe axis, while the wires of probe
2, a DISA 55P61, were lying in a plane parallel to the probe axis. The probes utilized five
micrometer diameter tungsten wires giving an length/diameter ratio of 250. Overheat ratios were
set to 1.8. The wires were calibrated for every test to reduce the possible errors associated with
property changes of the wires. In addition, this procedure eliminated the need for temperature
compensation as the ambient temperature did not vary by more than ± 1° C over the course of any
individual test.The minimum distance between the wing surface and the probe was 3.0 mm due to
probe geometry.
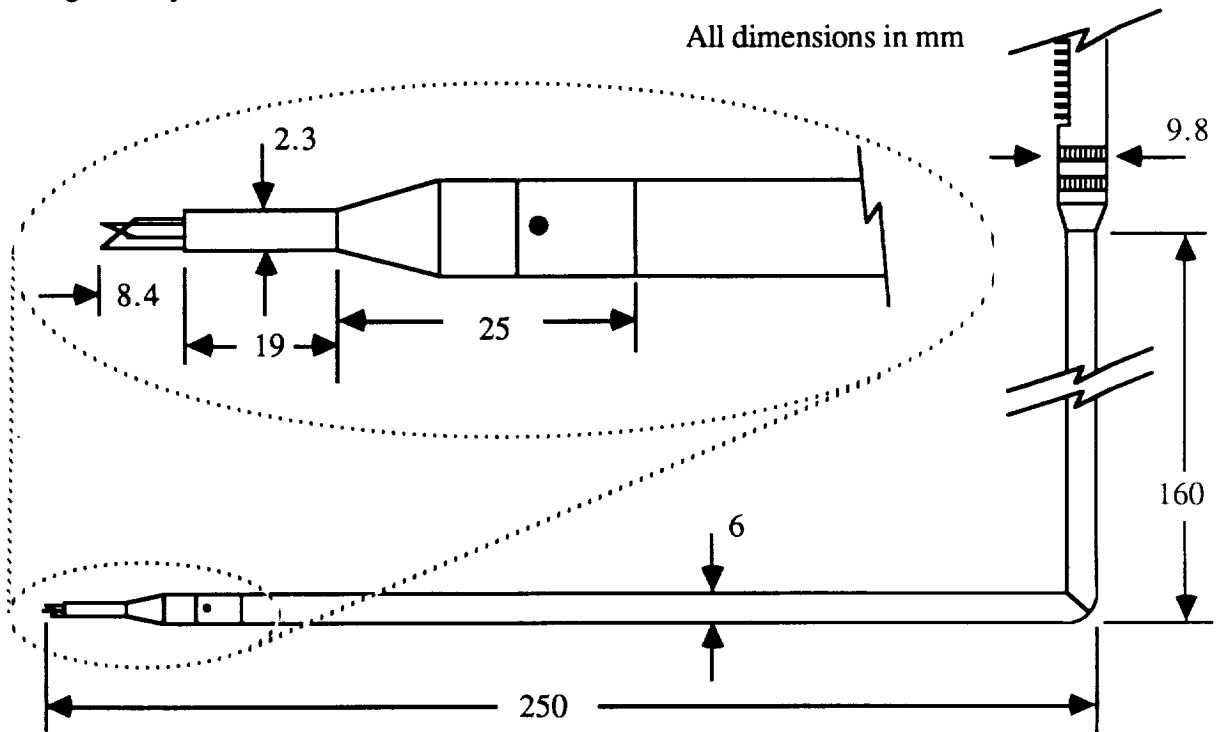
All dimensions in mm

Figure 4.5 Hot Wire Probe Geometry

In order to fully determine the three velocity components and their associated directions it was necessary to take four normal grid sweeps above the wing at each chordwise location. The initial two grid sweeps used probe 1 with wire 1 at the reference of zero degrees and wire 2 at negative 90 degrees using the geometry in Figure 3.12 and in accordance with that of Sherif and Pletcher (1987). The probe was then rotated 45° about its axis and a second sweep initiated. This provided enough information for the velocity magnitudes to be determined. The second probe was used to take two sweeps with the plane of the wires parallel to the wing and perpendicular to it respectively. This second set of sweeps determined the direction of the transverse (v) and normal (w) velocity components. It was assumed that the direction of u was always in the positive direction as the probe was kept in the flow forward of the breakdown region.

The cross wire probes were monitored using a TSI IFA 100 Model 150 constant temperature anemometer system. The accuracy of the anemometer given by the manufacturer is such that as the probe resistance is brought to zero, the difference on the actual resistance measured is:

	meter	Ω
Probe Resistance	0000	8.500
	0010	8.504

Hence, if the worst case scenario is presumed with the meter capable of displaying ± 0005 or 0.002 Ω then an estimate of the desired overheat ratio can be obtained. Maximum error for an overheat ratio of 1.8 is estimated to be ± 0.08%. Details can be found in Appendix C. A TSI model 570 signal conditioner was used in conjunction with the anemometer to provide a DC coupled offset of 1 volt ± 0.15%. The 570 signal conditioner applied a gain of 5 ± 0.15% to the signals and low pass filtered at 1000 Hz ± 10% before they were sampled by the computer.

4.7 Data Acquisition and Reduction System

Data was acquired using a Macintosh II computer equipped with a National Instruments MIO-16H-9 12 bit D/A board. All the signals were obtained in the differential mode using uniform gains and a -5 to 5 volt range. The available precision for these settings corresponding to one least significant bit of the 12 bit A/D converter was 2.44 millivolts. The sampling rate was set to 25,000 Hz. Two channels were used to acquire the hot wire voltages and the dynamic pressure was obtained on the third channel with a resolution of 1.22 millivolt/bit.

The data was reduced to velocity values using a least squares fit based on the calibration to determine the effective velocities. The method of Sherif and Pletcher (1987) was then applied to determine the magnitudes of the velocity components. Direction was determined at the same time using the information form the third and fourth wire configurations.

Several reduction codes were written for the post processing of the data. These codes accomplished a wide variety of tasks and, for simplicity, a schematic overview is given in Figure 4.6.
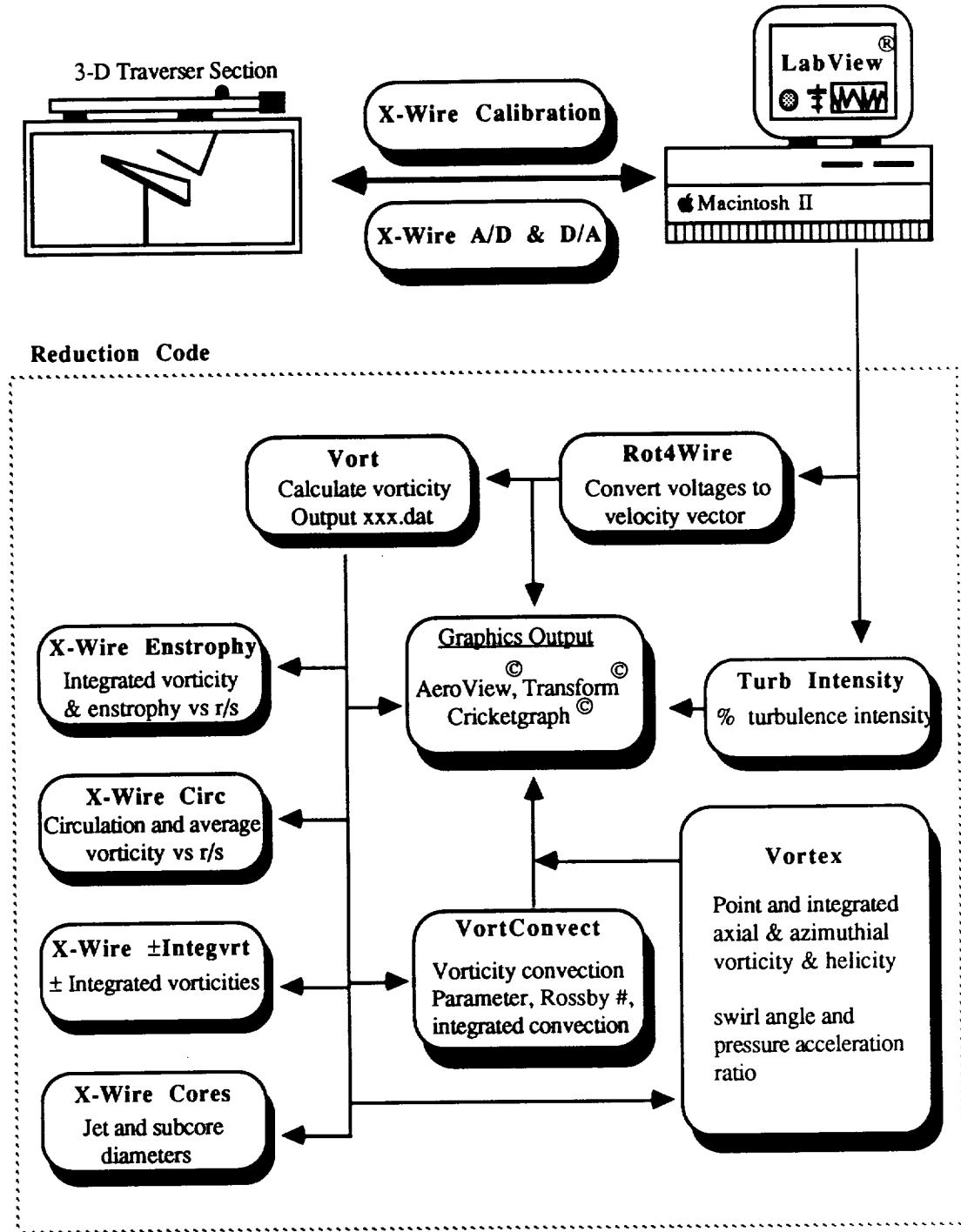
Figure 4.6 Data Acquisition and Reduction Schematic

CHAPTER V

RESULTS AND DISCUSSION

The results of this study are divided into several sections, beginning with the surface flow visualization. Several interesting features were noted from the visualization, which have not been reported by previous investigators and so are presented here. The major part of this chapter deals with the data obtained from the cross wire velocity measurements. First, the velocities are discussed and compared with previously obtained data. An indication of the unsteady nature of the flow is also revealed from the fluctuations in the measured wire voltages. The data is then analyzed in light of its derived properties such as the vorticity and the circulation. Dimensional scaling and various ways of interpreting the data are offered as a means for characterizing the behavior of the vortex. Parameter correlations are presented next, using both conventional ratios, such as the swirl angle, and ratios typically not examined in this context. A brief mention is made of some interesting spectral behavior in the vortex core upstream of breakdown and this is followed by a look at the core dimensions calculated from the cross wire data itself. Lastly, the surface and off-surface pressure data is detailed in light of the ability of these measurements to indicate the onset of breakdown. The total pressure measurements are combined with the velocity data to examine the concepts introduced at the end of the previous chapter.

5.1 Surface Flow Visualization

The interpretation of the 'skin friction' lines, that is the lines resulting from surface flow visualization technique, can indicate a great deal about the nature of the flow. Extensive

discussions on flow topology deciphered from delta wing surface flowlines are given by Peake and Tobak (1980) and Delery (1990). Investigators, such as Kjelgaard and Sellers (1990) have conducted tests to establish locations of the major features for comparison with numerical predictions. In the present study, surface flow visualization on the 70° and 75° planforms was performed to examine any changes on the surface flow patterns specifically due to breakdown. No evidence of transition to a turbulent boundary layer was observed. Since the Reynolds number based on chord was much less than 500,000, this was in agreement with the earlier statements of Naarding and Verhaagen (1988) that the entire boundary layer on the upper wing surface can be expected to remain laminar. Several other interesting features were noticed, however, and are presented below.

Typically, investigators have found that the surface visualization will reveal the presence of secondary and even tertiary separation and reattachment lines on a flat plate delta wing. Carcaillet, Manie, Pagan, and Solignac (1986) applied topological rules to interpret their visualization photographs for a 75° sweep wing at $\alpha = 20$. A cross sectional schematic of the interpretation of their visualization data is presented in Figure 5.1a. The major features, including the presence of the primary, secondary, and tertiary vortex structures and their respective separation and attachment lines, were observed. Naarding and Verhaagen (1988) also observed the presence of a tertiary vortex system on their unit aspect ratio biconvex delta wing. They point out, though, that this tertiary flow structure is confined to laminar boundary layer flows.

Carcaillet, Manie, Pagan, and Solignac further suggest that the attachment point of the secondary vortex is almost identical to the primary separation location. Thompson (1975) postulates that a vortex structure may exist in this region between these two nodes, as is detailed in Figure 5.1b. Based on this, Dixon (1989) concludes that the primary vortex is not fed by a continuous sheet of vorticity, but is comprised of a stationary, shear layer vortex which feeds the main vortex. The

primary vortex

C1

F1

CF2

F3

A1

S2 A3 S3 A2 S1

A4

F : Focus
A : Attachment saddle point
S : Separation saddle point
C : Saddle point

leading edge

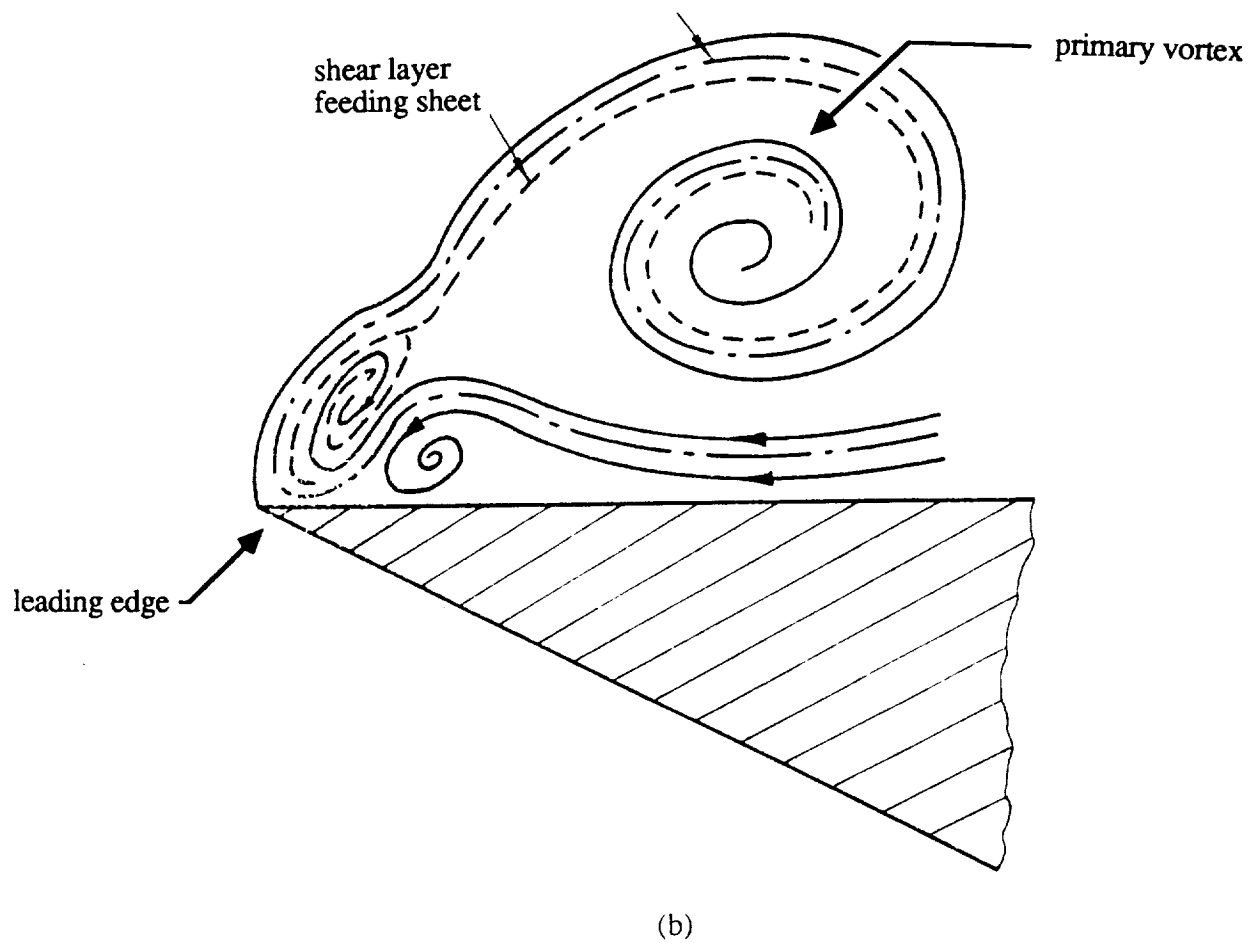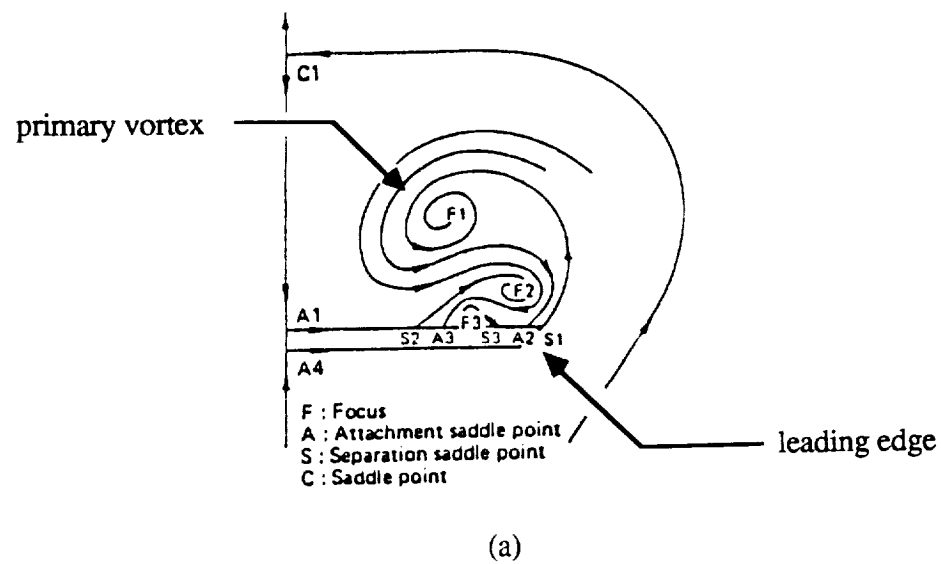(a)

shear layer
feeding sheet

primary vortex

leading edge

(b)

Figure 5.1 Vortex Topology a) $\Lambda=75°$ $\alpha = 20°$ (Carcaillet, Manie, Pagan, and Solignac, 1986)

b) Proposed Stationary Shear Layer Vortex Thompson (1975)

present surface flow experiments indicate, however, that if some region of vortex structure exists between the secondary vortex attachment point and the leading edge, it would have to be rotating in a sense opposite to that in Figure 5.1b, based on the direction of the surface flow pattern.

Present experimental results indicated a very complex surface pattern extending from just inboard of the secondary vortex separation line to the leading edge. The results of a surface flow visualization test at $\alpha = 30°$ for the $\Lambda=75°$ delta wing planform is shown in Figure 5.2a. A close-up is shown in Figure 5.2b. The detailed features observed in the region between x/c = 0.3 to 0.4 were handsketched in Figure 5.2c from the model itself. Although all the features can not be explained, three interesting observations can be noted. The first is the darker region on the surface just inboard of the secondary separation line. This is common to the flow of the majority of cases considered here. It is possible that this indicates a local acceleration of the flow, although one might expect the flow to be slowing as it approaches the point of separation. The second interesting area is that located just inboard of the leading edge. This too appears darker, but the surface lines are plainly seen. The secondary vortex attachment line appears to lie just inboard of this darker region and the flow is thought to be traveling outwards to rejoin the leading edge flow. However, the surface lines point in the downstream direction which, unless there is a reverse flow region, indicates the surface flow to be travelling towards the center of the wing. This would indicate that any rotating flow present in this area would have the same sense as the secondary vortex, opposite to that proposed by Thompson (1975).

The final feature worth noting, which occurred on most of the planforms, involved an area of reversed flow on the surface of the wing. This occurred just outboard of the secondary attachment line. The area can be observed near the aft portion of the wing in Figure 5.2a. A closer look is given in Figure 5.3 for the 70° sweep wing at 25° angle of attack. The 'puddles' left by the
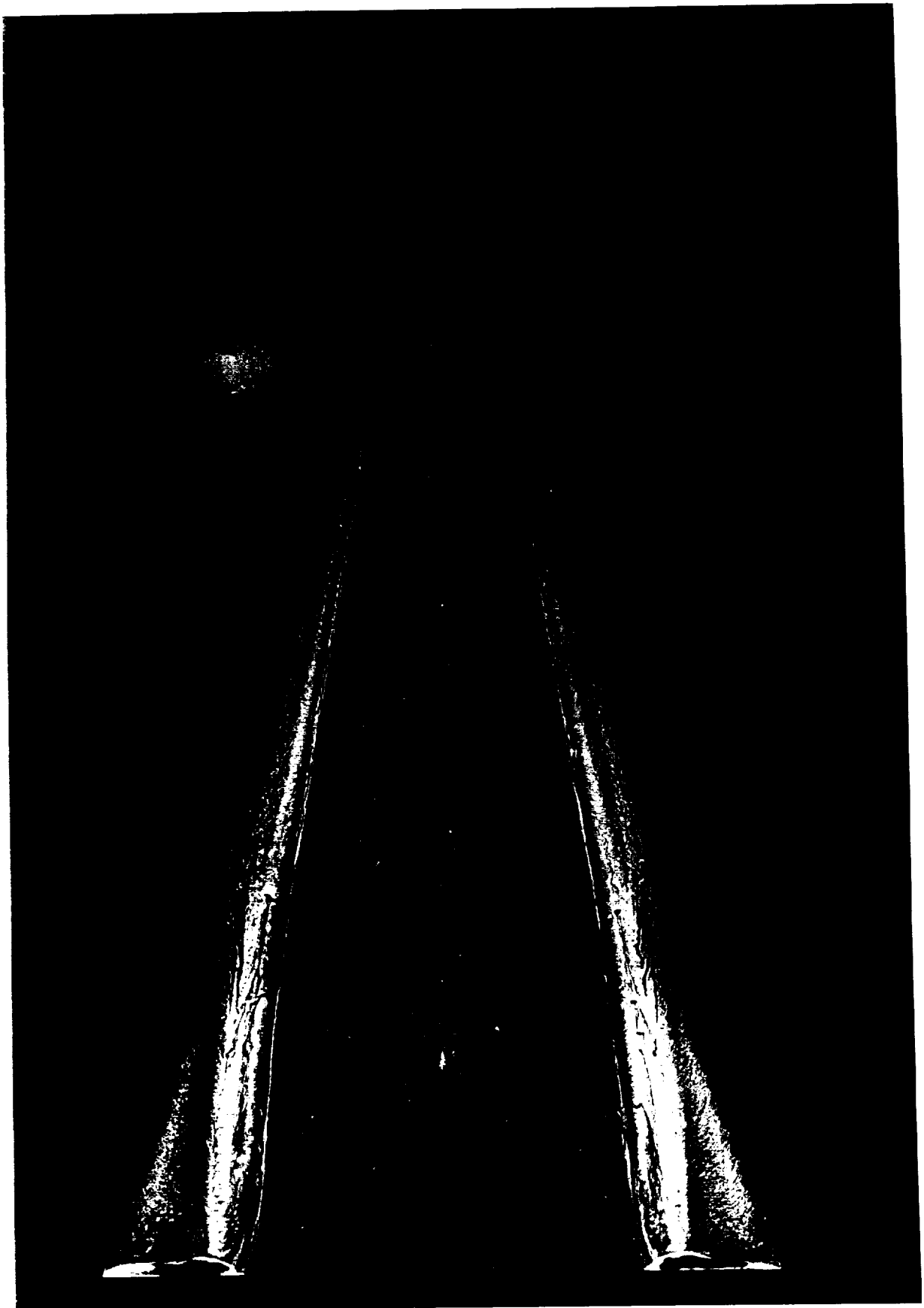
Figure 5.2a Leading Edge Details for Λ=75° α = 30° , Planform
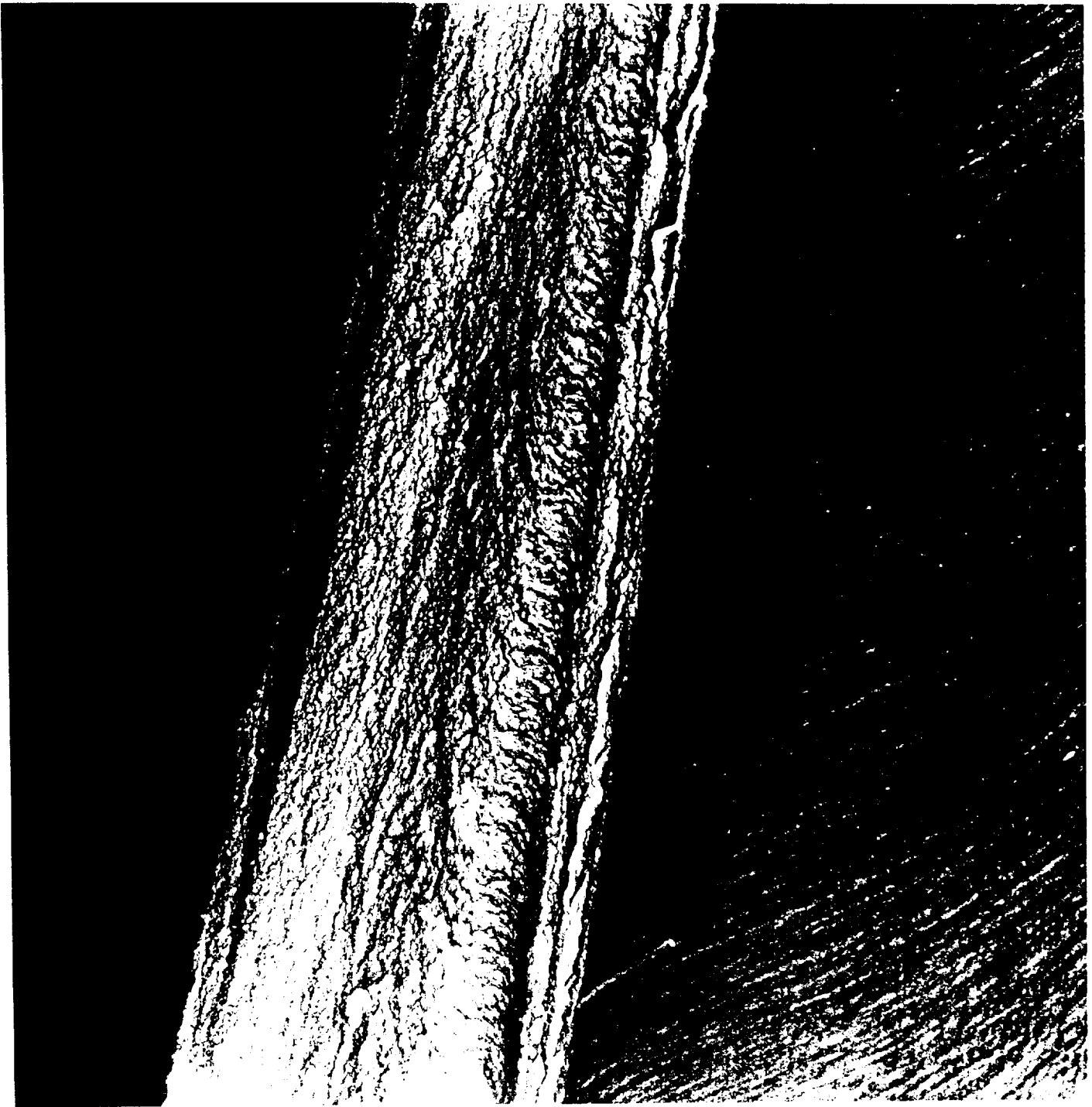
Figure 5.2b Leading Edge Details for $\Lambda=75°$ $\alpha = 30°$, Closeup of Leading Edge
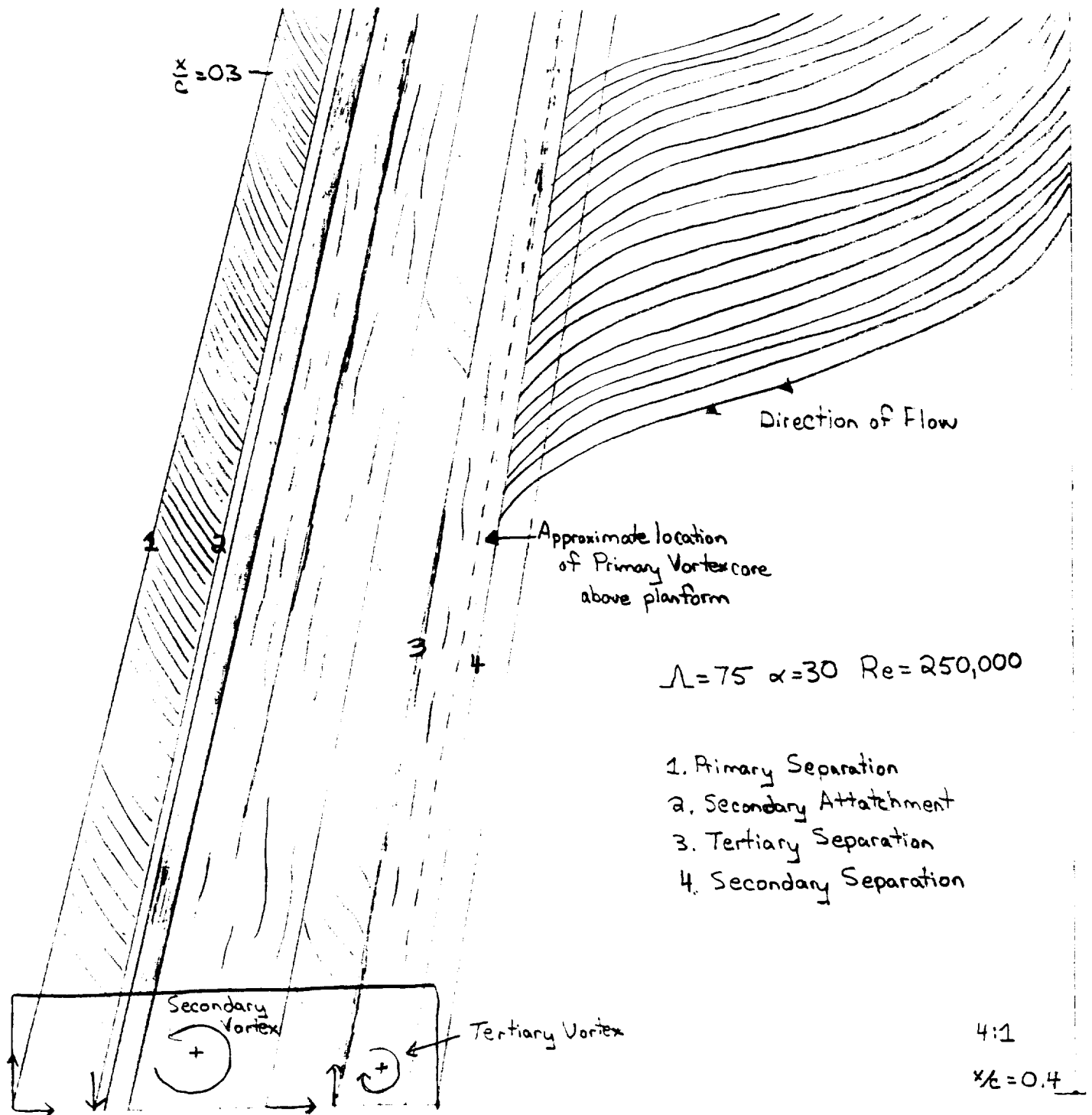
Figure 5.2c Leading Edge Details for Λ=75° α = 30° x/c = 0.3 to 0.4 at 4:1 scale

flow moving upstream are clearly evident. Earnshaw and Lawford (1964) also recorded much more pronounced evidence of flow forward from the trailing edges for lower wing sweeps and greater angles of incidence. The flow patterns that are presented for their higher sweep wings appear to contain features similar to that in in Figure 5.3 although they do not discuss aspects of this specifically.

Figure 5.3 Reversed Flow Region Details for $\Lambda=70°$ $\alpha = 25$

Gross changes in the surface pattern due to the movement of breakdown were not noticeable as shown on the 70° wing in Figure 5.4a, where no breakdown is present on the wing, and 5.4b, in which breakdown occurs at approximately $x/c = 0.4$.
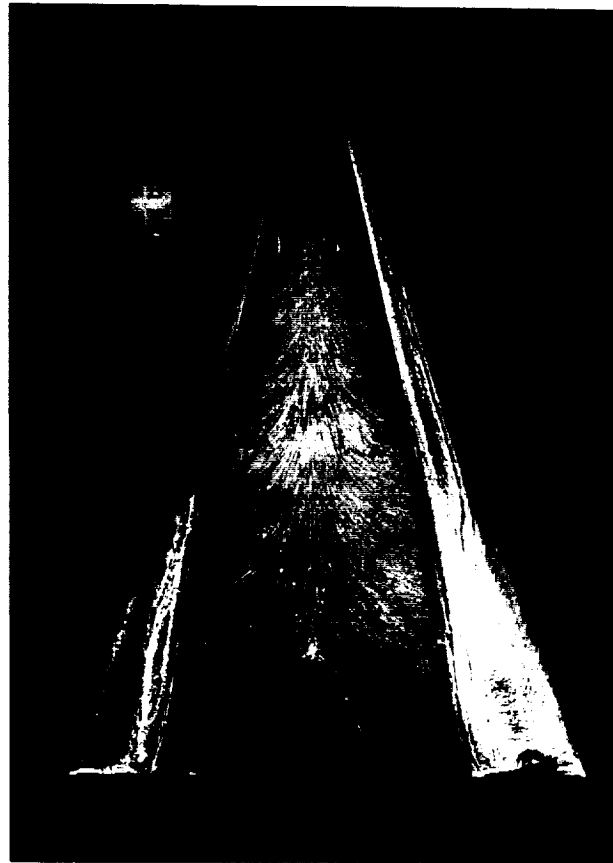
Figure 5.4a Angle of Attack Effect for $\Lambda=70°$, $\alpha = 25°$, no breakdown present

The only real feature that appears to have changed is the region just inboard of the leading edge. At the higher angle of attack, this region begins to widen closer to the apex. Note also the darker region inboard of the secondary vortex, mentioned previously. At $\alpha = 25$, the region extends to the trailing edge, but at $\alpha=35°$ it is less evident aft of about x/c = 0.7. It is not until $\alpha = 40°$, Figure 5.4c, that the surface shows a major topological change and the effects of breakdown can be more dramatically seen.

The breakdown is now at 20% chord and all traces of the darker region on the inboard side of the secondary separation line have disappeared aft of about x/c = 0.4. A weak separation line is still evident, however the complex structure noted earlier between the leading edge and this line is all but disappeared.

Figure 5.4b Angle of Attack Effect for $\Lambda=70°$, $\alpha = 35°$, breakdown at x/c = 0.4

Similar features were observed on the 75° wing. The dark region inboard of the secondary vortex was much more pronounced. Figure 5.5a is a closeup of the apex region, up to about 10% of the chord, at an angle of attack of 35°. The darker area is seen to extend from the apex. The bottom surface near the apex, as shown in Figure 5.5b, exhibited dark regions on the surface near

the apex as well. This darker area, on the underside of the planform, decreased in size with angle of attack and vice versa. There did not seem to be any local change in the direction of the surface lines between this region and the lighter colored areas next to it. A suggested explanation is that the solution for marking the flow simply dried at a faster rate in these areas, which would indicate a larger local velocity.

Figure 5.4c Angle of Attack Effect for Λ=70°, α = 40°, breakdown at x/c = 0.2

a)
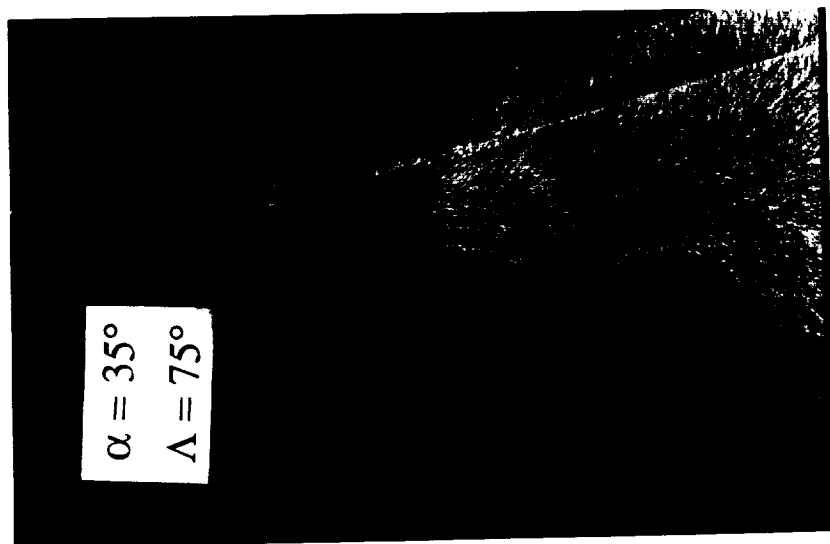
b)

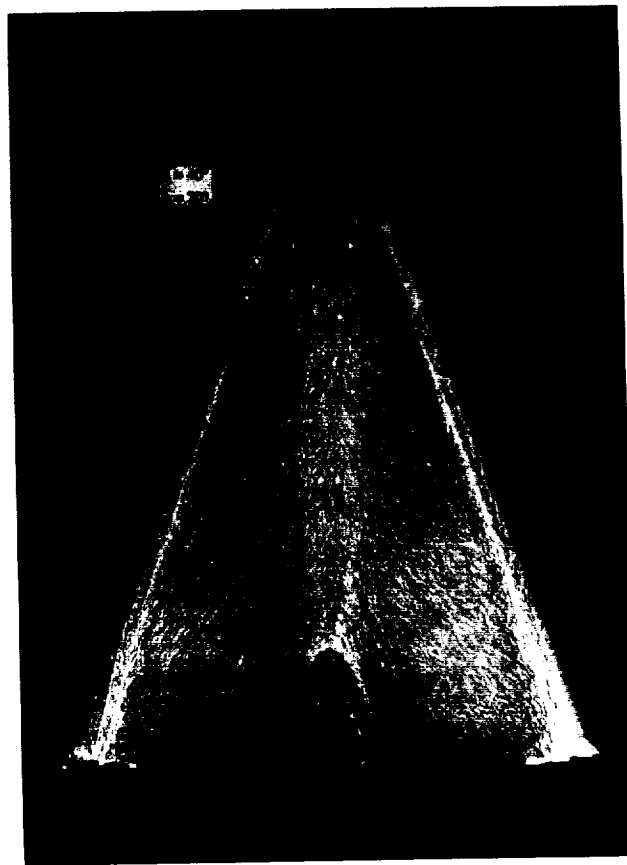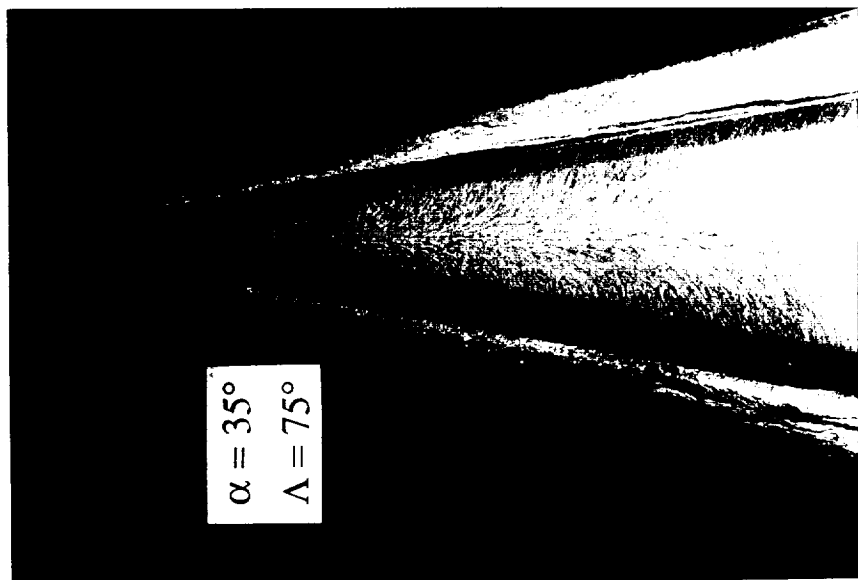Figure 5.5 Apex Details, x/c = 0 to 0.1 Λ=75° α = 35° a) Upper Surface b) Lower Surface

The surface flow visualization experiments provided several interesting insights on the nature of the topology of the vortex flow field. As demonstrated by other investigators, the presence of a tertiary vortex system is apparent. Local darker surface regions on the underside of the wing near the apex were noted to decrease with angle of attack. Additional dark regions inboard of secondary vortex separation line, on the leeward side of the wing, were seen to persist at all angles of attack until complete separation occurred. At higher angles of attack, these dark regions did not appear to extend completely to the trailing edge. These regions extended and intersected each other at the apex. Finally, the surface flow directly inboard of the leading edge and outboard of secondary vortex attachment line indicates a flow direction inwards from the trailing edge, towards the wing centerline, and in the axial direction. If this was caused by a local vortex, it would have the same sense of rotation as the secondary vortex.

5.2 Cross-wire Measurements

Velocity field data was acquired at a series of chordwise stations using the cross wire technique described earlier. A sample of the surveys are presented and compared with data acquired by Payne (1987) using a seven hole probe. The changes in the velocity profiles with distance from the apex is then examined along with the unsteadiness of the measured field. The velocity data was subsequently manipulated to derive field properties such as vorticity and circulation. These are described in the sections following. Dimensional scaling is used extensively to examine the behavior of these properties as the chordwise location and angle of attack were varied. Both integrated or average field distributions as well as discrete values are detailed. Finally, correlation parameters, such as the Rossby number and extensions of the discussions in Chapter 2, are presented. A listing of the data matrix, along with as some of the measured properties, is given in Appendix B.

5.2.1 Velocity

A typical axial velocity distribution measured by the present technique for $\Lambda = 75°$ at an angle of attack of 20° and $x/c = 0.5$ is given in Figure 5.6a. Note that the distances in the y and z direction are scaled by the local semispan. Thus, a $y/s = 1.0$ corresponds to the leading edge of the wing. The axial velocity u/U_∞ is the velocity normal to the measurement plane, which was perpendicular to the chord line, at the given chordwise station. The jetting core structure of the vortex is quite well defined, with the majority of the measured field maintaining a velocity above the freestream velocity. Measurements encompassed a z/s of 0.055 to approximately 1.0 and were taken from the chord centerline out to a spanwise location of $y/s = 1.2$ beyond the right edge of the wing. Grid increments were set to a y/s and z/s of 0.03 at each station.

Comparison with previous data obtained by Payne (1987) using a seven hole probe (SHP) was used to evaluate the performance of the cross wire measurement technique. The inherent complexity of the equations given in Chapter 3 make an assessment of the error difficult for each variable in the equation. In addition, the values of k_1 and k_2 were taken to be constant at 0.3 and 1.1 respectively, when they are in fact a function of the flow vector at extreme angles. Finally, four spatial passes were required for each survey, and although each was carefully aligned and each traversal was from the centerline outboard, the error in the traversing system contributes a cumulative error for each station. Thus a quantitative comparison with other data was used appraise the technique.

Seven hole probe data for the same test conditions in Figure 5.6a is given in Figure 5.6b. The field of Figure 5.6a is also rendered in color in Figure 5.6c for comparison. Both sets of data compare favorably to each other, however several differences are observed. The cross wire data exhibits a peak axial velocity of $u/U_\infty = 2.33$, which is about 6% greater than that indicated in the SHP data. Both profiles exhibit larger velocity gradients on the lower side of the vortex.
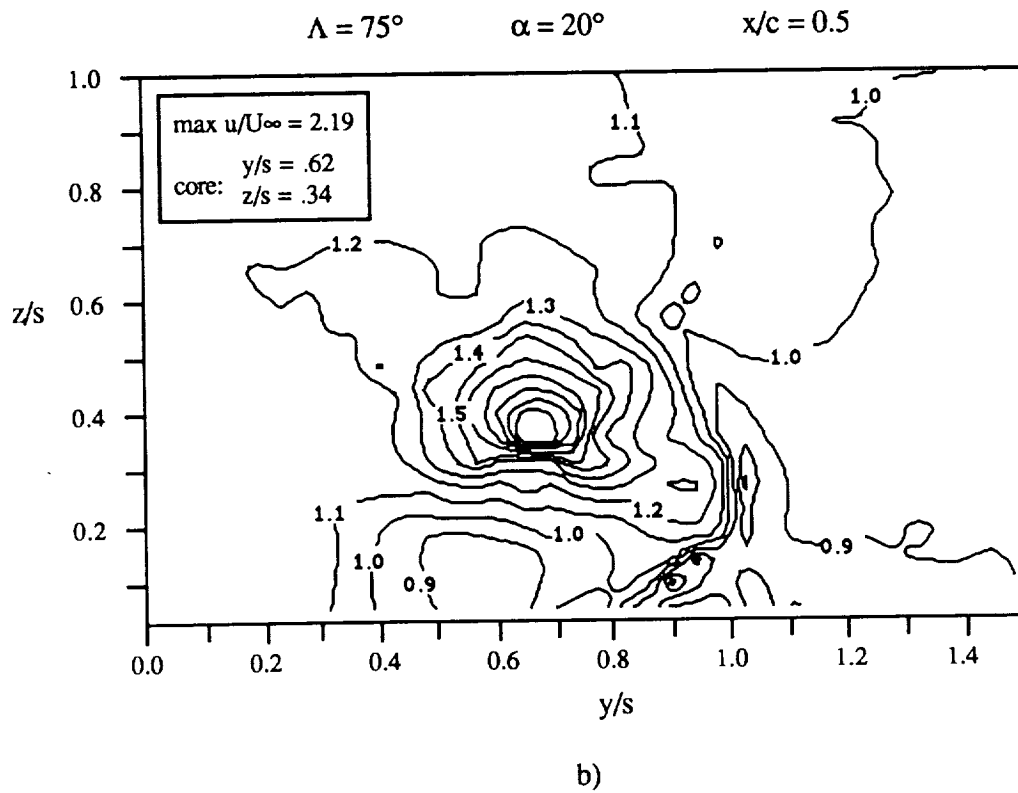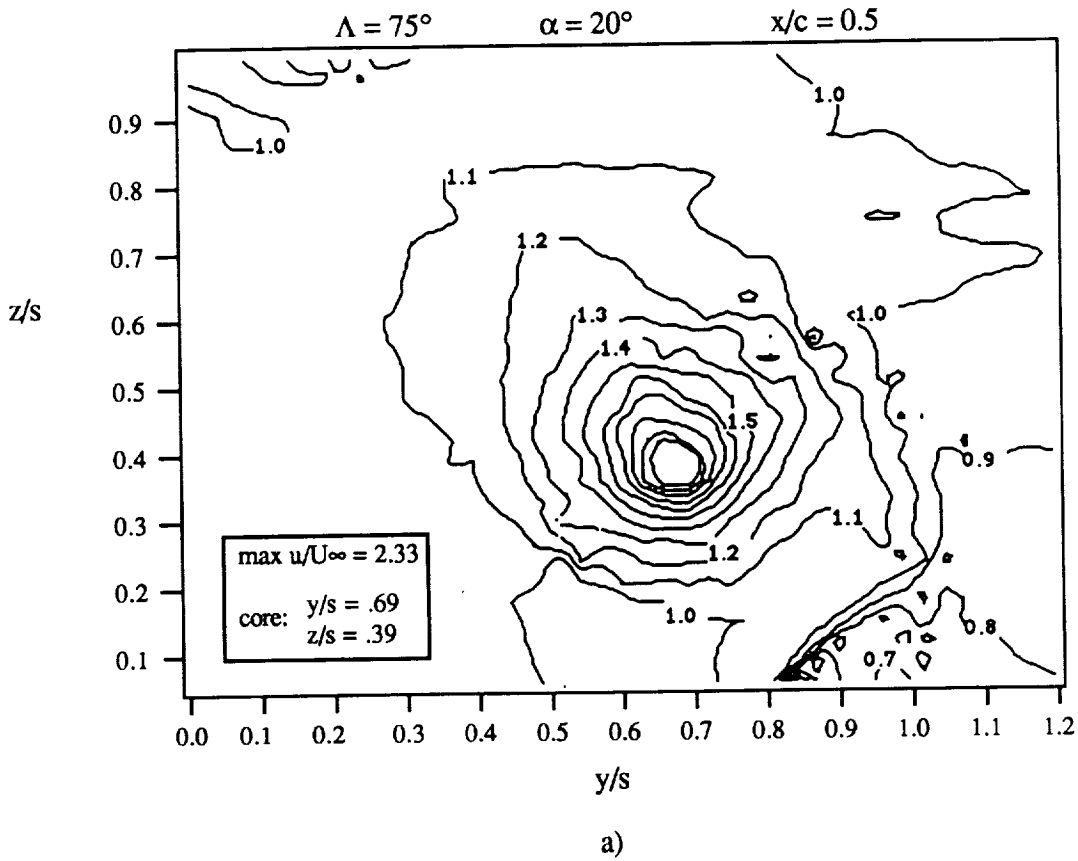
Figure 5.6. Axial Velocity for $\Lambda = 75$ at $\alpha = 20$ a)Cross wires b)SHP

The core locations, based on the position of maximum velocity, for the cross wire data, y/s = 0.69 and z/s = 0.40, lie further outboard and away from the wing than the SHP data, y/s = 0.62 and z/s = 0.34. This is believed to be probe induced, the cross wire probe being approximately three times larger than the seven hole probe. The core location for the seven hole probe data, based on the position of the lowest value of the total pressure coefficient, Cp_t, was located at
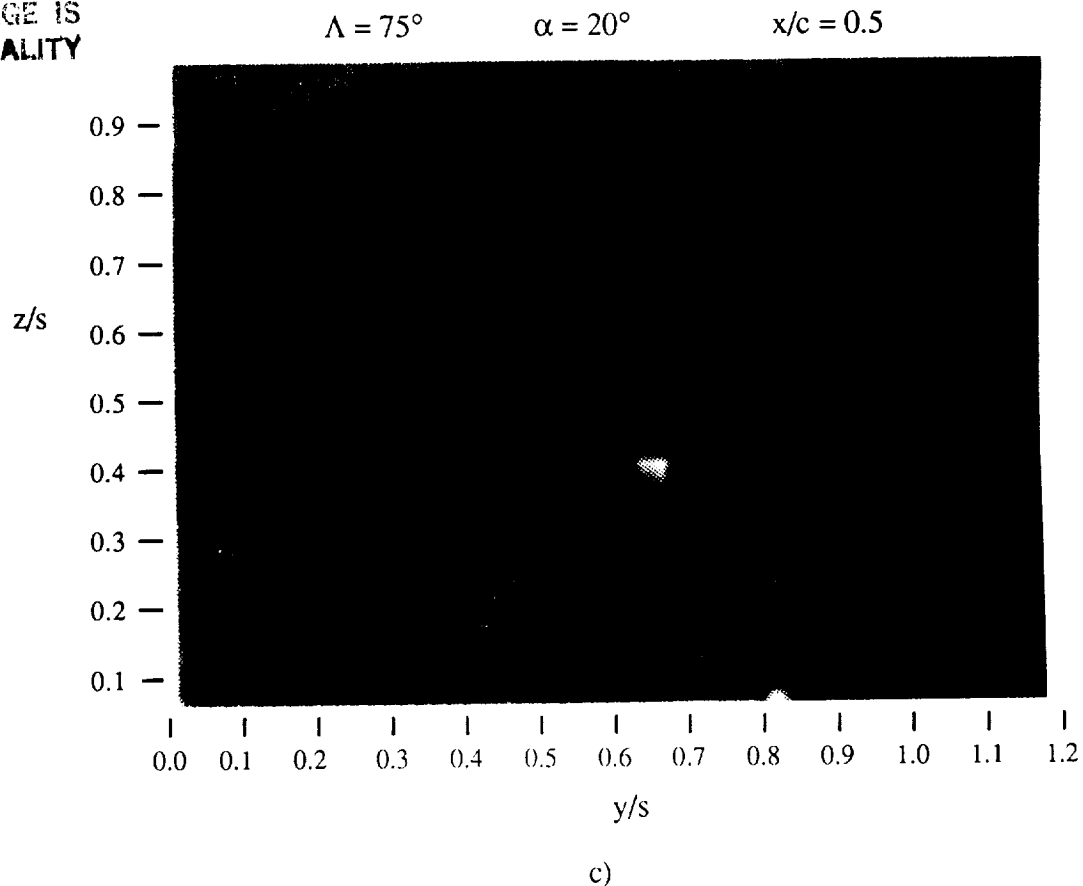
Figure 5.6 Axial Velocity $\Lambda=75°$ at $\alpha = 20°$ c) Cross Wire Color Image

y/s = 0.66. The resolution of the SHP data is 0.04167 in both directions, which, if applied to the core location at y/s = 0.66, would account for both the y/s = 0.62 of the SHP velocity contour and y/s = 0.69 of the cross wire data.

Directly underneath each vortex lies a regime of flow moving at below freestream velocity. This region is larger on the SHP profile and appears to be distorting the vortex above it. This is in contrast to the cross wire data. It is unknown whether this is a phenomenon of the flow or a direct result of the interference of the probe. Examination of the SHP total pressure profiles taken by Payne (1987) revealed values of $Cp_t > 1.0$ in this region, which is physically impossible. This would indicate that the interference effects associated with the nearness of the probe to the wall are substantial, possibly for both probes. Surface visualization has indicated that the flow is approaching the secondary vortex separation point in this region and there is a sizable component of velocity in the spanwise direction (Figure 5.4a, 5.5a). This turning of the local velocity vector can account for the decrease in the axial component. The same effect can be seen just outboard of the leading edge, $y/s = 1.0$. The presence of the shear layer itself can be detected from the data in Figure 5.6b, at $y/s = 1.0$, but is not nearly as evident in the cross wire data in Figure 5.6a.

At $\alpha = 30$, the vortex structures are seen to be stronger as presented in Figure 5.7. Lower than freestream flow is again present below each vortex. A stronger evidence of the shear layer is seen in Figure 5.7a. The cross wire data again indicates a greater maximum axial velocity, $u/U_\infty = 3.2$, versus 2.98 for the SHP data. The core locations for the cross wire data now lie inboard of the SHP locations. The total pressure data from the SHP experiments indicate a z/s location of 0.43 for the maximum Cp_t compared to 0.47 based on a maximum axial velocity. With this in mind, the core locations can be seen to coincide, allowing for the possible error of half the resolution of each respective grid increment.

A third comparison of the cross wire data with the SHP data for a different wing planform is made in Figure 5.8. In this particular instance, $\Lambda = 70°$ and $\alpha = 20°$, the data compares very well. The core locations are identical, both laterally and normal to the wing. The peak velocity of the cross wire data exceeds the SHP data by less than 2%. In addition, the size of the low

$\Lambda = 75°$ $\qquad \alpha = 30°$ $\qquad$ x/c = 0.5

a)

$\Lambda = 75°$ $\qquad \alpha = 30°$ $\qquad$ x/c = 0.5

b)
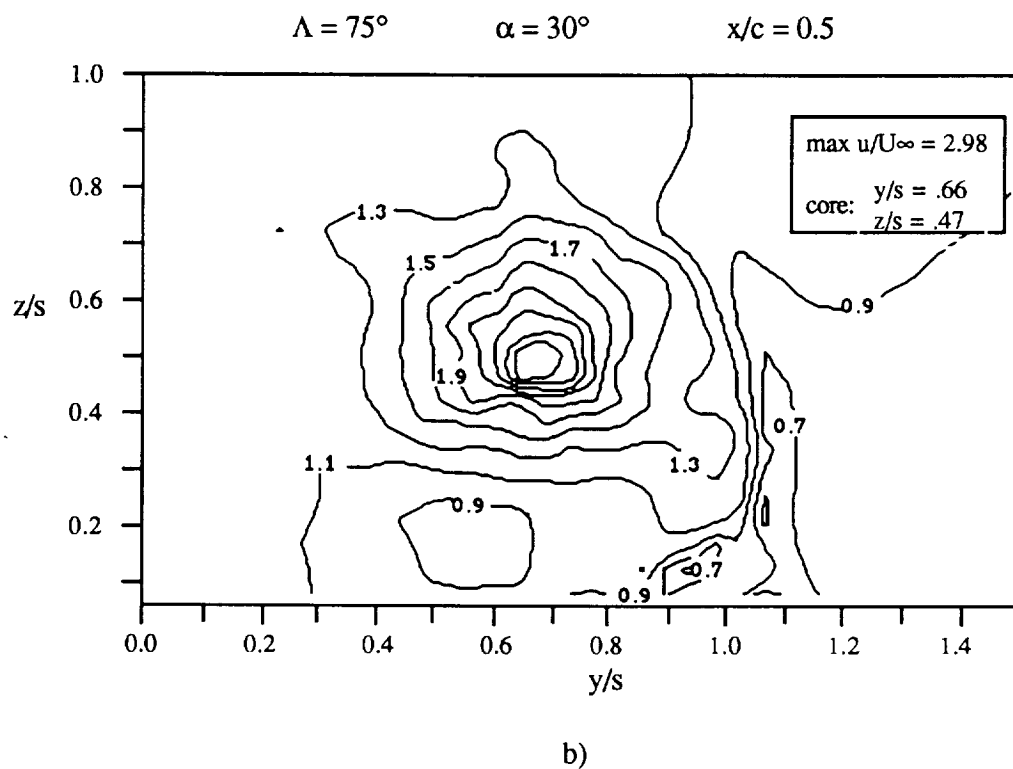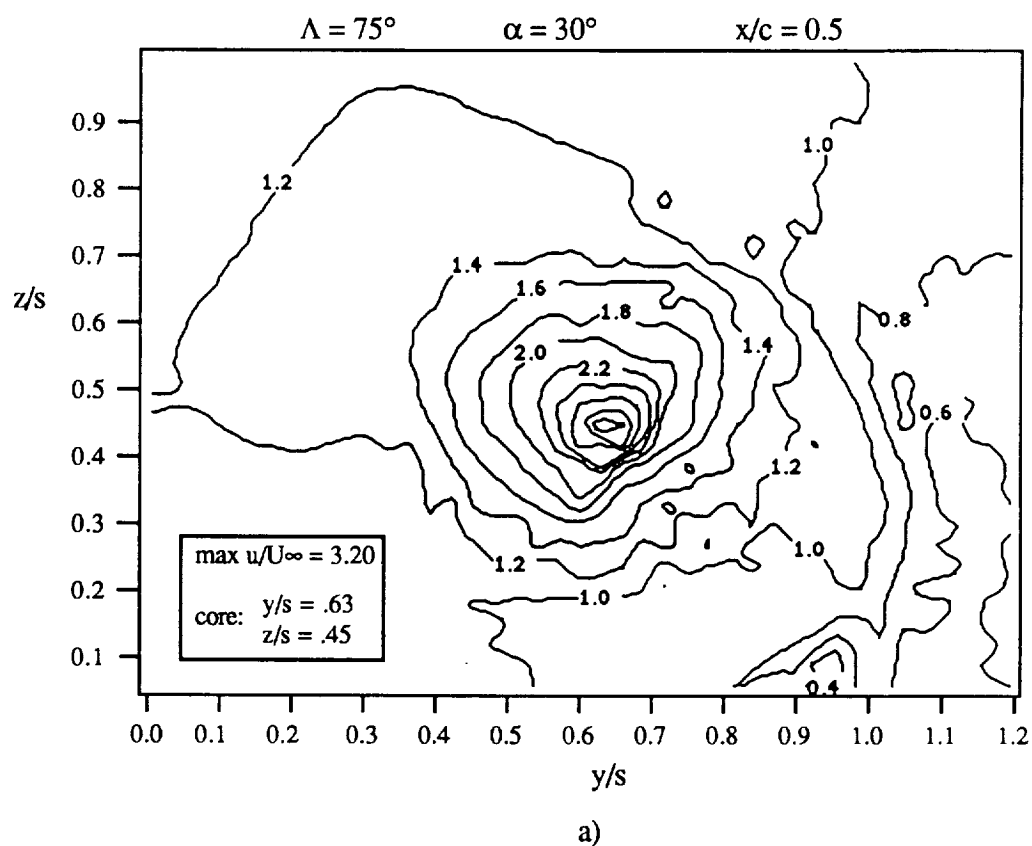
Figure 5.7. Axial Velocity for $\Lambda = 75$ at $\alpha = 30$ a)Cross wires b)SHP

$\Lambda = 70°$ $\alpha = 20°$ $x/c = 0.5$

max $u/U\infty = 2.64$

core: $y/s = .66$ $z/s = .29$

a)

$\Lambda = 70°$ $\alpha = 20°$ $x/c = 0.5$

max $u/U\infty = 2.60$

core: $y/s = .66$ $z/s = .29$
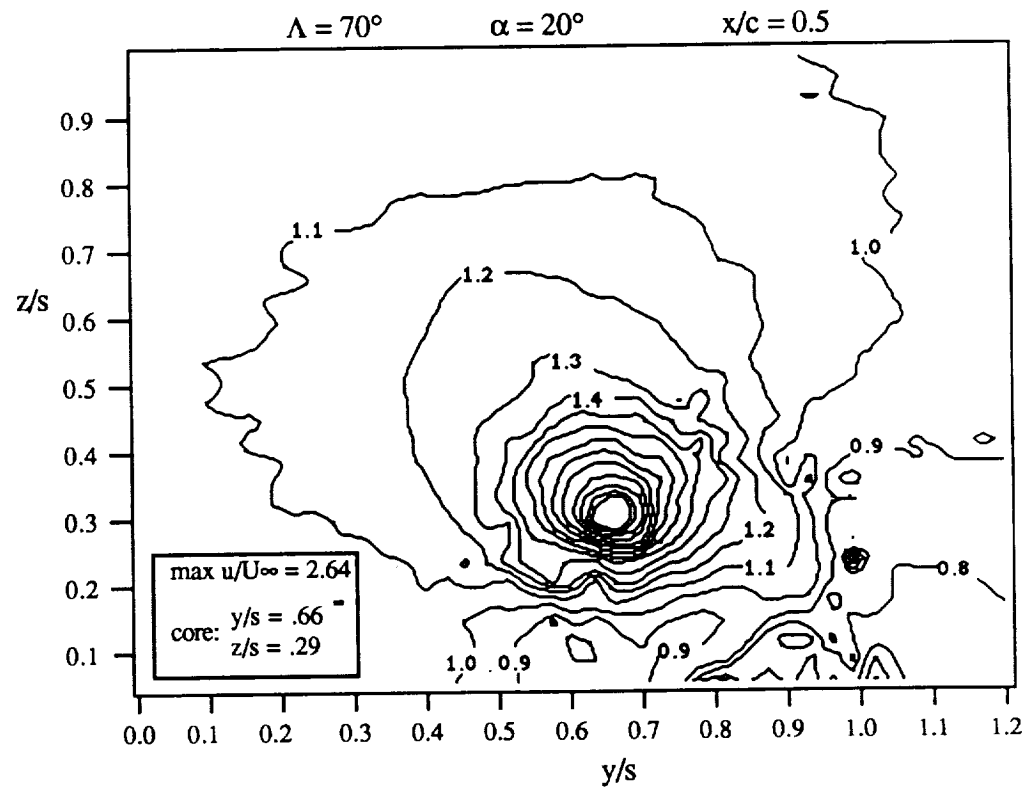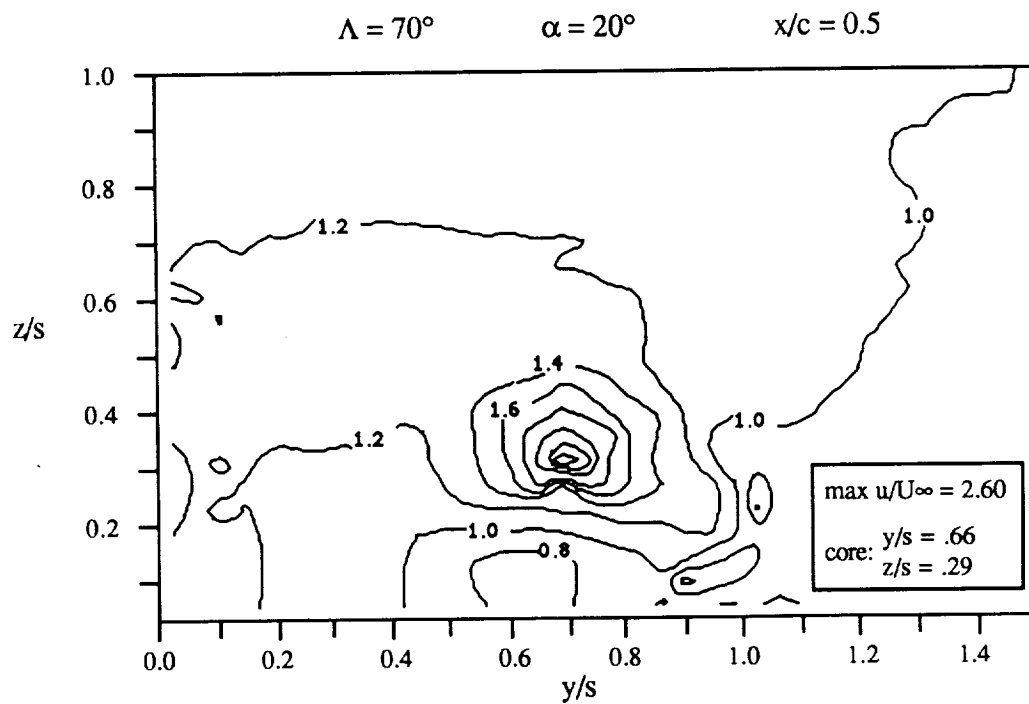
b)

Figure 5.8. Axial Velocity for $\Lambda = 70$ at $\alpha = 20$ a)Cross wires b)SHP

axial velocity regimes underneath the vortices are seen to be very similar. The most outstanding difference is that the $u/U_\infty = 1.2$ contour does not encircle the vortex in Figure 5.8b as in 5.8a.

The in-plane velocities, v/U_∞ and w/U_∞, for the $\Lambda = 75°$, $\alpha = 20°$ and $x/c = 0.5$ survey are contoured in Figure 5.9a and 5.9b respectively. Negative values, following the convention in Chapter 1, are represented by the dotted lines. For both components, the greatest error can be seen to occur in the region where the velocity approaches zero. More correctly, it occurs where the velocity component experiences a change of sign. The contours do not appear to be evenly spaced in this region but seem to crowd the zero contour. The sensitivity of the crossflow components to changes in the measured flows can be severe in regions where v and w are much less than u. Along the core, an increase in the input voltage of wire 1 by the standard deviation of the measured voltage itself resulted in less than a 1% change in the calculated value of u, but over an 80% decrease in the magnitude of v. This was equivalent to about 23% of the freestream value. Regions of the flowfield containing velocity components of similar magnitude indicated changes in the velocites of approximately 15% for changes to the input voltages of one standard deviation of the measured signal. Details can be found in Appendix C.

A final, more quantitative comparison, was made between the cross wire and the SHP data by comparing the cross sectional traverses through the vortex core. The axial and transverse velocities from this traverse, corresponding to the $\Lambda = 75°$, $\alpha = 20°$, $x/c = 0.50$ data in Figure 5.6, are plotted in Figure 5.10a against spanwise distance. The z/s location for the traverse was based on the maximum value of u/U_∞. Both of the cross wire velocity components can be seen to be shifted outboard of the SHP data. The axial peak differences are equivalent to that noted earlier. Inboard of the core center, the tangential velocity from the cross wire data maintains a larger, negative value. In contrast to this, the cross wire data indicates a smaller magnitude value of the axial velocity component, in the area between the core center and the chord centerline. This trend is also observed in the the cross sectional traverses of Figures 5.7 and 5.8 as plotted

$\Lambda = 75°$ $\alpha = 20°$ $x/c = 0.5$

a)

$\Lambda = 75°$ $\alpha = 20°$ $x/c = 0.5$

b)
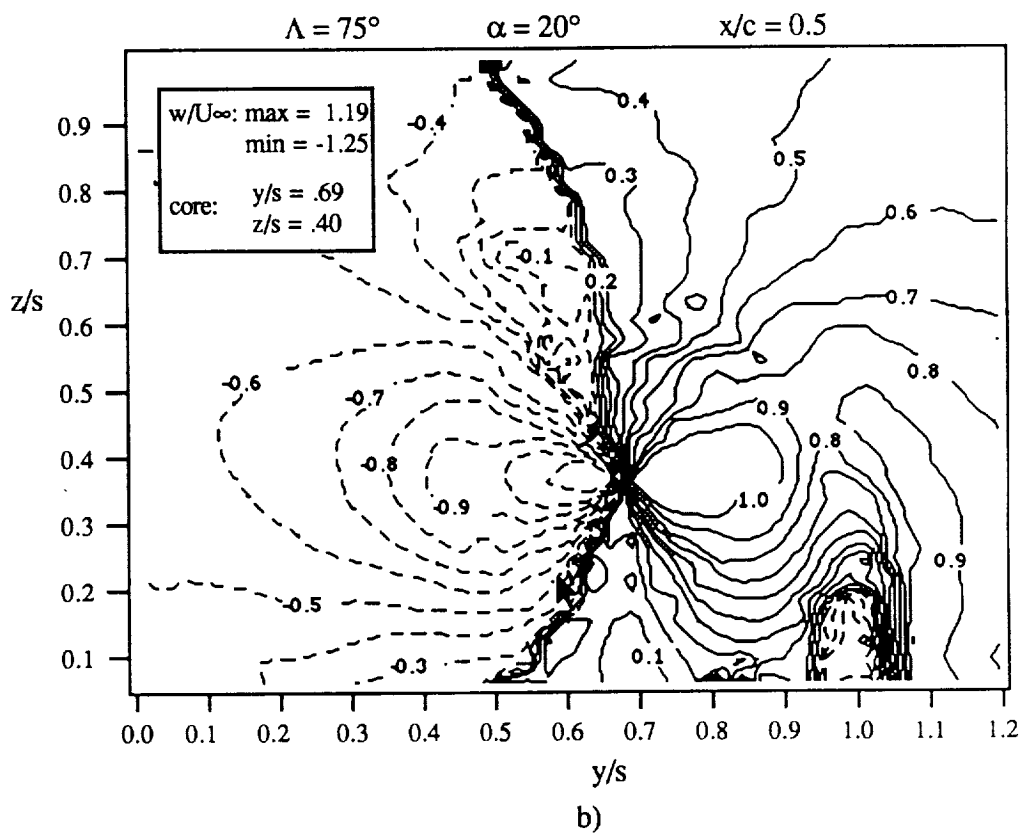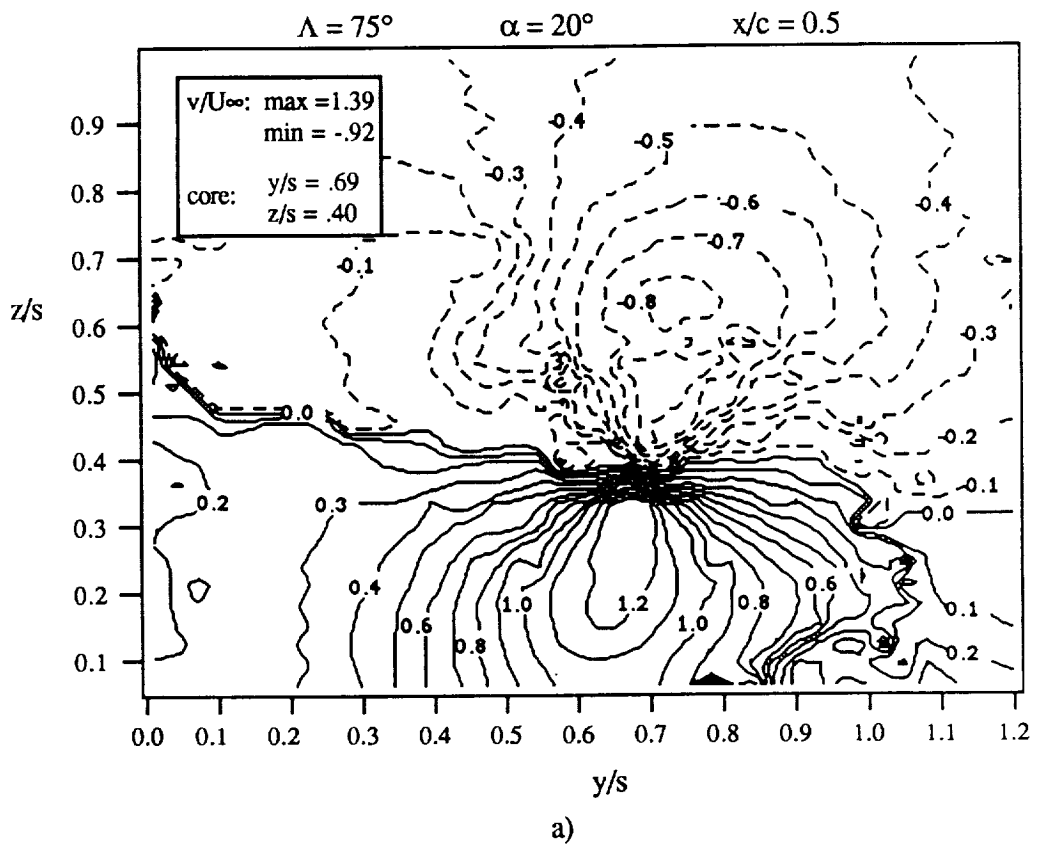
Figure 5.9. Crossectional Velocities for Λ=75 at $\alpha = 20$ a)v/U∞   b)w/U∞
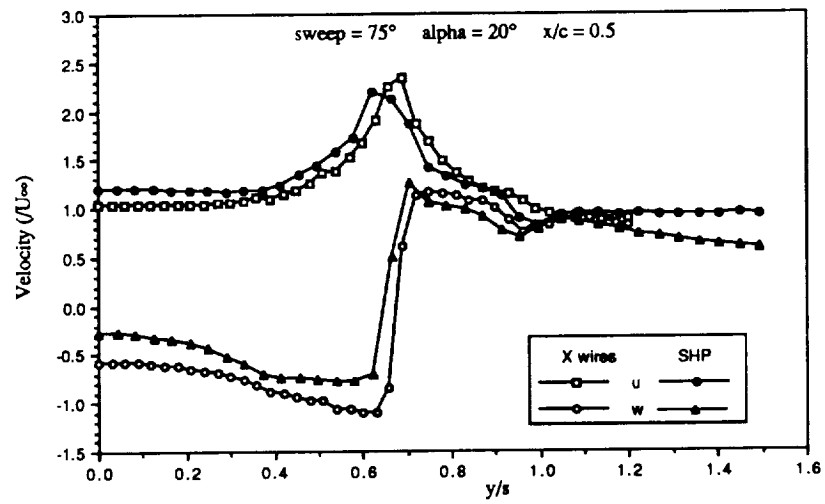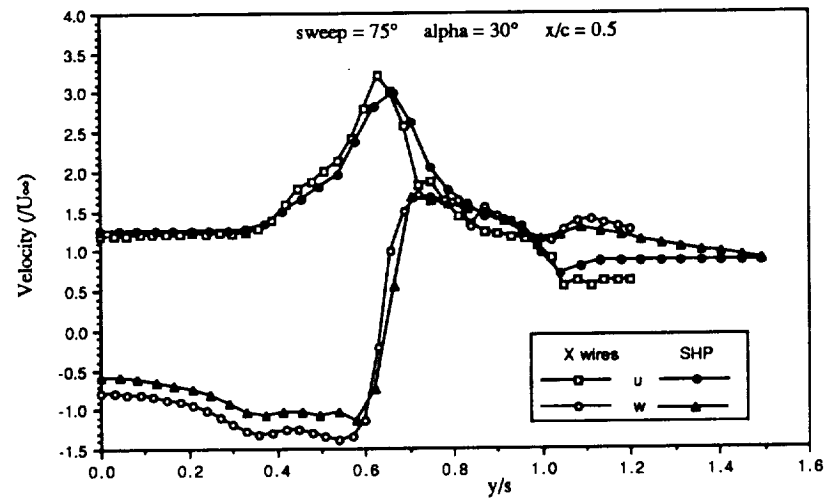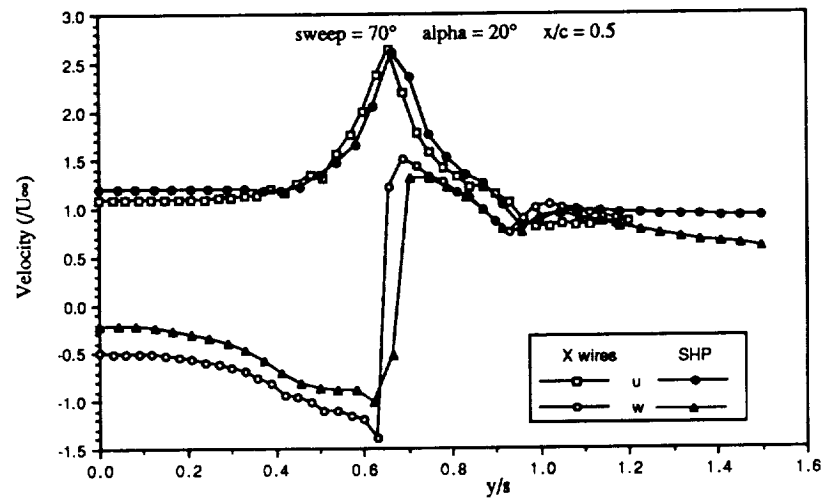
Figure 5.10 Axial and Tangential Velocity Core Profiles a) sweep = 75, alpha = 20
b) sweep = 75, alpha = 30 c) sweep = 70, alpha = 20

in Figures 5.10b and 5.10c respectively. There is no major indication of a shift in the location of the core for either 5.10b or c. There is a noticeable increase in the maximum magnitudes of the tangential component for the $\Lambda = 70°$ planform in Figure 5.10c. One might attribute this to grid resolution differences, however data was acquired at similar spatial locations for each experiment. More likely, the differences lie in the measurement technique. Since the flowfield is sensitive to probe intrusion, and the cross wire technique used a larger probe, the error would seem to arise in this measurement.

Based on the above comparison, the cross wire data was concluded to compare well with the SHP data. Payne (1987) also showed the SHP data to correlate well with LDV data in the same study for the flowfield upstream of breakdown, and thus the present velocity measurements represent the flowfield well. The cross wire data was then evaluated with respect to the repeatability of the data itself.

Three of the chordwise stations, where data was acquired above the 75° planform, are shown in Figure 5.11. Discrepancies were observed. The largest variations were observed nearest the apex, as in Figure 5.11a at x/c = 0.3. Both the axial and tangential profiles indicate deviations in magnitude along certain portions of the profiles. Aft of this station, the axial profiles appear very repeatable. Peak values in the tangential velocities did show variations, as noted in Figures 5.11b and 5.11c, of up to 10% in the worst cases.

For the data of Figure 5.11b, which represents three independent velocity surveys, profiles were examined at a series of z/s locations corresponding to locations near the wing surface and between the surface and the core location. The u, v, and w component are plotted in Figures 5.12, 5.13, and 5.14 respectively. Repeatability, including sudden peaks and drops is good. The axial velocity profiles show the smallest deviations. A sharp, very repeatable drop from positive to negative velocity is recorded in the v component as indicated in Figure 5.13a. This
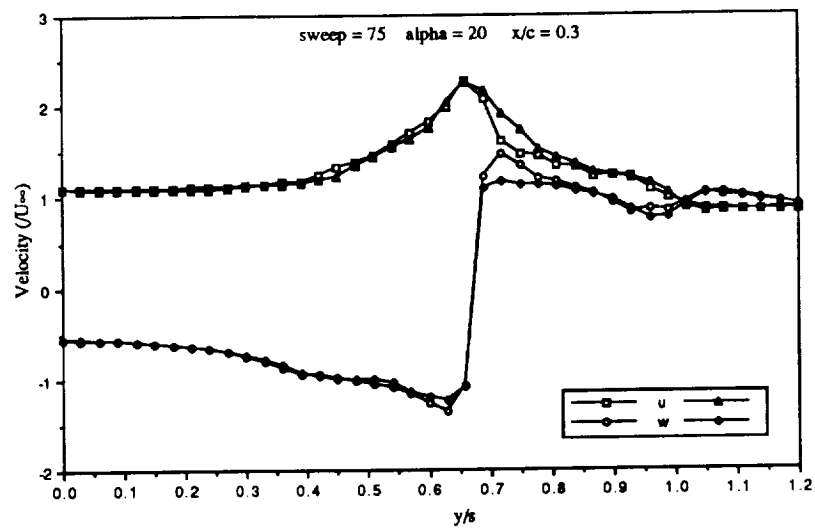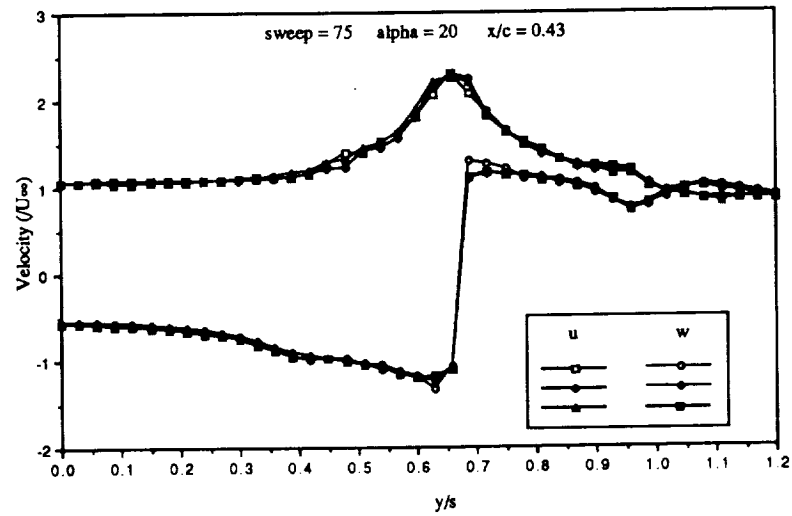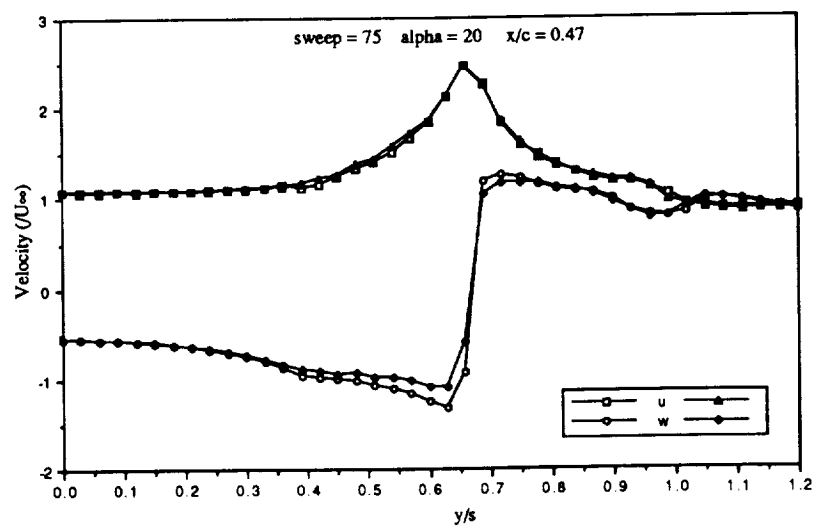
Figure 5.11 Velocity Profile Comparison at sweep = 75 alpha = 20   a) x/c = 0.3   b) x/c = 0.43   x/c = 0.47
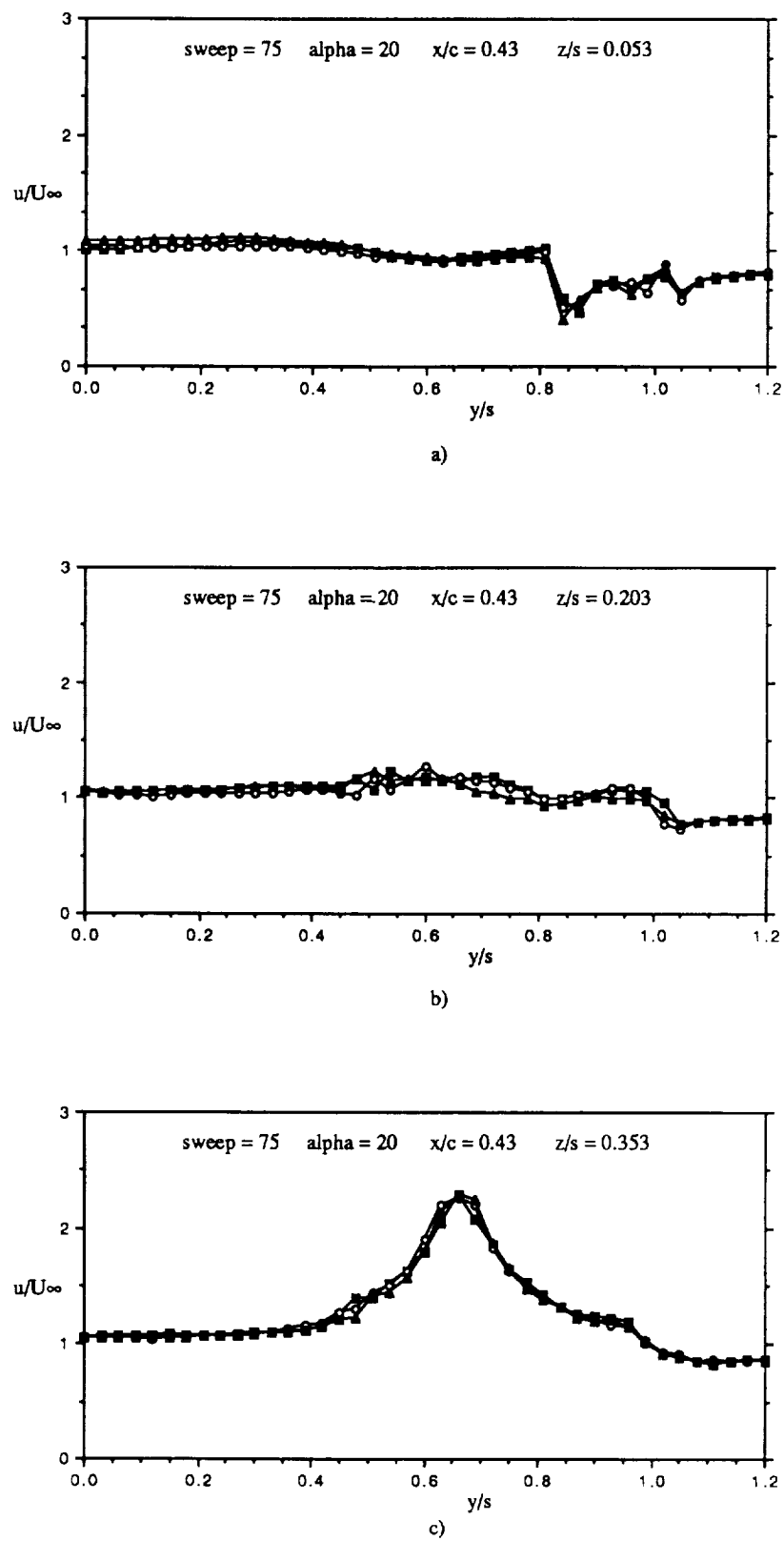
Figure 5.12 Axial Velocity Profile Comparison a) Surface b) Midcore c) Core
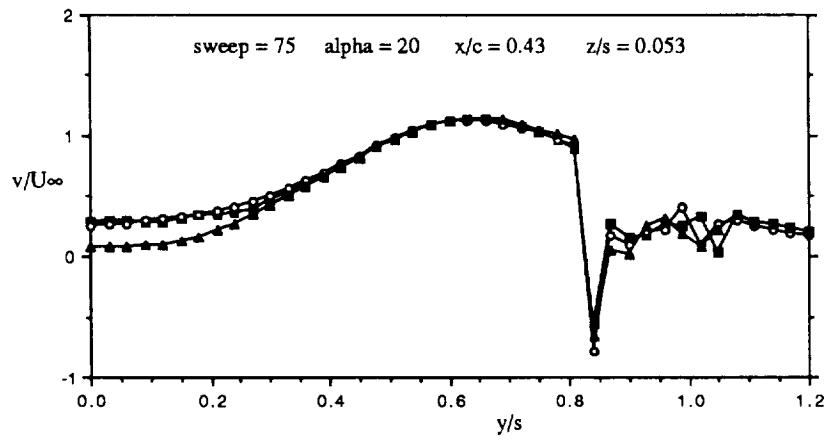
a)
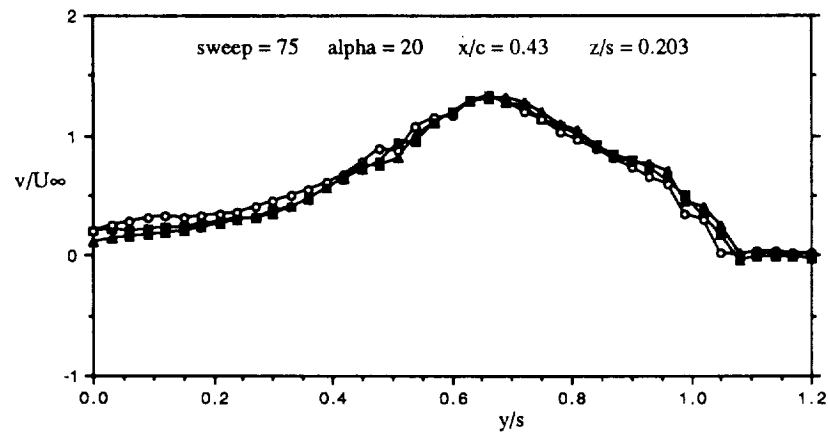
b)
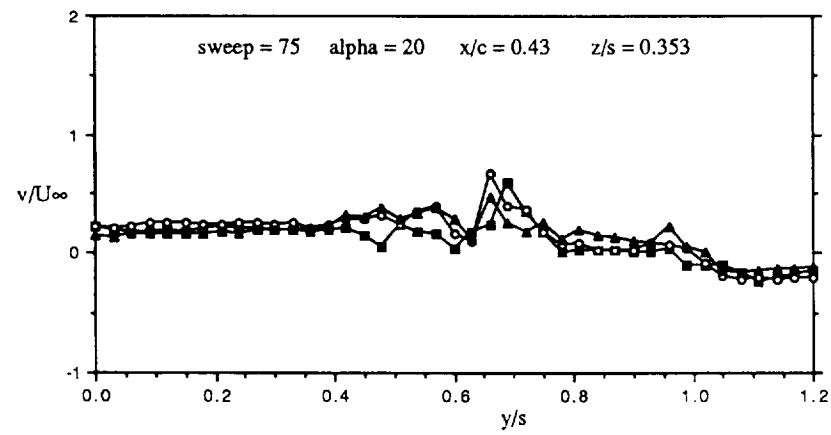
c)

Figure 5.13 Spanwise Velocity Profile Comparison a) Surface b) Midcore c) Core
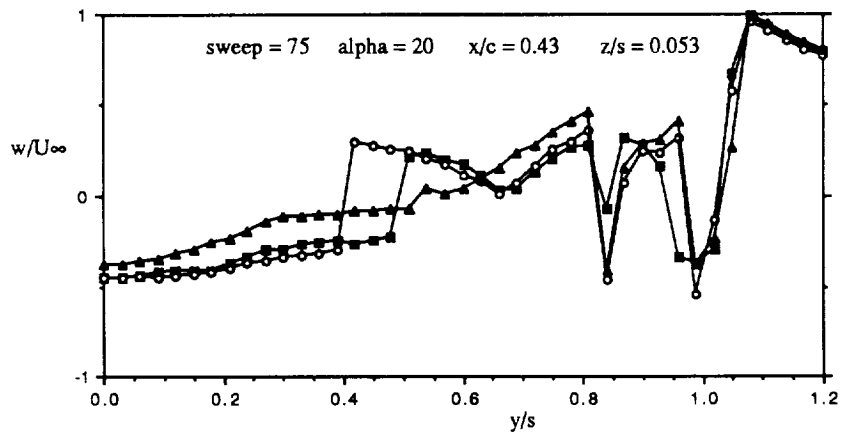
a)
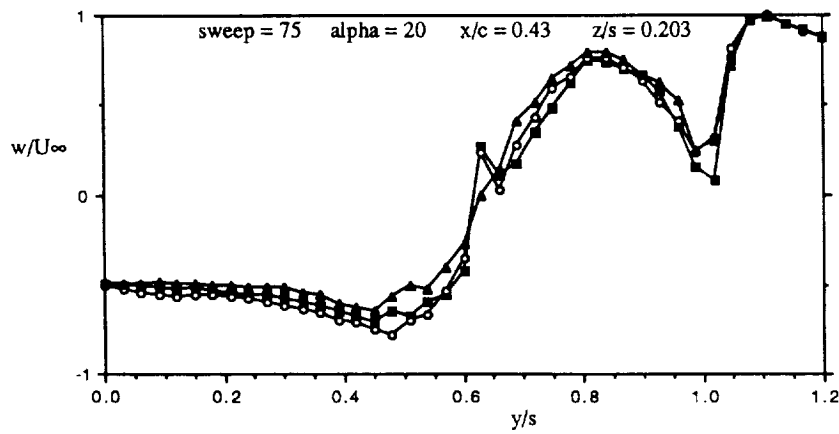
b)
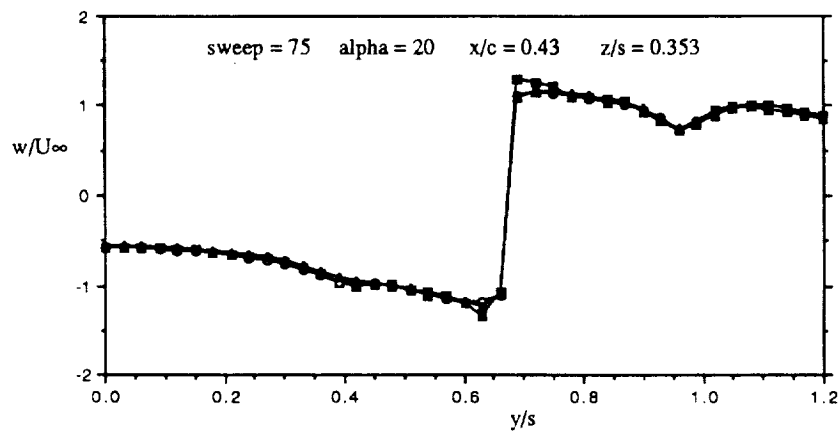
c)

Figure 5.14 Normal Velocity Profile Comparison a) Surface b) Midcore c) Core

was observed at almost every chordwise location. Comparison of this spanwise location of approximately y/s = 0.85 with the surface visualization results in Figures 5.1 and 5.2b indicates this location to be directly beneath the secondary vortex. The reversed flow direction is therefore to be expected.

The largest deviations are seen in the w velocity component at a position near the wing surface, Figure 5.14a, and the v component through the core, Figure 5.13c. Two of the profiles in Figure 5.14a give indication of incorrect signs in the region of y/s = 0.4 to 0.6. It should be kept in mind that the technique used to reduce the data is most suited to strongly three dimensional flows and suffers if one component is much less than the others.

The chordwise variation of the velocity data profiles is given in Figure 5.15. The axial and tangential components obtained from the core traversals are overlaid for chordwise stations of x/c = 0.3 to 0.8. Each profile is plotted against its local spanwise direction. All the profiles exhibit similar characteristics, both in shape and magnitude. This indicates the flowfield in this region to be scaling in a linear fashion, indicative of a conical behavior. The largest differences occur outboard of the core location. For consistency, every spanwise pass for each survey was made in the direction from the chord centerline to the leading edge. As the probe encounters the core region, it has the tendency to 'push' the core slightly ahead of itself as it is encountered. If the probe is exactly on the z/s location of the core axis, this results in a slight displacement of the core laterally which may offset the position of the maximum velocity recorded. However, if the probe is above or below this height, the spatial location of the core is displaced below or above its natural location. In addition, each velocity profile in Figure 5.15 represents the z/s location where the maximum u/U_∞ value was recorded. Because of resolution, this may not be the maximum in the field. The same applies to the tangential velocities.
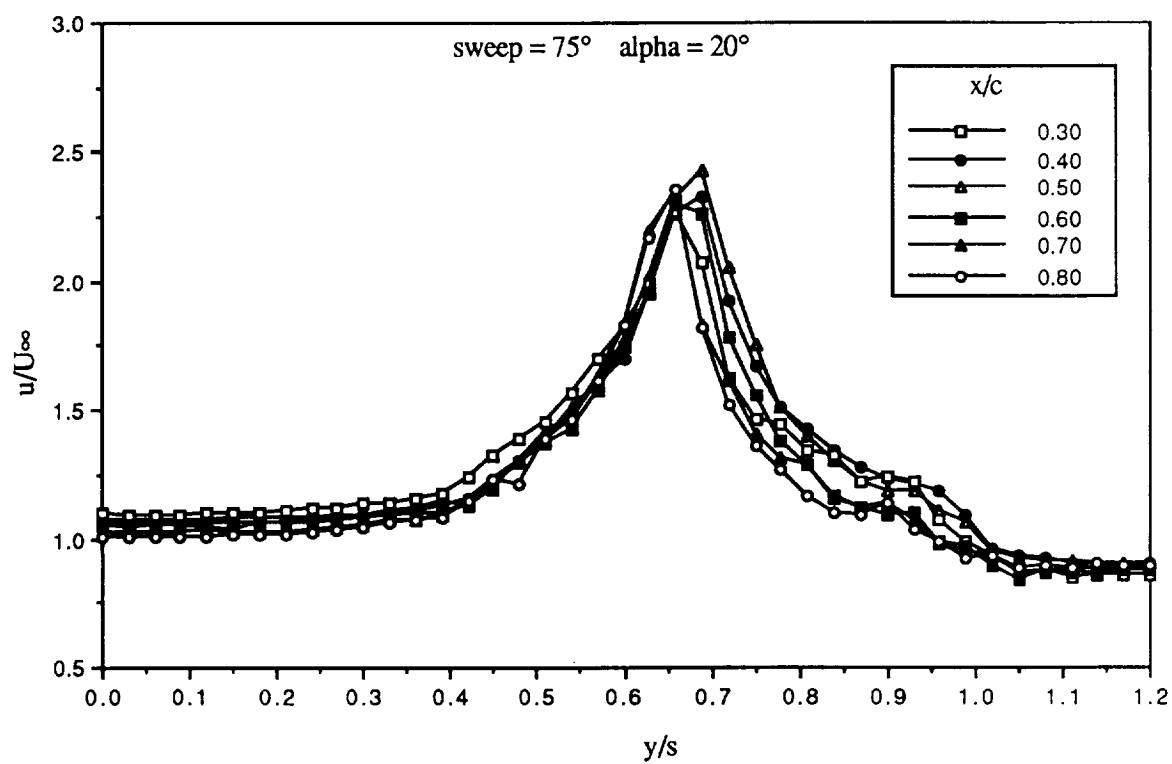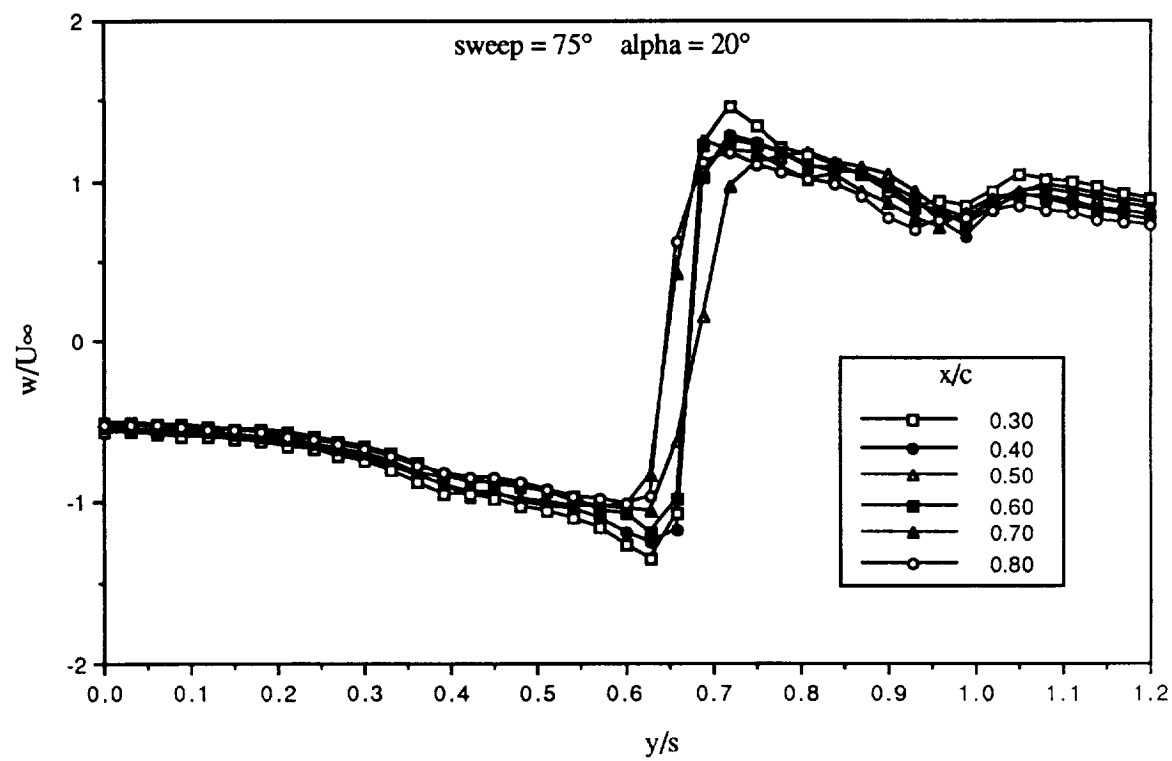
Figure 5.15 Chordwise Velocity Profile Comparison Λ=75 α=20 a) Axial b) Tangential

Two other aspects of interest that result directly from the velocity field data can be immediately examined. The behavior of the maximum axial velocity in the core, with respect to magnitude as it proceeds in a chordwise direction, has been a source of discussion for several investigators, as noted in Chapter 1. The majority of the data was acquired for the 75° sweep planform at 20° angle of attack and the maximum axial velocity components are compiled in Figure 5.16. No breakdown was occurring on the wing in this configuration and the data falls roughly in a band of u/U∞ = 2.0 to 2.5. The values crest in magnitude at about x/c = 0.6 and become less to either end of the wing. The grid resolution for this data was y/s = z/s = 0.03 at each station. Therefore the grid increment size in actual units is increasing towards the apex. If the subcore region behaves in a cylindrical manner, as has been proposed by other investigators, the resolution of the subcore flow should also increase as the apex is approached. The direct implication of this is that the decrease in the axial velocity towards the apex represents a real
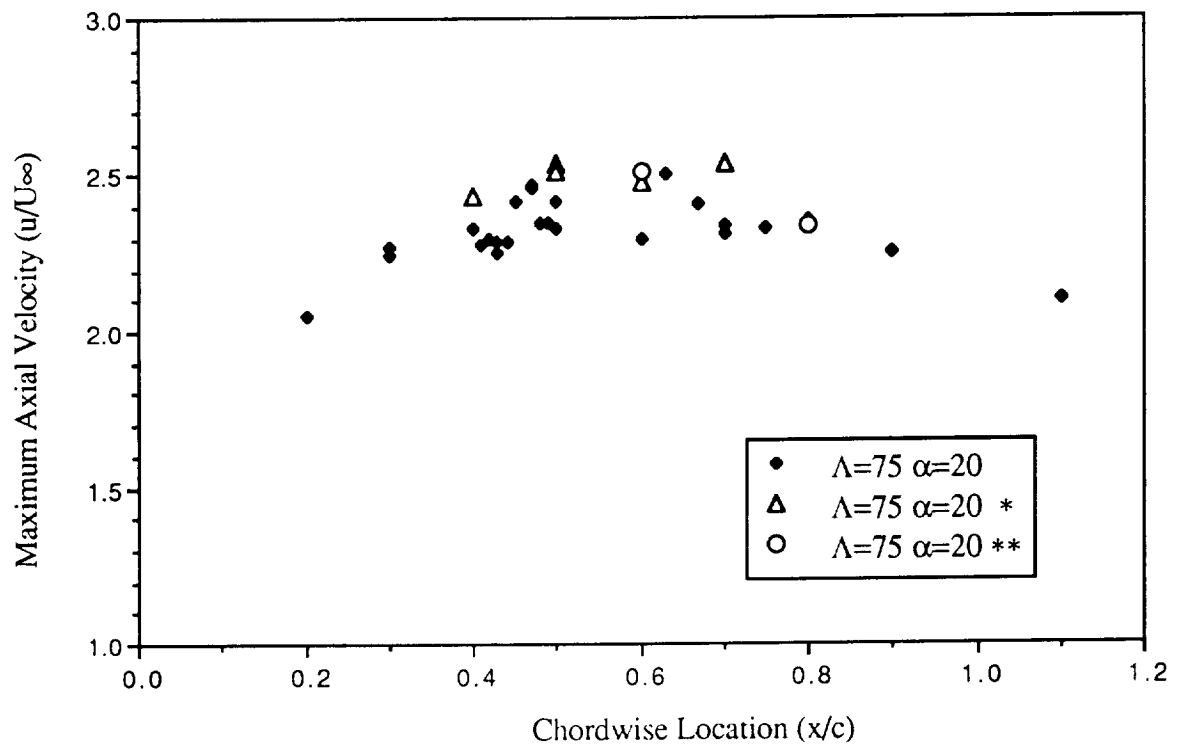
*, ** See below

Figure 5.16 Chordwise Distribution of Maximum Axial Velocity at $\Lambda = 75°$ $\alpha = 20$

phenomenon. Since breakdown was not present on the planform, the decrease in axial velocity towards the trailing edge could be a direct result in the decrease in the actual grid size. It should be remembered, however, that the actual resolution of the probe is increasing towards the trailing edge, since the probe size is fixed and the vortex size is increasing. The data marked with an asterisk and the double asterisk represent increases on the resolution of the survey grid by two and three times, respectively. Similar trends are seen for both configurations and although the y/s = 0.015 case, *, at x/c = 0.7 is greater in magnitude, it too falls onto the y/s = 0.03 data by x/c = 0.8.

The Λ = 75° at α = 30° data, in Figure 5.17, shows a large drop in the axial velocity aft of the x/c = 0.4 mark. Breakdown was occurring at approximately x/c = 0.55 to 0.60 and no data was taken rearward of this position. The velocity does drop over a distance of about 10% of the chord before breakdown. Data for the 70° planform is also included. Breakdown for the 70°
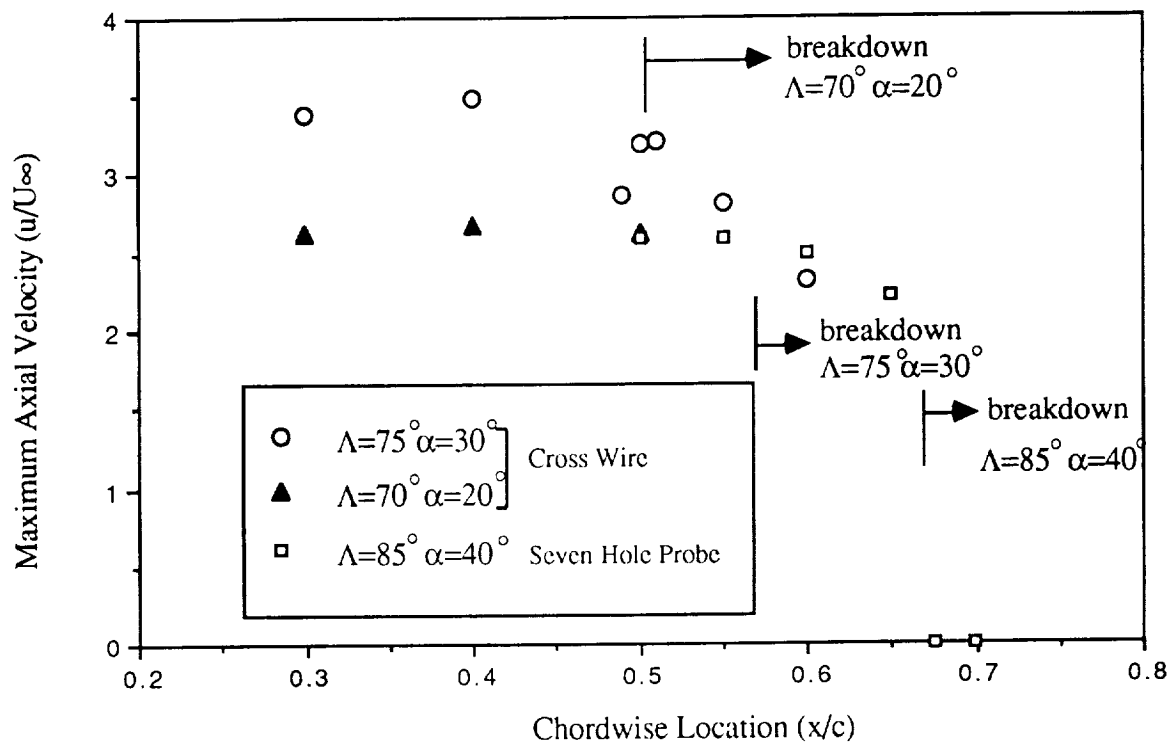
Figure 5.17 Chordwise Distribution of Maximum Axial Velocity with Breakdown Present

wing data was observed at about the x/c = 0.5 to 0.55 station. Only a very slight indication of an imminent drop in the velocity was observed, however, at the x/c = 0.5 position. No data was available after the onset of breakdown. Both sets of data in Figure 5.17 suggest that the axial velocity does not vary appreciably in a region some distance forward of the breakdown zone. For comparison, SHP data from Payne (1987) for an 85° sweep wing at 40° angle of attack is also presented in Figure 5.17. There is only a small indication of the upcoming drop in the velocity due to the breakdown. Stations more than 5% forward of the breakdown location exhibit no major change of the maximum axial velocity. Upstream of the wing, the axial velocity component must begin with a freestream speed and then accelerate over the apex and along the core as the vortex develops. From the present data, the axial velocity continues to increase up to some distance before breakdown. A position is eventually reached where the velocity does not increase further, but reaches some maximum, remaining at that magnitude for some distance, until falling abruptly through the breakdown region.

The last topic of interest dealing directly with the velocity data is the intensity of the fluctuations when the velocity signals were acquired from the hot wires. Since the derivation of the velocities required data that was not taken simultaneously, a direct determination of the turbulence intensity of the velocity can not be obtained. The mean voltage signal and the associated standard deviation for each wire, however, can be used as an indicator of the local fluctuation intensity of the flow. By taking the ratio of the standard deviation to the mean, and multiplying by 100, a percent fluctuation intensity was defined. Intensities for the 75° sweep planform at $\alpha = 20°$ based on the data from wires 1 and 2 of the first spatial pass are represented in Figures 5.18a and 5.18b respectively. With the probe in position two, two more sets of information were obtained. These correspond to Figures 5.18c and 5.18d.

Since the orientation of the wire to oncoming flow is different for each configuration, as noted in each figure, the sensitivity to the local fluctuation is different and hence each plot shows
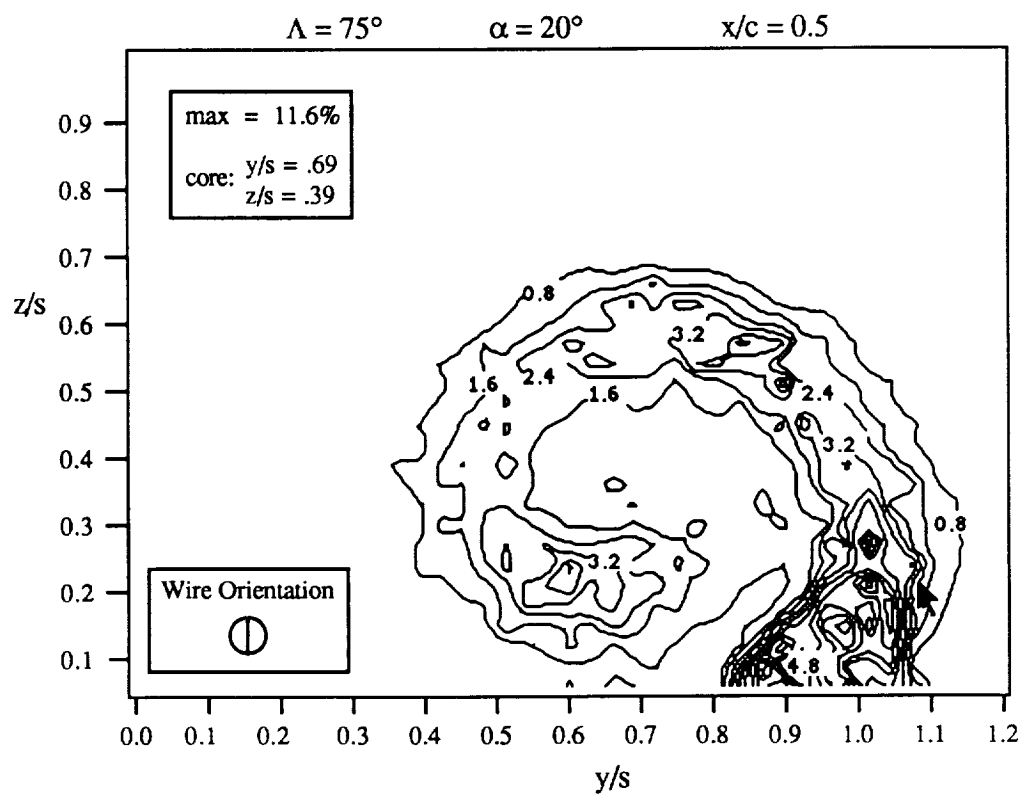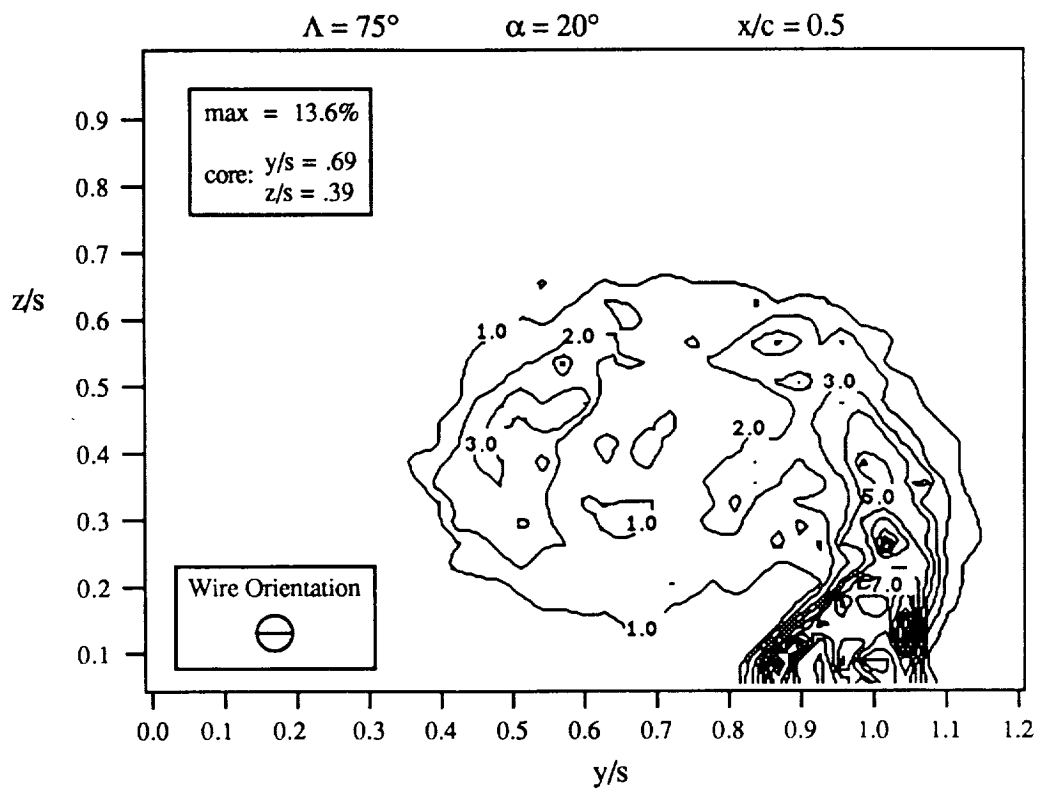
Figure 5.18. Fluctuation Intensity at $\Lambda=75$, $\alpha=20$, x/c=0.5 a) Position 1 Wire 1 b) Position 1 Wire 2
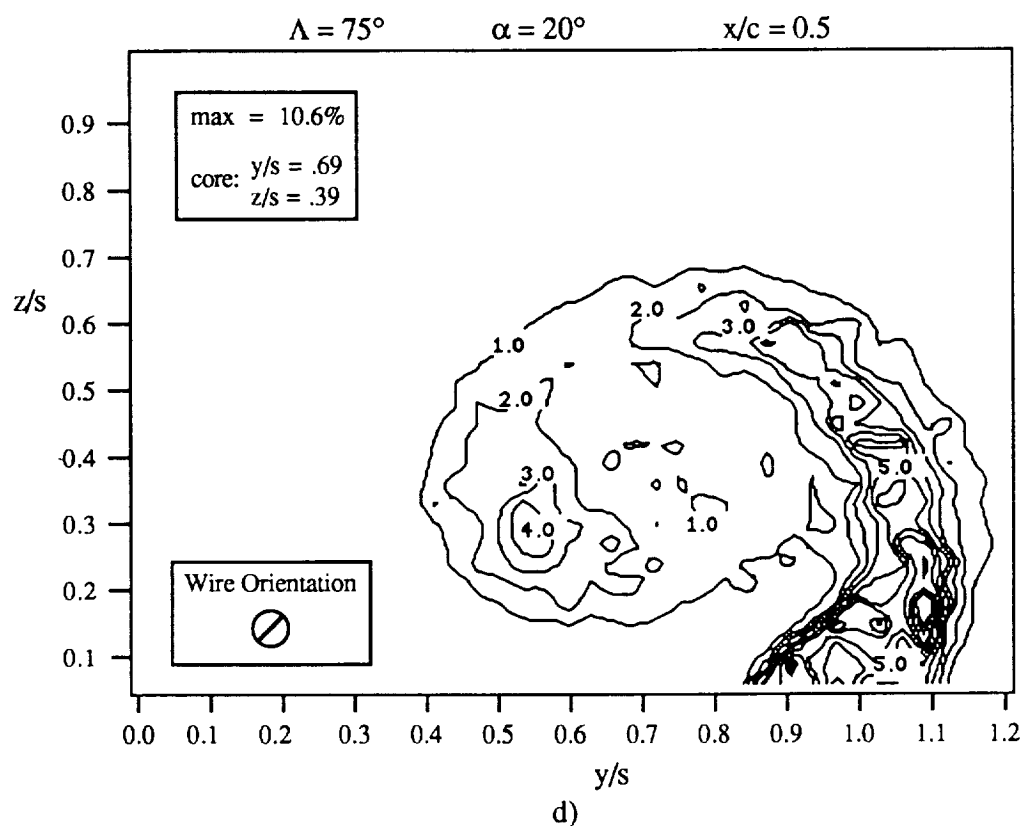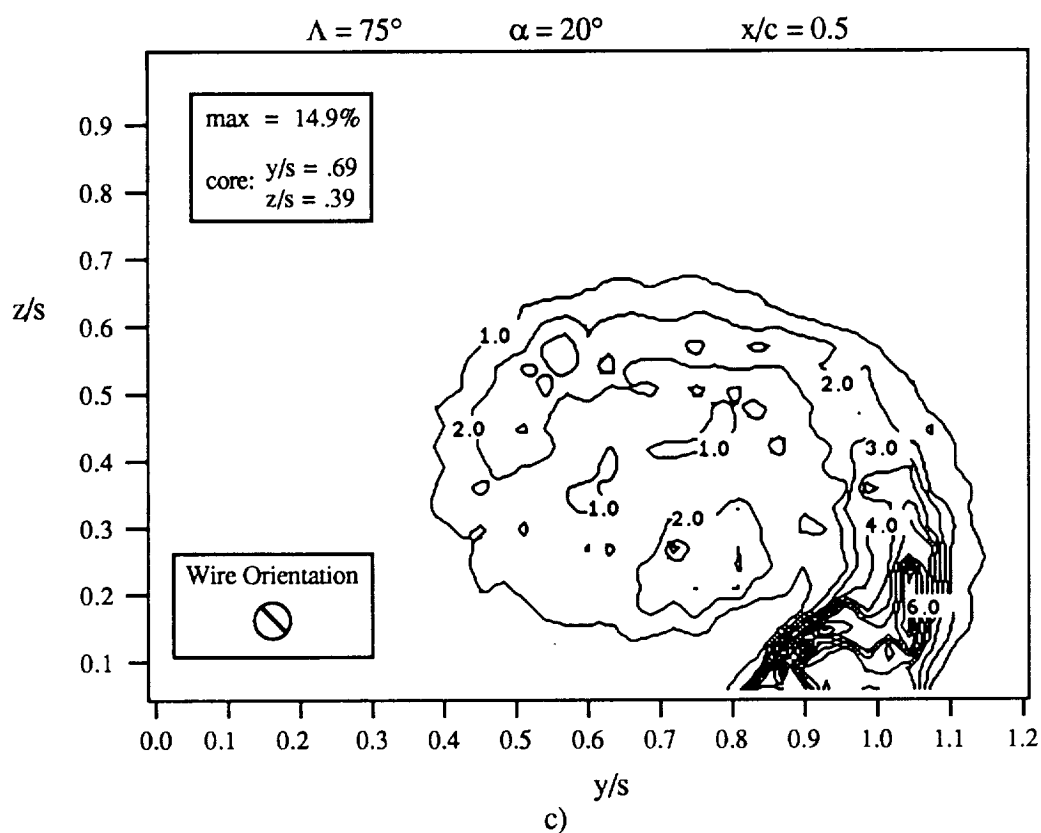
Figure 5.18. Fluctuation Intensity at Λ=75, α=20, x/c=0.5 c) Position 2 Wire 1 d) Position 2 Wire 2

variations in the levels of intensity. The largest fluctuations occur in the region of the shear layer as it leaves the wing. The fluctuation intensity can actually be seen to mark the wrapping up of this layer above the wing as well, especially in Figure 5.18a and 5.18c. A maximum intensity of almost 14% was recorded with the wire parallel to the wing in Figure 5.18b. The orientation of the wire can actually be determined by closer observation of the figures themselves. In Figure 5.18a, there is a drop in the intensity in the area of $y/s = 0.5$ and $z/s = 0.4$, the region where the
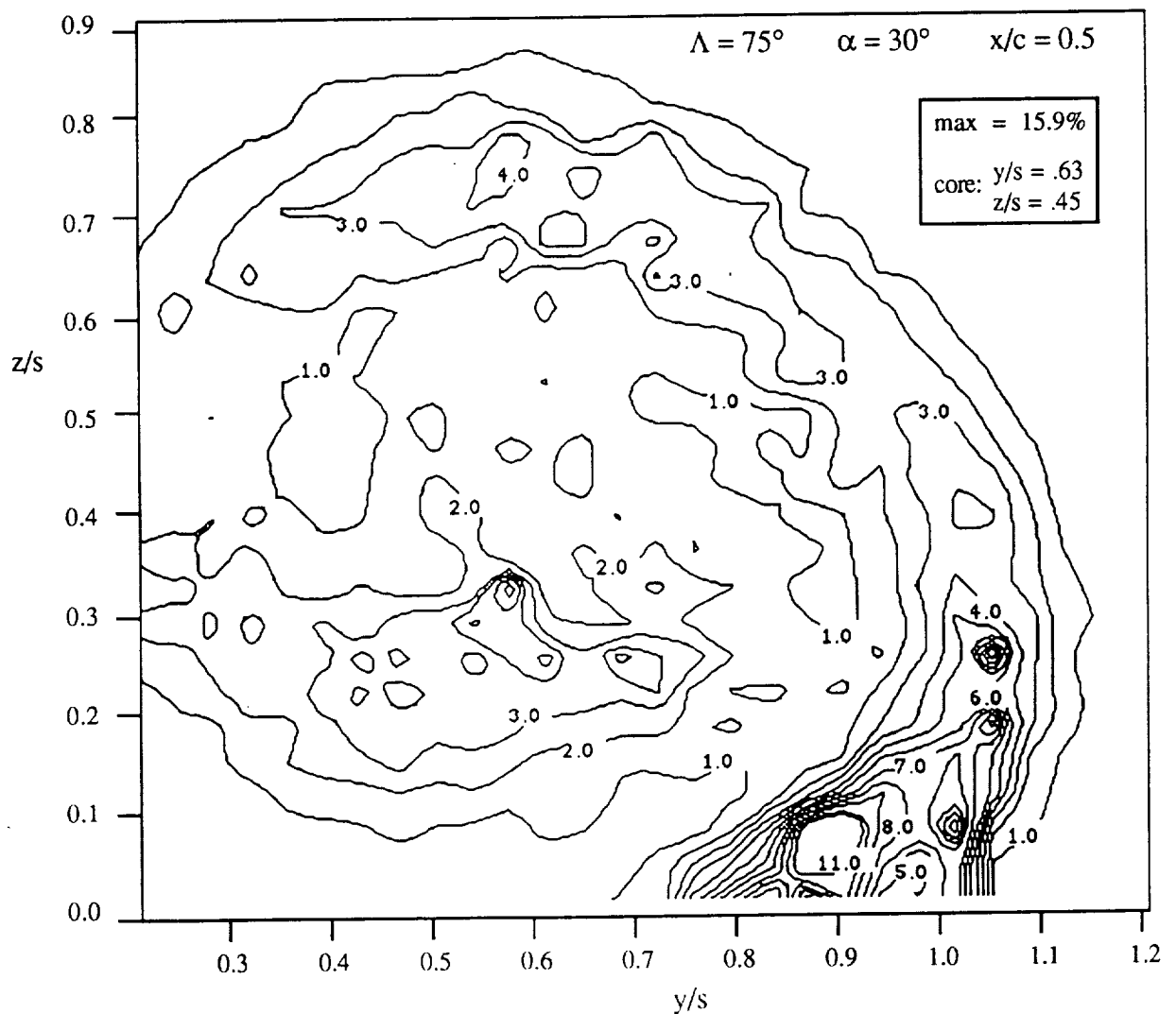
Figure 5.19 Fluctuation Intensity at $x/c = 0.5$ for $\Lambda = 75°$ at $\alpha = 30°$

flow is oriented along the axis of the wire. This would be true in the flow coming over the wing as well, however the effect is masked by a much stronger leading edge flow. The wire parallel to the planform in Figure 5.18b shows its insensitivity in the regions of flow parallel to its axis as well, namely at $y/s = 0.7$ and $z/s = 0.2$ and 0.6. Similarly, Figures 5.18c and 5.18d reveal fluctuation deficits along lines at 45° to the plane of the wing. Even stronger fluctuations were recorded above the planform at an angle of attack of 30°. A sample of this data is given in Figure 5.19. Intensities as large as 16% were noted.

The contours suggest that another region of strong fluctuations exists in the secondary vortex. To facilitate observation of this, Figure 5.18b was enlarged and is presented with a color contour of the flow in Figure 5.20. Directly inboard of the leading edge lie pockets of intensity on the order of that in the shear layer. Whether this is due to the local influence of the shear layer or not is unclear. As indicated in Figure 5.6a and Figure 5.9 the velocity vector in this region is considerably lower in the secondary vortex than that in the shear layer. Hence, any local fluctuations register as larger values when normalized by their average, whereas on an absolute scale they would in fact be smaller.

The intensity data reveals some additional noteworthy characteristics of the vortex flow. Strong fluctuations are present in the secondary vortex flow regime as well as the shear layer. This may be an indication of the naturally turbulent nature of the flow in these regions. The boundary layer induced on the wing by the primary vortex is laminar and any transition to turbulence would have to occur outboard of the secondary separation point. It has also been suggested that some type of periodic phenomena may exist in the vicinity of the leading edge flow, such as discrete vortex shedding by Gad-el-Hak and Blackwelder (1985). Since a periodic phenomena would increase the magnitude of the measured fluctuations, it could be surmised that there may also be some type of periodic phenomena occurring in the secondary vortex. Finally, it is interesting to observe that as the shear layer is followed as it wraps up into the core region,

a)

b)
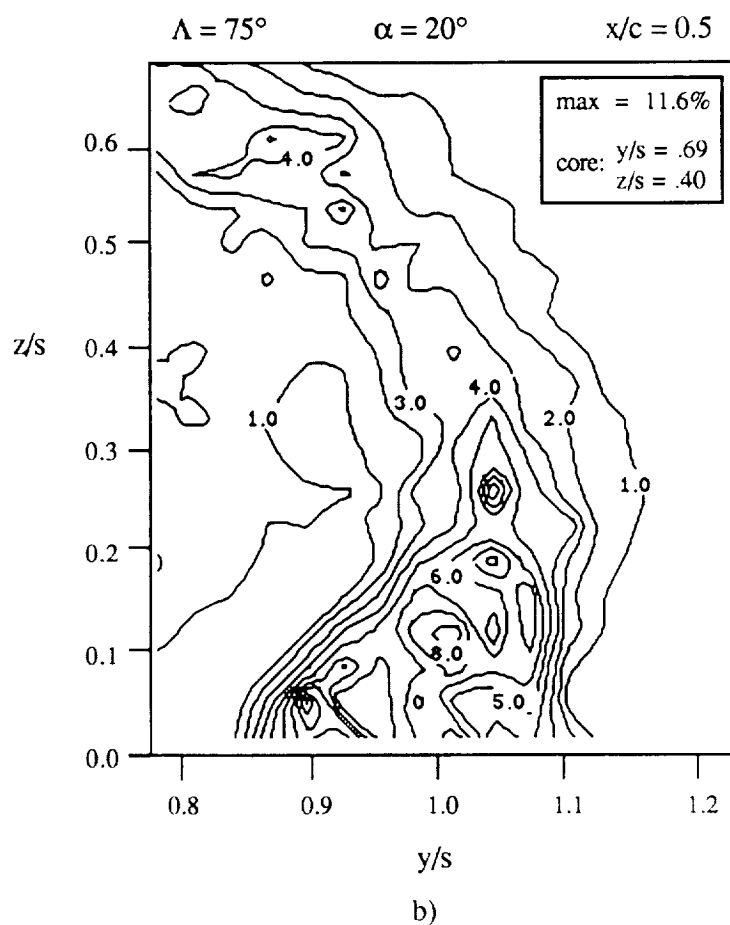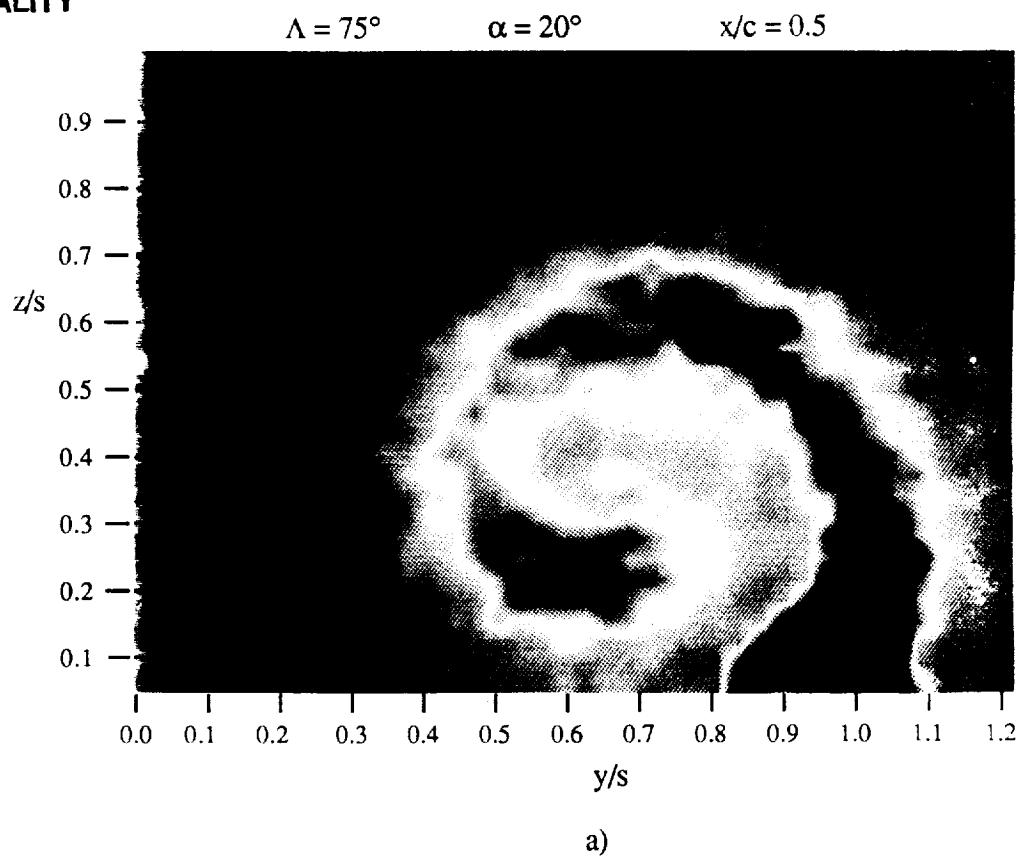
Figure 5.20 Fluctuation Intensity at $\Lambda=75°$, $\alpha=20$, $x/c = 0.5$ a) Color map b) Leading Edge Detail

the level of the intensity of the fluctuations drops by over an order of magnitude to a virtually negligible value along the axis of the vortex.

Based on the overall consistency of the velocity data above, and the good correlation with the SHP data, is was determined that the velocity profiles measured with the cross wire technique satisfactorily represented the vortex velocity field. Axial velocities indicated that for no breakdown flows the variation in the magnitude about the mean over the majority of the chord is $\pm 5\%$, dropping by about 15% near the apex region. Both the magnitudes and locations of the structures, including the shear layer region and core location, are well represented and compare favorably with previously obtained data. Hence, the data could be manipulated further to examine other derived properties of the flow, such as vorticity and circulation.

5.2.2 Vorticity

The velocity field data was centrally differenced spatially to obtain the axial vorticity component:

$$\Omega_x = \frac{\partial w}{\partial y} - \frac{\partial v}{\partial z} \tag{5.1}$$

The resulting vorticity field for the $\Lambda = 75°$ $\alpha = 20°$ data of Figure 5.6a is contoured in Figure 5.21a. A repeat test appears in Figure 5.21b for comparison. The majority of the axial vorticity is concentrated in the region immediately around the core of the the primary vortex. The extent of this region is approximately y/s = 0.55 to 0.75 and z/s = 0.3 to 0.5. Outside of this regime, the flow presents itself as essentially free of the axial vorticity component. A smaller region of flow with vorticity of the opposite sign and a much lower magnitude is located in the vicinity of

$\Lambda = 75°$ $\alpha = 20°$ $x/c = 0.5$

a)

$\Lambda = 75°$ $\alpha = 20°$ $x/c = 0.5$

b)
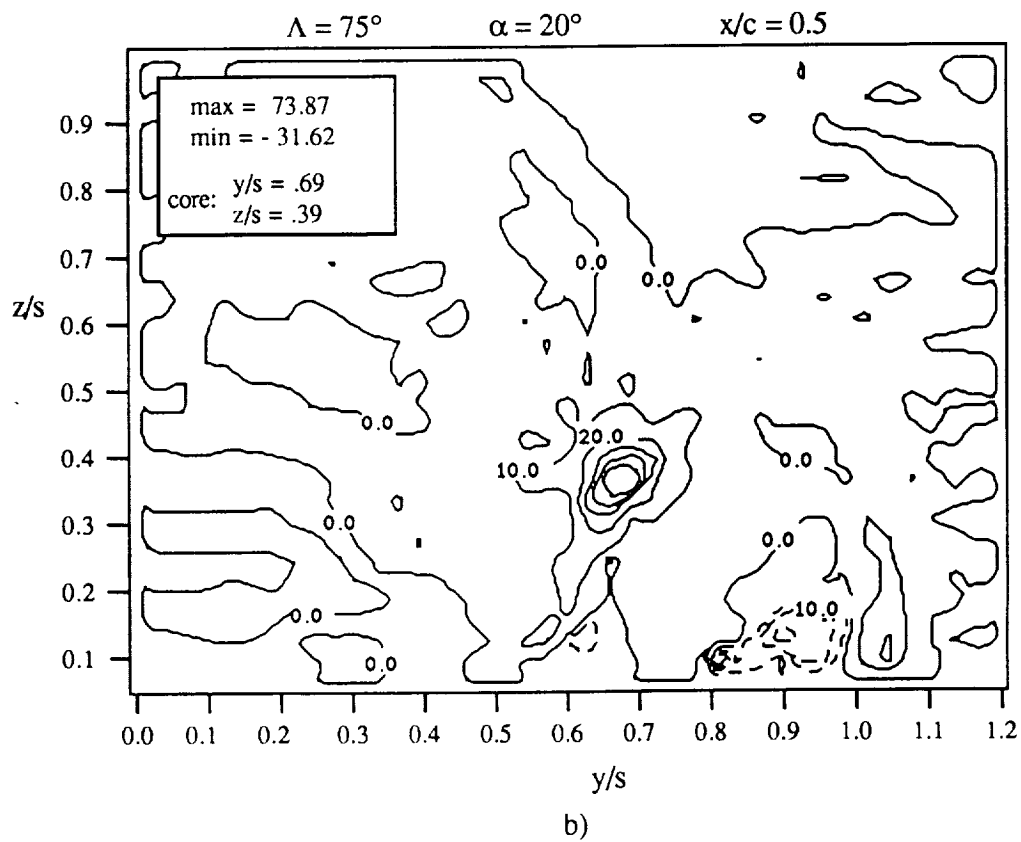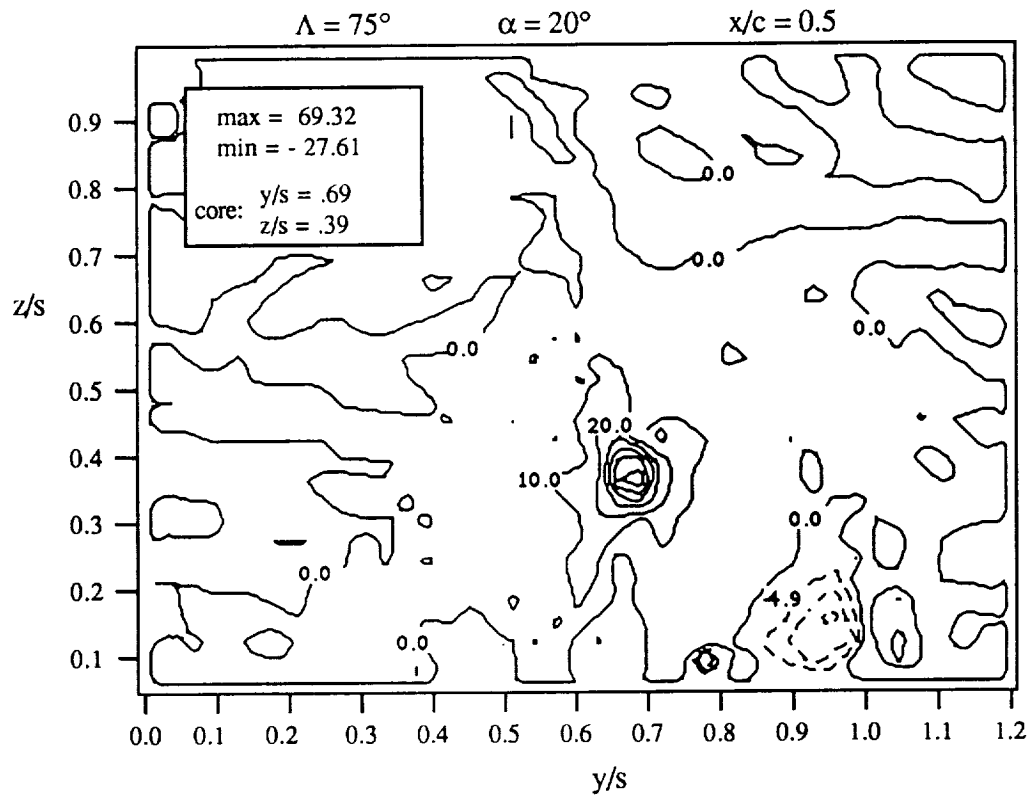
Figure 5.21. Axial Vorticity at $\Lambda=75$, $\alpha=20$, $x/c = 0.5$ a),b) Repeat Tests
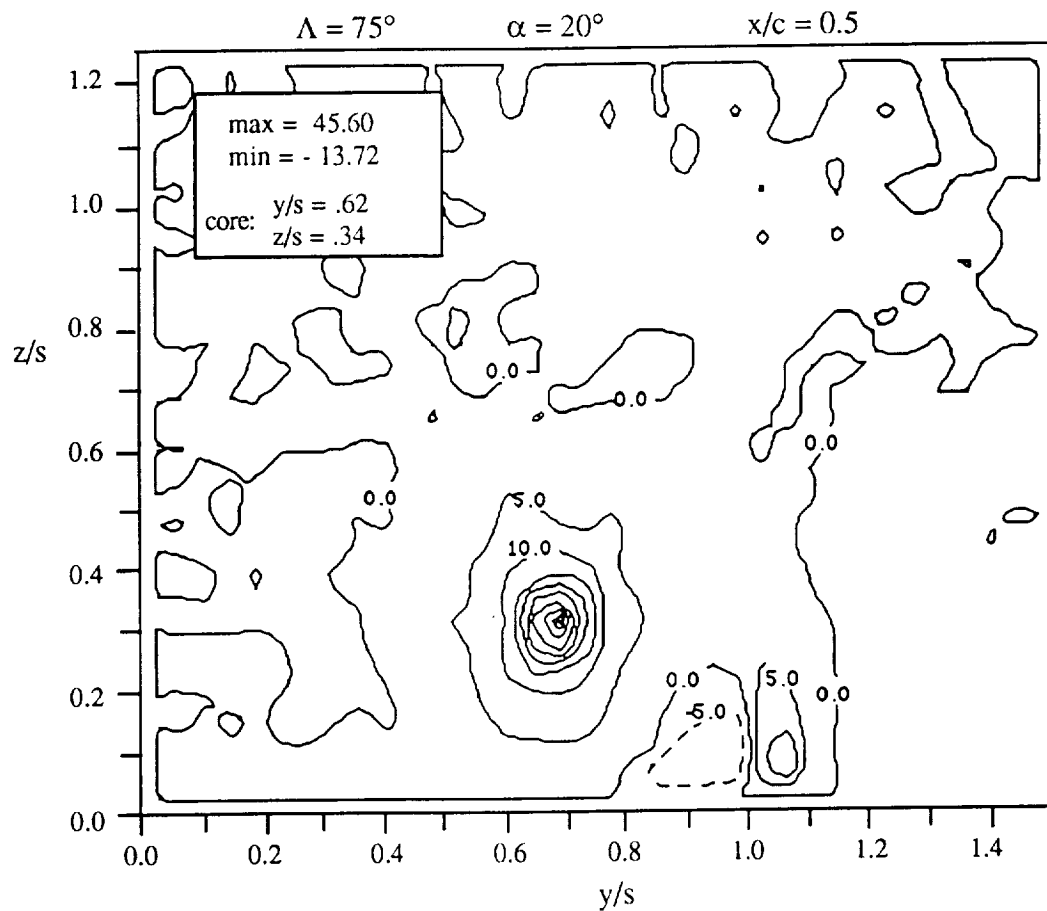
Figure 5.22. Axial Vorticity at $\Lambda=75°$, $\alpha=20°$, x/c=0.5 SHP Data

the secondary vortex. The recorded maximum and minimum values differ by about 7% and 14% respectively. The calculated axial vorticity for the seven hole probe data of Figure 5.6b is presented in Figure 5.22. Substantially smaller magnitudes of for both the positive and negative maximums, over 30% and 50% respectively, are evident when compared to the cross wire data. This is suspected to be a direct result of the increase in the grid resolution of the cross wire data, which is 30% finer than that used by the SHP. As previously emphasized in Table 1 of Chapter 2, the aspect of grid resolution should be strongly addressed when calculation of point properties in flow regimes containing large gradients is performed.

The most obvious difference is in the form of the contours themselves. The cross wire data displays a significantly more ragged appearance away from the core region than the SHP data. The nature of this jaggedness is believed to arise from two sources. Despite the repeatability of the velocity data, the error associated with maintaining the exact same spatial locations increases with each of the four successive cross wire passes required for a complete survey. Since the vorticity depends on this spatial derivative, a slight discrepancy in the actual location will be magnified in the resulting vorticity values. An estimate of the uncertainty in the vorticity due to the error in the spatial measurement depends on the chordwise station measured. At $x/c = 0.3$ this uncertainty is less than 1% using the resolution of the measuring system as the maximum error. Aft of this location, the uncertainty decreases further. Note that this uncertainty is based solely on spatial error and does not account for the error assiciated with the values of the velocity. Appendix C contains further details. The second source of error stems from the sensitivity of the technique to direction in regions of lower speeds. This seems to correspond with the contour shapes, for as distance from the core regions is increased, the contours become more distorted..

A hypothesis presented in Chapter 2 was that the vortex structure may be unable to exist in the cohesive, pre-breakdown nature if a maximum local value of vorticity in the vortex, say $\Omega_{x_{max}}$, is reached. The usual convention is to nondimensionalize the calculated vorticity by the ratio of the root chord to the freestream velocity to provide an overall view of the absolute vorticity in the entire flowfield. As mentioned previously, the use of the local spanwise distance provides a means to scale each cross sectional flow plane in order to examine the effect of the local geometry on the flow characteristics. If the flow scales in this manner, it demonstrates a conical behavior.

The maximum value of vorticity was obtained at each station as well as the minimum. These values are presented in Figure 5.23 for the 75° sweep wing at 20° and 30° angle of attack.
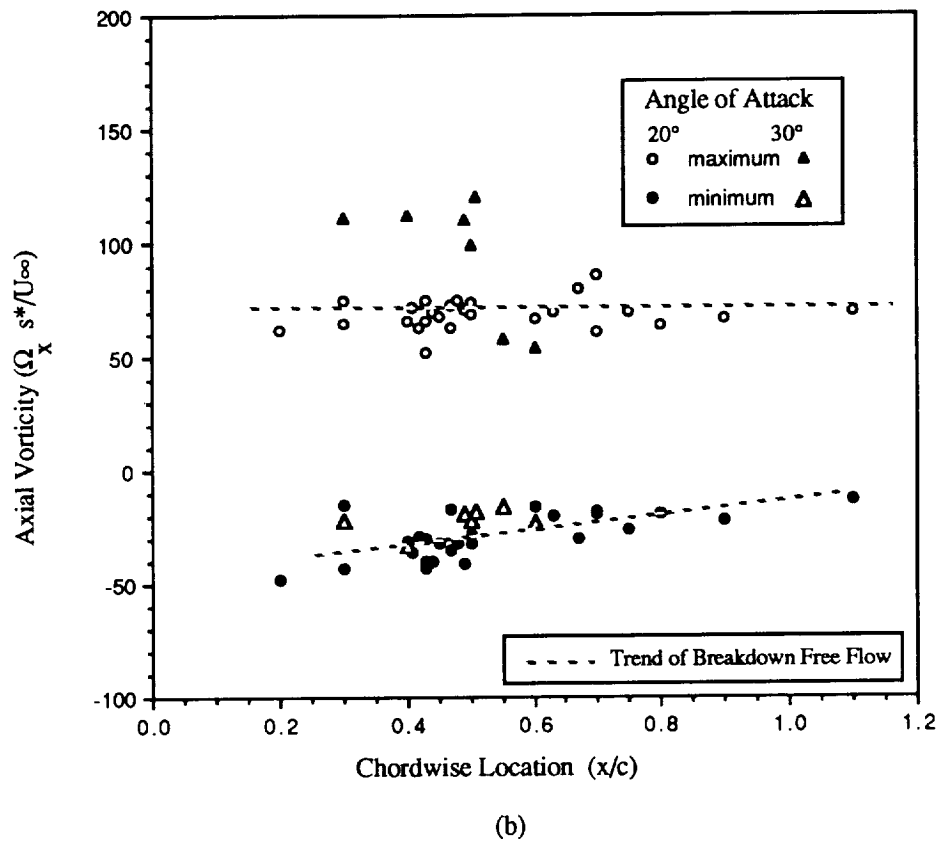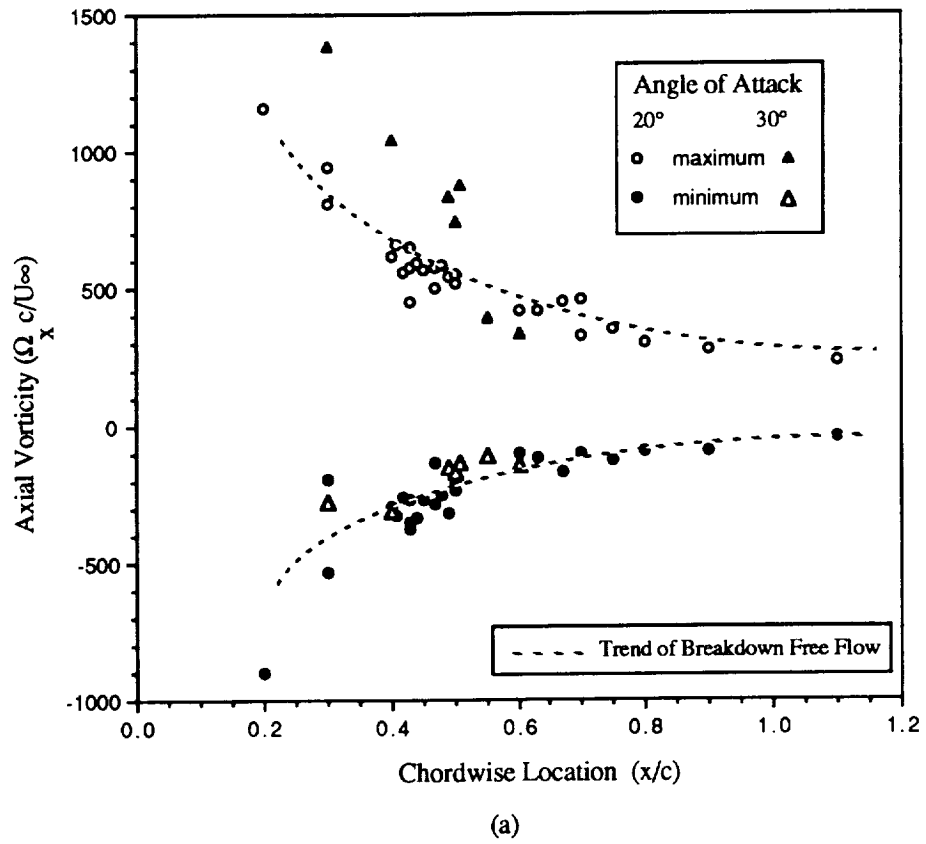
Figure 5.23. Chordwise Variation of Maximum and Minimum Vorticity
for 75° Sweep a) Scaled by chord b) Scaled by local semispan

Note that breakdown is occurring over the wing at the angle of attack of 30° between the 0.50 and 0.55 x/c location. No breakdown occurred over the wing for the 20° angle of attack case. The data is nondimensionalized using the two conventions mentioned above, the local semispan and the chord. From Figure 5.23a, in which the vorticity is multiplied by the ratio of the root chord to the freestream velocity, the magnitudes of both the positive and negative maximum values are seen to decrease with increasing distance from the apex. The positive values of vorticity in Figure 5.23a show a slight drop in magnitude at this station, however the negative values indicate no change at all. If the vorticity is now nondimensionalized by the local semispan, $s*$, as shown in Figure 5.23b, the data indicates a constant value behavior in the chordwise direction for both the positive and negative values. The previously noted drop in the positive value for the 30° case is now more evident.

The scatter in the data can be attributed to several factors. The vorticity is a measure of the smallest scales of the flow. Details of the velocity gradients will be lost if the grid is not sufficiently fine. The grid size increment for the data in Figure 5.23 is 3% of the local semispan. Finer grids were taken for certain configurations and are plotted in Figure 5.24. Data acquired on the larger chord halfspan model is included as well. The magnitude of the positive axial vorticity increases with increasing grid resolution, as might be expected since smaller flow scales can be resolved. The effect on the maximum negative magnitude was not of the same order, however, possibly due to the small size of the secondary vortex. It should be kept in mind that these values of vorticity were obtained by differentiating discrete data which has the effect of increasing the error associated with such measurements. As the grid sizing becomes smaller, though, the relative error in each spatial measurement will increase the scatter of the derived vorticity, since the absolute error of the traversing system is fixed. Hence, simply examining the maximum value of the vorticity does not make a definitive statement of the status of the vortex at that chord station.
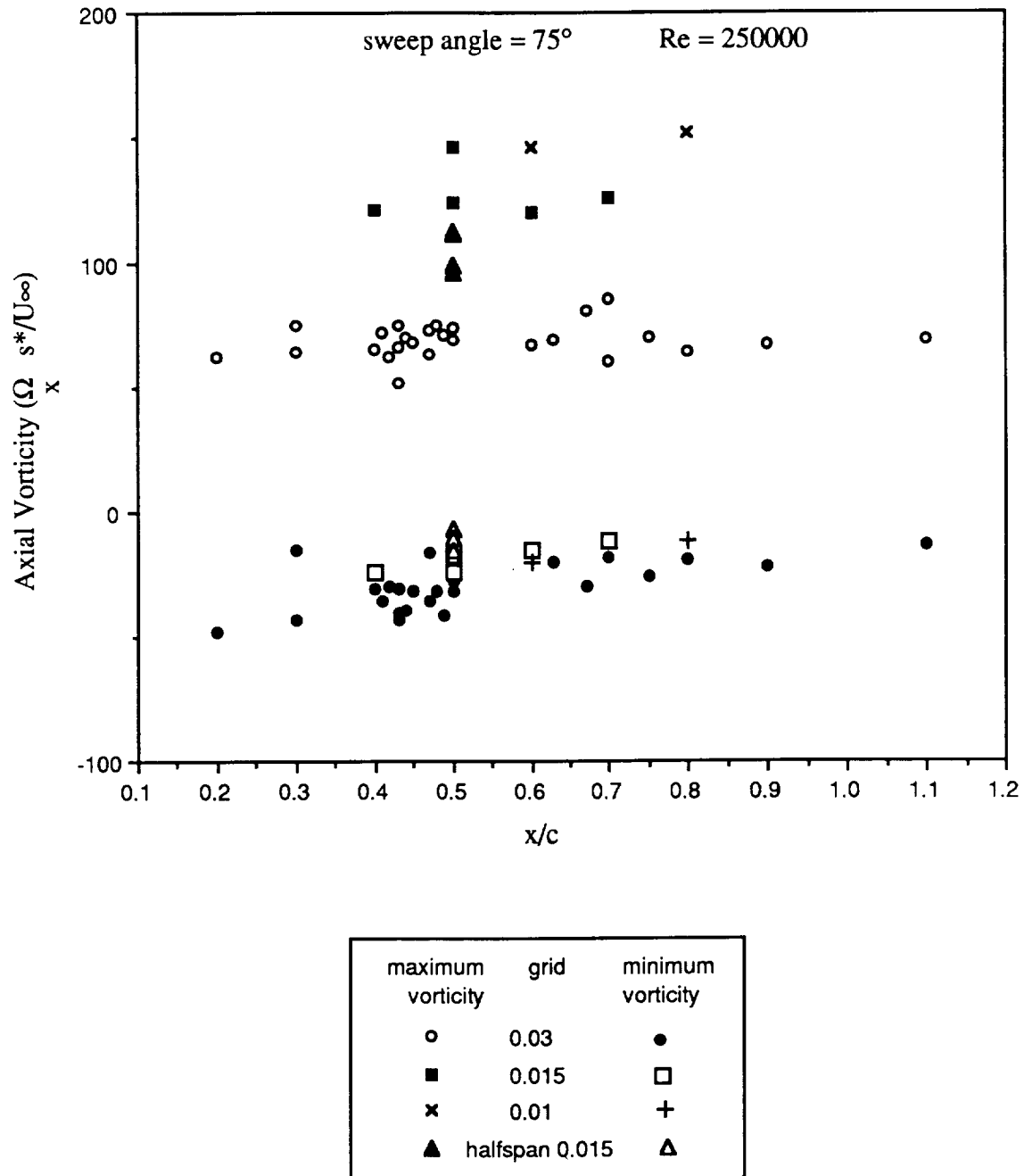
Figure 5.24. Effect of Relative Grid Size on Maximum and Minimum Vorticity

The leading edge sheet continually feeds vorticity into the vortex flowfield along the entire length of the delta wing. In conjunction with the earlier proposal of a maximum vorticity criteria, was the hypothesis that the vortex can only exist in the pre-breakdown state if the amount of vorticity is below a certain level. The axial vorticity profiles throughout the vortex were therefore examined for possible maximum amounts of this distributed vorticity at a chordwise location. Integrating the positive and negative values of the axial vorticity separately over their respective areas leads to the results shown in Figure 5.25.

Figure 5.25 contains data for several different configurations and methods of data acquisition. It is important to keep in mind that only the 75° sweep planform at $\alpha = 20°$ is maintaining a breakdown free flow above the wing. Both of the other planforms have a breakdown region slightly aft of the $x/c = 0.5$ station. From Figure 5.25a, the amount of negative vorticity present above the wing is observed to be relatively similar for all three configurations, the $\Lambda = 70°$, $\alpha = 20°$ case having the largest magnitude at each respective chord location. For all three planforms, the integrated positive values show a marked increase with distance from the apex. The magnitude of the 70° sweep data at 20° angle of attack is seen to be approximately the same as the values associated with the 75° sweep at an angle of attack of 30°. The 70° wing will generate a stronger vortex than the 75° wing if both are at the same angle of attack, but since the 75° wing is at $\alpha = 30°$ while the 70° is at 20°, the strength of the 75° wing vortex is increased. Scaling the data by s* causes the positively integrated values to remain relatively constant or slightly decrease with increasing chord location. In addition, the $\Lambda = 70°$, $\alpha = 20°$ case is now seen to fall in the same region as $\Lambda = 75°$, $\alpha = 20°$. The negative vorticity values remain together at approximately a constant value for all three cases.
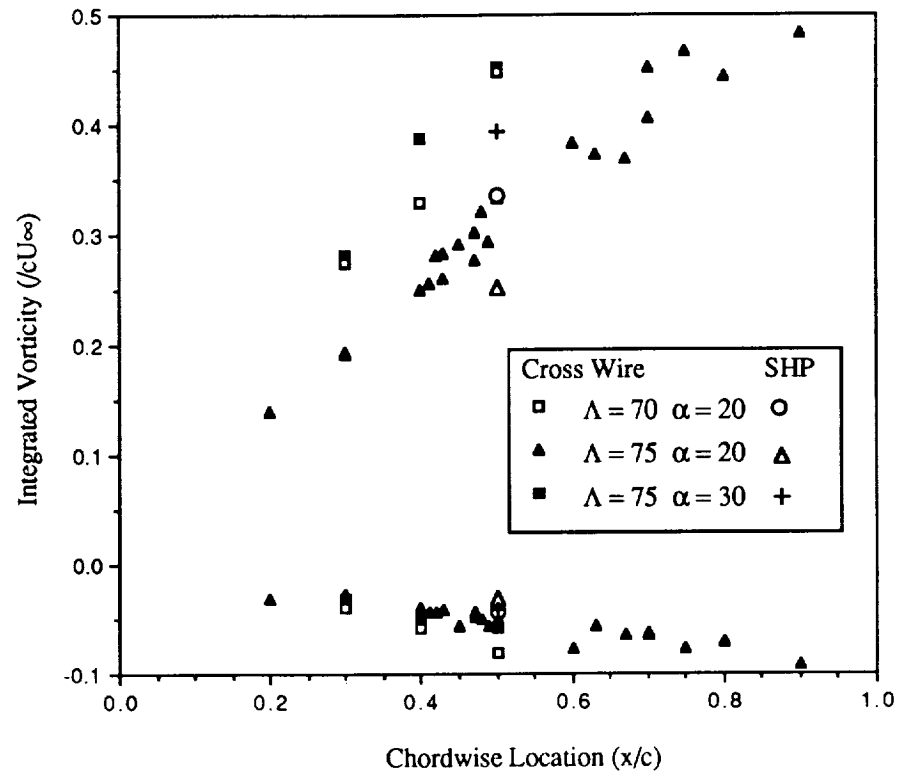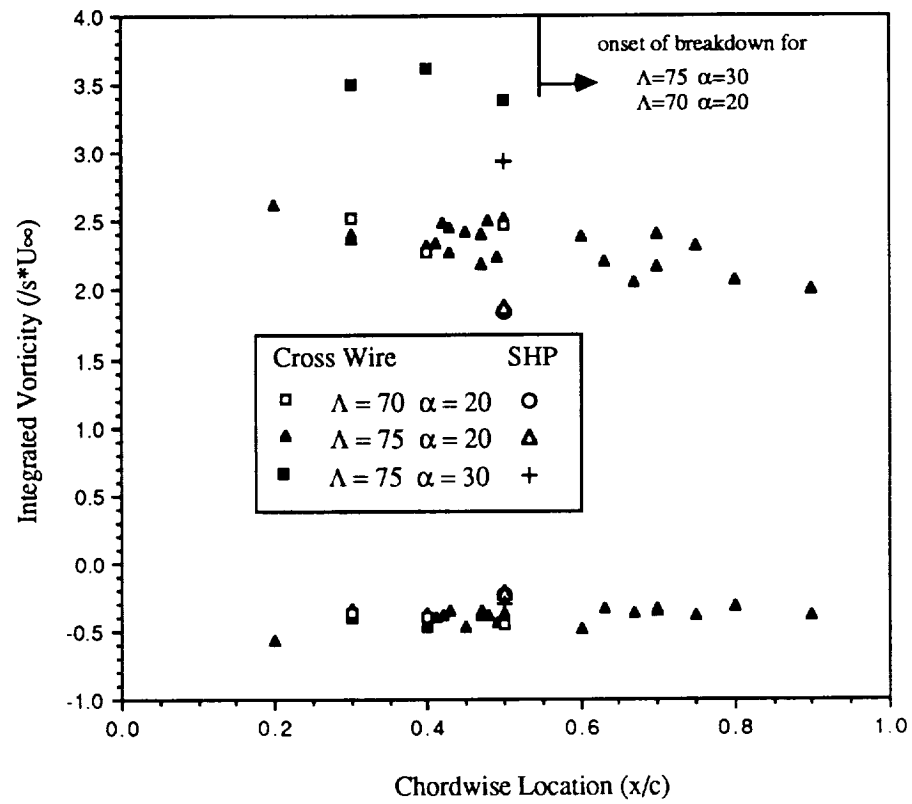
Figure 5.25. Integrated Vorticity a) Scaled by chord b) Scaled by local semispan

In an effort to examine the validity of the theoretical ideas proposed by Brown and Lopez (1988) values of azimuthal and axial vorticities, $\Omega_{\emptyset}$ and Ω_x respectively, were examined. Recall that the basic premise of Brown and Lopez was that a negative azimuthal vorticity

$$\eta = \frac{\partial V_r}{\partial z} - \frac{\partial V_z}{\partial r} \qquad (5.2)$$

will induce a negative axial velocity and initiate the breakdown process. The calculation of $\Omega_{\emptyset}$ and Ω_x was based on the grid traverse through the core center utilizing polar coordinates. Under the assumption that the radial velocity and its gradient were negligible compared to the other terms along the traverse through the core:

$$\Omega_{\emptyset} = - \frac{\partial V_x}{\partial r} = - \frac{\partial u}{\partial r} \qquad (5.3)$$

and

$$\Omega_x = \frac{V_{\emptyset}}{r} + \frac{\partial V_{\emptyset}}{\partial r} = \frac{w}{r} + \frac{\partial w}{\partial r} \qquad (5.4)$$

The nondimensional calculated values of Ω_x and $\Omega_{\emptyset}$ are given in Figures 5.26a and 5.26b. The axial vorticity is seen to increase to a maximum at the center of the core. A slight rise also occurs at r/s = 0.30, probably due to the shear layer in the feeding sheet. The earlier maximum, presented in Figure 5.21 and based on the spatial derivative in Cartesian coordinates, shows a comparable value. Values were also derived from the seven hole probe data of Payne (1987). The SHP data follows the cross wire data probe, but does not exhibit the maximums present in the latter at the core center or at the leading edge shear layer, r/s ≈ 0.3. The majority of the axial vorticity component is contained within 20% of the semispan, r/s = ± 0.10 about the core center location.

In a similar manner, $\Omega_{\emptyset}$ also increases as it nears the core centerline, however it drops to a value of zero at r/s = 0. Since $\partial u/\partial r$ is always negative with increasing distance from the core, as
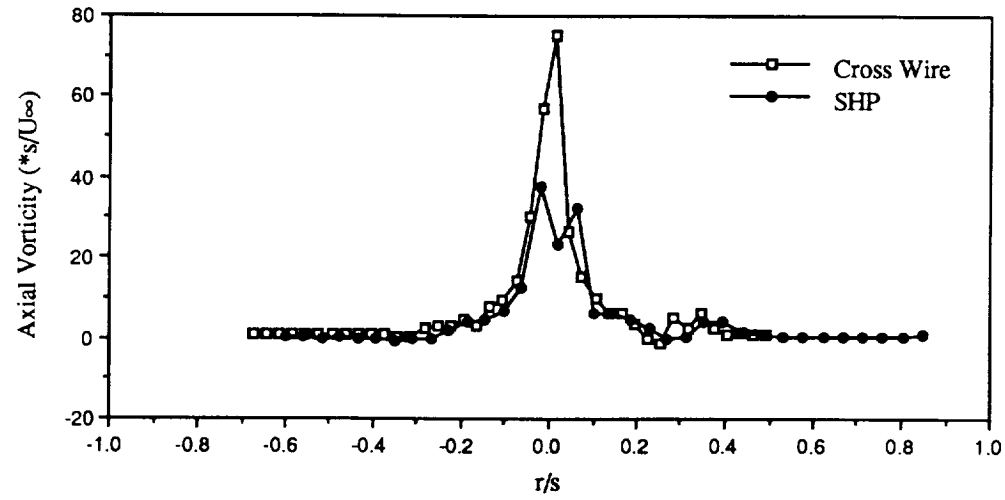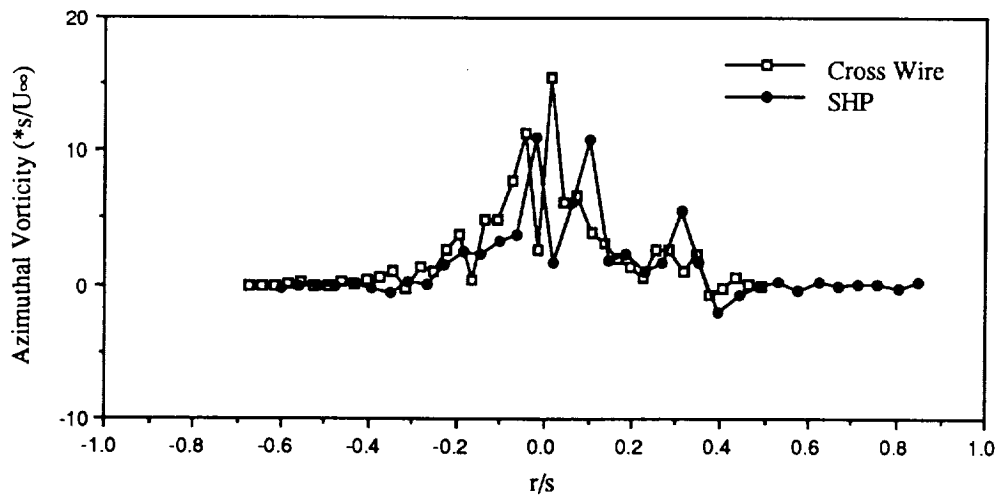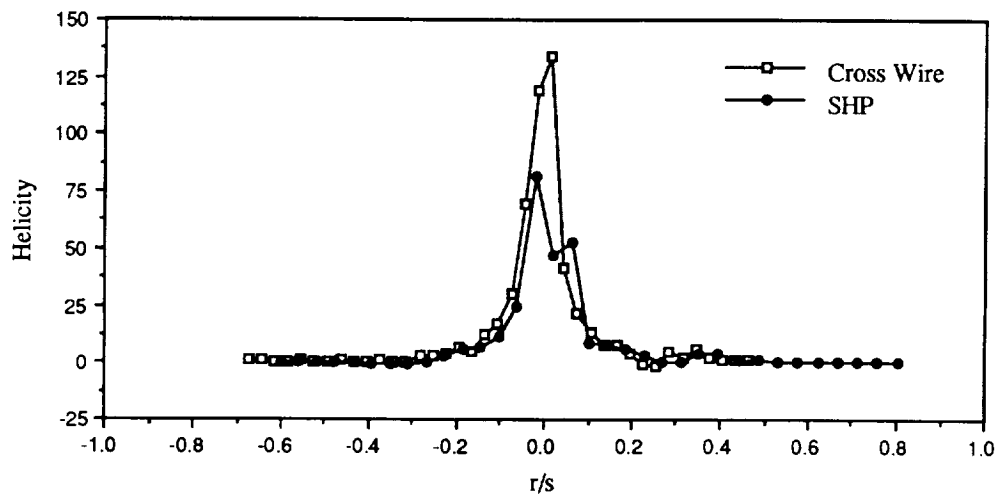
Figure 5.26 Core Vorticity Profiles for sweep = 75°, alpha = 20°, x/c = 0.5 a) Axial Vorticity
b) Azimuthal Vorticity c) Helicity

indicated in Figure 5.15, $\Omega_\emptyset$ is always positive except at r/s = 0 where u is a maximum and the gradient becomes zero. The azimuthal vorticity is seen to have a wider, more erratic distribution than the axial component. It also appears to have a rise at r/s = 0.30 due to the feeding sheet. The SHP data has also been overlaid on this figure. The scatter of both curves is believed to be based mostly on the lack of resolution. The most important thing to note is that for the majority of the profile, the values are positive. This would be in agreement with the theory of Brown and Lopez as these locations are pre-breakdown. The values do become negative in one region, however, just outboard of the leading edge, r/s $\approx$ 0.3. The axial velocity suffers a deficit in this region, leading to a positive $\partial u/dr$. The axial helicity profile is also included in Figure 5.26c. The deficit in the SHP data on the axis is due primarily to the lower vorticity magnitudes.

If the axial vorticity profiles are now overlaid for each of the measured x/c locations, Figure 5.27a, similar profiles are seen to exist at each station. Both $\Lambda = 75°$, $\alpha = 30°$ and $\Lambda = 70°$, $\alpha = 20°$ cases exhibited similar features. It was hoped that some indication of the imminent breakdown, especially with the $\Lambda = 75°$, $\alpha = 30°$ case, would be evident from these distributions. The $\Lambda = 75°$, $\alpha = 20°$ vorticity data scales in the same manner as the axial velocity profiles, that is linearly with distance from the apex which indicates a conical behavior of the flowfield. The data for the $\Lambda = 75°$, $\alpha = 30°$ configuration does not give any indication of the upcoming flow transition, however the probe was still upstream of breakdown.

The vorticity profiles were then nondimensionally integrated along each respective semispan to derive a set of values indicative of the local vorticity density distribution. These values are given in Figure 5.27b. As would be expected from Figure 5.27a, the $\Lambda = 75°$, $\alpha = 20°$ no breakdown case revealed a relatively constant value in the chordwise direction. The single SHP point for the $\Lambda = 75°$, $\alpha = 20°$ configuration falls at the lower edge of the band of this data. The $\Lambda = 70°$, $\alpha = 20°$ values also fall in this range, while the data for $\Lambda = 75°$, $\alpha = 20°$ maintains slightly higher integrated values, possibly indicating a local maximum at the 40% station.

a)

b)
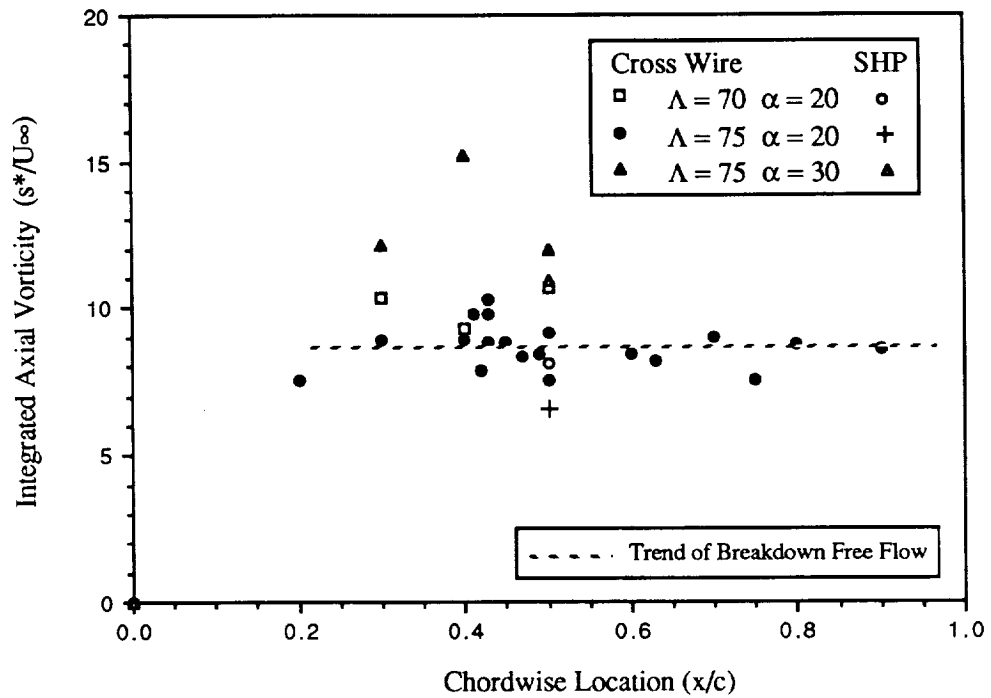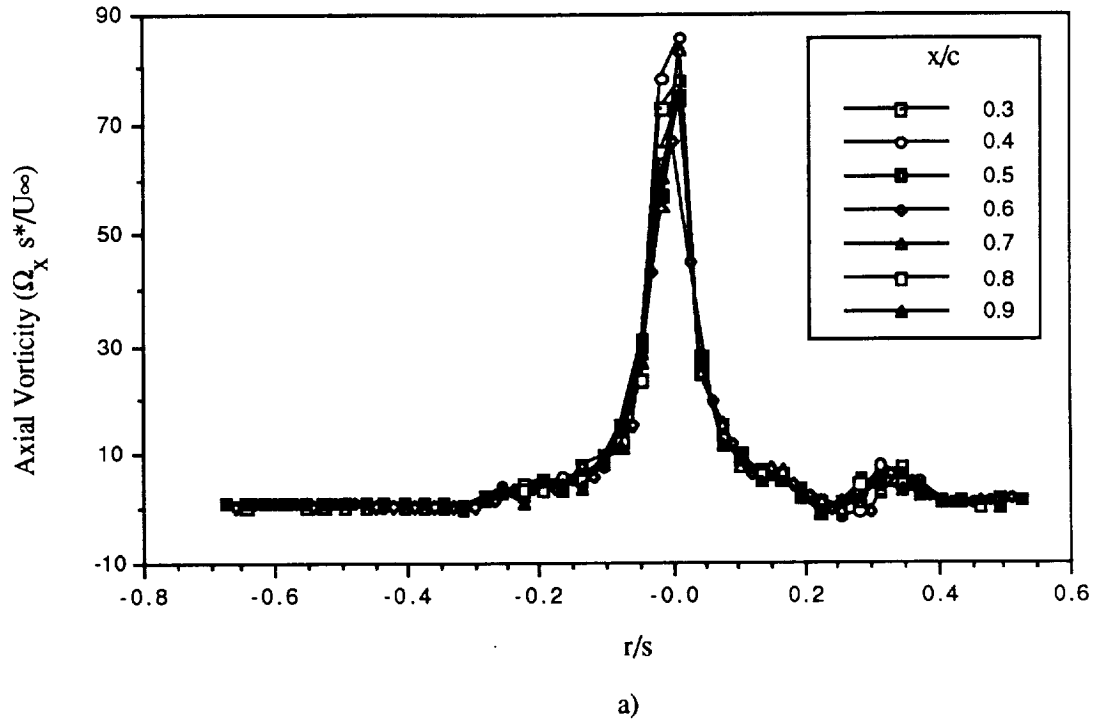
Figure 5.27. Axial Vorticity Distributions a) Present Profiles b) Integrated Values

The calculated axial vorticity profiles of Iwanski LDV data presented earlier in Figure 2.3 were also integrated in the same spanwise manner and are plotted against their chord locations in Figure 5.27c. These profiles were taken at stations in the breakdown region unobtainable using the present cross wire technique. Both the integrated vorticity and the helicity, defined as the product of the axial velocity and vorticity components, appear to reach some maximum at a distance of about 10 to 15% of the chord upstream of the breakdown region. Whether this indicates that the vortex reaches a saturated or critical condition is still open to question, due to the scarcity of data upstream of breakdown. A rapid decline through the breakdown region and
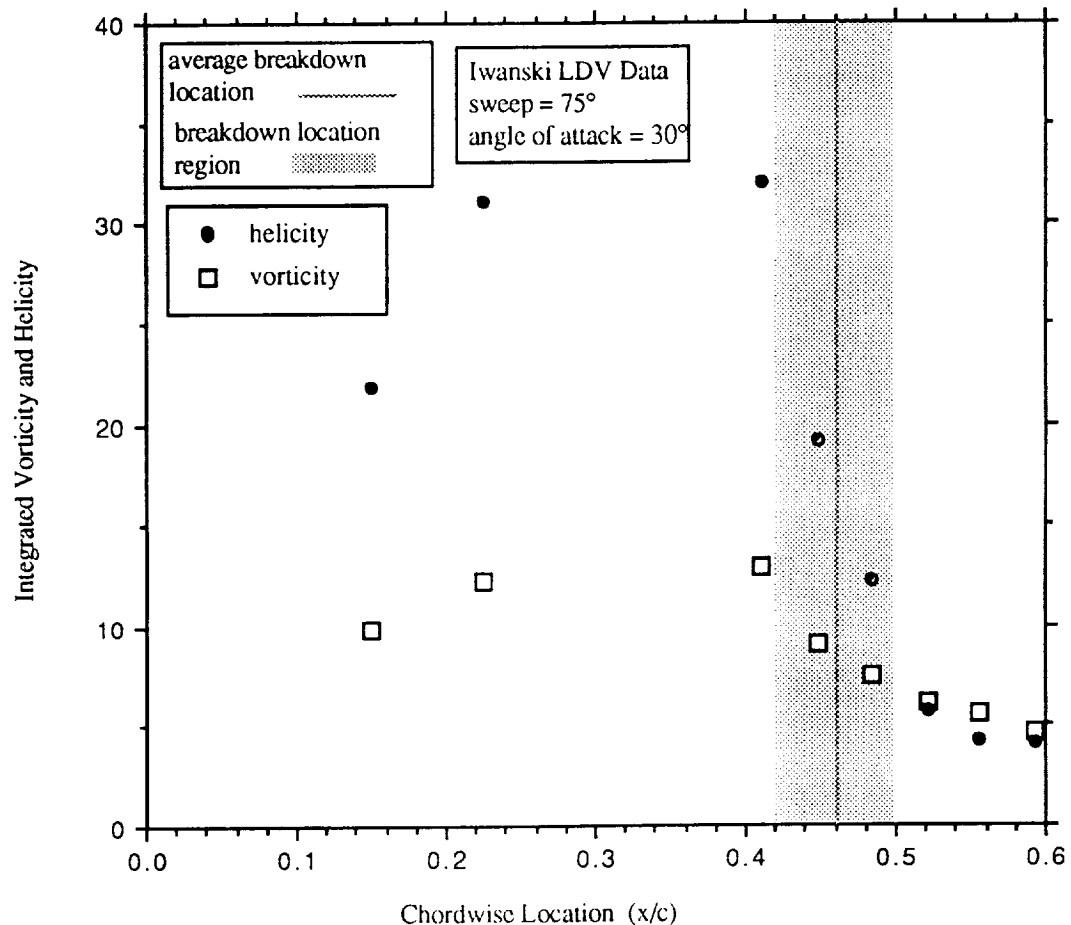
Figure 5.27 Axial Vorticity Distributions c) Integrated Iwanski Data

beyond, is then observed. The axial component of helicity, obtained by taking the dot product of the vorticity field with the velocity field, also appear to indicate a minimum at the 55% chord position. Helicity can be viewed as a correlation of the velocity and vorticity components in any one direction and the scaler parameter is a measure of the inhibiting process of the normal energy cascade from large to small scales (Davies-Jones (1982)).

The illustrative nature of the LDV results above, in contrast to the cross wire data, prompted additional derivations of the azimuthal vorticity component as a means of verifying the conjectures of Brown and Lopez (1988). Azimuthal vorticity values derived from Iwanski's LDV data are presented in Figure 5.28a. This component of vorticity was observed to become negative at certain spanwise locations, corresponding to the beginning of the breakdown region, thus supporting the conjectures of Brown and Lopez (1988). The azimuthal component appears to reach a maximum negative value, however as this data represents time averaged values of a highly fluctuating region and care should be taken when drawing conclusions. A further point should be made about the derivation of these values. As the core expands at the onset of breakdown, a radial velocity component must certainly exist. There is a real possibility that this now becomes a non-negligible quantity and would then act to provide a positive contribution to $\Omega_\emptyset$, serving to offset the negative component. This is not considered in the evaluation of Iwanski's data due to a lack of sufficient information. Pagan and Solignac (1986) also determined that the value of $\Omega_\emptyset$ becomes negative as the breakdown region is encountered. Their spatial results indicate local minimums shortly after the breakdown. They conclude that the entire vorticity vector, Ω, rotates from an essentially longitudinal direction to a generally tangential one in the breakdown zone as Brown and Lopez's analytical hypothesis surmise.

Physically there is no meaning to integrating the azimuthal vorticity distributions and thus the maximum values of $\Omega_\emptyset$ were plotted instead in Figure 5.28b. These values can also be interpreted as the maximum gradient of the axial velocity in the radial direction and are seen to
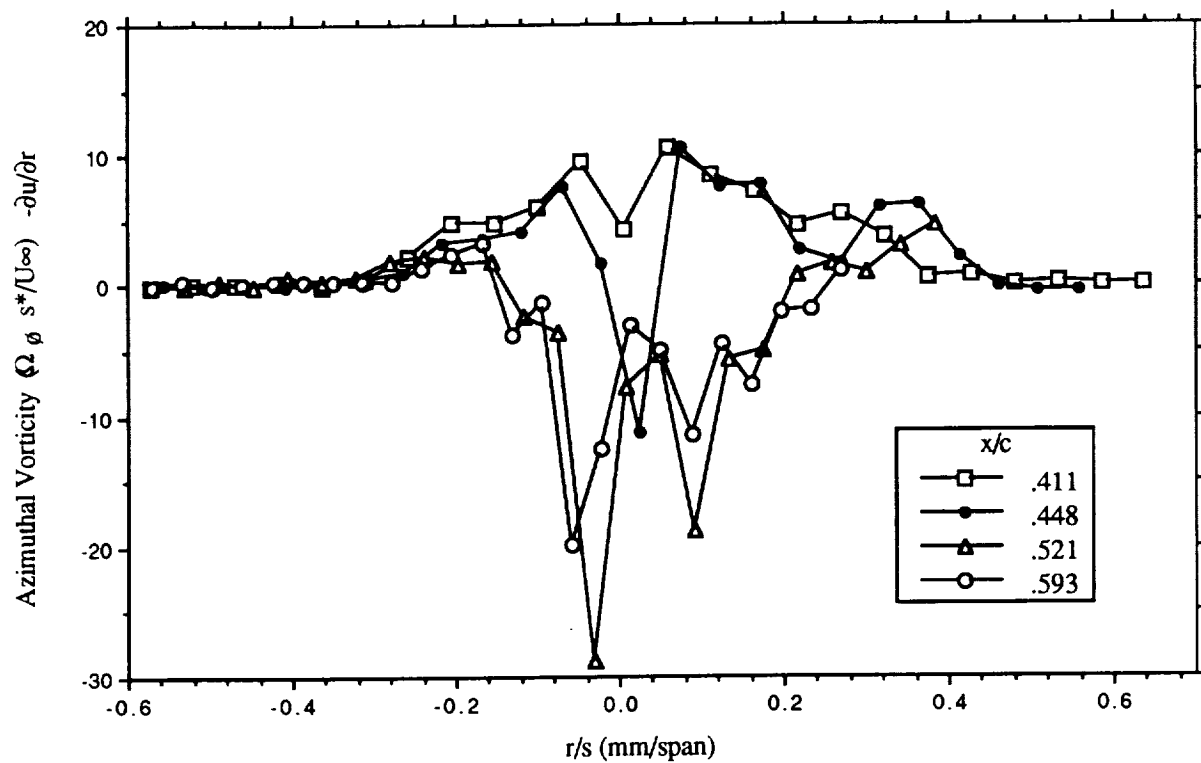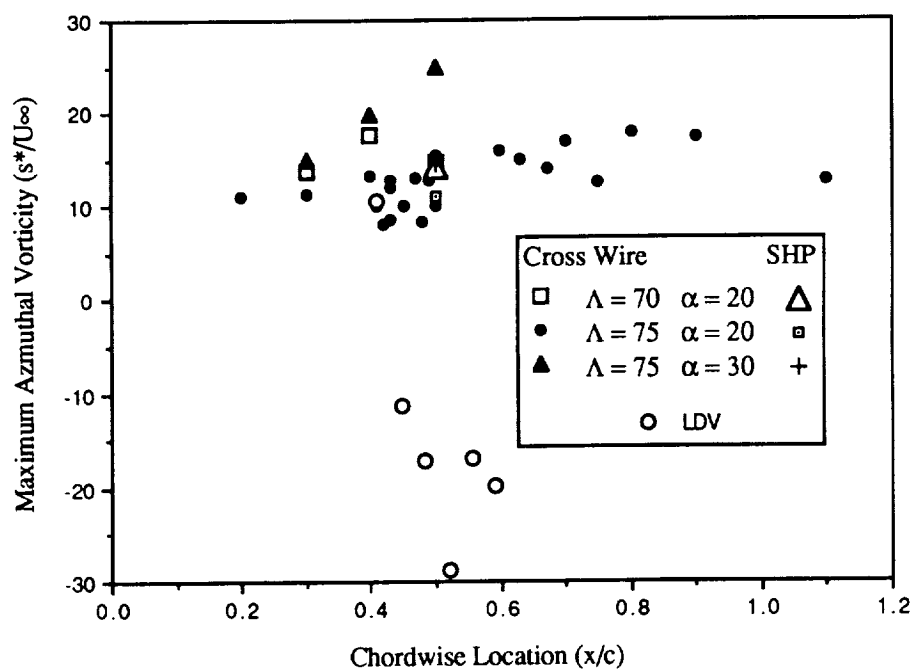
Figure 5.28   Azimuthal Vorticity Distributions a) LDV Data b) Maximum Azimuthal Vorticity

increase in the axial direction for the present $\Lambda = 75°$ tests, especially for the $\alpha = 30°$ case. The Λ = 70° reflects the same local peak about the 40% station. The data of Iwanski shows the change from a positive to a negative sense, as would be expected from Figure 5.28a. Unless there is a local axial velocity deficit present, $-\partial u/dr$ will always be positive. Other investigators have shown this deficit to occur in the breakdown region, but the present method was found to be inaccurate for regions of the flow where u is much less than v or w. The low axial velocity regions present at breakdown gave results which could not be considered reliable. In addition negative values of u could not be measured using this method.

The behavior of the axial vorticity strongly support the conical nature of the delta wing vortex in the region preceding breakdown. Scaling both the maximum vorticity values and the profiles based on a traverse though the core by the local spanwise geometry indicates that the distribution of the axial vorticity through the core is similar at each chordwise station. The majority of this axial vorticity component is seen to be concentrated in the region immediately around the core of the the primary vortex. The onset of breakdown, however, cannot be simply characterized by an experimentally derived point vorticity value. Grid resolution and the locally steep gradients deter this type of quantification. A relative decline can be observed, as Figure 5.23 suggests, but nothing absolute. The positive components of vorticity also seem much more sensitive than their negative counter-parts to chordwise location. The positive axial vorticity profiles also strongly indicate a conical flow behavior prior to breakdown. The integration of the vorticity profiles derived from the LDV data of Iwanski, indicates a maximum plateau region in the distribution of vorticity upstream of the breakdown region. Despite the scattered trends of the azimuthal component derived from the LDV data, the change from a positive to a negative sign, through the breakdown zone, appears to support the propositions of Brown and Lopez. Since all the vorticity components above were arrived at using calculations based on differentiating the experimental data, a possible reduction in associated errors might be obtained by analyzing the data after it has been integrated. This then leads to the following section.

5.2.3 Circulation

The circulation, Γ, was calculated in the plane of the survey grids and compared to the vorticity field over the area normal to it. The relationship between each is detailed below:

$$\Gamma \quad = \quad \int_{r} V \cdot dr \quad = \quad \int_{A} (\nabla \times V) \cdot dA \quad = \quad \int_{A} \Omega_x \, dA \qquad (5.5)$$

In order to evaluate the reliability of differentiating the discrete velocity field, the vorticity field distribution was spatially integrated and is presented for the $\Lambda = 75°$, $\alpha = 20°$ case, in Figure 5.29 along with the equivalent line integral. The values have been nondimensionalized by the freestream velocity and the root chord. They are plotted outward from the core center ($r = 0$), where the radial distance has been scaled by the local semispan. Each curve represents a chordwise location and the circulation is seen to grow in a chordwise manner. This is what one would expect, as more of the feeding sheet is being wrapped into the vortex as distance increases from the apex. The circulation increases at a decreasing rate from the center of the vortex and reaches a maximum inside of the planforms leading edge. The profiles experience an additional rise in circulation as the integration path encloses the shear layer outboard of the leading edge.

The circulation and integrated vorticity values are seen to correspond quite well, which would indicate that differentiating the velocity fields did not substantially increase the error. The circulation was not calculated along paths corresponding to a constant radius from the core center. Instead, square integration paths were followed, as the data fields for the v and w velocity components lie tangent to these lines of integration. The enclosed path formed a square enclosing a circle of radius equal to the r/s location. The uncertainty in the calculated circulation values, based on the error in spatial measurement, was estimated to be approximately half that of the vorticty, resulting in less than 0.25% at x/c = 0.5. As with the estimate in the uncertainty of the vorticity, no account is made of the error associated with the velocity. Payne (1987) stated that the overall
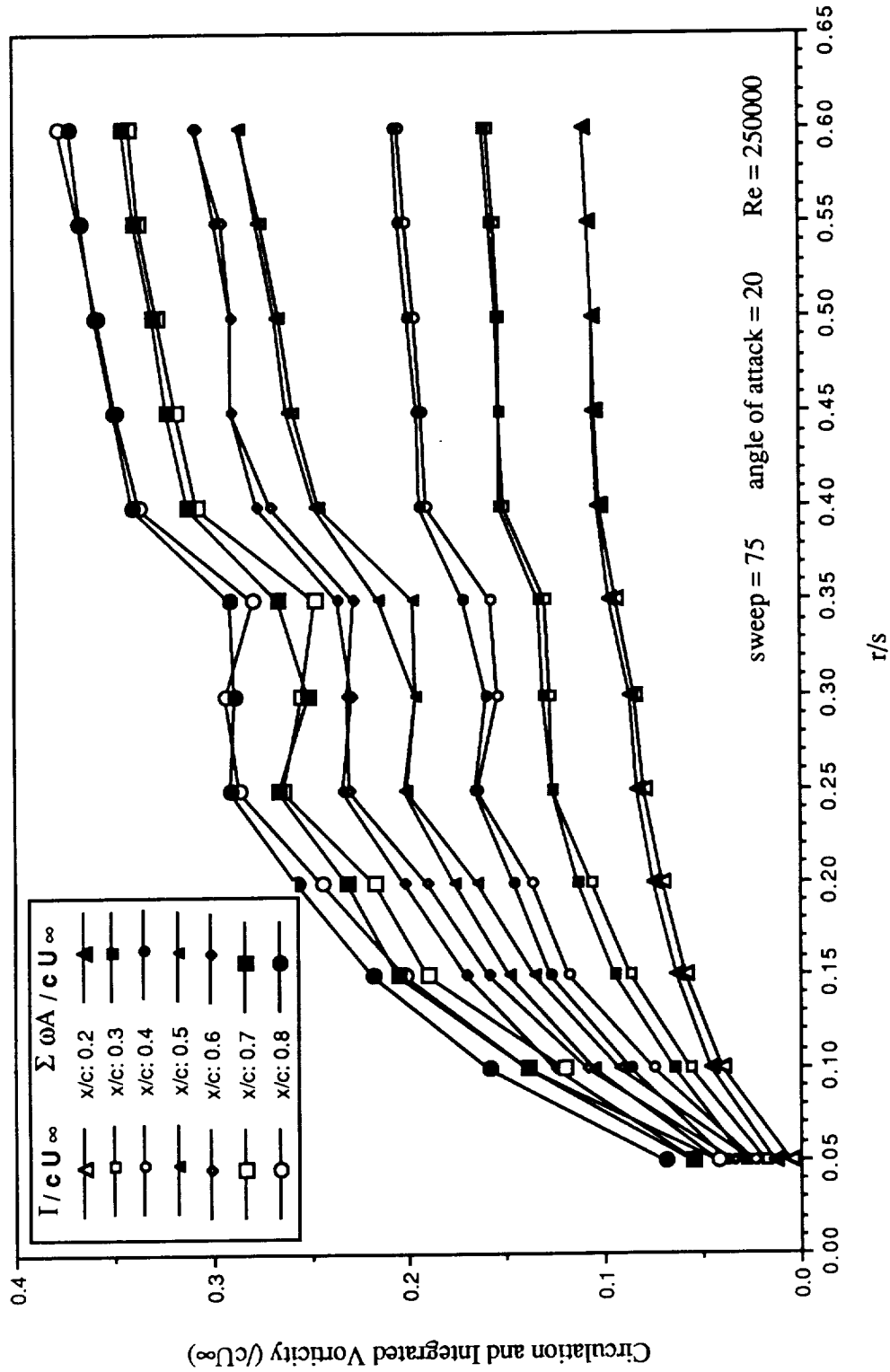
Figure 5.29. Radial Comparison of Circulation and Integrated Vorticity for 75° sweep planform at alpha = 20°

positional accuracy of the system is ± 1 mm. If this is taken to be the actual error in position, the uncertainty in the circulation rises to over 9%. The corresponding increase in the vorticity uncertainty is over 20%.

The circulation values for the $\Lambda = 75°$ planforms were then scaled by the local semispan, s^*, and plotted in Figure 5.30, to examine the dependence on distance from the apex. This has the effect of bringing the curves close together. The agreement of the resulting scaled profiles implies that the circulation at a constant angle of attack is increasing in direct proportion to the increase in local semispan. This linear increase of circulation in a chordwise direction for any radius re-enforces the conical nature flowfield assumption. Since Figure 5.30a represents two angles of attack for the same planform, a possible way to account for the difference in attack angle would be to further incorporate some function of α as a scaling parameter. As an example, the circulation values for three x/c locations are divided through by $\sin(\alpha)$ and plotted in Figure 5.30b. The data for $\Lambda = 70°$, $\alpha = 20°$ has also been added for comparison. The data does not collapse to a line, but rather a band. A universal curve of the form suggested in Figure 5.30b would be very useful, however it is difficult to ascertain the error present in each profile. For comparison, circulation profiles from the seven hole probe data of Payne (1987) were calculated and are given in Figure 5.31. A similar behavior is observed in Figure 5.31b when the values are scaled by the sine of the incidence angle and the resulting values fall in the range indicated in Figure 5.30b.

A closer look at Figures 5.31 and 5.32 indicates the growth of the circulation with radius to follow a definite pattern. That is, there is a region of increasing magnitude in a nonlinear manner, followed by a leveling off, and then the subsequent increase due to the shear layer. Thus the flow exhibits rotational qualities outside of the subcore. As outlined in Chapter 1, Figure 1.7, the archetypical vortex is divided into three regions: the solid body center and the rotational Euler region, which comprise the 'core', and the irrotational flow outside of this. Each
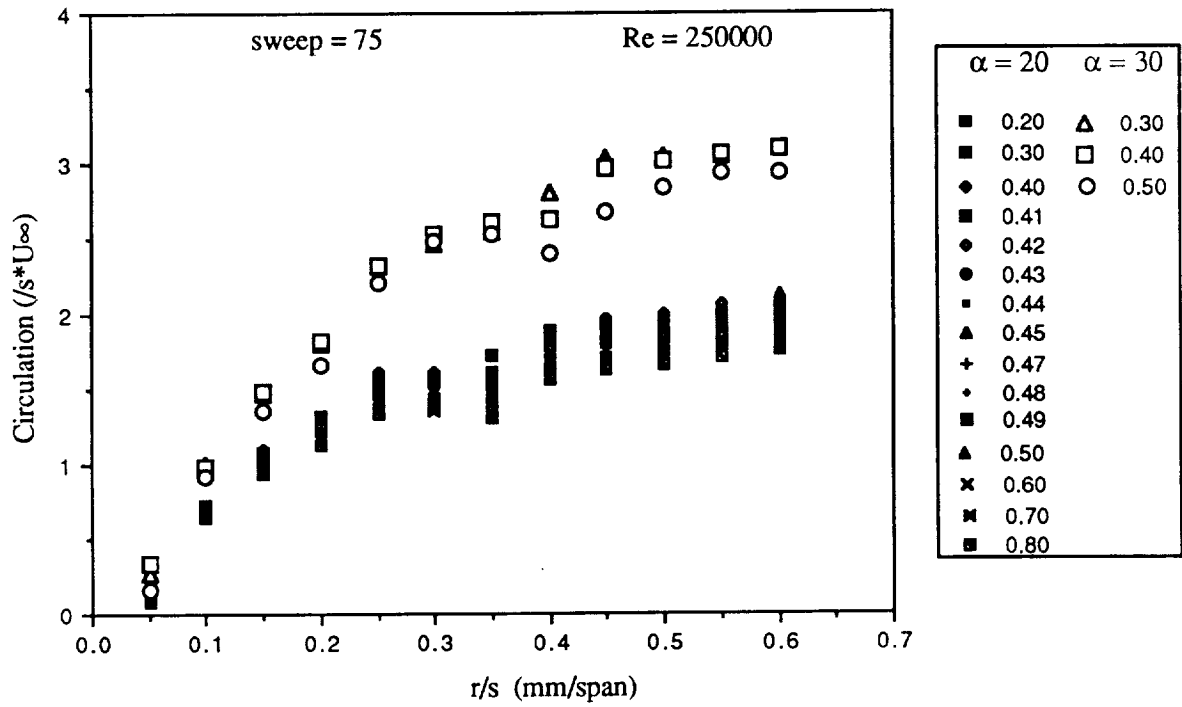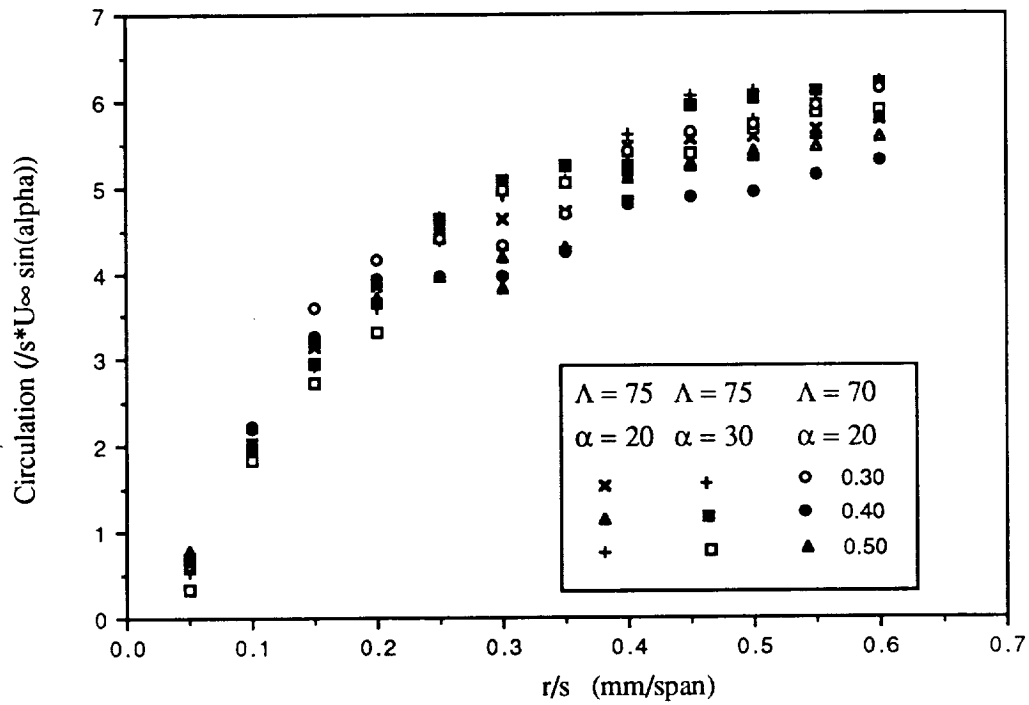
Figure 5.30 Effect of Scaling on the Radial Variation of Circulation a) Geometric b) Angle of Incidence
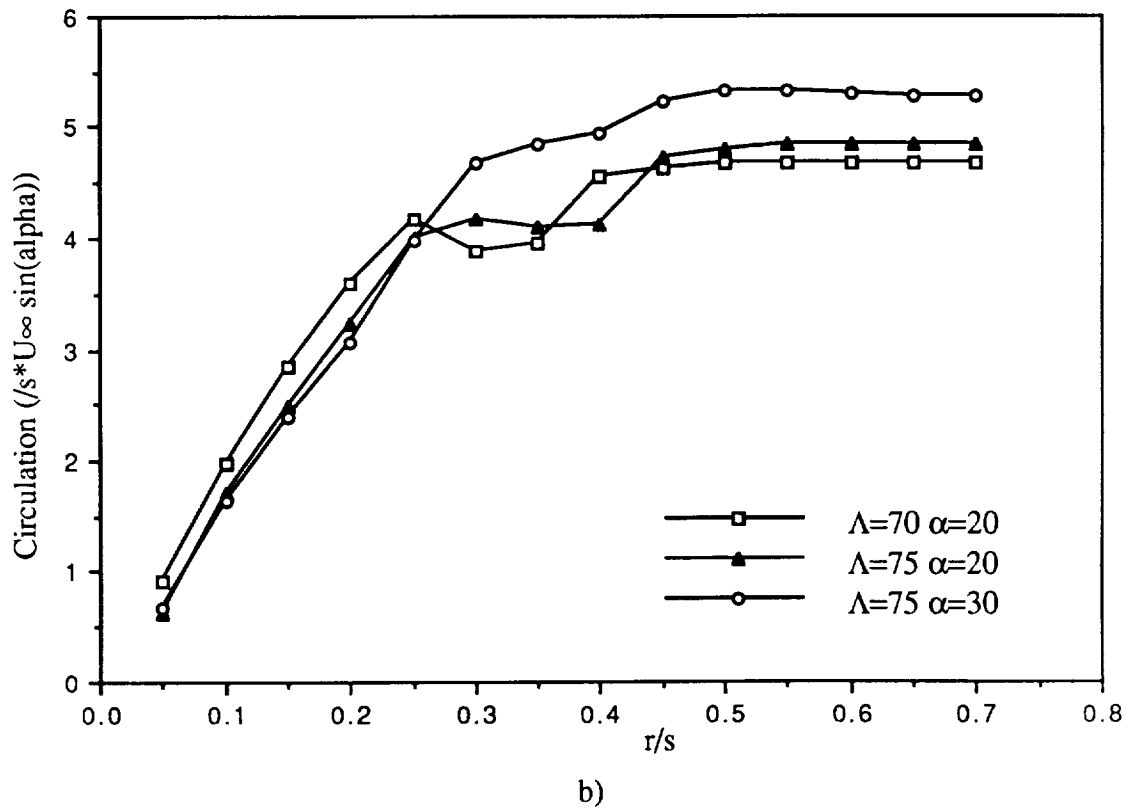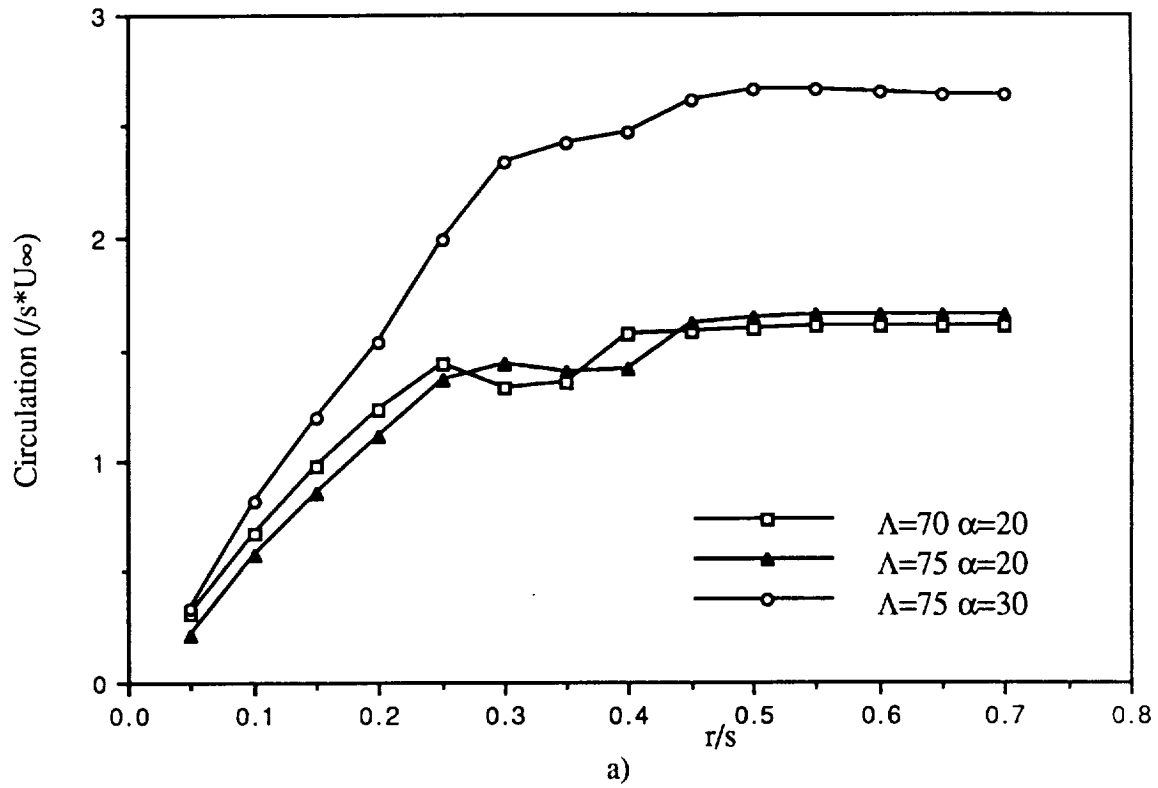
Figure 5.31 Radial Variation of SHP Circulation Data Scaled by a) Local Semipan b) Angle of Attack

of these regions will exhibit a distinct behavior in the radial variation of the circulation and the velocity profiles. A solid body core typically possesses a velocity distribution of the form v = ωr, for some radius r ≤ a where a is the radius of the maximum tangential velocity. The tangential velocity profiles presented earlier in Figure 5.15 suggest a linear velocity distribution through the core region. The resulting circulation profile would therefore increases parabolically with distance from the core center. None of the circulation profiles in Figures 5.29 to 5.31, however, indicate this upward concave behavior. The curves all possess negative second derivatives with respect to r for r < leading edge. Since the subcore diameter is on the order of 10 to 15% of the local semispan, as will be discussed later, the upwards curvature may not be present simply due to lack of resolution.

As illustrated in Figure 5.15, the tangential velocity was seen to decrease with increasing
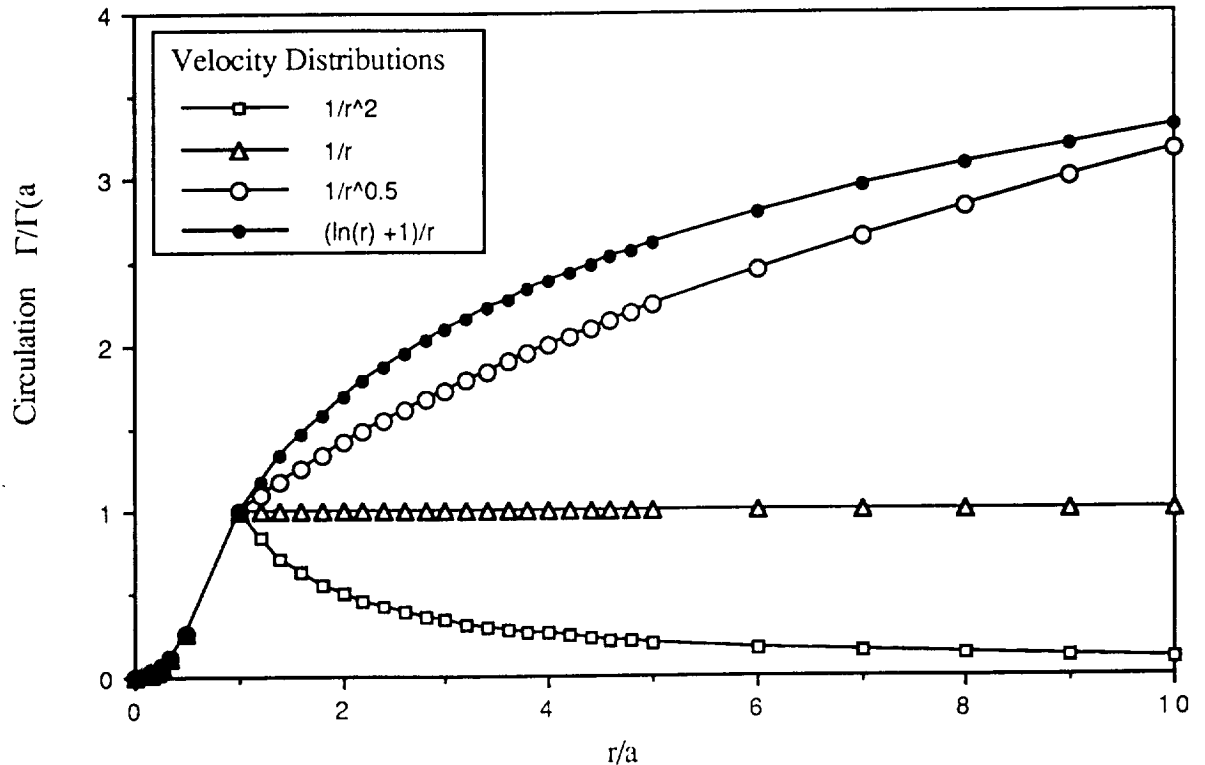
Figure 5.32 Theoretical Radial Circulation Distributions

radius for r > a. An irrotational flow, of the form $V_\theta = 1/r$, will demonstrate this behavior, but there will be no accompanying increase of circulation with radius as illustrated in Figure 5.32. Two other theoretical circulation profiles derived from velocity distributions based on an inverse relation of the radius were plotted in Figure 5.32 for comparison. An increase in the circulation similar to that in Figure 5.29 is seen for one of the distributions, possibly indicating a $1/r^n$ velocity distribution for n <1 exists at radial distances greater than the point of maximum tangential velocity.

Further insight on the nature of this rotational region can be gained from the work of Hoffmann and Joubert (1963) on turbulent line vortices. Based on their analysis of the equations of motion, utilizing the assumption that the 'inertia' terms are negligible compared to the Reynolds stress terms, a circulation distribution of the form below was derived

$$\frac{\Gamma}{\Gamma(a)} = A\left(\ln\left(\frac{r}{a}\right)\right) + 1 \tag{5.6}$$

where A is a constant. This is also plotted in Figure 5.32 with the corresponding velocity profile equation.

The data in Figure 5.30a and 5.31a was replotted in 5.33a and 5.33b using a logarithmic scale for the radius. The cross wire data, in Figure 5.33a, shows evidence of the suggested logarithmic dependence with radius for a turbulent vortex before the shear layer flow is encountered. Hoffmann and Joubert (1963) also obtained data at a series of stations downstream a vortex generated by a differential airfoil. They suggest a universal circulation distribution exists of the form

$$\frac{\Gamma}{\Gamma(a)} = 2.14 \log_{10}\left(\frac{r}{a}\right) + 1 \tag{5.7}$$
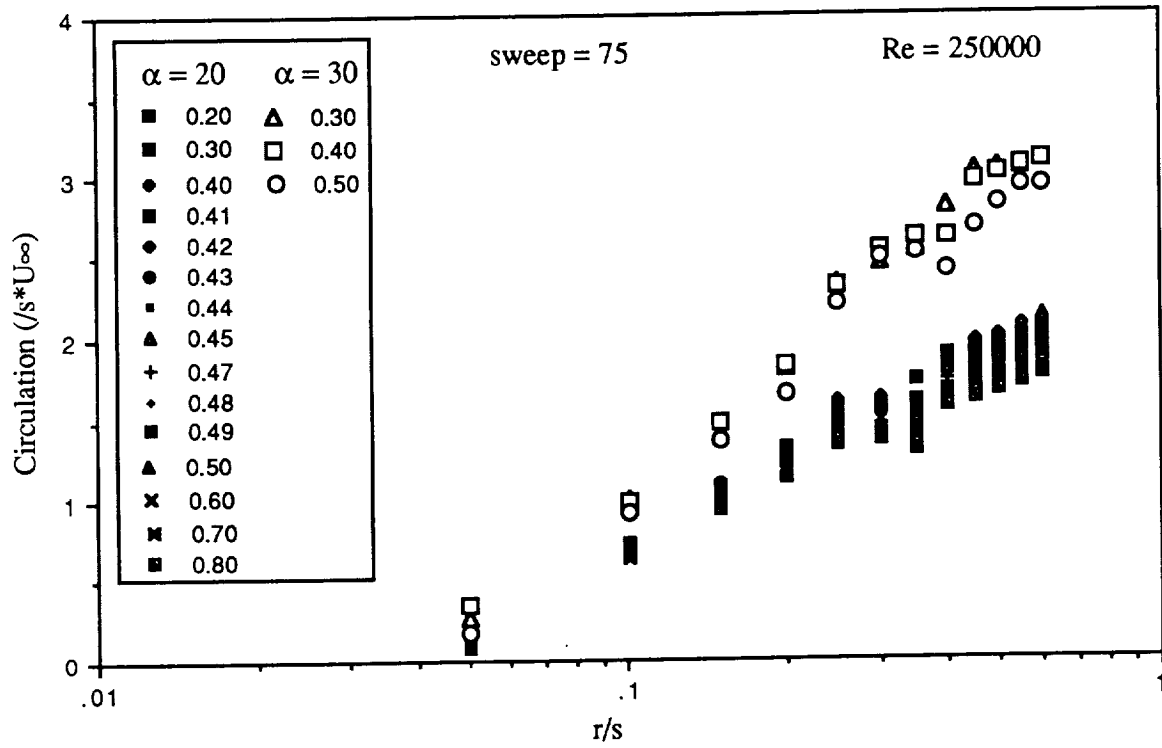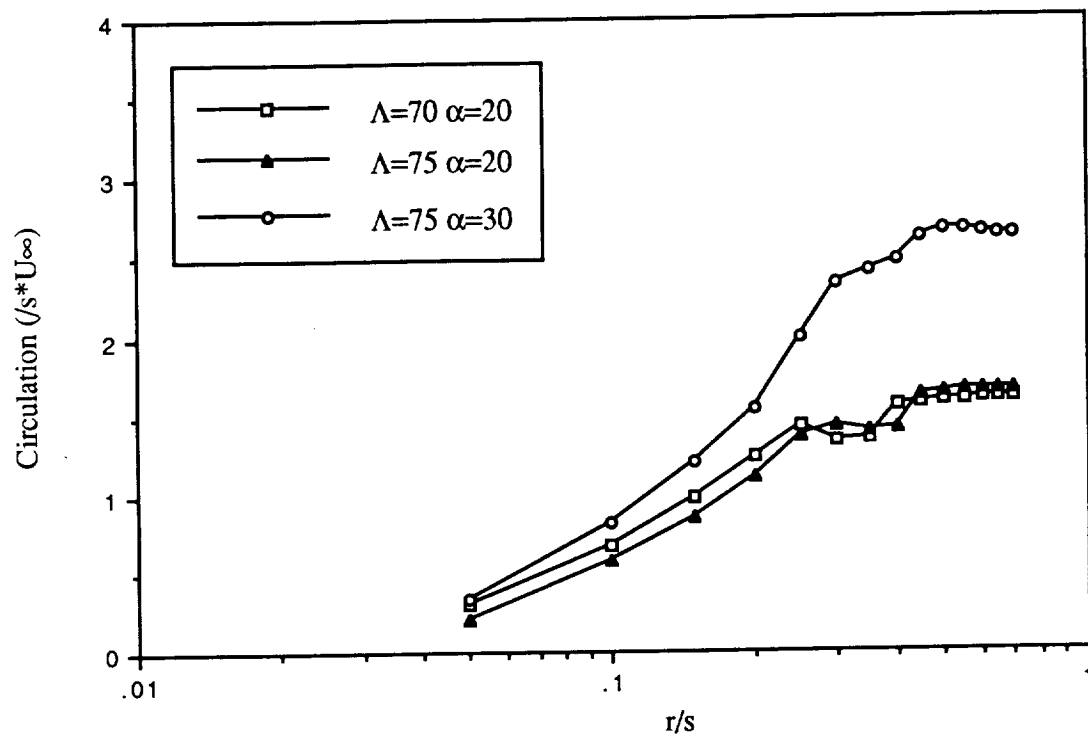
Figure 5.33 Dependence of Circulation on Logarithmic Radial Position a) Present Tests b) SHP data

This suggests a constant slope which is not apparent in the present cross wire data. Figure 5.33a indicates the slope for the planform at $\alpha = 30°$ to be greater than at $\alpha = 20°$. The slope of the curves follows a fit of $2\sin(\alpha)/\sin(\Lambda)$ which would lead to a circulation relation of the form

$$\frac{\Gamma}{\Gamma(a)} = \frac{2}{\Gamma(a)}\frac{\sin(\alpha)}{\sin(\Lambda)}\ln\left(\frac{r}{a}\right) + 1 \qquad (5.8)$$

Interestingly, a consistent logarithmic behavior is not evident from the SHP data as shown in Figure 5.33b, the most deviation occurring at the larger radii. The reason for the apparent discrepancy is unknown. Referring back to the linear scale plot in Figure 5.31, it can be seen that the radial increase of circulation shows less curvature than the cross wire profiles, even to the point of being linear with radius.

The previous circulation profiles in Figures 5.29 to 5.31 illustrate the distribution of the circulation in the radial direction. As noted, the profile magnitudes increase with radial distance to approximately $r/s = 0.25$, representing the extent of the primary vortex. A further increase in magnitude with increasing radius corresponds to contributions from the shear layer at the leading edge. The maximum value of the circulation, scaled by the chord, is plotted for the $\Lambda = 75°$, $\alpha = 20°$ planform at each chord station in Figure 5.34a to examine the axial variation of the vortex strength. Although there is some scatter in the data, a linear trend corresponding to the maximum radius of integration, $r/s = 0.6$ is to be seen . This may be attributable to the location of the lower boundary of the integration path, that being the upper surface of the wing for r/s distances greater than the z/s location of the vortex axis. The exact proximity of the probe to the wing surface will result in measurements of the spanwise velocity components that could vary in intensity. This would reduce the magnitude of the circulation in a different manner at each x/c station, leading to a the variation in the maximum values.
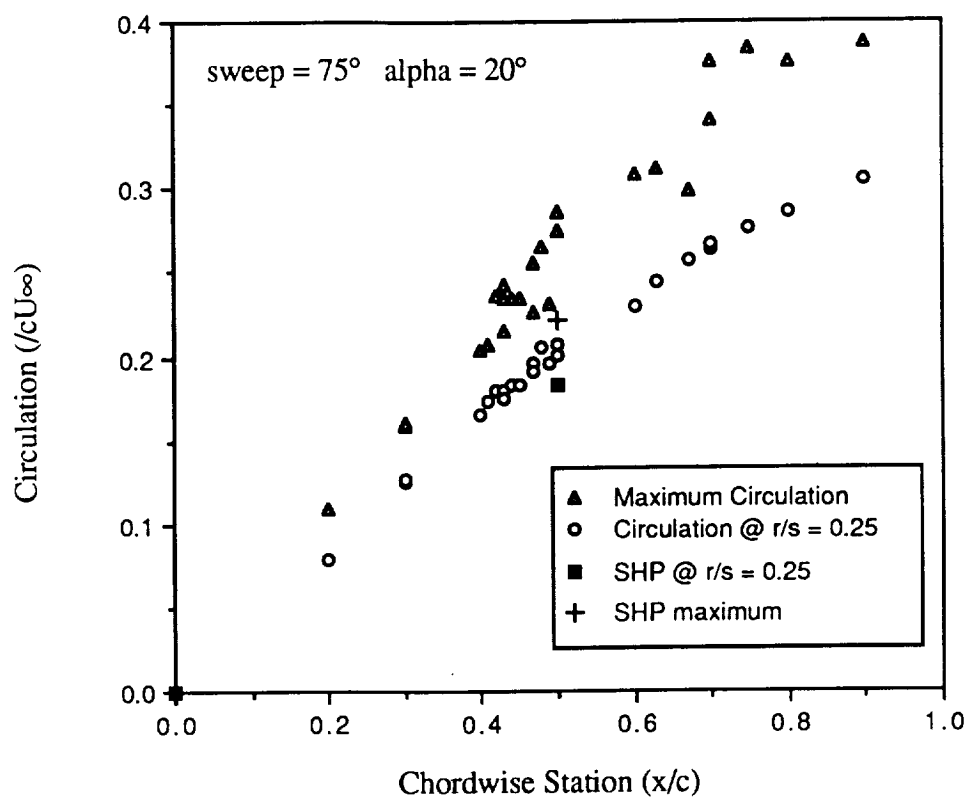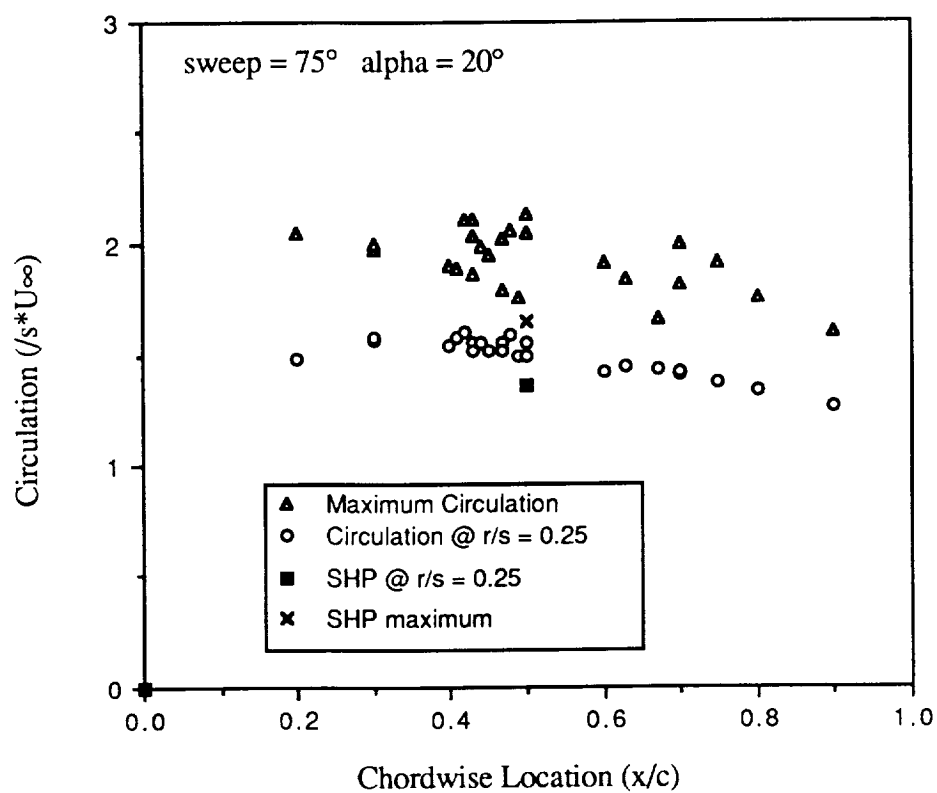
Figure 5.34 Chordwise Variation of Circulation Scaled by a) Chord b) Local Semispan

A better representation of the behavior of the vortex is obtained if the circulation values at the radial location where the profile initially levels off are plotted. The values for this radial distance of r/s = 0.25 are also plotted in Figure 5.34a. A much smaller scatter is present in the data. The values tend to follow a near linear distribution, except near the aft of the wing surface, whereupon a leveling off is observed. This further supports the arguments pertaining to the conical behavior of the delta flowfield, since a conical flowfield demonstrates the linear growth of circulation in a chordwise direction, as noted by McCune and Tavares (1988).

Scaling the values in Figure 5.34a by s* instead of the chord produces the distributions of Figure 5.34b. Both the r/s = 0.6 and r/s = 0.25 cases indicate values which are dropping slightly in the axial direction. The SHP data falls below the cross wire for both the r/s = 0.6 and the 0.25 radii. This may be due to the resolution increase of the cross wire data.

The data from the other wing configurations is presented in Figure 5.35a, along with that of Figure 5.34a, for r/s = 0.25 . The increase in vortex strength due to angle of attack is clear for the 75° sweep case, as one would expect. The $\Lambda = 70°$, $\alpha = 20°$ planform also generates a larger magnitude in circulation than that of the 75° sweep wing for the same angle of attack. Hence, as is already well documented in the literature, increasing the angle of attack for a given wing geometry, or decreasing the sweep angle for a planform at a given angle of incidence causes breakdown to occur closer to the apex. Both of these results therefore support the argument that, all things being equal, a stronger vortex will breakdown earlier, that is closer to the apex. One can surmise from this that there must be a limit to the strength, or amount of vorticity, beyond which the vortex can not sustain the pre-breakdown state.

An interesting observation is made, however, of the data if s* is again used as the scaling parameter in Figure 5.35b. The data for $\Lambda = 70°$ is seen to come much closer to, or even below, that of $\Lambda = 75°$ for $\alpha = 20°$.This would imply that there is a similar, or slightly lower, total
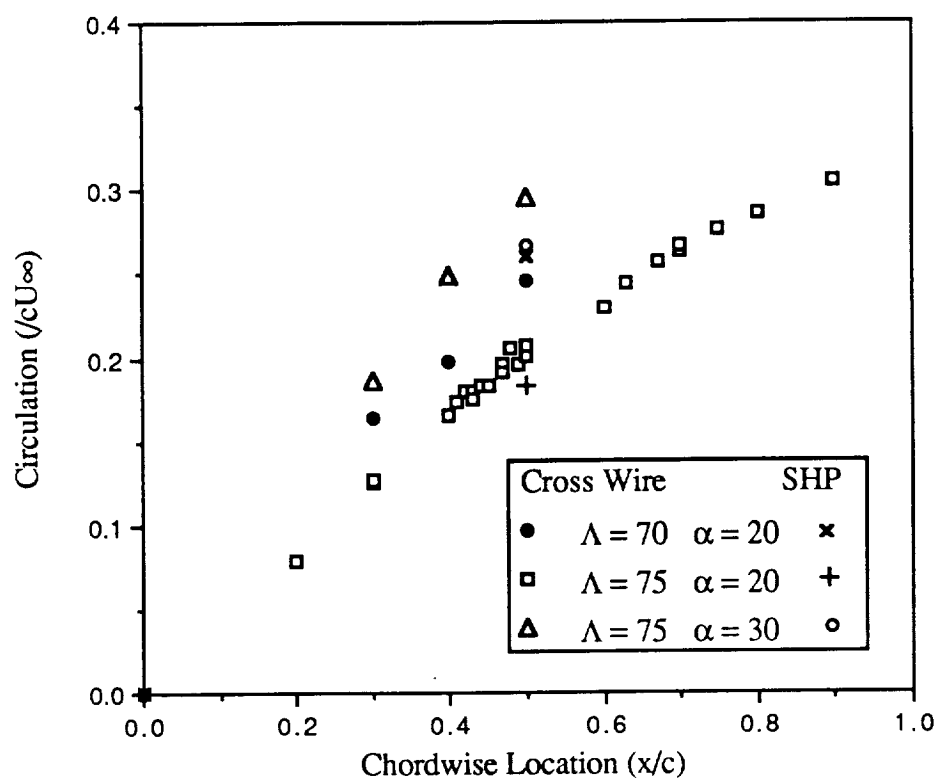
a)
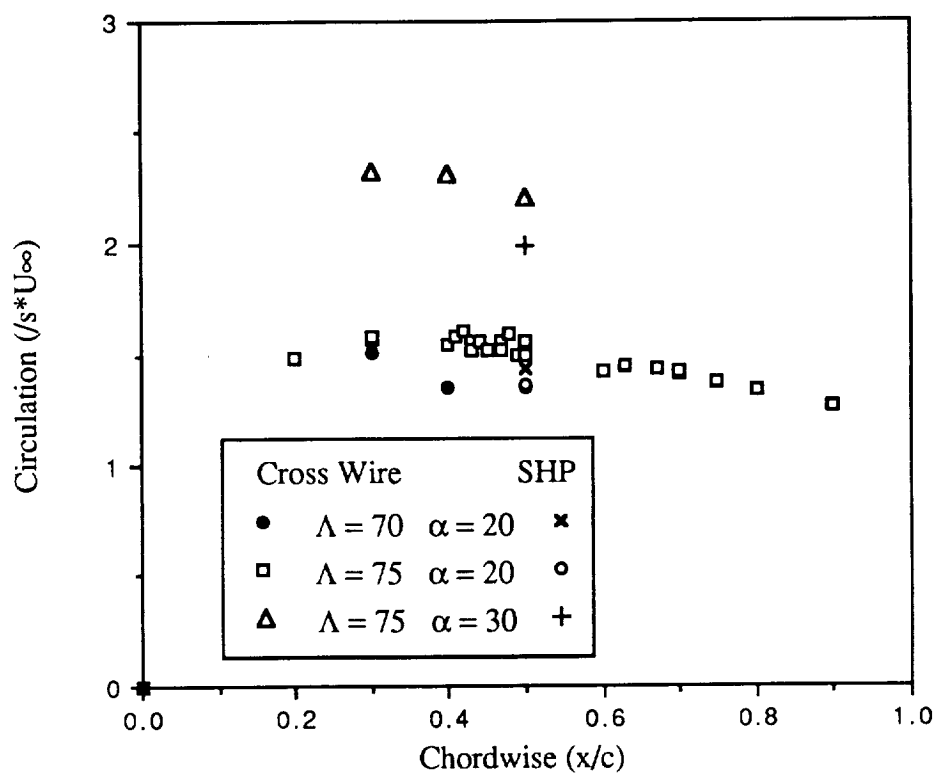
b)

Figure 5.35 Chordwise Dependence on Circulation at r/s = 0.25 Scaled
by a)Chord b) Local Semispan

amount of distributed vorticity over the 70° wing per unit span at any chordwise station than the 75° wing, despite the larger absolute values. Since breakdown occurs on the 70° sweep wing at about the $x/c = 0.5$ chord station and the $\Lambda = 75°$ for $\alpha = 20°$ planform does experience breakdown at all, it could be construed that knowing the local strength of the vortex is not enough to quantify the vortex state with regards to breakdown at any given chordwise station.

To further illustrate the chordwise behavior of the circulation, consider the SHP data obtained by Payne (1987) above a $\Lambda = 85°$ for $\alpha = 40°$ planform at several stations directly in the breakdown region. Derived circulation values at $r/s = 0.25$ and 0.7 are presented in Figure 5.36. The circulation values are seen to fall through the breakdown region. Since the measured circulation is directly related to the axial vorticity component, either the axial vorticity has been redistributed or it has become less. Both reasons are correct possibilities. Brown and Lopez
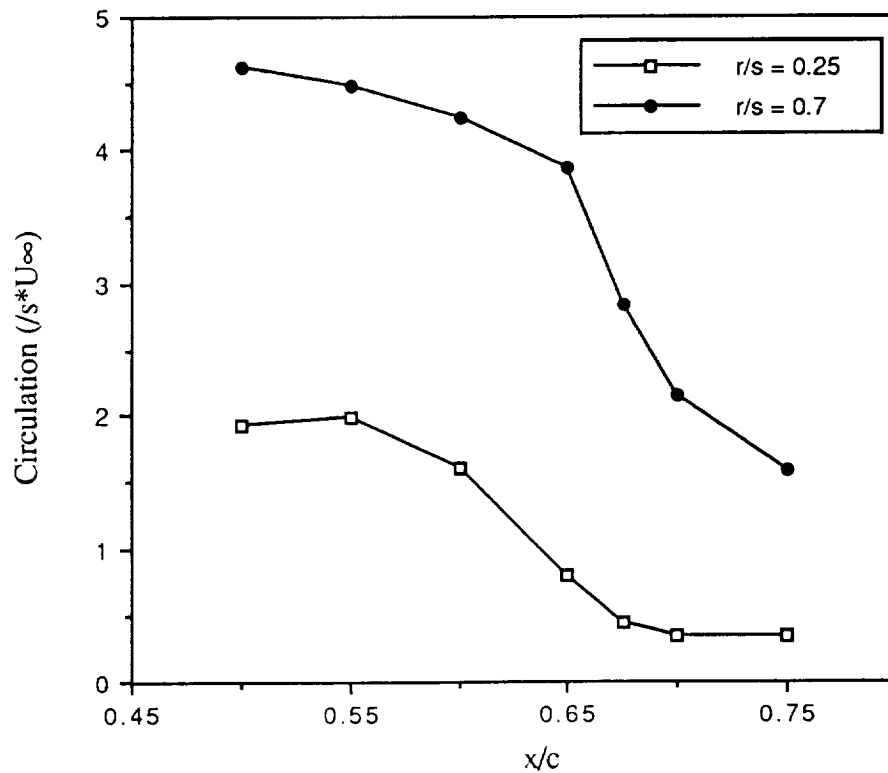
Figure 5.36 Chordwise Dependence of SHP Derived Circulation for $\Lambda = 85°$ and $\alpha = 40°$

(1988) postulated that the predominantly axial vorticity vector rotates at breakdown, away from the axial direction to a predominantly tangential direction. This would explain the drop in the values of calculated circulation. Alternatively, the expansion of the core causes the vorticity to be spread over a larger area and the integration path would therefore result in lower circulation values. The total circulation would continue to rise, however, as distance increased from the apex, since vorticity is still being added to the vortex structure though the shear layer.

Hence, it can be concluded that at breakdown the expansion of the core must be accompanied by an redistribution of circulation over the entire vortex, possibly in a combination of expansion and turning of the vorticity vector. This supports a hypothesis that it is not just the total amount of circulation present which determines whether the vortex breaks down or not. It is the concentration of that circulation which gives rise to the breakdown. Just as vorticity is integrated over the area it acts to give a value of the circulation, the circulation can be multiplied over the area it encompasses to give an indication of the density of the circulation. This would also serve to explain the nature of the circulation values discussed with respect to Figure 5.35b above.

The range of angles of incidence and sweep angles investigated by Payne allows the dependence of circulation on these variables to be examined. The derived values are presented in Figure 5.37. All the circulation values correspond to a chordwise location of x/c = 0.5. The circulation at every configuration grows in a linear manner with angle of attack. As the breakdown moves ahead of the x/c = 0.5 station for the higher angles of attack, the circulation values drop, in the same manner as was pointed out in Figure 5.36. This again seems to support the Brown and Lopez (1988) argument the the longitudinal, or axial vorticity component loses some intensity to the tangential direction. For the three lowest sweeps the circulation is also seen to decrease in some constant fashion with an increase in sweep. This becomes more evident in Figure 5.37b when the data is scaled by the local span.
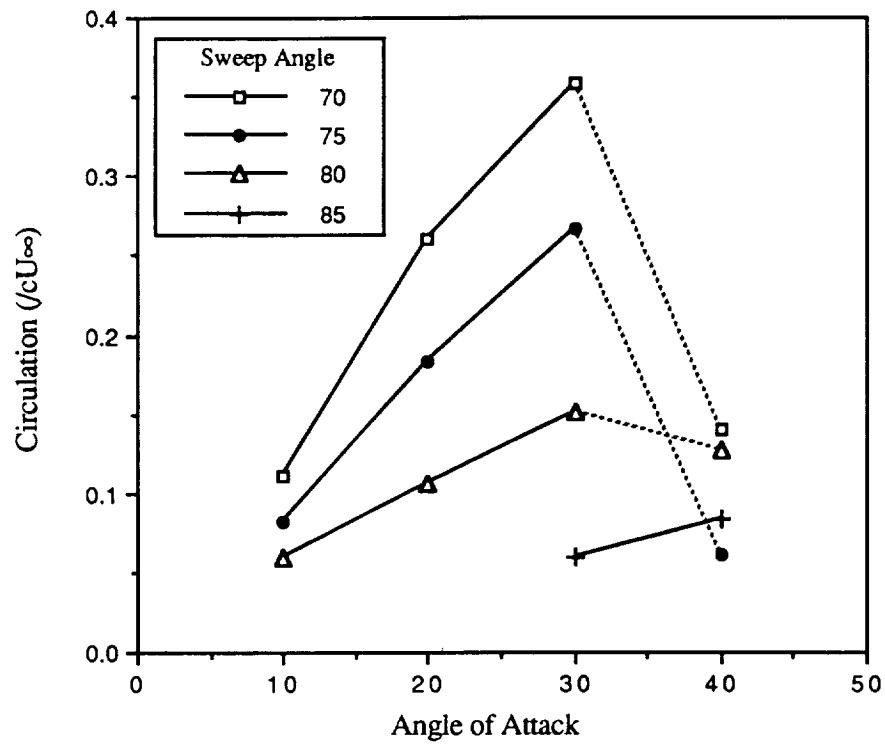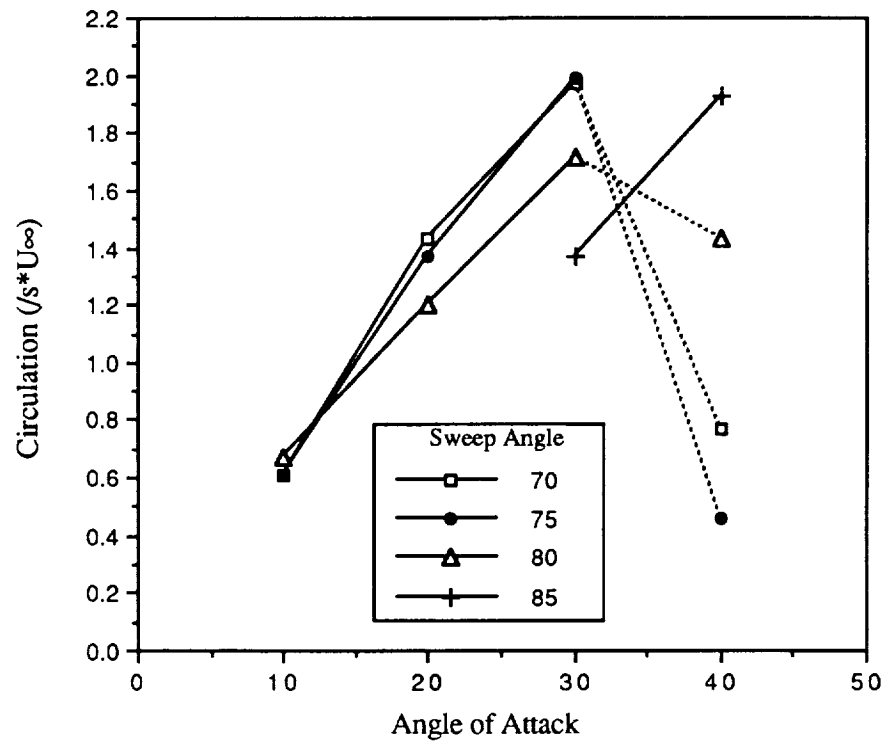
Figure 5.37 Dependence of Circulation on Sweep and Angle of Attack
a) Scaled by chord b) Scaled by local semispan

The behavior of the circulation, as examined in the preceding discussion, supports the axial vorticity and velocity distributions trends in indicating that a near conical flowfield exists for the the majority of the pre-breakdown leading edge vortex. The flow scales with the local geometry, and to a lesser extent with the sine of the angle of incidence. The radial circulation profiles for the present tests exhibit a logarithmic dependence on radius. The strength of the vortex increases in a linear manner with distance from the apex and with angle of attack for a fixed chord location. This increase in strength is inevitably followed by breakdown which reduces the value of circulation in the v-w plane, or axial vorticity density, about the vortex axis. Breakdown cannot eliminate the circulation present and thus the onset of breakdown cannot be solely attributable to the total vortex strength in absolute terms, for the total circulation of the vortex is still increasing with x/c, even after breakdown . Instead it is believed that the local circulation taken about the core region plays a most significant role in the onset of breakdown. There is a sharp decrease in this value after breakdown, presumably in a non-reversible manner for the flow never transitions to the pre-breakdown state. The local strength of the vortex is not believed to be the sole initiator of breakdown. The circulation is determined only from the velocity flowfield and no indication is given about the pressure forces present. No account is taken of the the axial flow component.. To this end, the investigation turned to the correlation of the flow properties from a parameter perspective. The most widely used of these is the swirl angle.

5.2.4 Swirl Angles and Other Correlation Parameters

The swirl angle defined as the inverse tangent of the tangential velocity component to the axial component. The magnitude of this angle reaches a maximum of approximately 42° to 50° in the flow directly preceding breakdown. Values computed from the current tests based on traversals through the vortex core are plotted in Figure 5.38 alongside of those derived from the
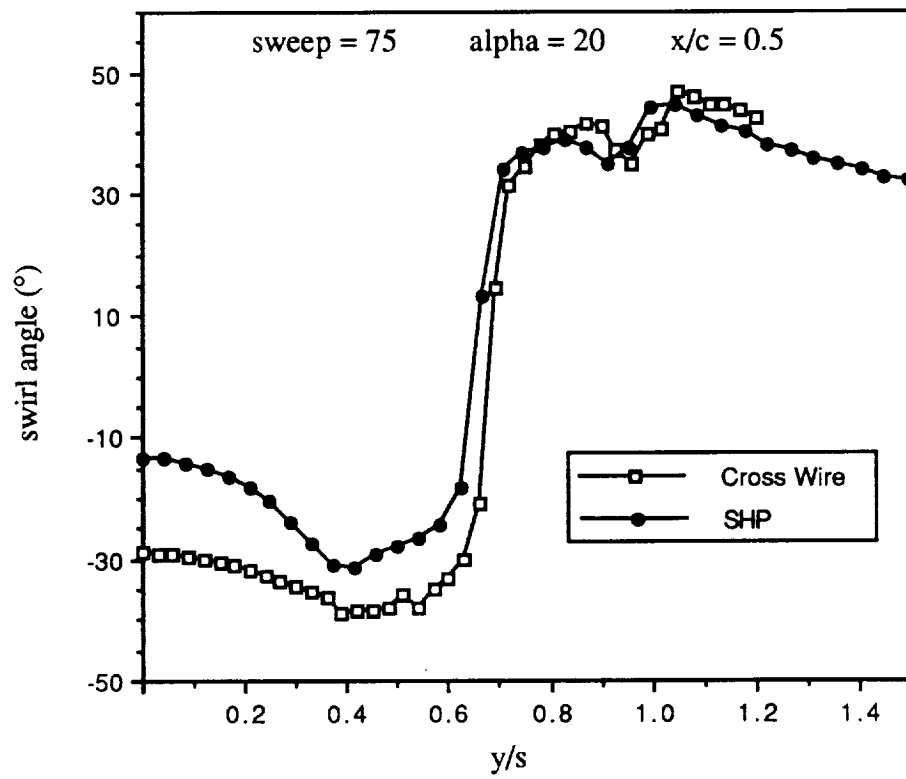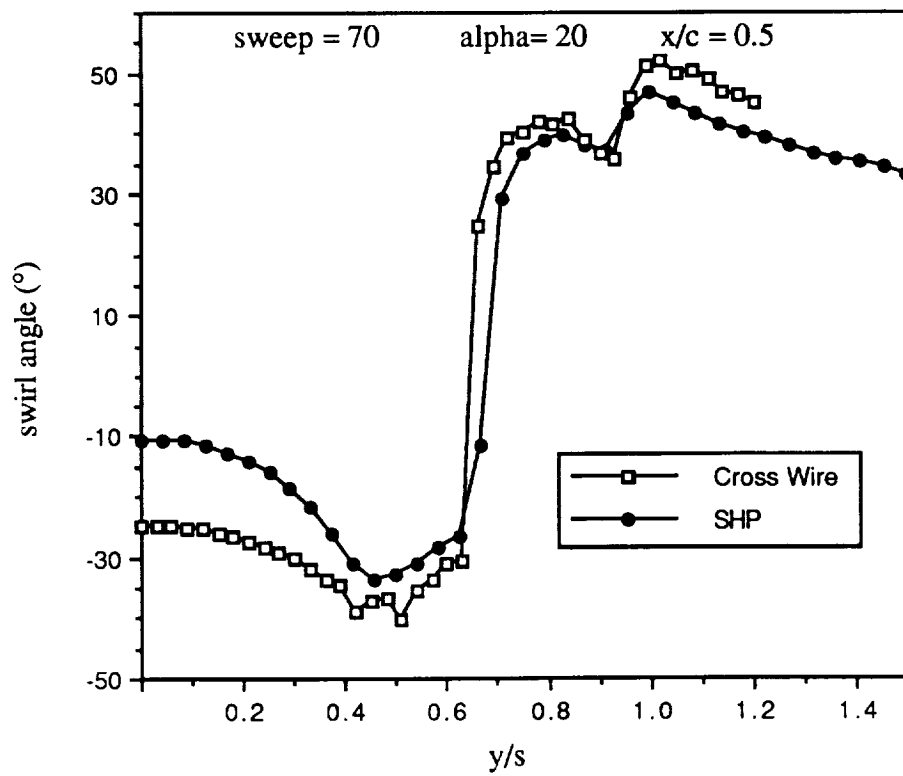
Figure 5.38 Vortex Core Swirl Angles a) sweep = 75° alpha = 20° b) sweep = 70° alpha = 20°

SHP data. The cross wire data gave larger swirl angle values by about 5° both inboard and outboard of the vortex core when compared with the SHP data. Even larger angles were recorded outboard of the leading edge, reaching as high as 52° in the 70° sweep shear layer. The reason for these discrepancies lie in the measurement of the axial component as noted in Figure 5.10. The SHP data gave velocities which were larger in magnitude, resulting in lower swirl angle values than the cross wire data.

The change in the swirl angle with distance from the apex is displayed for all three of the present test planforms in Figure 5.39. The maximum values are seen to change little for each wing. The 20° angle of attack cases in Figures 5.39a and 5.39b are observed to maintain swirl angles of about 40° despite the difference in sweep. The increase in attack angle to 30° in Figure 5.39c increased the maximum swirl by another 10°. This change indicates that the swirl angle is sensitive to the flow, for at x/c of 0.5 the 75° sweep wing at $\alpha = 30°$ is much closer to breaking down than at $\alpha = 20°$. Yet the 70° sweep wing is also closer to breaking down and gives no indication of a larger swirl angle. Since swirl angle is only a measure the ratio of rotational velocity to the axial convective velocity, it does not account for any local shearing in the fluid. The swirl angle gives an indication of the direction of the flow and of how it is being turned locally, but does not indicate whether there is a change in the local fluid rotational rate.

A more physically descriptive parameter can be determined using the both local vorticity and velocity vectors. Brown and Lopez (1988) use the ratio of these two vectors in their study as an precursor to breakdown. Since only the axial vorticity component is available in the present study, the swirl parameter derivation outlined in Chapter 2 from the tornado studies, which is an indication of the convection of vorticity, is examined here. The parameter is simply the ratio of the local axial vorticity to the local axial velocity as defined by
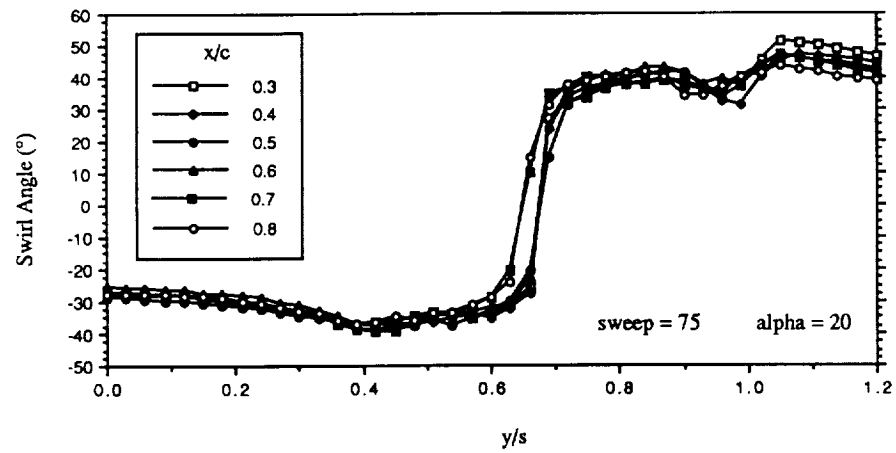
a)
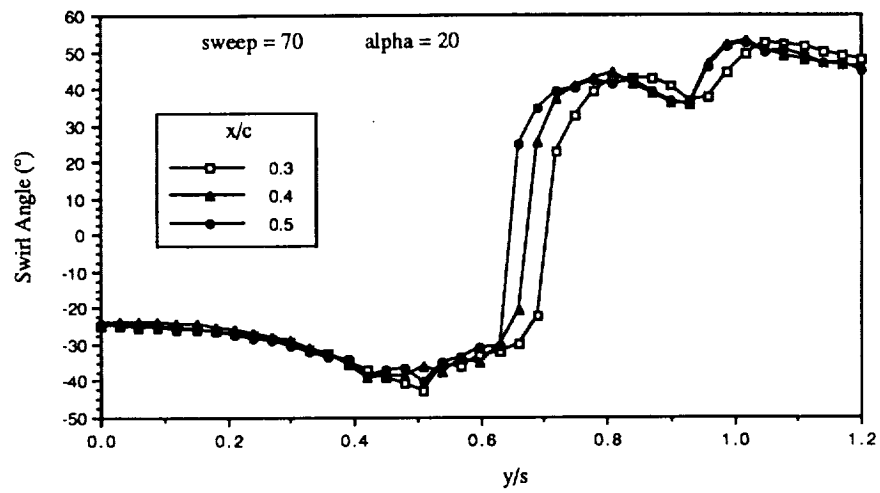
b)
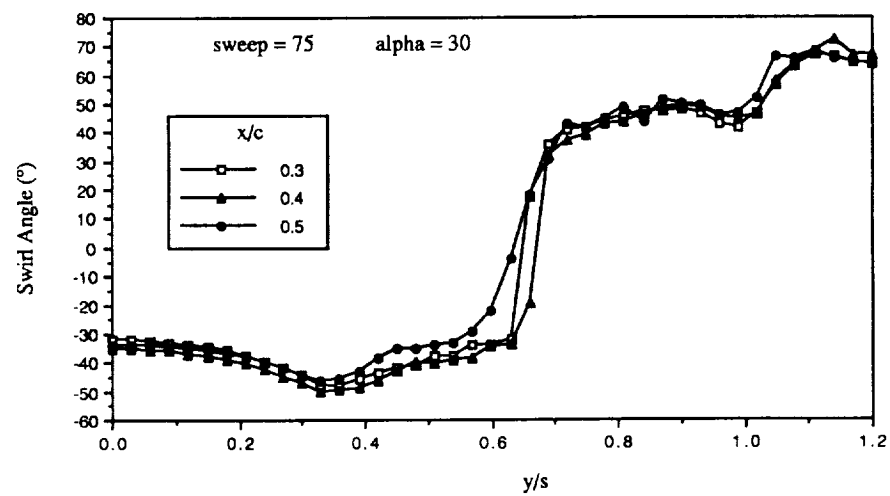
c)

Figure 5.39 Chordwise Variation in Vorex Core Swirl Angle a) sweep = 75 alpha = 20
b) sweep = 70 alpha = 20 c) sweep = 75 alpha = 30

$$S = \frac{\Omega_X \, s^*}{V_X} \qquad (5.9)$$

Computed fields for the 75° sweep wing at α =20° and x/c = 0.4 and 0.7 are given in Figure 5.40. Both stations show comparable values and area of concentration. Three areas of intensity are noted: the core of the primary vortex, the secondary vortex and the shear layer. The vortex core reveals large magnitudes of this swirl parameter, despite being scaled by the locally large axial velocities, because the majority of the positive vorticity is concentrated there. The secondary vortex region also indicates a local concentration of this parameter, albeit in the negative sense. Both the secondary vortex and the shear layer region are areas where the axial velocity component is less than freestream and this serves to increase the local convection parameter. The maximum and minimum values at each station are directly comparable.

The SHP data for this wing is presented in Figure 5.41a. Although there is a qualitative comparison in terms of the associated regions of intensity, the maximum and minimum values are lower by as much as 40% and 30% respectively. The grid resolution is again believed to be the primary cause of this. The areas do seem to be of a comparable size, however, indicating a comparison may be possible in terms of integrated values. The SHP data at α = 30° is also included as Figure 5.41b. The maximum and minimum values are slightly higher in magnitude. It also appears that the region of the negative convection values, bounded by the zero contour line has increased in size, relative to the α = 20° case.

The maximum and minimum convection parameter values for the present tests are plotted in Figure 5.42. If the chord is used as the length scale, the values follow a behavior similar to the vorticity values in Figure 5.23. The positive and negative magnitudes are decreasing with distance from the apex. It could be argued, however, that the presence of the probe in the

a)

b)
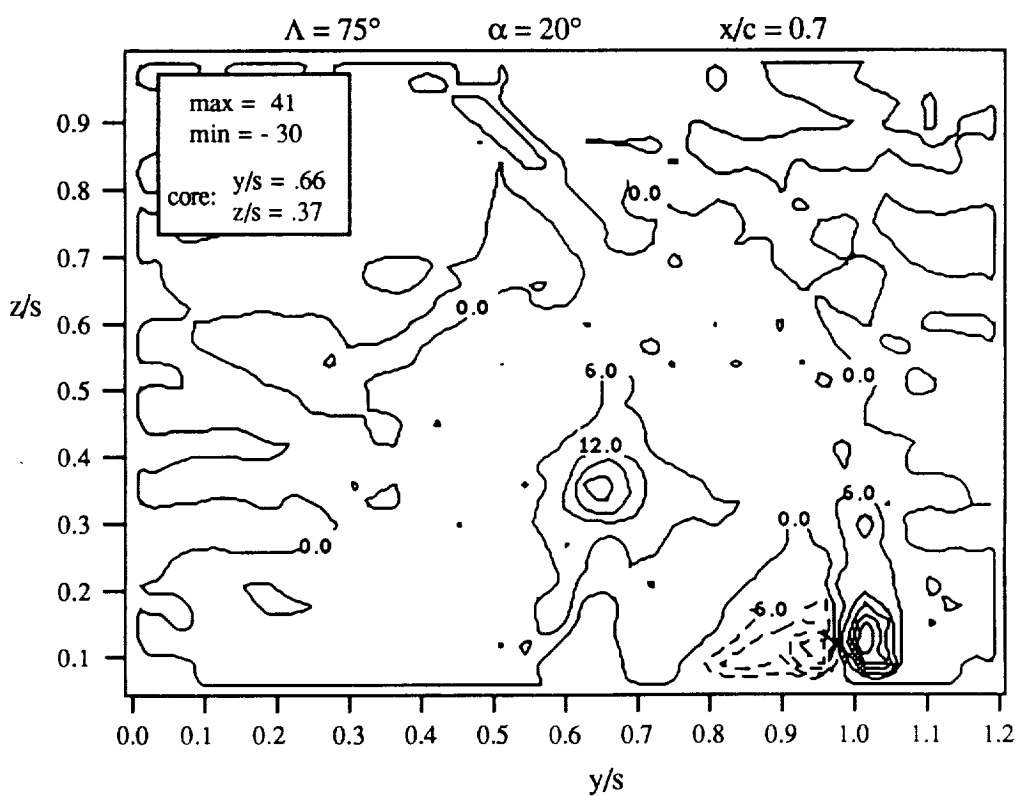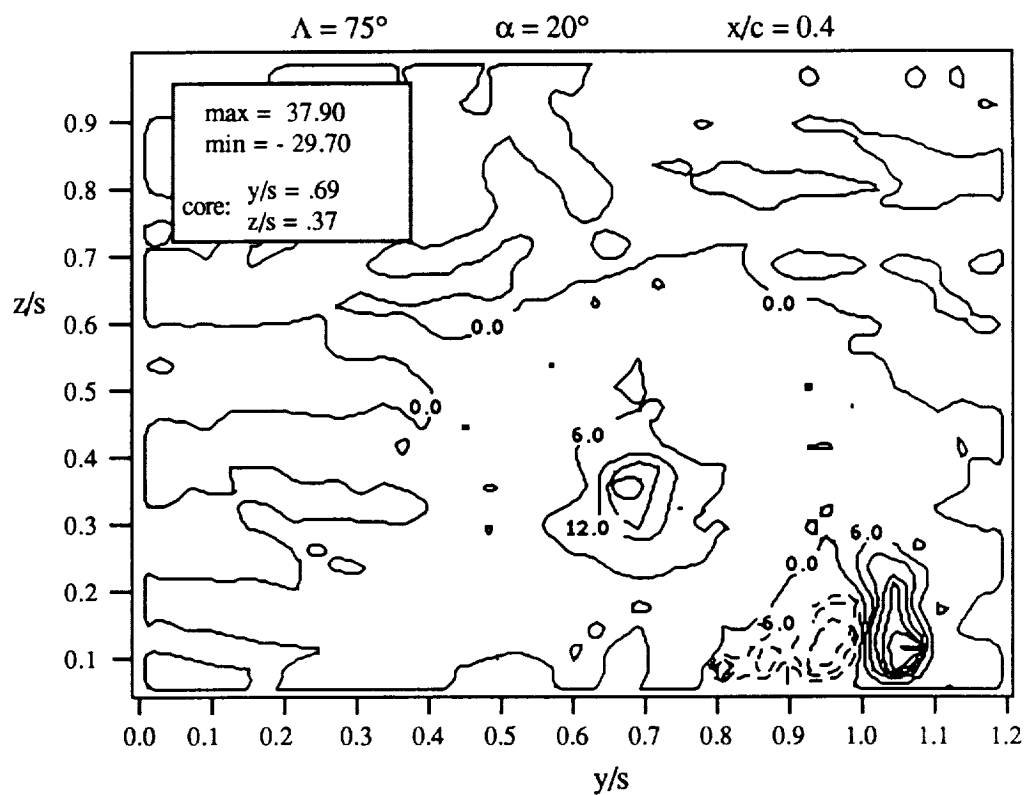
Figure 5.40 Convection Parameter at Λ=75 α=20 a) x/c = 0.4 b) x/c = 0.7

smaller vortex structure near the apex, while not causing breakdown, may serve to locally accelerate the flow artificially and measure erroneous gradients. This could result in larger vorticity values. The $\Lambda = 75°$ $\alpha = 20°$ planform data marked with an asterisk indicates data taken at a higher grid resolution. A single asterisk stands for a $y/s = z/s$ increment of 0.015 while two asterisks denote an increment of 0.010. These increased resolution values indicate a similar range of convection values. The finest grid results are up to 100% greater than the nearest larger grid values. This directly results from the observed vorticity values in Figure 5.24.

The convection parameter was integrated over the area of the survey, as was done to the vorticity for comparison with the circulation. When scaled by the chord, Figure 5.43a, the integrated values for the survey plane decrease in a chordwise direction, quite steeply. The relative state at each station, indicated in Figure 5.43b, show a similar distribution at each x/c location. It might be expected that the integrated values would show a relative decrease as breakdown was approached for the $\Lambda = 70°$ $\alpha = 20°$ and the $\Lambda = 75°$ $\alpha = 30°$ configurations near x/c = 0.5. No indication of this is apparent. Seven hole probe data is include for comparison. The values fall below their cross wire counterparts, presumably due to resolution.

As a final approach to the type of convection considerations discussed, a Rossby number was calculated for the above flows to examine its significance, if any. The parameter was defined as

$$R_O = \frac{\text{Average subcore axial velocity}}{\text{Average subcore axial vorticity * radius of the subcore}} \qquad (5.10)$$

Figure 5.44 illustrates the values of this parameter for the present study. The majority of the values fall to either side of $R_O \approx 1$. Repeat tests for the 75° planform at 20° angle of attack and x/c = 0.5 indicate a substantial variation. The proposed nature of this parameter is to decrease as
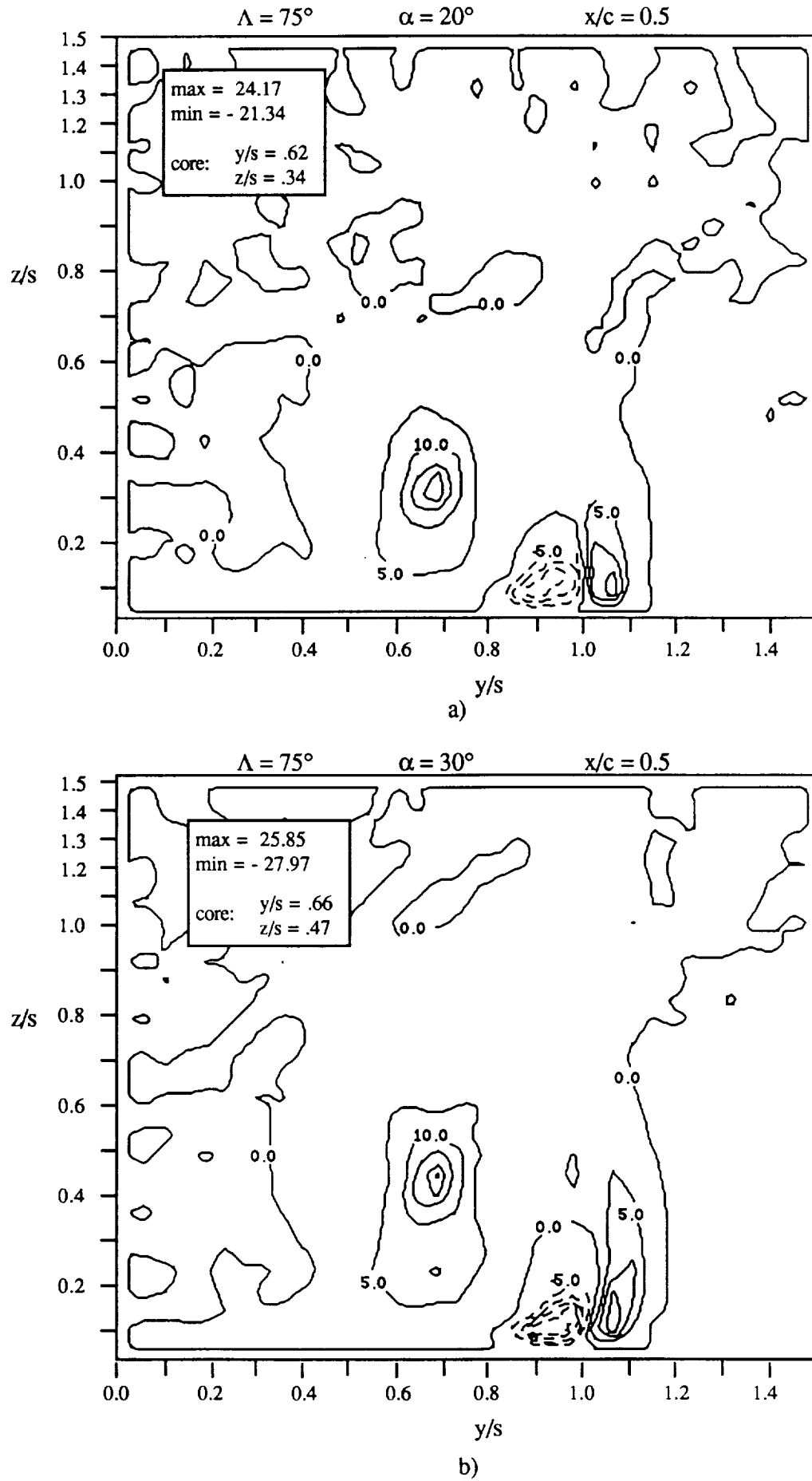
Figure 5.41 SHP Convection Parameter at x/c = 0.5 a) Λ=75 α=20 b) Λ=75 α=30
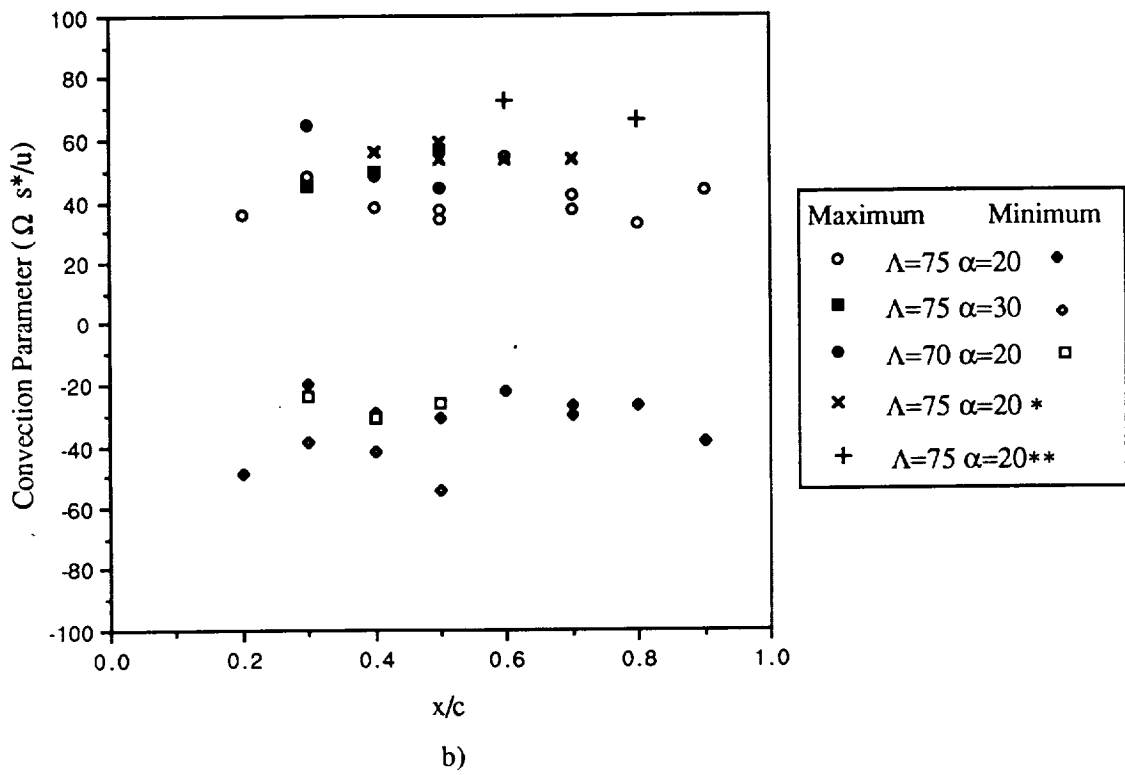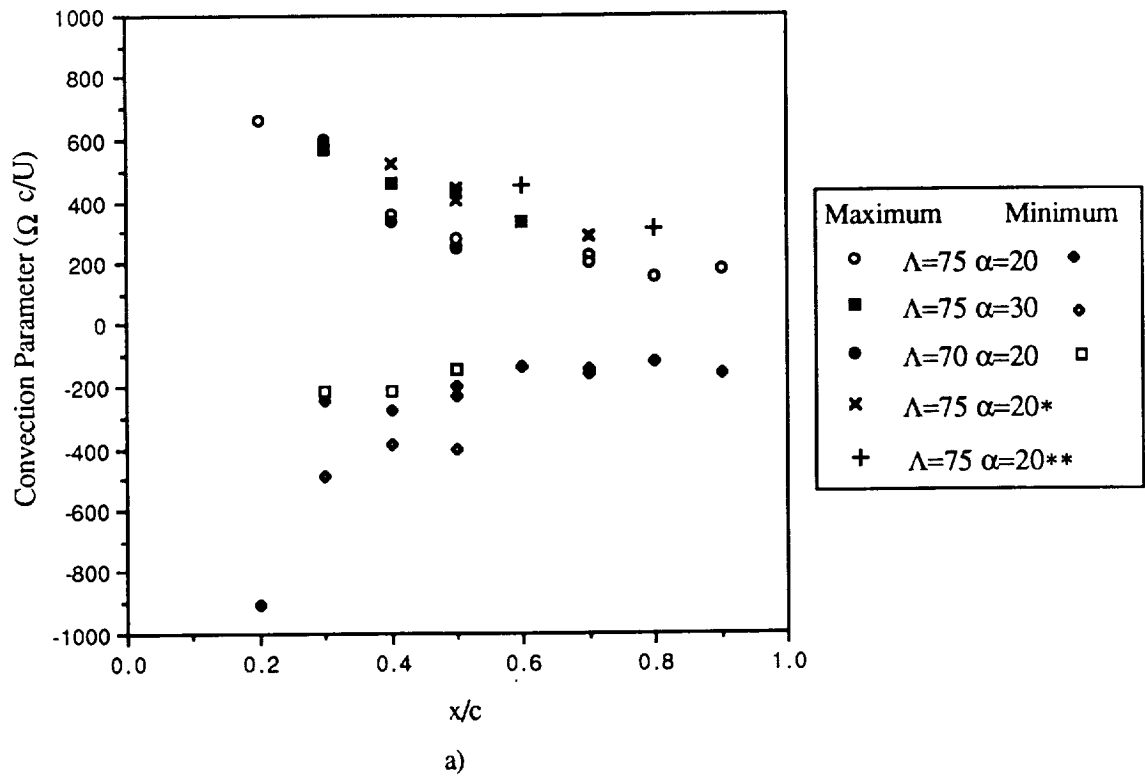
Figure 5.42 Chordwise Dependence of Convection Parameter a) Scaled by Chord b) Scaled by Local Semispan

a)

b)
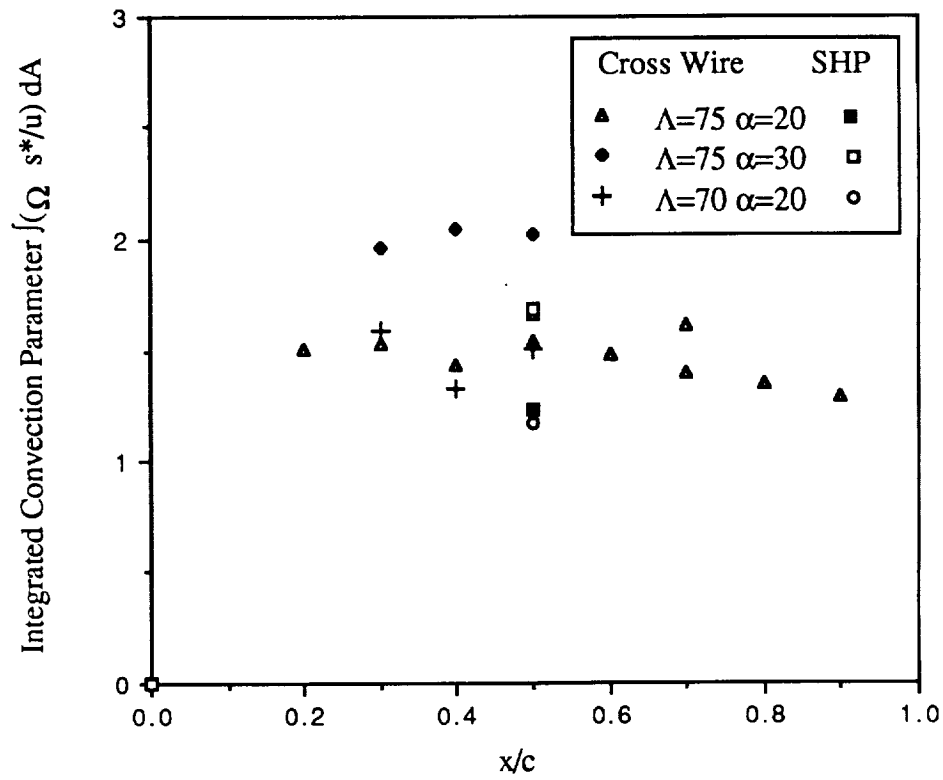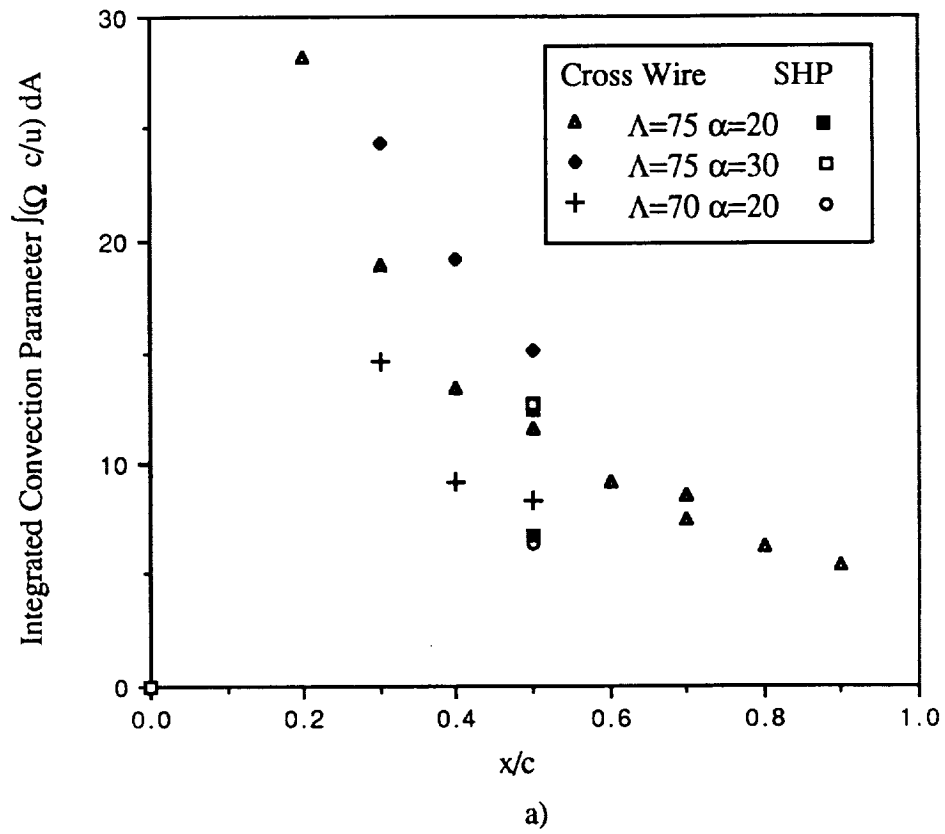
Figure 5.43 Integrated Convection Parameter a) Scaled by Chord b) Scaled by Local Semipan

the breakdown region is encountered. Very slight evidence of this is indicated from the $\Lambda = 75°$ $\alpha = 20°$ or the $\Lambda = 70°$ $\alpha = 30°$ tests. The finer grids, marked with an asterisk, seem to approach a value of 1.1. The SHP data is considerably larger in magnitude, again owing to the lower vorticity values. Overall the results of this parameter evaluation with respect to the onset of breakdown, and that of the convection parameter above, are inconclusive.

The series of parameters evaluated above were based on the local and integrated properties of the flowfield. In a sense, these can be regarded as conditions that result from changes in the planform configuration or external flowfield. It is also possible to set up parameters to incorporate these external conditions, such the sweep angle and angle of attack, along with the
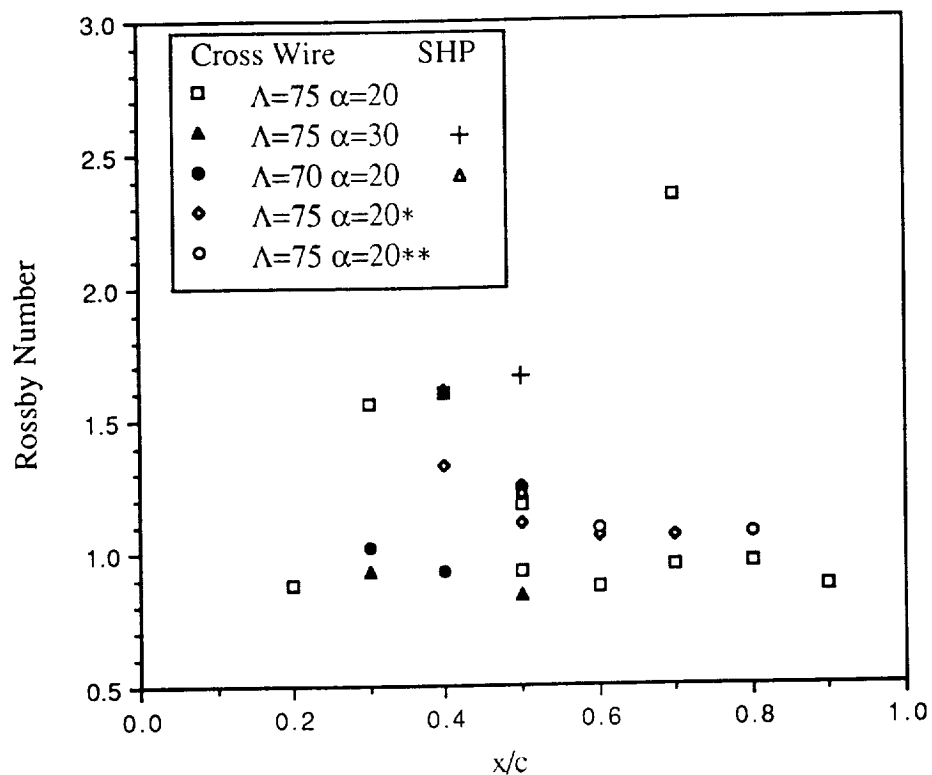
Figure 5.44 Rossby Number Dependence on Chord

measured flowfield properties. This has already been done, to a certain extent, by scaling the field properties by the local semispan and even the sine of the angle of attack. As outlined in

Chapter 1, this line of reasoning was incorporated by Hemsch and Luckring (1990) in their correlation results for the measured vortex circulation. Their derivation, as a function of the Sychev parameter and expressed in terms of the apex half angle ϵ is:

$$g = \frac{\Gamma}{U_\infty\, c\, \tan^2\epsilon\, \cos\alpha} = AK^n \qquad (5.11)$$

where

$$K = \frac{\tan\alpha}{\tan\epsilon} = \frac{1}{k_1}$$

for some value n. Hemsch and Luckring noted that if g and K are plotted in a log-log format, a fit of the form $g = AK^{1.2}$ was seen for data obtained from Wentz and MacMahon (1967), $\Lambda = 62°$ and Delery, Pagan, and Solignac (1987). Values of g an K ranged from 0.5 to 10.0 and 0.2 to 2.0 respectively. Theory by Smith (1971) proposed a relation of the form $g = 4.63K^n$. The g and K parameters were derived from the seven hole probe data of Payne (1987) and plotted in Figure 5.45a with that of Wentz and MacMahon as well as a curve of Smith for n = 1.2. Payne's data represents sweep angles of 70°, 75°, 80°, and 85° at various chord locations. It is seen to extend the line of Smith to a g of 100 and a K of 10.

The data from this investigation, representing three K values, was also plotted in Figure 5.45a, however the expected collapse of data was not immediately evident. Hemsch and Luckring used data that was acquired in the wake of the models. Since the present tests were conducted at locations above the wing surface, a further scaling of g by the local chord ratio, x/c, was found to bring the data into line with that of Smith as shown in Figure 5.45b. The data of Payne was also scaled by x/c and is shown in Figure 5.45b. Thus it would appear that this relation strongly correlates the vortex strength with the angle of attack and the wing geometry.
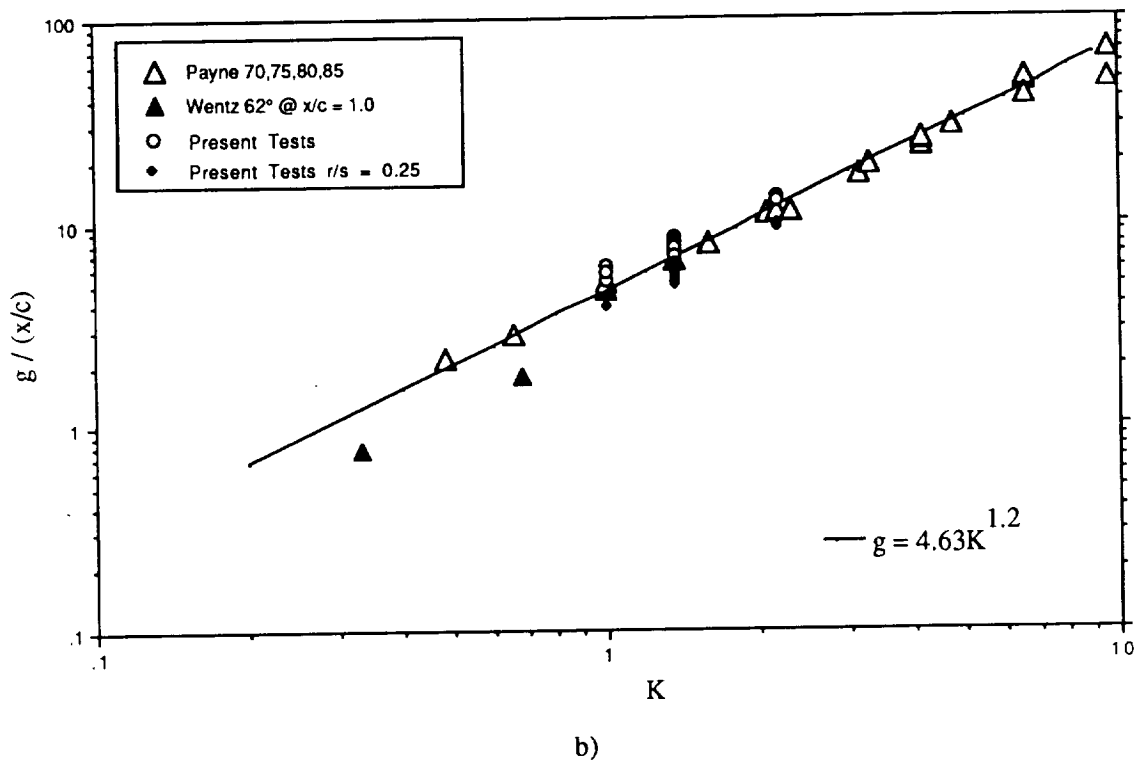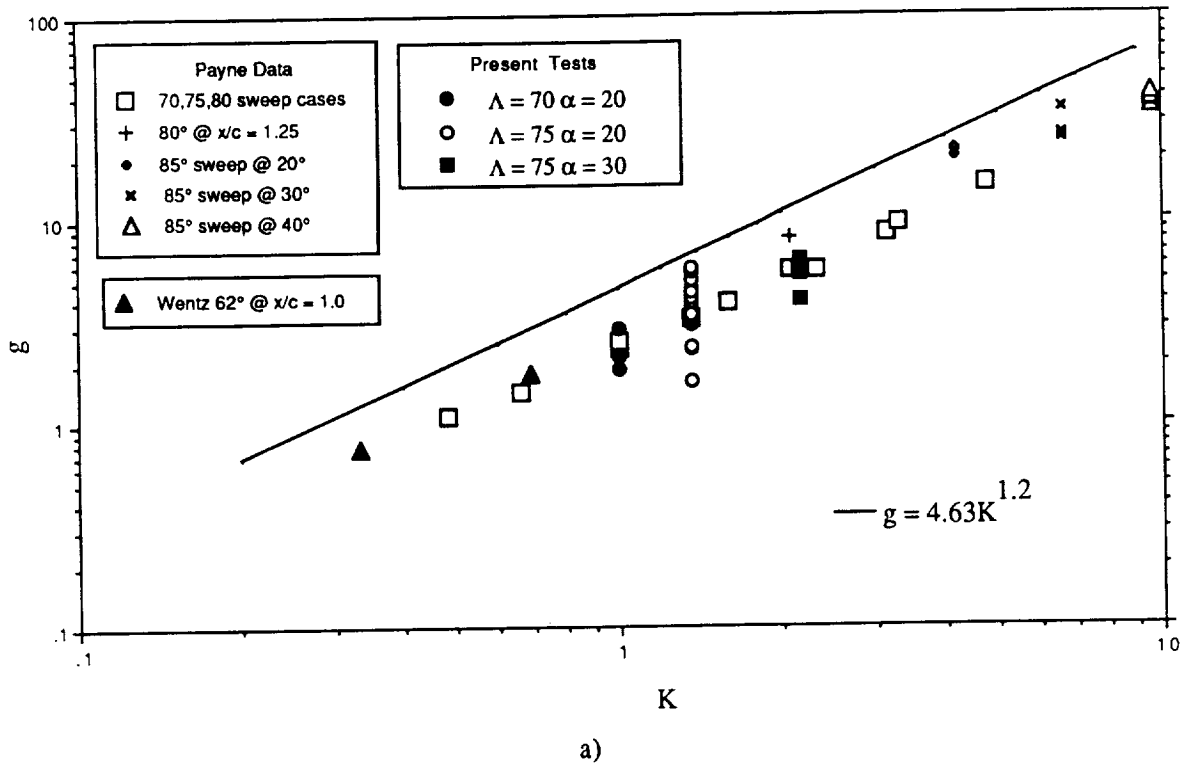
Figure 5.45   Correlation of Hemsch and Luckring a) g vs K, b) g/(x/c) vs K

If the above expression of Hemsch and Luckring is manipulated to include the ratio x/c and expressed it in terms of s*:

$$g = \frac{\Gamma}{U_\infty \; s^* \; \tan\varepsilon \; \cos\alpha} \tag{5.12}$$

If g is further divided through by K, the constant A is expressed as:

$$A = \frac{\Gamma(\tan\varepsilon \; \cos\alpha)^{n-1}}{U_\infty \; s^* \; (\sin\alpha)^n} \qquad \text{or} \qquad A = \frac{\Gamma(\tan\varepsilon \; \cos\alpha)^{0.2}}{U_\infty \; s^*(\sin\alpha)^{1.2}} \qquad \text{for } n = 1.2$$

It is interesting to see how closely this corresponds to the function used in Figure 5.31b. If n is set equal to 1 in the above expression, they would be exactly identical.

The derivation of Hemsch and Luckring correlates the data quite well, however, the expression $g = f(K)$ is such that the independent variables of α and ε appear on both sides of the equation. Physically, the circulation is not inversely proportional to some function of the semi apex angle, but increases as ε increases. Perhaps more representative evaluation of the data can be done by simply plotting the dependent versus the independent variables in the manner:

$$\frac{\Gamma}{U_\infty \; c \; (x/c)} = f(\tan\alpha \tan\varepsilon) = f\left(\frac{\tan\alpha}{\tan\Lambda}\right) = f(K') \tag{5.13}$$

Note that the local chord is now employed instead of the local semispan as done in the previous section, removing the implicit dependence on Λ from the left hand side of the equation. This relation using K' is plotted in Figure 5.46 for a sample of the present data. The data behaves in a linear manner with what appears to be a larger spread in the data than was evident in the correlation of Hemsch and Lucking. If the axis of the plot are changed to accommodate a larger
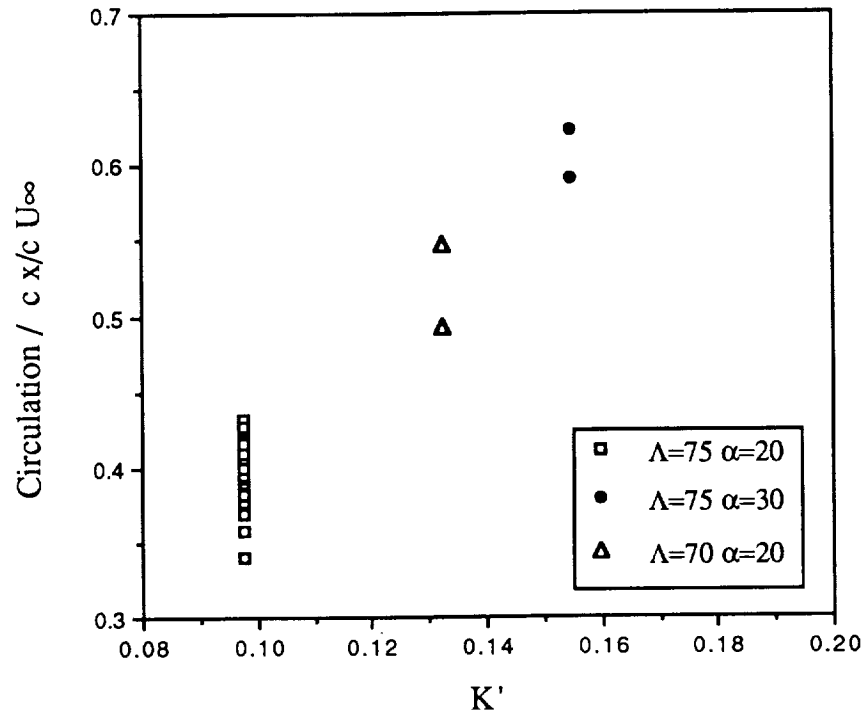
a)
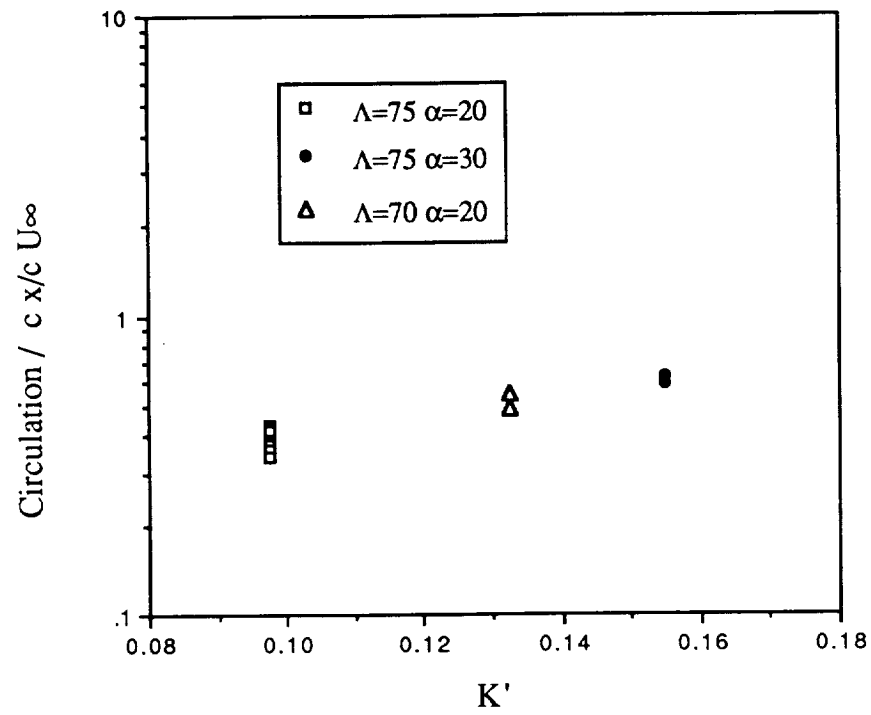
b)

Figure 5.46 Circulation Correlation with K' for r/s = 0.25
a) Linear Scale b) Logarithmic Scale

linear maximum or are replotted in a logarithmic format, as in Figure 5.46b, a trend similar to that in Figure 5.44 can be observed. The linear nature of this parameter is further demonstrated by scaling the circulation by K' and shown in Figure 5.47. The data for the 75° planform at 20° angle of attack indicates a downward trend. If breakdown was imminent, the curve would drop off, as would be expected from the SHP data in Figure 5.36. No indication of this trend is seen for the other two test configurations.

A relation of the form examined by Hemsch and Lucking appears to provide one of the best correlations of the present data and that in the literature over a wide range of test conditions for conditions upstream of the breakdown region. The behavior of the convection parameters correlate the flow upstream of the breakdown as well, but seem to be more sensitive to the nature of the flow than the Hemsch and Lucking relationship, perhaps because of the logarithmic
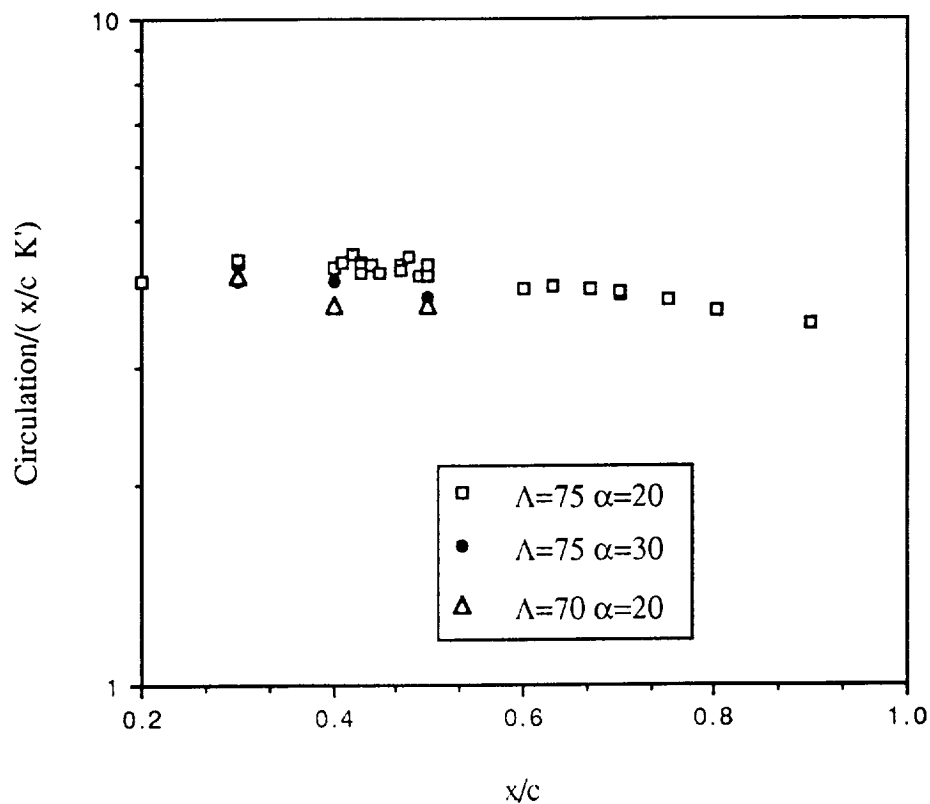
Figure 5.47 Chordwise Dependence of Scaled Circulation Parameter

format. No concrete evidence of an impending breakdown is present in terms of a distinct chordwise change in the convection parameter representation or the Hemsch and Lucking relationship. This would indicate that the breakdown phenomena is very localized spatially and does not transmit substantial time averaged information upstream. Since the change in any type of these time averaged parameters in a streamwise manner is not indicative of breakdown, it appears for the moment that data must be acquired directly in the breakdown region, as was done with the SHP, to directly observe any direct change on any of these relations. It may be that to measure some indication of the onset of breakdown in the upstream flow a time dependent signal correlation will be required.

5.2.5 Core Spectral Behavior

Several chordwise stations on the 75° sweep planform, at 20 and 30 degrees angle of attack, were examined to determine if there was any characteristic frequencies, or possible standing waves, associated with the axial velocity component. A single hot wire was positioned in the core and the voltage signature was analyzed in terms of its frequency content given by a power spectrum distribution. The following spectral data are ensemble averages of twenty spectra as the power spectrum routine was constrained to a maximum of 1024 points. The sampling frequency was 6000 Hz as higher rates indicated no dominant frequencies above the 3000 Hz range.

Before the spectrums are examined, a typical pre-breakdown signal is given in Figure 5.48, followed by a signature of the post breakdown flowfield. The passage of more turbulent flow structures is evident in Figure 5.48b. The resulting power spectrum in Figure 5.49a, however, did not reveal any dominant frequency for the post breakdown signals. The post breakdown spectrum indicates a much greater magnitude of the entire spectrum at the lower frequencies than the x/c = 0.4 pre-breakdown. The x/c = 0.4 spectrum is magnified in Figure 5.49b and reveals a
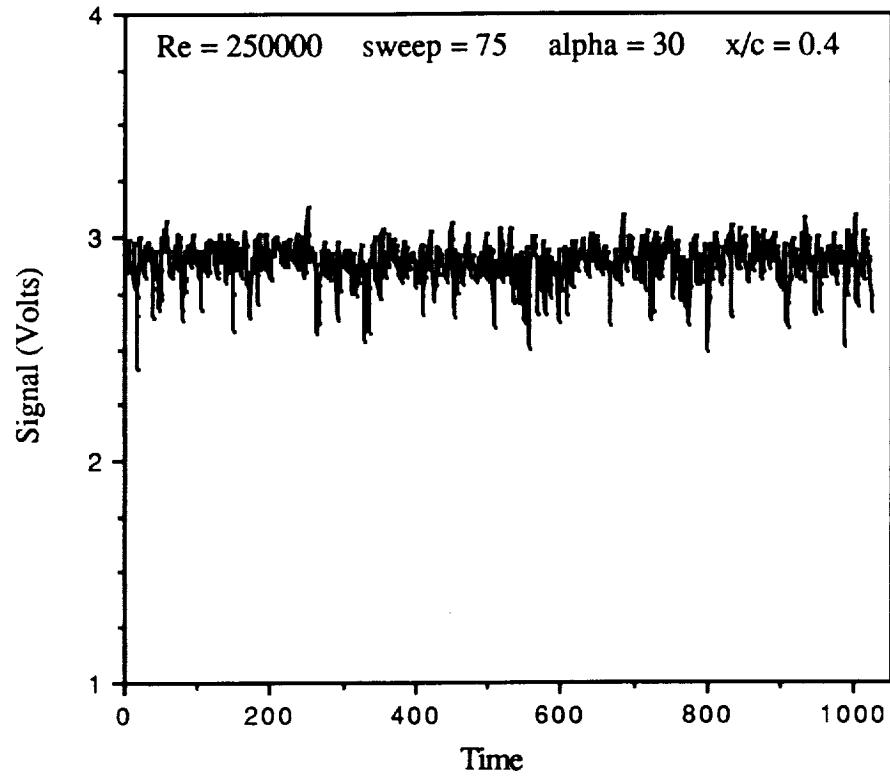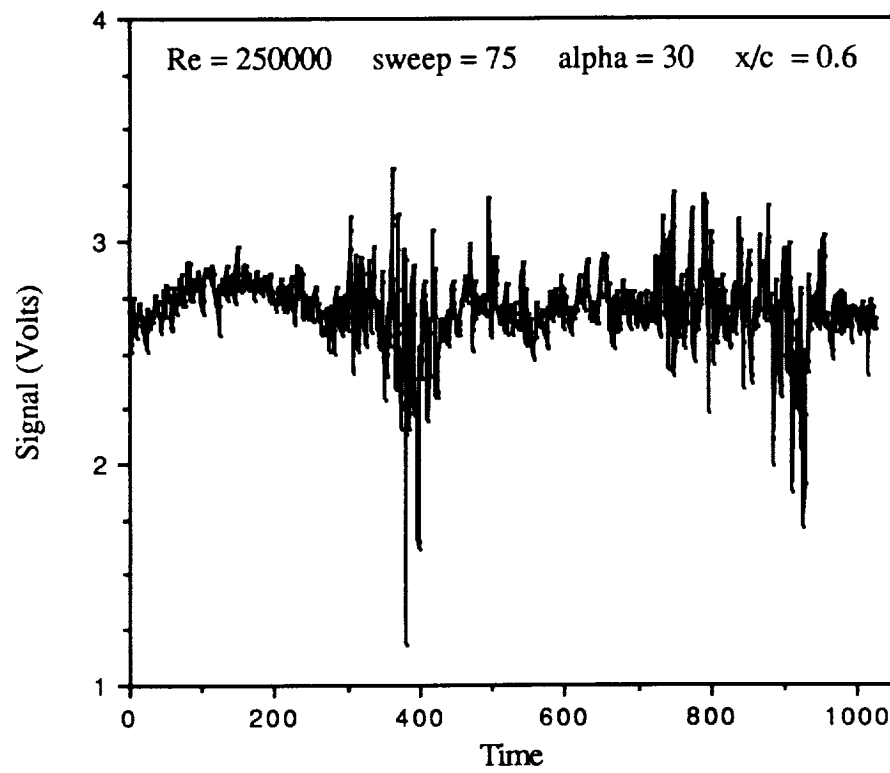
Figure 5.48 Axial Core Voltage Signal a) Pre-breakdown b) Post-breakdown
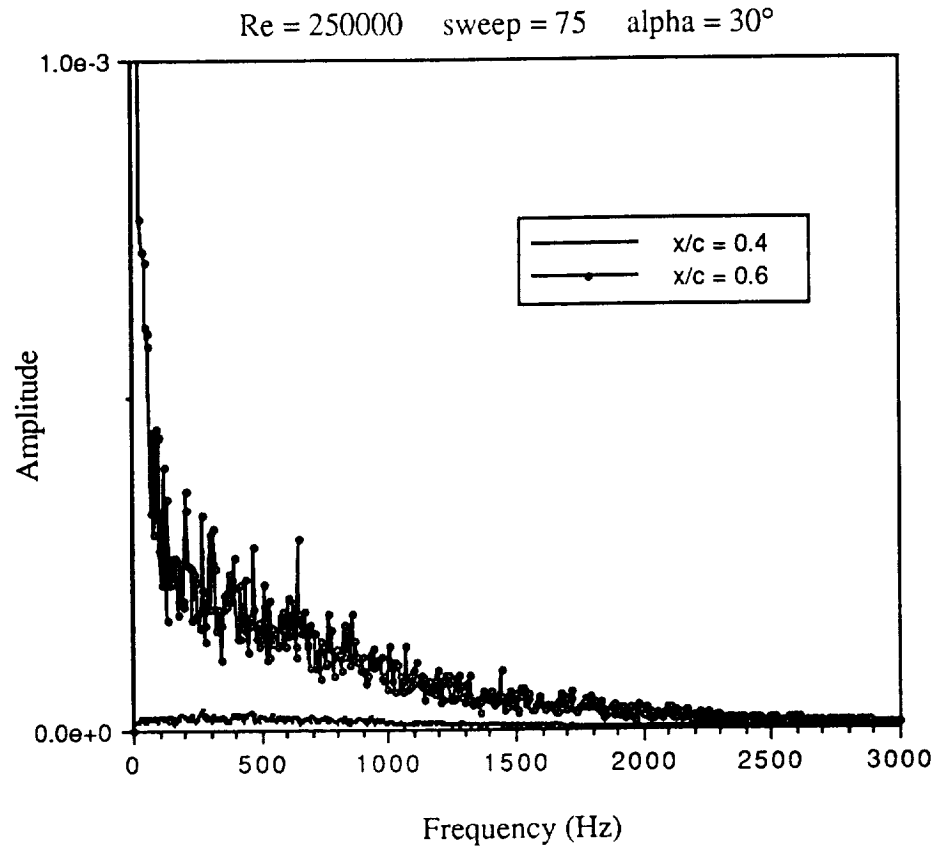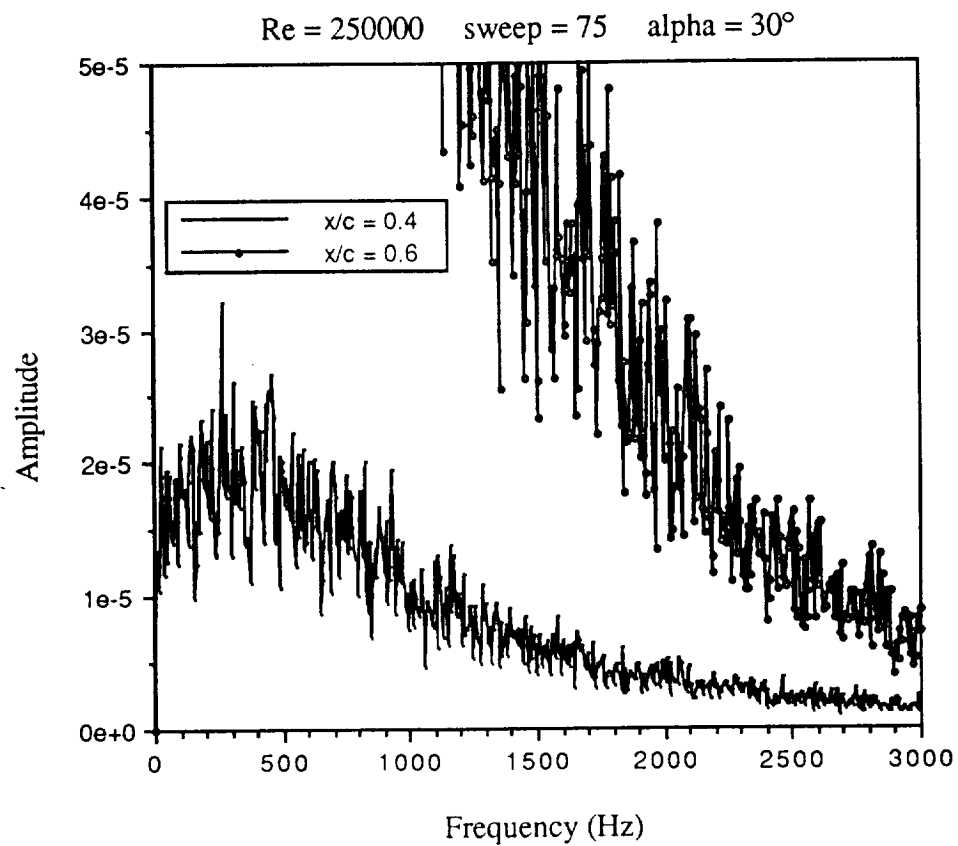
Figure 5.49 Core Power Spectrum a) Pre and Post Breakdown b) Magnified Image

small peak at about the 300 Hz range. The x/c = 0.6 spectrum rises sharply in magnitude as zero Hz is approached. If enlarged there appears to be a peak between 5 and 10 Hz. Since the frequency resolution for these tests was only about 6.1 Hz, however, the peak could actually be an indication of low frequency noise.

This peaking of the spectrum between 250 to 500 Hz appeared to be characteristic of all the pre-breakdown signals. The magnitude of the signal was greater at 30° than 20° for the x/c = 0.3 location as seen in Figure 5.50a although the profiles had similar shapes. As the Reynolds number was reduced, the difference in magnitude of the signals was seen to increase.

At x/c = 0.5, in Figure 5.50b, close to the breakdown location for α = 30°, the power spectra were seen to differ considerably from Figure 5.50a. There is a resemblance to the x/c = 0.6 profile of Figure 5.49a in terms of shape for α = 30. It is possible that the α = 30° spectrum in Figure 5.50b represents the flow in the breakdown region. The magnitude of the fluctuations is seen to have dropped considerably compared to the spectrum in Figure 5.50a. The α = 20° spectrum is seen to exhibit a larger magnitude in Figure 5.50b compared to Figure 5.50a.

The peak present in the power spectrum was also observed to grow in magnitude as x/c was increased. Spectra at chordwise stations of x/c = 0.3, 0.5, 0.7, and 0.9 are presented in Figure 5.51 for an angle of attack of 20 degrees. An abrupt change in the spectrum profile from x/c = 0.7 to 0.9 is evident. The transition resembles the pre to post breakdown transition noted in Figure 5.49a. The magnitude is considerably lower at x/c = 0.9 than 0.7, similar to Figure 5.50b. Whether this is a result of probe induced breakdown or of proximity to the trailing edge of the wing is unknown.

The freestream flow was tested with no model in the tunnel at the various Reynolds numbers to observe any frequency contributions from the wind tunnel. The values presented in Figure 5.52 lie three orders of magnitude below the amplitudes shown previous. There is a peak
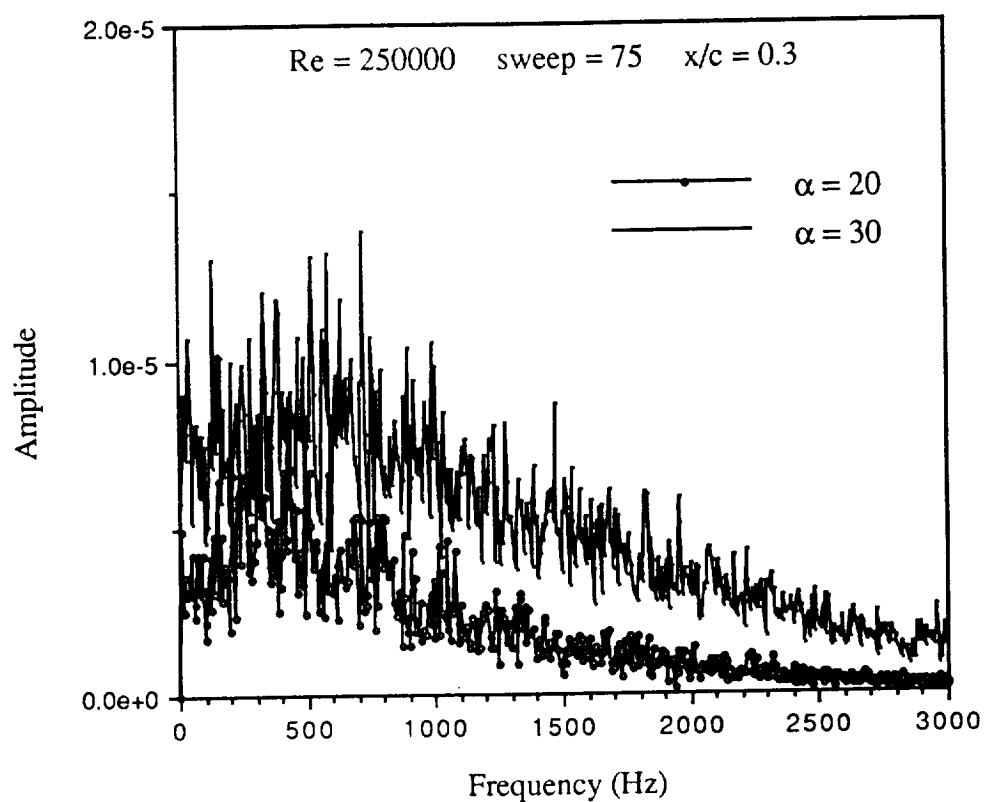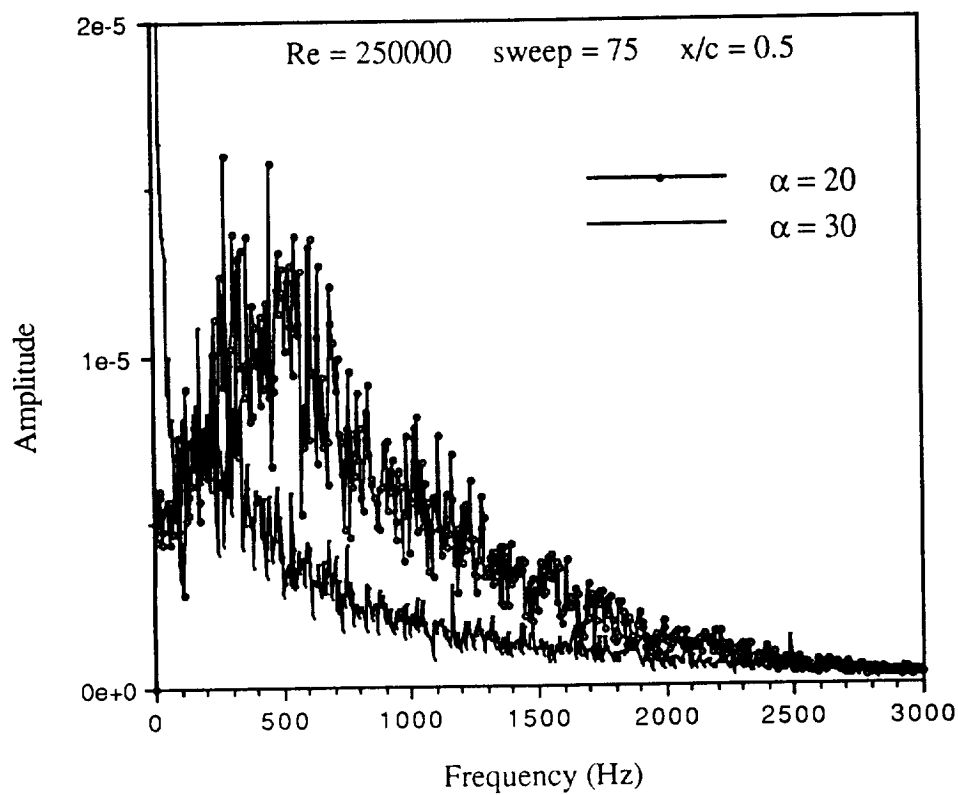
Figure 5.50 Effect of Angle of Attack on Power Spectrum a) x/c = 0.3 b) x/c = 0.5

Re = 250000   sweep = 75   alpha = 20°

x/c = 0.5
x/c = 0.7
x/c = 0.9

Amplitude

Frequency (Hz)
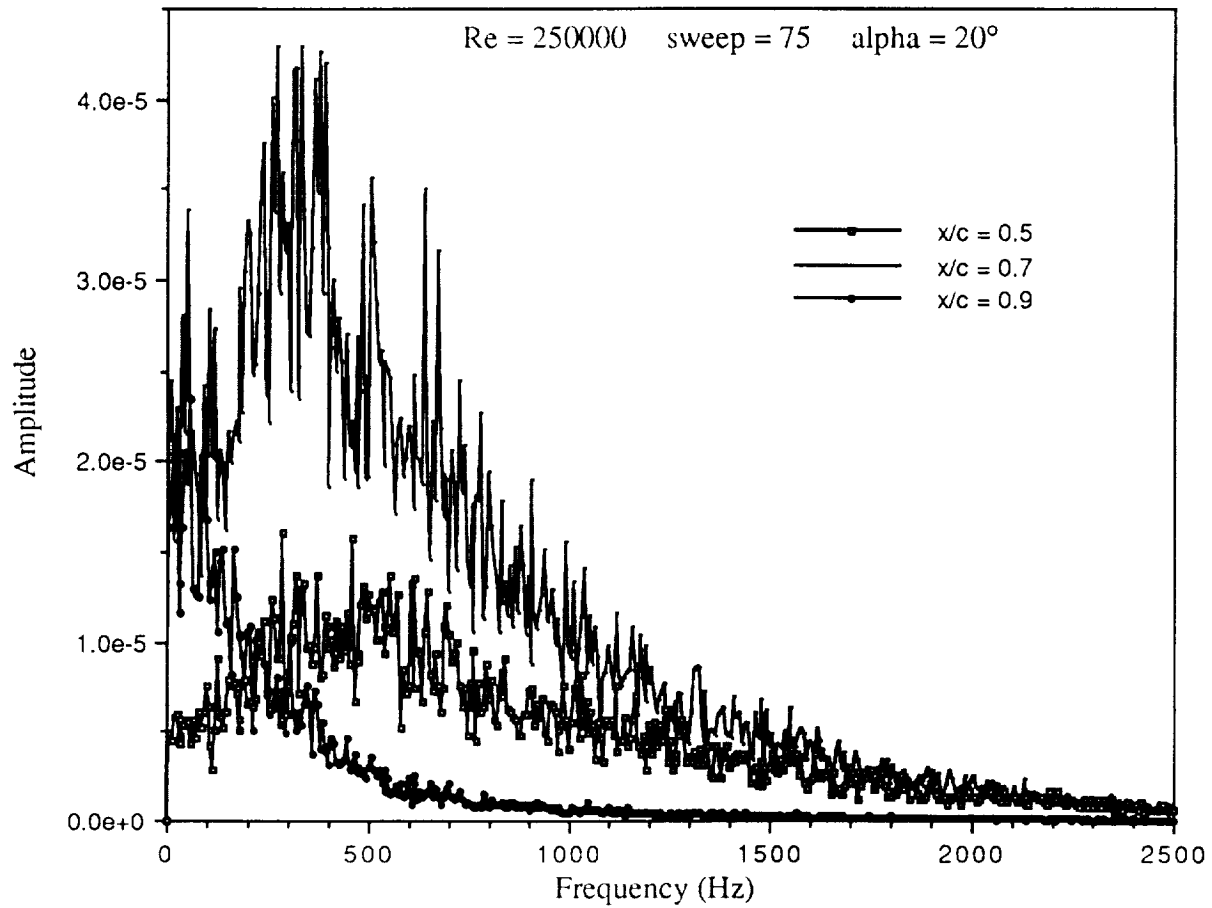
Figure 5.51 Chordwise Dependency of Core Power Spectrum at 20° Angle of Attack

Re = 250000   Freestream   V = 9.8 m/s

Amplitude

Frequency (Hz)
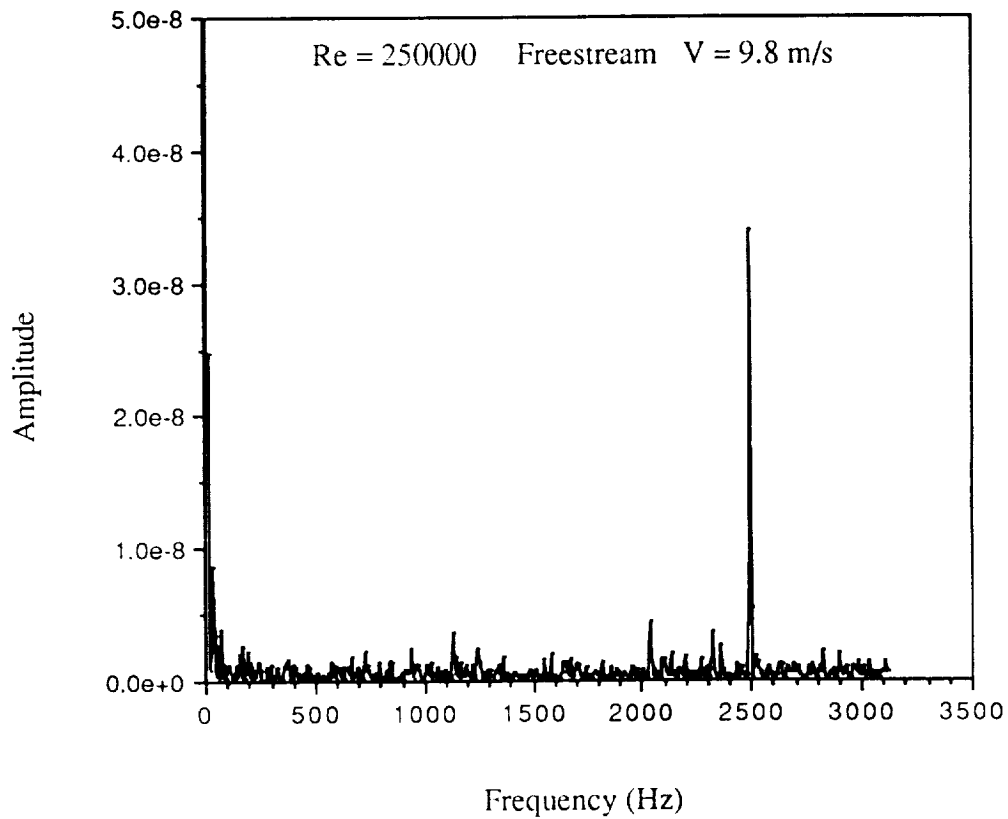
Figure 5.52 Freestream Power Spectrum at Re = 250000

between 5 and 10 Hz, but this maximum value is smaller than any of the previous values by a factor of about 100. On the otherhand it may be that the flow field above the delta wing is sensitive to these low frequency components and that they serve to create the peaks evident on the lower end of the spectrums in Figures 5.49b and 5.50b.

5.2.6 Core Dimensions

Flow visualization has indicated another interesting phenomena that would substantiate arguments of a cylindrical behavior of the subcore region and a conical nature of the outer portion of the core. Although the outer flow region of the vortex scales with the local geometry of the wing, the subcore maintains what appears to be a constant diameter as seen in Figure 2.5. If titanium tetrachloride smoke is introduced into the core, Figures 2.5a, the traced diameter does not widen at the same rate as the outer flow in the axial direction. In what resembles an inverse image of the above in Figure 2.5b, the void produced in the core region when kerosene smoke is introduced upstream of the model also remains constant in diameter with an increase of distance from the apex. The nature of the velocity profile data leads to the possibility of two core size definitions: a jet core due to the presence of the axial velocity component and a much smaller core based on the distance between the maximum and minimum values of w or V_ϕ, usually referred to as the subcore. If a minimum value of u/U_∞ is used to set a threshold cutoff, a jet core can be defined and the growth rate compared to that of the subcore defined above. Verhaagen has defined a third type of core based on the vorticity profile. This rotational core is based on the radius to which the vorticity falls to a certain level, in the same manner as the jet core outlined above.

The core diameters evaluated from the $\Lambda = 75°$ $\alpha = 20°$ data are presented in Figure 5.53. The jet core is defined as the diameter of the axial velocity profile above a threshold of $u/U_\infty =$
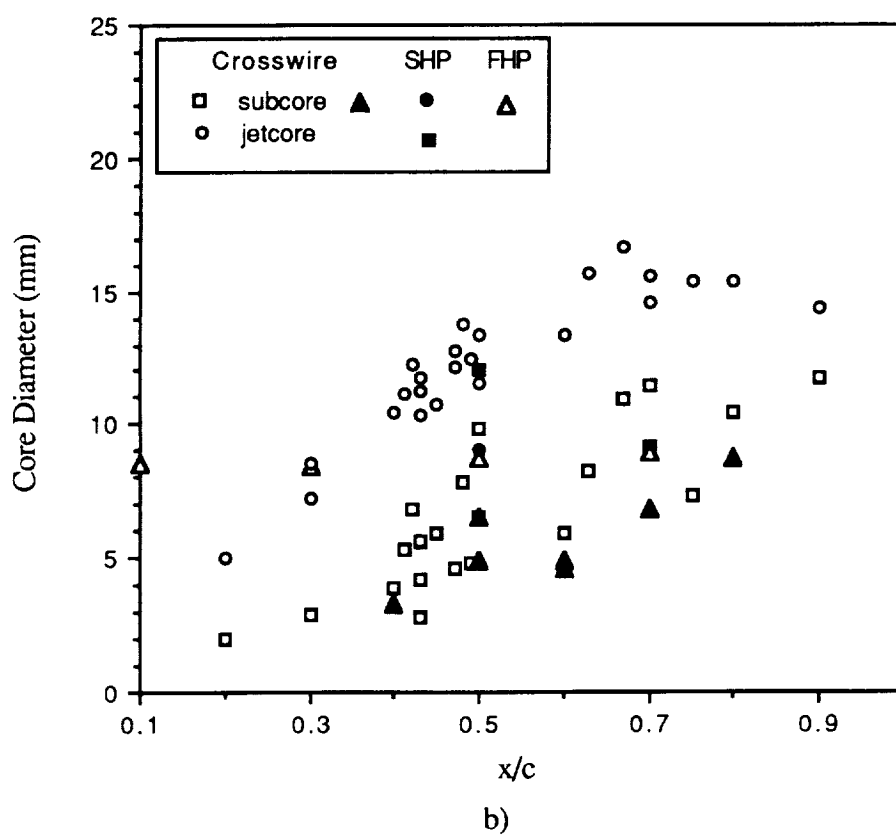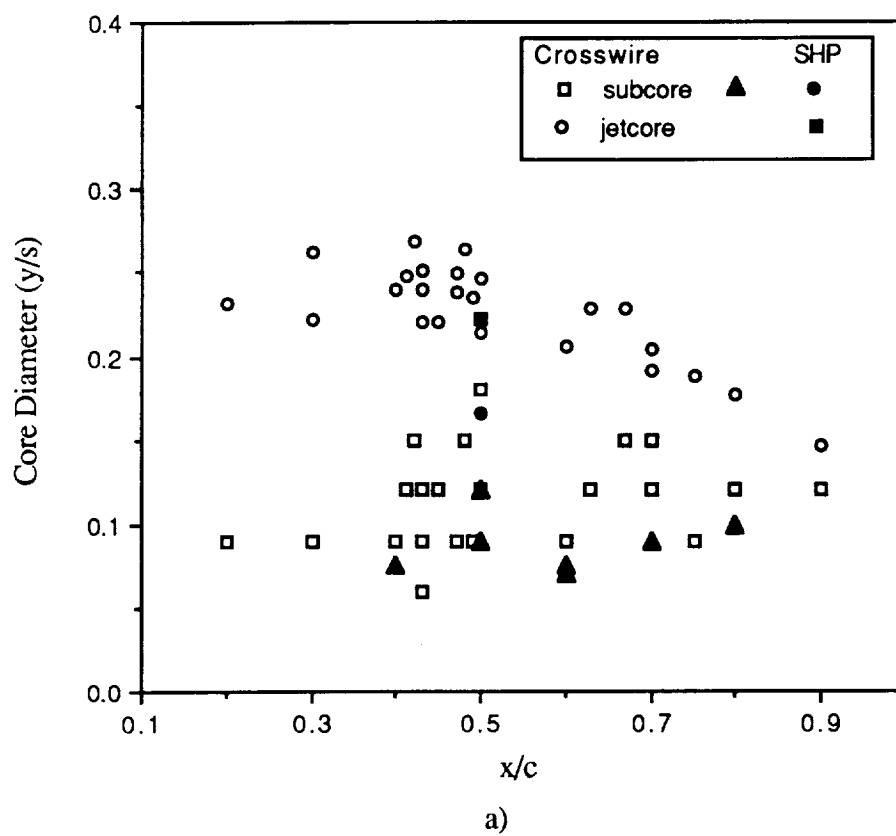
Figure 5.53 Vortex Core Diameters a)Scaled by Local Semipan b) Absolute

1.5. This was felt to be the minimum u/U_∞ cutoff, since the core tends to widen appreciably as u/U_∞ is decreased further. Both the local semispan and absolute units are given in Figure 5.53a and 5.53b respectively. The grid resolution of 0.03 y/s leads to more scatter in the determination of the size of the subcore than the jet core. Finer grid resolution data corresponding to y/s = 0.015 and 0.010 are also indicated in Figure 5.53a and 5.53b by the solid black triangles. Figure 5.53b indicates that both the jet core and subcore are growing in size, the jet core at a slightly larger rate than the subcore. When scaled by the local semispan in Figure 5.53a, the relative jet core diameter is seen to decrease in the axial direction as the trailing edge is approached. This is confirmed by Figure 5.53b where the absolute size of the jetcore is leveling off near the trailing edge. The finer grids also indicate the subcore to be increasing slightly in size towards the trailing edge, although a constant diameter can be interpreted over the central portion of the wing. The scatter of the data makes interpretation difficult and more data will be required at a finer grid resolution before any definitive statements can be made.

Core size evaluated from the SHP data for the same geometry is plotted in Figure 5.53 along with the cross wire data and falls in the same range. Five hole probe data from Verhaagen and van Ransbeeck (1990) is also included in Figure 5.53b. They measured a subcore diameter from x/c = 0.1 to 0.7 on a 2.22 m, 76° swept delta wing. The constant diameter would indicate a cylindrical rather than conical flow. Data obtained from Hawk, Barnett, and O'Neil (1990), however, points to a linear type of core growth with chordwise distance over a 762 mm chord, 70° swept wing. These discrepancies again indicate that due to such factors as grid resolution, which is usually not compared between experimental data sets, differing statements concerning observable properties can exist between investigators and comparisons should be examined in light of these factors.

The core sizes calculated for the other planforms of the present study are presented in Figure 5.54 along with the SHP equivalents. Both techniques indicate similar diameters for both
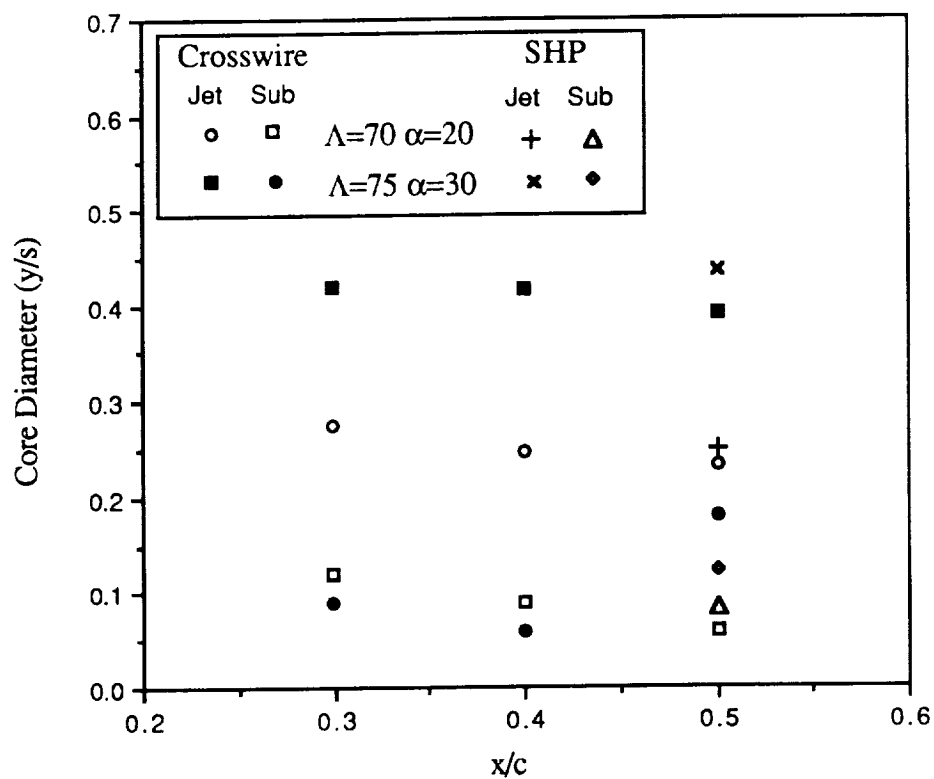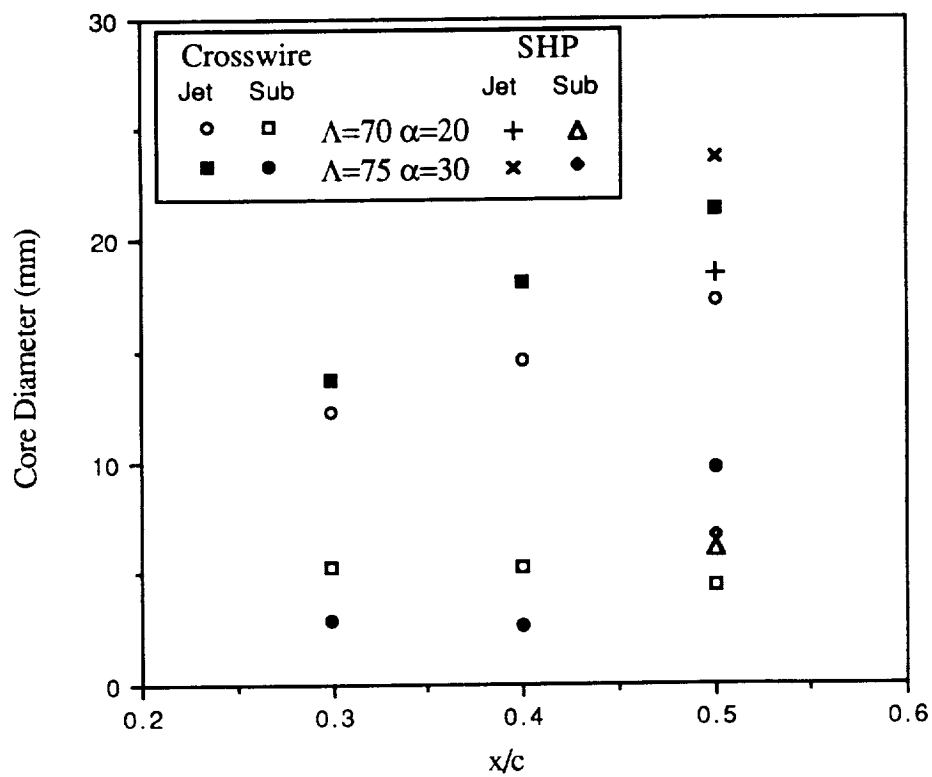
Figure 5.54 Geometric Effect on Vortex Core Diameters a)Scaled by local span b) Absolute

the jet and sub core. The $\Lambda = 75°$ $\alpha = 20°$ jet core is substantially larger than the 70° planform. The subcore exhibits a constant value over the chordwise distance shown. Both planforms in Figure 5.54 have breakdown occurring on the wing in the vicinity of the x/c = 0.55 location. Since there is only one point at each chordwise station, and this data is taken over the central portion of the wing, the trend of the data in the chordwise direction is difficult to ascertain.

The data above would seem to indicate that the the subcore is growing in diameter in a downstream direction, not at the rate of the local wing geometry, perhaps, but growing nonetheless. The flow visualization in Chapter 2 suggests that the growth rate, if any, is small and not easily seen visually. This indicates that care must be taken when making quantitative judgements from flow visualization. On the other hand, the scatter in the data and the indication that at times there does appear to be a constant diameter for some x/c range points to the need for a more precise measurement technique before coming to a strong conclusion on this subject. In addition, there is a probe interfering with the flow when the measurements were taken which is not present the flow visualization. The effect of this probe, which was on the order of the subcore diameter, has the tendency to displace the core are the result of this on the core diameter has not been quantified.

As mentioned at the beginning of this section, a core diameter can also be defined according to the region containing the rotational flow. Based on this definition, Verhaagen and van Ransbeeck (1990) report the rotational core to occupy approximately 35% of the local semi span. From the cross wire data in Figure 5.27,based on a threshold vorticity value equal to 90% of the maximum, a rotational diameter equal to 30% of the local semispan is measured. If the rotational core definition is to contain all the rotational region, that is until the axial vorticity drops to zero, 90% of the local semispan would have to be included.

5.3 Pressure Measurements

The effect of pressure on the behavior of the vortex structure and the breakdown location is very substantial as has been pointed out by several investigators in Chapter 1 and discussed in Chapter 2. Payne (1987) measured a change in the slope of the total pressure coefficient on the vortex axis versus chordwise position curve from negative to positive at the 60% chord mark for a 85° swept wing at a 45 degree angle of attack. This is then followed by a significant rise in the value of C_{pt}. These measurements were taken through the breakdown region and agree physically with what would accompany the local stagnation of the axial velocity component.

It was therefore decided to observe the changes in the pressure distributions on and above a delta wing to examine if the pressure distribution gave an indication that breakdown was evident. Whether this came as a result of some maximum value of the local surface pressure coefficient or a critical change in the pressure gradient, $\partial p/\partial x$, this could then be incorporated into a parameter for the breakdown prediction.

5.3.1 Surface Pressures

The tests conducted with the surface pressure models centered on three factors: the influence of the planform size on the measured pressures, the effect of the sting mount location, and whether or not it was possible to trace the path of the breakdown by observing the pressure signature on the wing surface.

The values of the surface pressure coefficient, Cp, along a ray extending from the apex, gave no obvious indication that a breakdown existed at some chord location over the wing. The

data along the y/s =0.6 location exhibited the lowest values of Cp, indicating they were closet to being under the core, and thus will be the only values which will be discussed here.

The 16 inch model Cp values are presented in Figure 5.55a. The value of $\partial p / \partial x$ is always seen to be positive. Increasing the angle of attack only serves to increase the nonlinearity of the curve, but no indication of where the breakdown position could be determined. This is also observed from the data presented by Roos and Kegelman (1990) although it was not explicitly stated by them. This would seem to indicate that the use of this variable in developing a breakdown parameter would be minimal. No plateau is observed and no drastic sign change in the slope occurs. Kirkpatrick (1970) noted a definite step type of change in the value of C_N verses angle of attack as the breakdown moved forward on a 68° wing, if the spanwise pressures are integrated. Roos and Kegelman comment that although the lift aft of breakdown decreases with incidence, the overall lift continues to increase until the flow is fully separated from the wing. In any event, simply observing the surface pressure signatures is not enough to determine a breakdown location which was the intent here.

There was an interesting change discovered in the pressure measurements when they were repeated on the 16" chord wing. This second set of data, presented along with the initial data in Figure 5.55b, was taken with the wing centered in the tunnel. The first set of tests were conducted with the wing much closer to the tunnel floor and severe differences appear at angles of attack of 35° and greater. The close proximity to the wall appeared to delay the stall of the wing in the first series of tests until over 45 degrees, as compared to the typical angle of attack around 35 degrees. The second set of data shows and indication of the onset of stall at 35° at the x/c = 0.7 location. The α = 40° data shows a rise in the pressure at all stations on the centered wing as compared to the wing near the tunnel floor. The latter was then seen to experience a similar pressure rise once an angle of attack of 50° was reached.
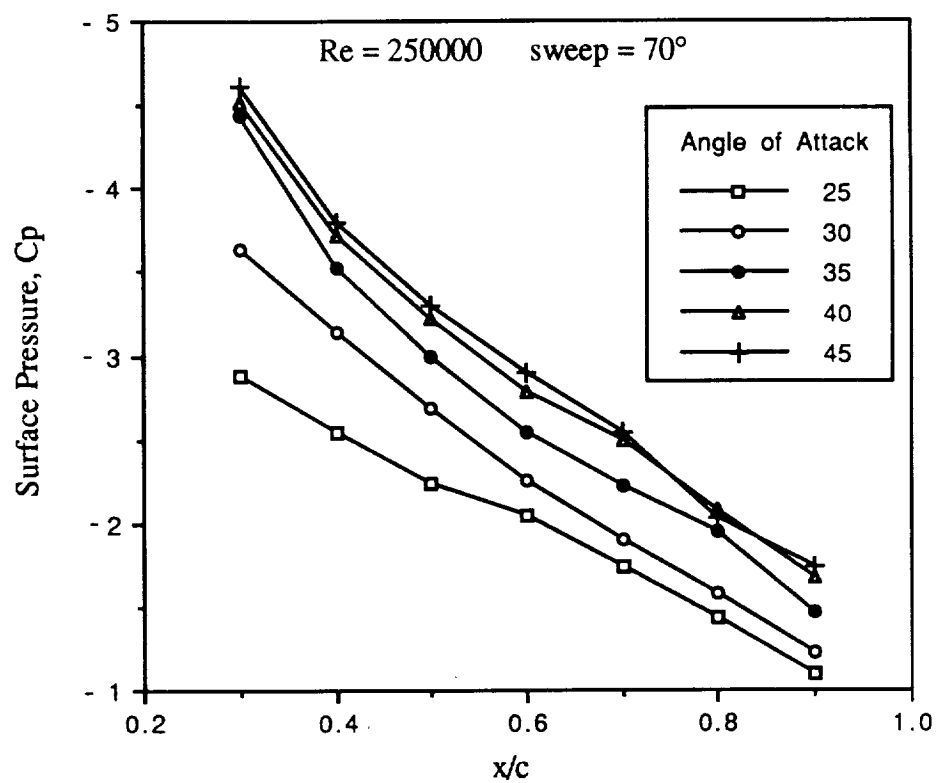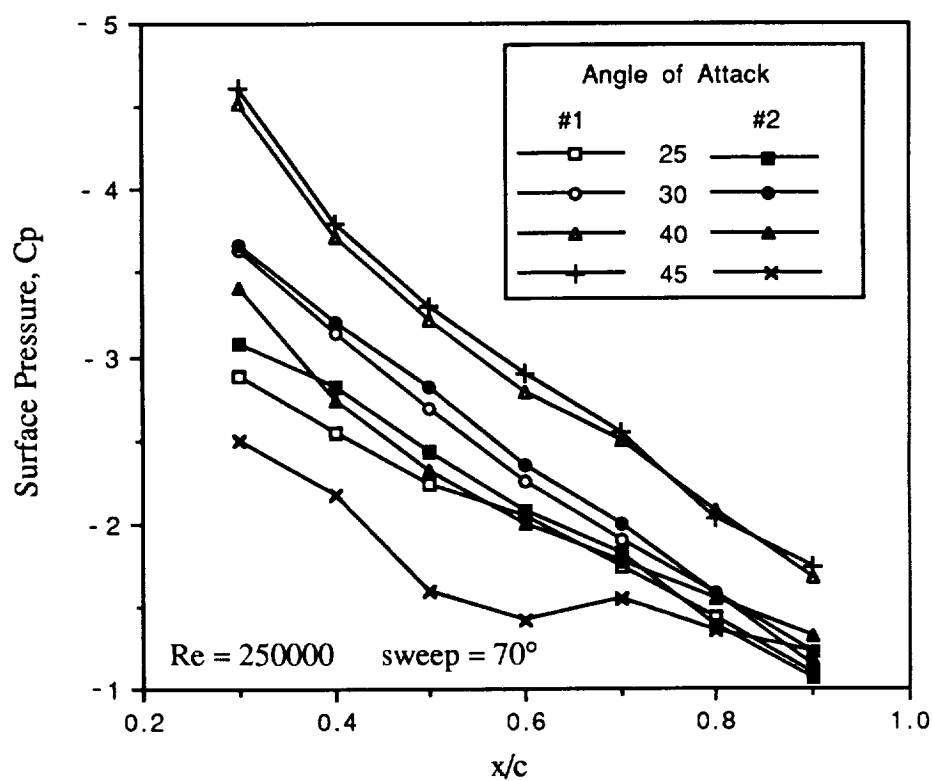
Figure 5.55 Surface Pressure Distribution, y/s = 0.6, 70° sweep a) Uncentered b) Centered
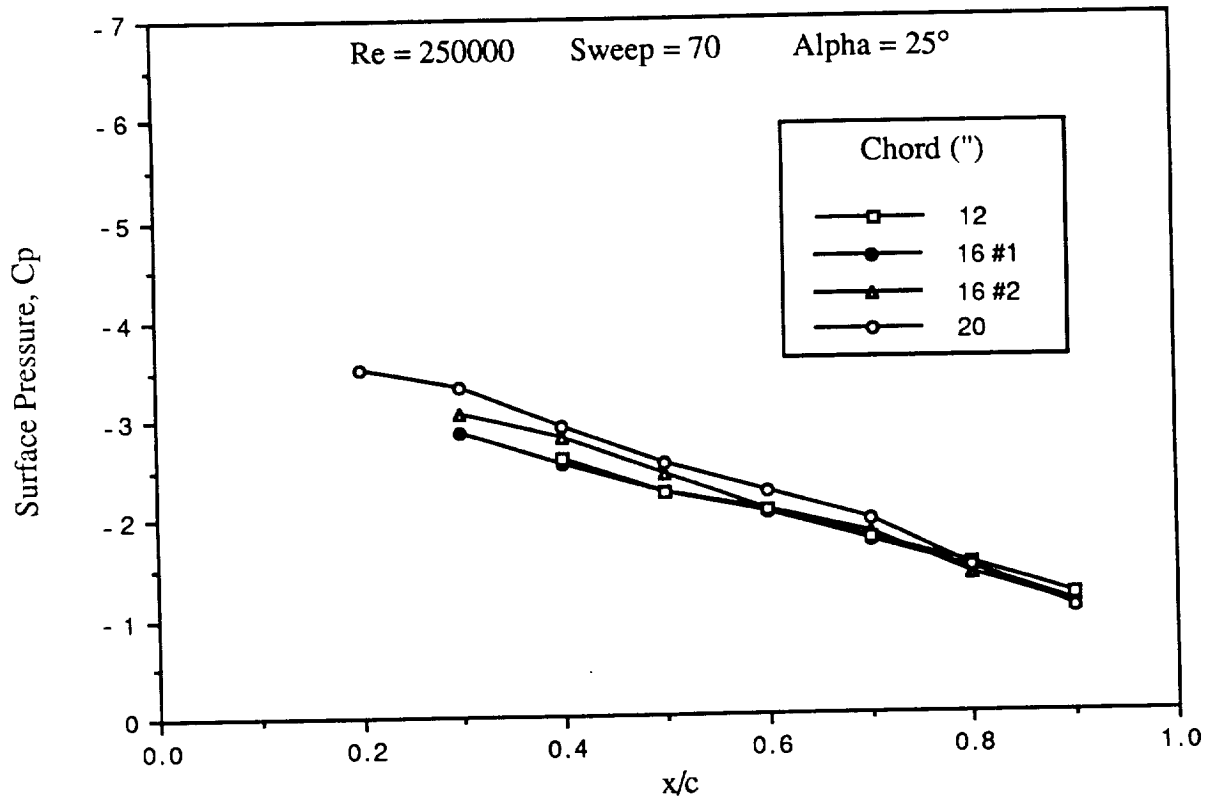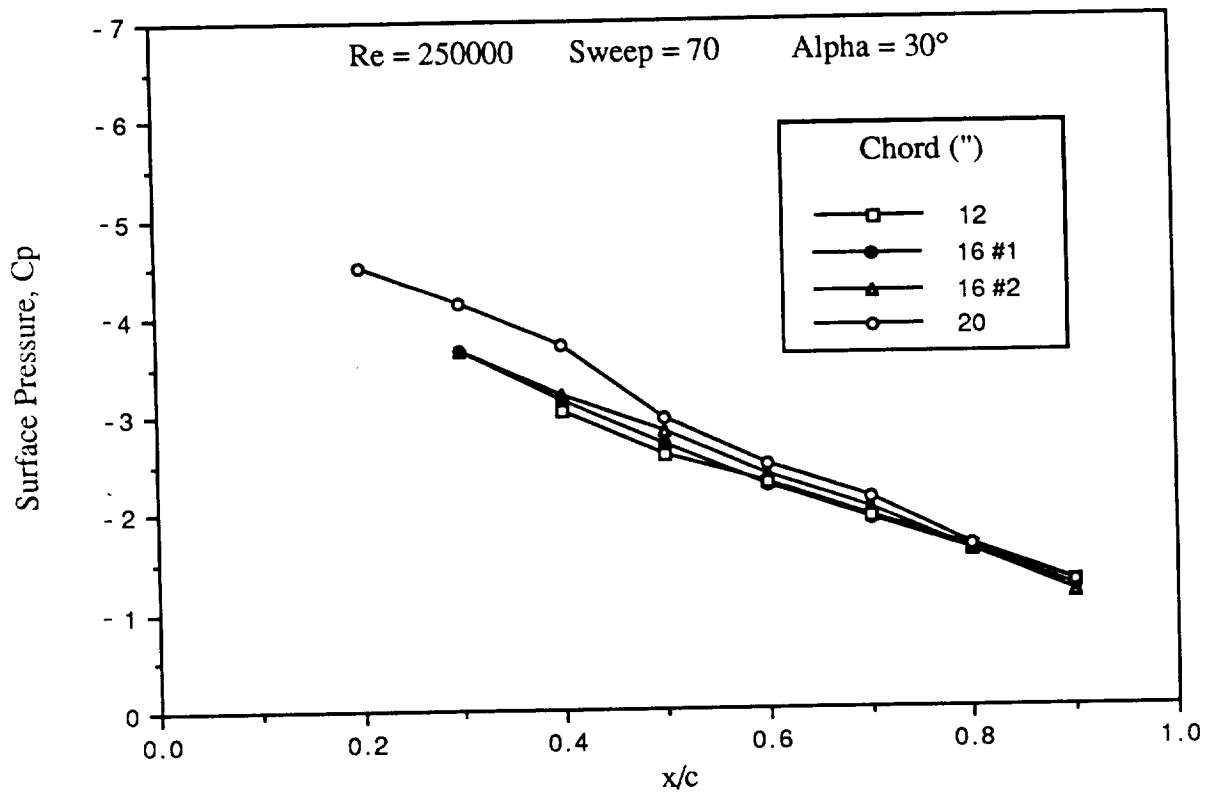
Figure 5.56 Effect of Chord Length on the Surface Pressure Distribution a) 25° b) 30°

The effect of increasing and decreasing the chord length relative to the 16 inch model is shown in Figure 5.56. Each plot represents an angle of attack ranging from 25 to 45 degrees. Both 16 inch cases are included. The 12 and 20 inch models have the sting mounted in the same absolute location to simulate a reduction and extension of the trailing edge respectively, relative to the 16 inch model. At angles of attack below 40°, the models show similar profiles, although the 20" model exhibits a consistently lower pressure field. At 35° the 12" model indicated a considerable pressure rise which would corresponds to a stall according to the $C_{l\alpha}$ curve. The centered 16" model also exhibited the verge of this transition as mentioned previous. The 20" model indicates a still lower pressure profile, which continues to drop as the angle of attack is increased to 45° in Figure 5.56d. The profile of the centered 16" model approaches that of the 12" case by $\alpha = 45°$, but no indication of stalling is present on the 20" model.

The effect of the sting location is illustrated in Figure 5.57. On both the 12 and 20 inch models, the sting was first positioned at the same absolute location as the 16" model, that being 8 inches from the apex. The mount was then changed to the local x/c = 0.5 mark which is closer to the apex of the 12" by 2" and close to the 20" model trailing edge by the same amount. Overall the resulting pressure profile differences are minimal. The 12" model shows slightly lower values Cp for the x/c = 0.5 location, while the 20" model gave slightly higher pressures. This could be stated such that for both models, movement of the sting rearward decreased the measured Cp values. The largest difference, of approximately 9.5%, occurred at $\alpha = 30°$ for the 12" model. In general the 12" and 16" centered models correlate quite well, while the 20" model was found to have consistently lower pressure values.

The surfaces pressure distributions gave no indication of the onset of breakdown when viewed along rays extending from the apex. It was not until total separation occurred over the wing that there could be a noticeable difference in the $\partial P/\partial x$ behavior at the surface. Because of the lack of a definitive trend in this measured parameter, it is ineffective as an indicator of the
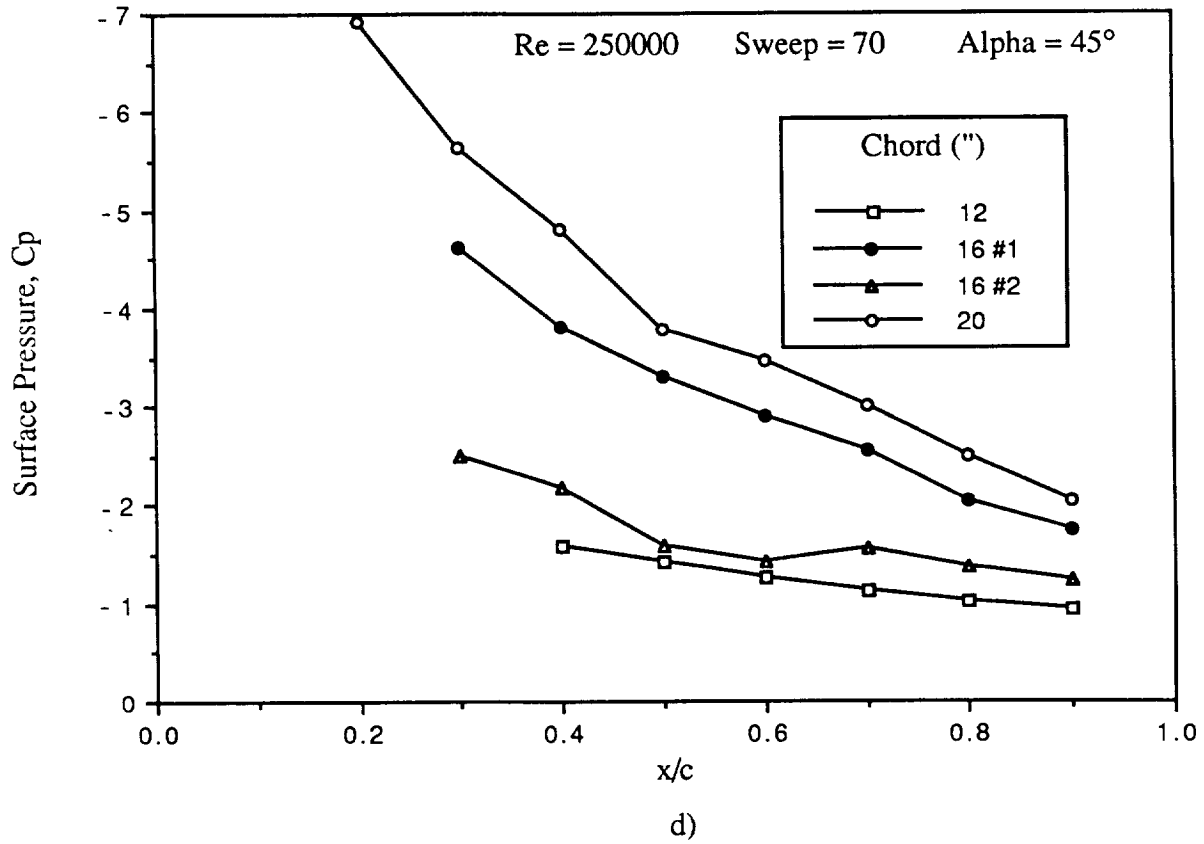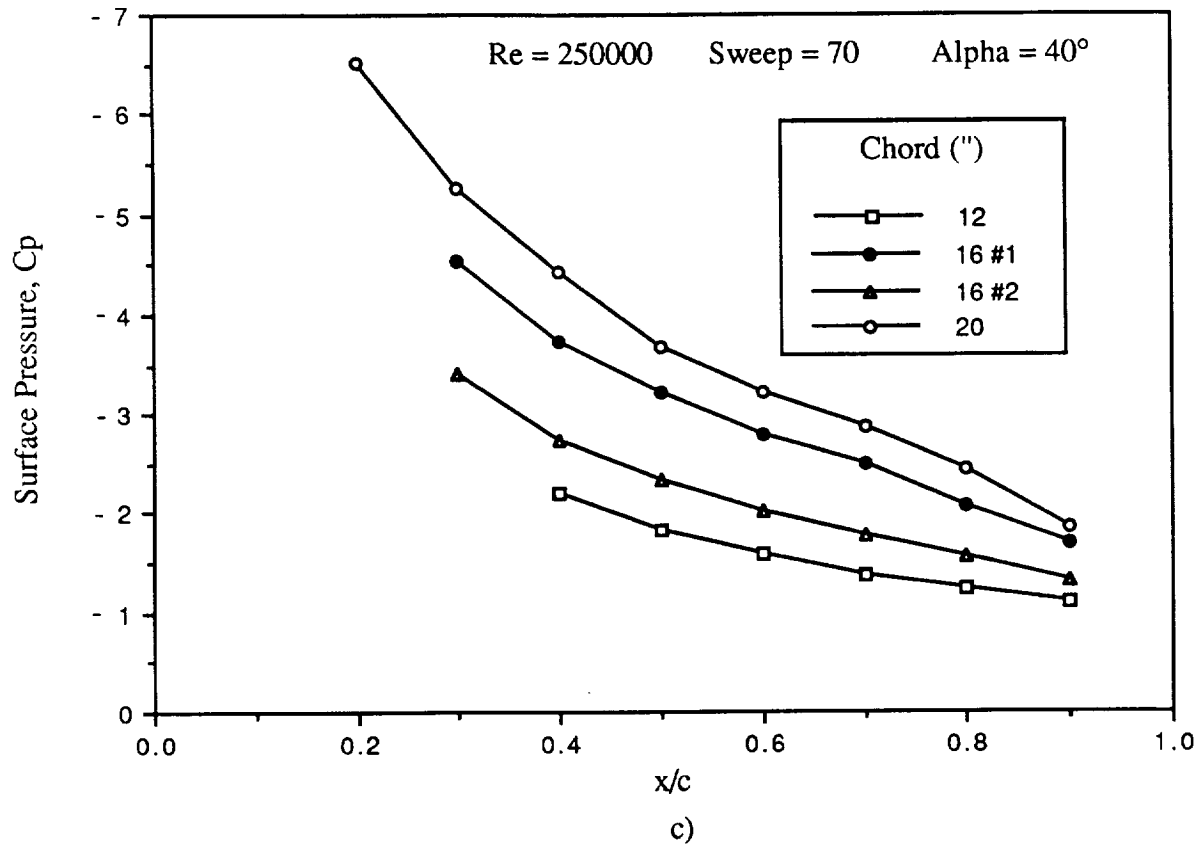
Figure 5.56 Effect of Chord Length on the Surface Pressure Distribution c) 40° d) 45°
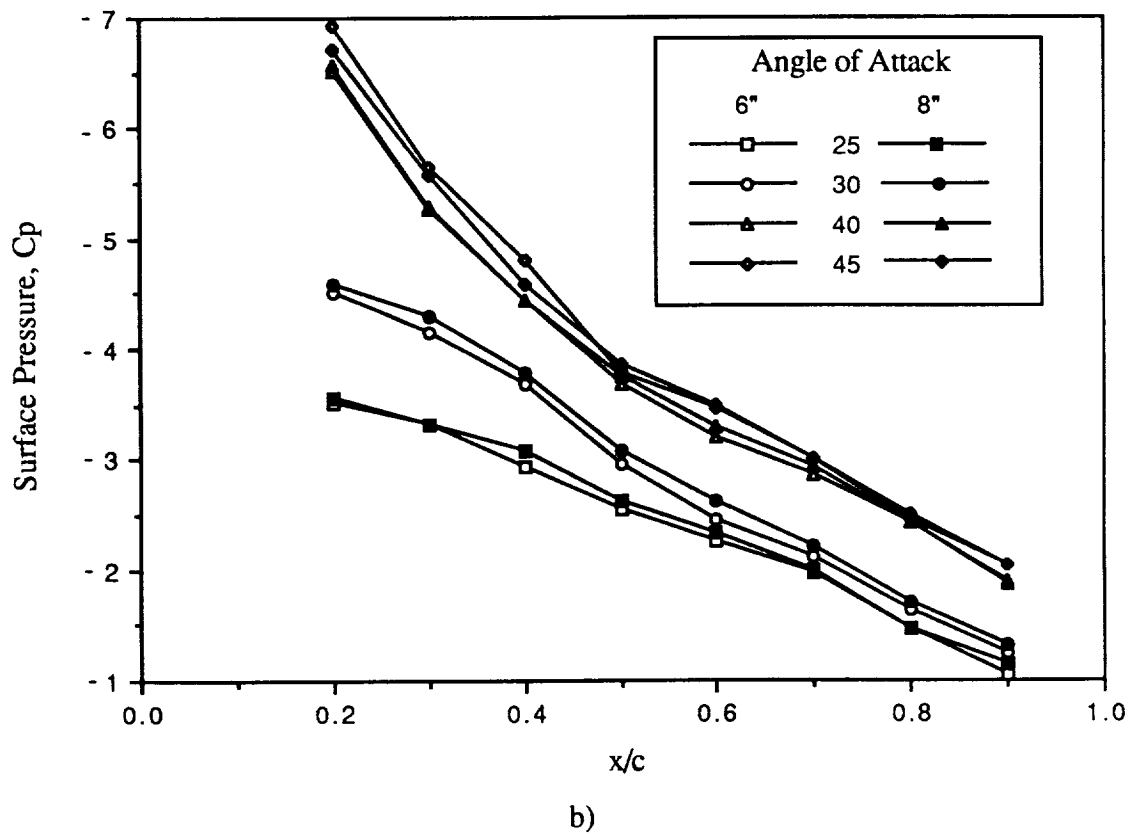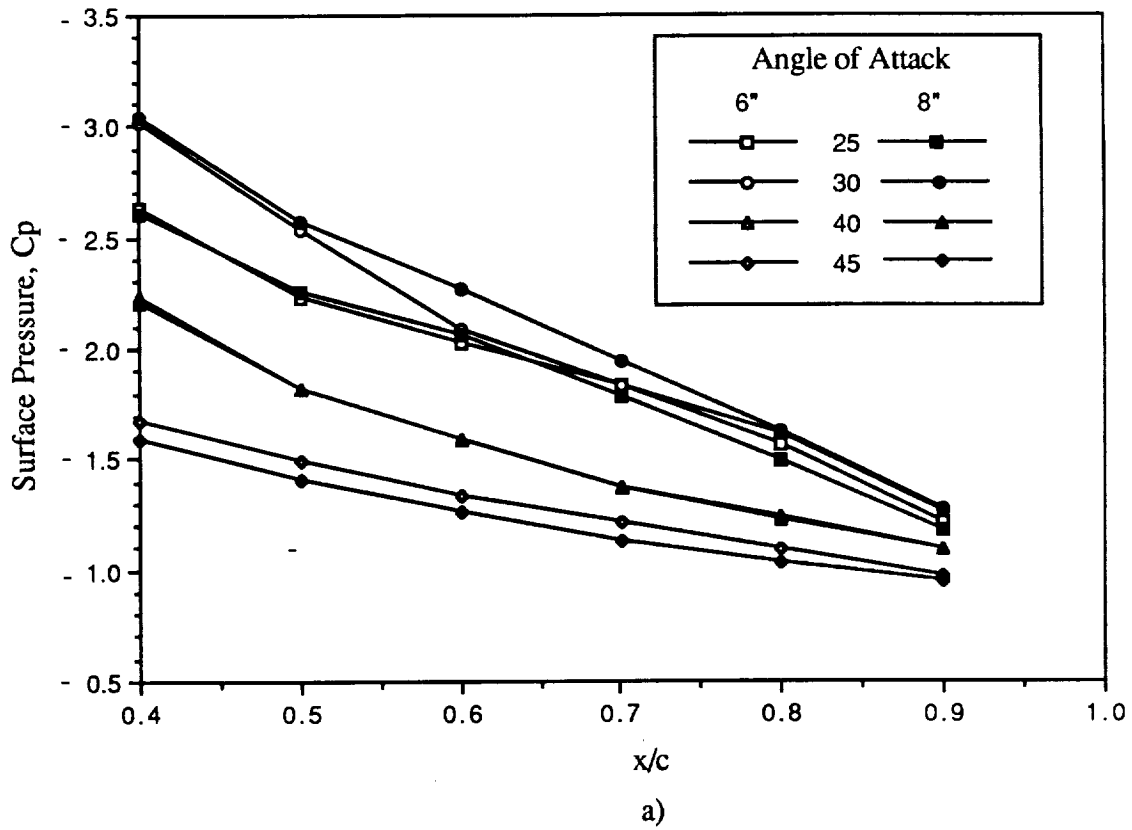
Figure 5.57 Sting Location Effect on Surface Pressure Distribution a) 12" chord b) 20" chord

onset of breakdown and would contribute little if included in a correlation parameter. It is apparent that the blockage effects involved with the measured wing configurations are not negligible. This factors are already known, however, and blockage correction procedures are available. More importantly because of its subtlety, and perhaps not as well known, is that the mounted position of the model in the tunnel is critical to representing proper flow conditions.

5.3.2 Total Pressure and Centripetal Acceleration in the Core

Total pressure measurements were made, via the total pressure probe, above the 75° sweep wing with the primary intent of examining the ideas put forth in section 2.2. The intent was to compare the balance of the radial pressure gradient with the centripetal acceleration of the fluid. The data obtained from the total pressure probe could be combined with the velocity data of the hot wire surveys to evaluate these parameters. The total pressure data is presented in Figure 5.58a in the form of total pressure coefficient, C_{pt}, against chordwise location. Two angles of attack were tested, 20° and 30°. Previous flow visualization with the hot wire on the $\alpha = 20°$ tests showed no breakdown occurring, either naturally or induced by the hot wire probe. The $\alpha = 30°$ case indicated that breakdown was induced by the hot wire probe to occur at about 55% of the chord, where it would naturally occur in the wake.

From Figure 5.58a, it can be seen that the pressure measurements indicate breakdown is not occurring on the 30° case until perhaps at about the x/c = 0.8 station. There is no probe induced breakdown at the x/c = .55 location. The total pressure probe is considerably smaller than the hotwire configuration as seen in Figures 4.4 and 4.5. Whether breakdown was actually occurring at the 80% station was not observed visually, however it was certainly not occurring where it does with the x-wire probe. Thus any comparison, such as that in section 2.2, must be

a)

b)

c)
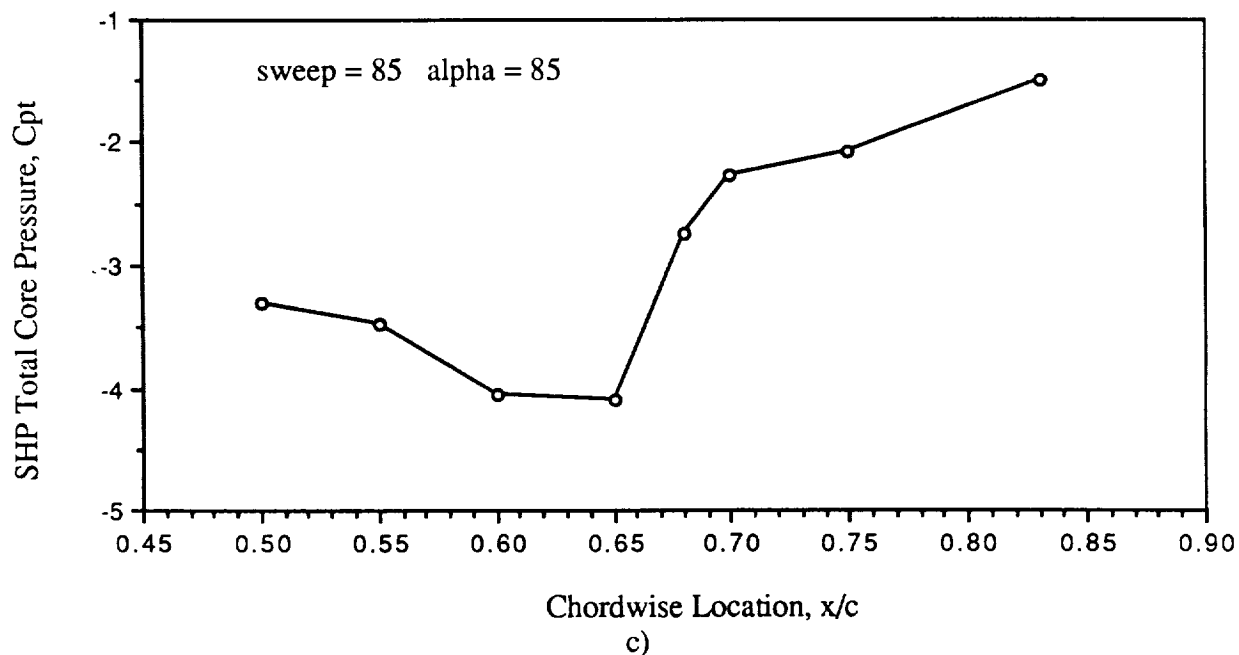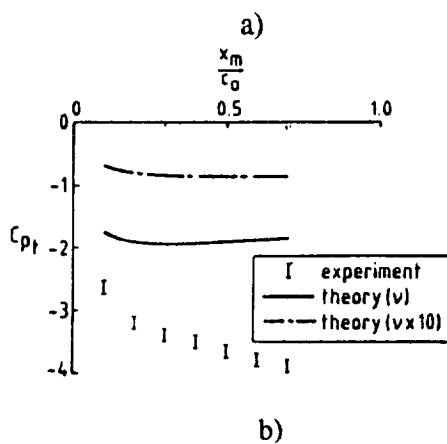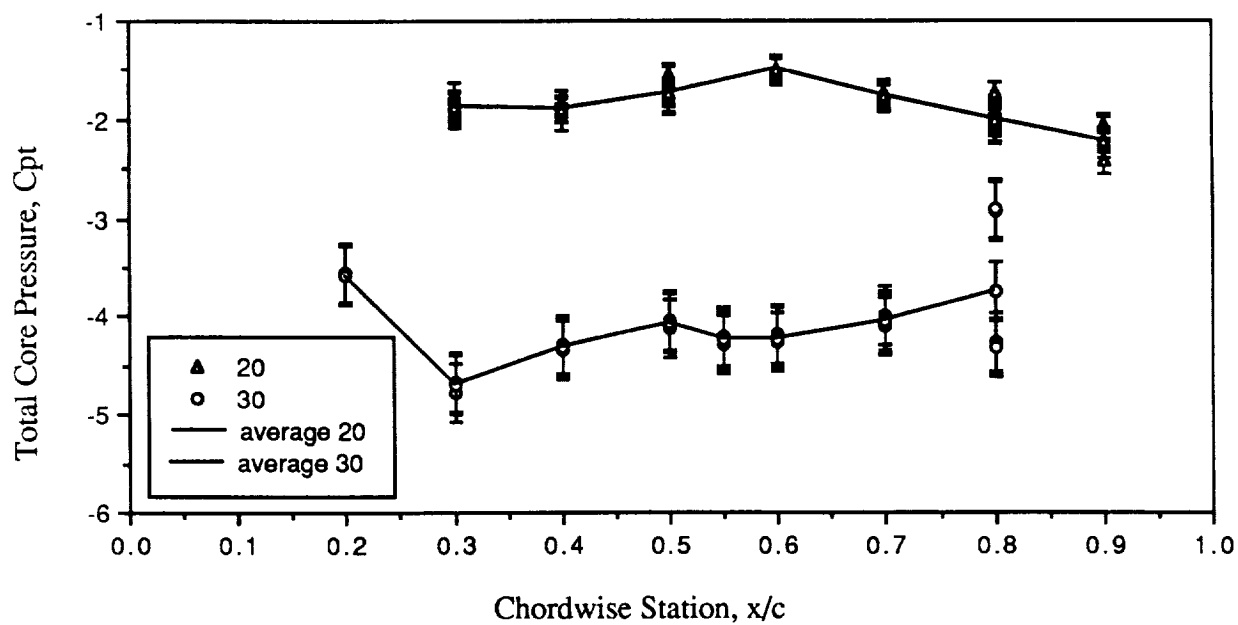
Figure 5.58   Vortex Core Total Pressure Distribution a) Present Tests
b)FHP (Verhaagen and van Ransbeek, 1990) c)SHP

made forward of the breakdown induced by the hotwire probe. This serves to indicate how sensitive the vortex flow is to the intrusion of a probe and most especially the size of the probe.

The 20° case reveals an increase in the the total core pressure with distance, up to about x/c = 0.6, followed by a subsequent decrease, but careful interpretation of the data is required. As the probe is moved rearward on the delta wing, the local flow increases in size accordingly and the probe size becomes relatively smaller when compared to the local vortex station. Thus it may be that an area encompassed by the probe tip as a single point measurement further near the apex, may now be resolved into several points. In essence the probe can now measure a lower pressure more accurately, if it exists, since it is not being smeared into a single point. This implies that the actual core pressures nearer the apex may be lower than measured. In other words, if the pressure is decreasing in the axial direction, the relative probe size may be the cause, whereas if it is increasing as x/c increases, the phenomena would not be a result of the probe resolution. Conversely, the $\alpha = 30°$ measurements show a rise in the core pressure, after an initial drop, up to the x/c = 0.8 station and it can be surmised that the pressure is actually rising. Error bars represent the maximum error associated with the largest measure Cpt values .

Recall, from Chapter 1, that Lambourne and Bryer (1961) noted that the total pressure was seen to have a nearly constant value along the length of the vortex at roughly Cpt = -5.0 for a 65° sweep wing at $\alpha = 15$. Kegelman and Roos (1990) report a similar constant total pressure with axial distance for 60° and 70° flat plate delta wings. Naarding and Verhaagen (1988) reported a drop in the axial total pressure with increasing x/c as well as a sharp drop near the apex for their 76° sweep wing at $\alpha = 20$. Their data is given in Figure 5.58b for comparison and is seen to have Cpt values lower than the present values by up to 100%. They explain the difference between their data and that of Lambourne and Bryer is because Naarding and Verhaagen used a probe size on the order of the viscous core size. The present tests used a probe on the order of 1/3 to 1/4 the size of the subcore. The better resolution of Lambourne and Bryer would explain

their lower pressure values, but does not explain the reduction of values as Naarding and Verhaagen move closer to the apex. Smearing of the pressure profile due to a locally large probe size, would result in higher pressures, not lower. Kegelman and Roos (1990) also point out that the area where this significant total pressure loss occurs becomes proportionately smaller with increasing x/c. This could indicate that the subcore region, where the majority of the pressure loss occurs, is maintaining an constant absolute size.

Lambourne and Bryer mention that three factors on which the pressure distribution along the axis depends. The first of these is that increasing vortex strength tends to provide a falling axial static pressure. One might also propose that a lower axial pressure or a greater radial pressure gradient would allow for the existence of a stronger vortex. In either case, the strength of the vortex would seem to be directly dependent on the local radial pressure gradient, however it is established or influenced by external factors. Therefore the proposed ratio of forces was introduced at the end of Chapter 2 and will now be examined in more detail.

Four ratios were suggested to characterize the vortex state at a given axial station. The first two were based on the ratio of the difference in pressure between the core axis and the freestream, either static or total, to the maximum centripetal acceleration measured at the edge of the subcore. The latter two required the local pressure at the edge of the subcore. Unfortunately it is not possible to obtain these two latter ratios, even with the total pressure data available from the SHP surveys. If the total pressure probe is not aligned directly with the local flow vector, the total pressure is not being measured. One might argue that, given the velocity vector, the dynamic components could be added to the measured pressure at the required location to obtain the total pressure. This would be true in a field which did not have any losses. Since the leading edge vortex indicates a drop in the total pressure at the axis relative to the external flow, it is impossible to know the total pressure at a given radius without actually measuring it.

The two pressure/acceleration ratio, PAR, terms were therefore calculated in the following manner based on the ratio:

$$\frac{2 \, \Delta P}{\rho V_{\phi 2}^{2}}$$

The ratios are defined explicitly as:

Ratio 1: ΔP = freestream static pressure - axis static pressure = $P_{\infty} - P_{axis_{\infty}}$

$$\frac{2 \, (P_{\infty} - P_{axis_{\infty}})}{\rho V_{\phi 2}^{2}} = \frac{-(Cpt - u^{2})}{w^{2}} \tag{5.14}$$

Ratio 2: ΔP = freestream total pressure - axis total pressure = $P_{t_{\infty}} - P_{t \, axis}$

$$\frac{2 \, (P_{t_{\infty}} - P_{t \, axis})}{\rho V_{\phi 2}^{2}} = \frac{-(Cpt - 1)}{w^{2}} \tag{5.15}$$

where

$$u = \frac{V_{axis}}{U_{\infty}} \qquad w = \frac{V_{\phi 2}}{U_{\infty}}$$

and is obtained from the hotwire data at that station.

An example of the SHP total pressure data at the core axis and and the associated velocity profiles is given in Figure 5.59. The maximum value of the tangential velocity occurs at the edge of the subcore, indicated by the two solid vertical lines. The pressure coefficient used is the maximum recorded and the axial component required for ratio 1 was also taken as the maximum. The calculated ratio 1 and ratio 2 PAR values are plotted in Figure 5.60a against their respective angle of attack. Since all the stations were taken at an x/c location of 0.5, changes in the axial direction are unobtainable.

The ratios based on the static pressure distribution, ratio 1, are up to four times greater than the ratio 2 values based on the total pressure. The concept of the PAR itself implies that a value greater than one indicates the pressure gradient is sufficient to keep the vortex together. In this respect all the calculated values support this for they were taken in the pre-breakdown flow. The ratio 2 values are closer to a value of 1 and might be thought of as to the more representative of the flow. It is the local static pressure, however, that determines the local fluid forces and this is the more proper term to consider in this evaluation. As stated previously, a more indicative ratio
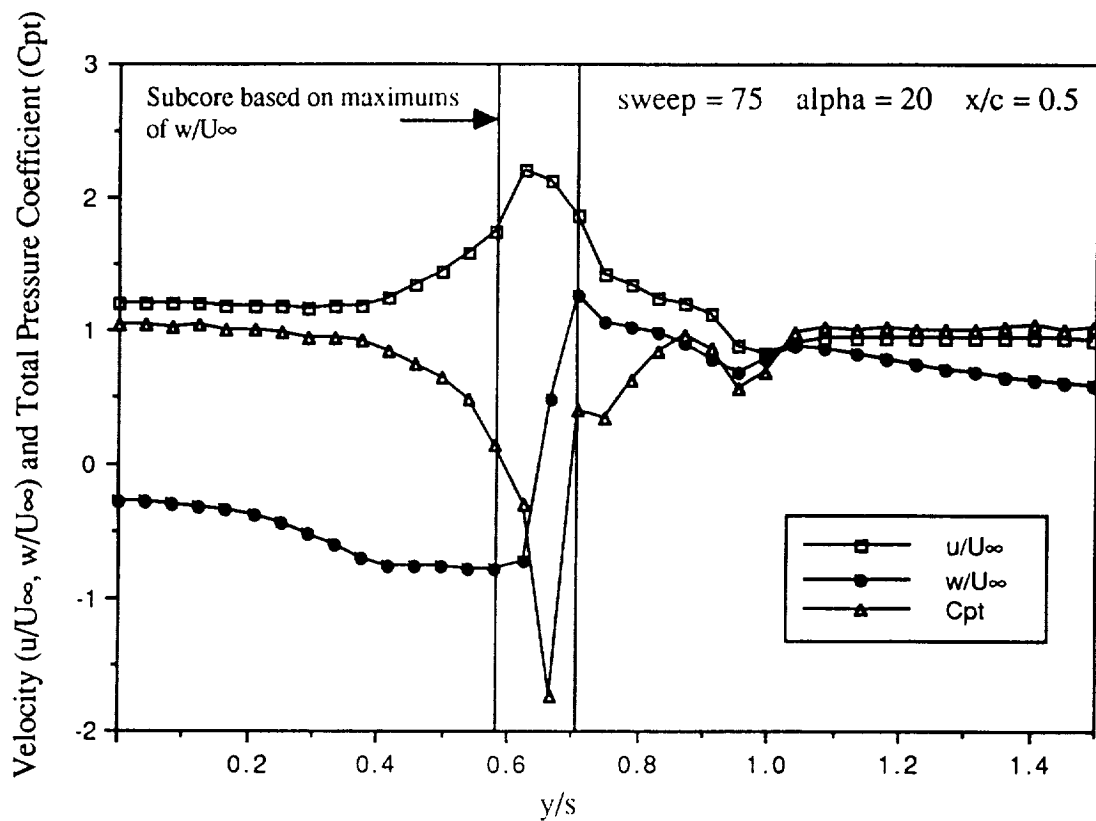
Figure 5.59 SHP Total Core Pressure and Velocity Profiles $\Lambda = 75°$, $\alpha = 20°$ x/c = 0.5

would be obtained by knowing the actual pressure gradient at the radius of the maximum tangential velocity, but this is unavailable.

Seven hole probe data was available for a chordwise evaluation of the 85° sweep wing at 45° angle of incidence. The computed values are presented in Figure 5.60b. Interestingly, the profiles peak in the region just before breakdown. Since the core expands, it would be expected that the ratio would drop below one, rather than increase. After breakdown, the vortex is again in a state of balance and a ratio of one or greater would be expected. Close examination of the data revealed that at the station where the peak occurs in Figure 5.60b, the tangential velocity had dropped, but the minimum Cpt did not indicate any rise until the next x/c station. Care must be taken with these values since they represent time average quantities in a fluctuating field. Time averaging may have smoothed out the instantaneous drops in the core pressure which would send the PAR to below 1. One would expect this ratio to be greater than 1 in the post breakdown flow as well, for it too is a stable rotating vortex.

Lastly, the data from the present tests and the corresponding similar geometry planform results from other investigators is presented in Figure 5.61. The majority of the ratio 2 PAR values are slightly above 1. Values derived from the five hole probe data of Verhaagen and van Ransbeeck (1990) registers larger values of the ratios due to their larger magnitude Cpt values. The cross wire data shows similar trends for both the ratios, a relatively constant value, followed by a sharp increase after x/c = 0.7. The $\alpha = 30°$ cross wire data indicates a similar trend.

No strong trends are readily evident from the results of this pressure acceleration ratio. The values are all seen to be greater than unity which would be expected in the stable vortex flow, but the expected drop towards one as breakdown approached was not observed. More data is required, especially near the breakdown zone, and instantaneous velocities and pressures are required for the breakdown region itself. In addition the pressure and velocity should be recorded simultaneously. The unsteady nature of the flow in the breakdown region precludes any evaluation as to the instantaneous, local state of the flow, based on time averaged measurement techniques.
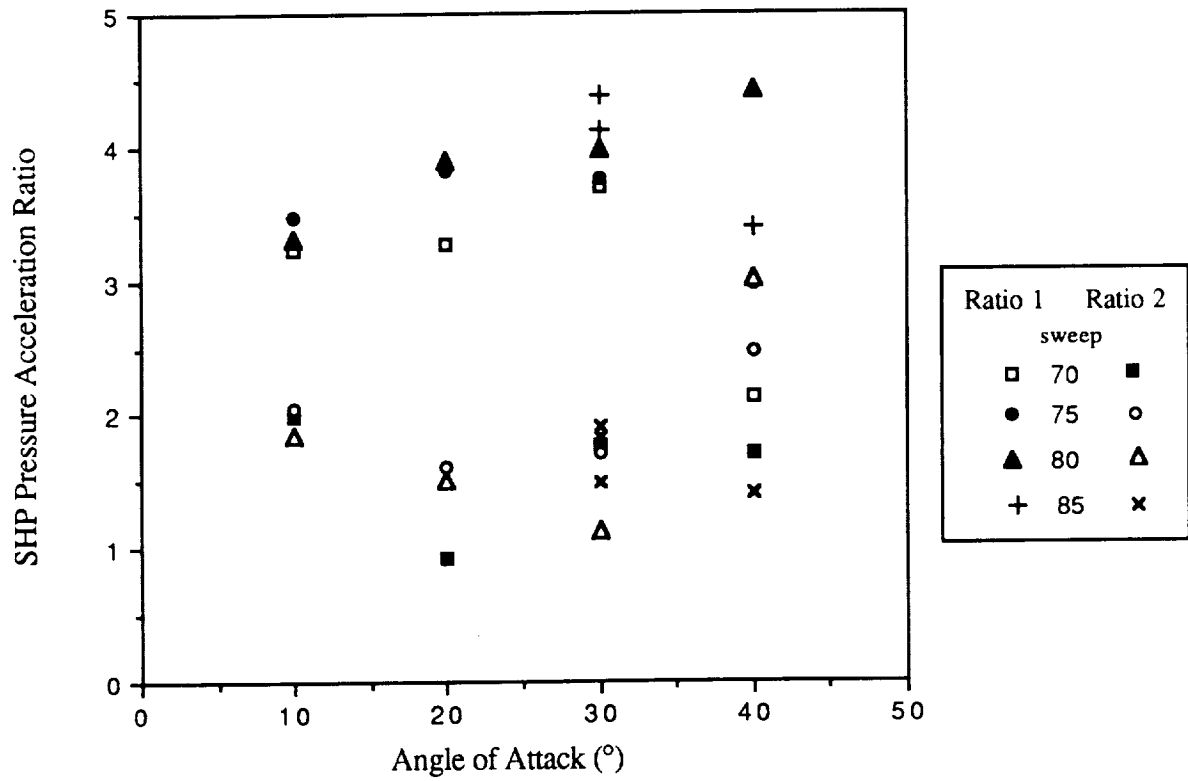
a)
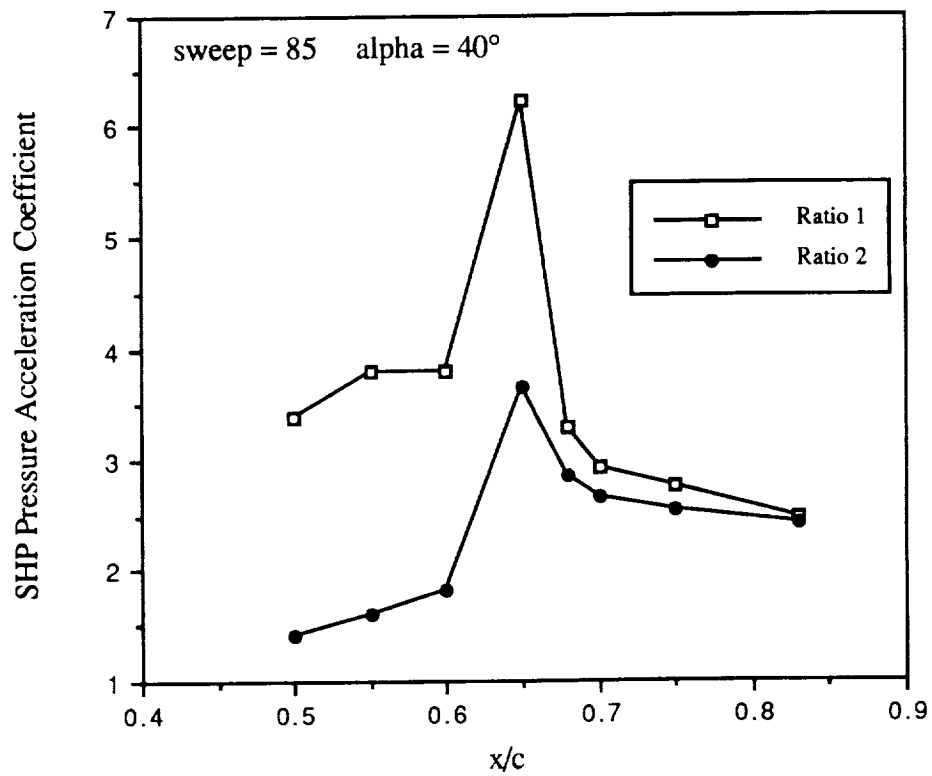
b)

Figure 5.60 Seven Hole Probe Pressure Acceleration Ratio
a) Incidence Dependence b) Chordwise Distribution
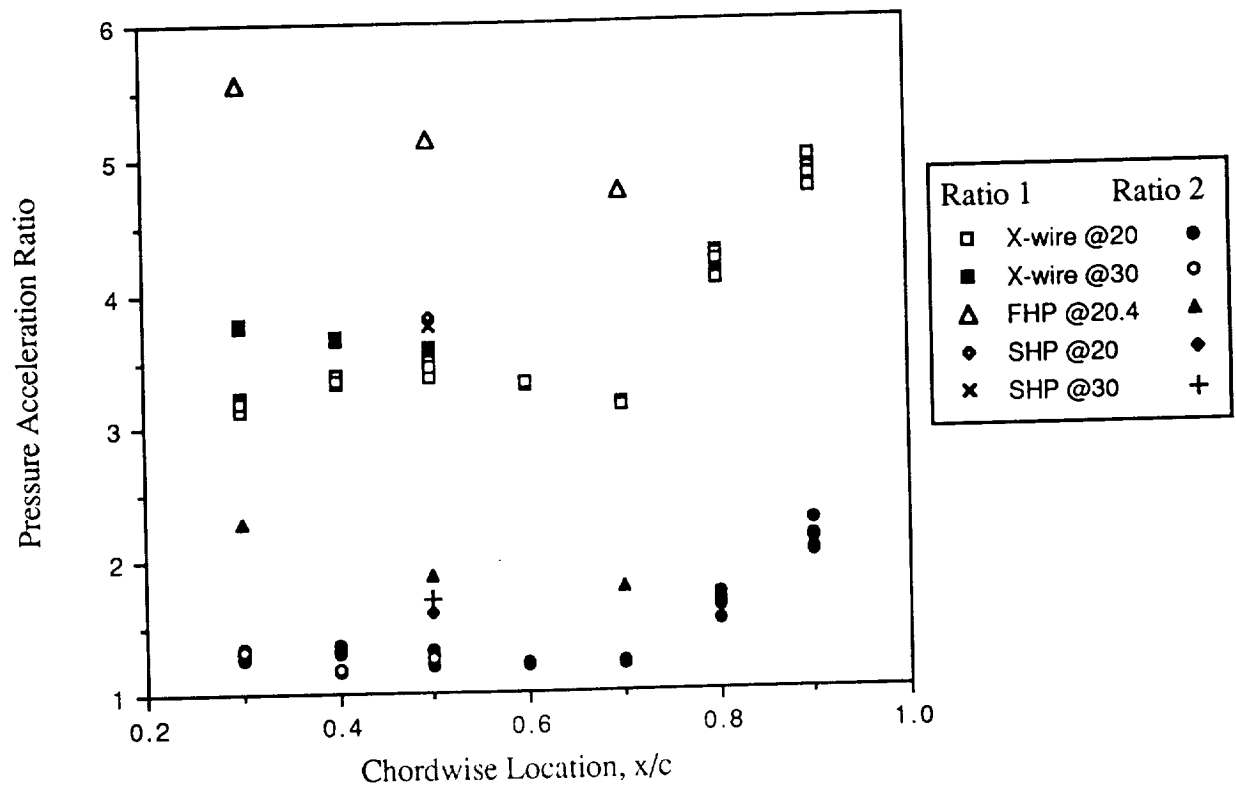
Figure 5.61 Pressure Acceleration Ratio at $\Lambda = 75°$ $\alpha = 20$

Although the above correlations do not give strong indications of the impending breakdown downstream of their position, this is not to say that they should be disregarded in evaluating the flowfield. The data used to derive these correlations is based on averaged quantities which were obtained at different times. In the broadest sense, they do indicate that the flow is in a stable condition and not about to breakdown, which is true since the data was acquired in a region of the flow upstream of the breakdown region. More data is required to properly evaluate the effectiveness of such parameters.

The results of the present study have led to several conclusions, mostly dealing with the vortex flowfield upstream of the breakdown region. The velocity fields have been compared and

discussed. The values of vorticity and circulation, as well as their spatial distributions, are good indicators of the flow variation in the chordwise direction. The breakdown region is seen to alter these values and distributions in a significant way. Dimensional scaling has been demonstrated to provide a means for correlating the vortex behavior . The conclusions of this study are summarized in a more complete form in the following chapter. In addition, several comments are made concerning the role of the vorticity and circulation in creating the flow conditions necessary for breakdown.

CHAPTER VI

CONCLUSIONS

The preceding discussion strongly supports the belief held by many investigators, both experimental and theoretical, that the flow over a delta wing, upstream of the breakdown regions and away from the apex and trailing edge regions, behaves in a conical manner. That is, properties remain constant along rays emanating from the apex. Dimensional scaling of the radial circulation distribution by the local semispan indicates the flow properties to be similar at each chordwise location for regions of pre-breakdown vortex flow. Spanwise vorticity and velocity distributions based on a single traverse through the core of the vortex also scale with the local geometry in the pre-breakdown state. This is a good indication that the local semispan is a representative length scale which should be included with any nondimensionalization scheme used to examine flows generated by swept leading edge geometries.

Further evidence of the conicity of the flow field is supplied by the nearly linear increase in strength of the vortex, at a given radius from the core axis, with distance from the apex. For a fixed chordwise station, the dependence of circulation on the angle of incidence was also found to increase linearly. The relation of the form examined by Hemsch and Lucking appears to provide one of the best correlations of the present data, as well as that found in the literature, over a wide range of test conditions. The correlation parameters indicate the sensitivity of the flow to the slenderness of the planform and incorporates both the effects of sweep and angle of attack. Inclusion of the relative chord location, x/c, as shown in the present study, accounts for regions where the vortex size and strength are increasing, such as over a delta wing.

This increase in strength is inevitably followed by breakdown which was seen to reduce the circulation about the vortex axis. The local concentration of axial vorticity is reduced while the azimuthal vorticity deceases throughout the breakdown zone. This supports the theory of Brown and Lopez (1988), who postulate that the physical mechanisms involved in breakdown rely on the production of negative azimuthal vorticity resulting from a tilting and stretching of the predominantly axial vorticity vector.

The nature of the flow to follow a conical behavior has been an underlying assumption in many theoretical derivations, including Stewartson and Hall (1963) and Mangler and Weber (1967). Some of these analysis, such as Stewartson and Hall, also employ a cylindrical subcore region. Flow visualization and to a certain extent the measured core diameters of the present tests, indicate that this cylindrical assumption is a realistic approximation. The best agreement for either of these geometrical flow considerations applies over the central portion of the planform, that is away from the apex and trailing edge regions. This was also shown to be the case with the experimental data of by Verhaagen and van Ransbeeck (1990). Near the apex, the geometry of the flat plate delta wing is such that the span of the wing is on the order of the thickness. The shape that the flow senses resembles that of a blunt body rather than a slender,thin planform and deviations from a conical flow assumption can be expected. In the same manner, the flow is altered as it approaches the trailing edge by the pressure recovery of the flow. The reversed flow regions, indicated by the surface visualization, support the presence of these effects. Overall, however, the majority of the flowfield properties are of a conical form, outside of the subcore region, and the use of this approximation in a theoretical analysis is valid. It should be kept in mind that this applies to the primary vortex structure. The flow near the surface is subject to changes depending on the nature of the boundary layer. The secondary vortex also appears to scale with the flow geometry, but flow visualization pictures have revealed some form of transition at a given chordwise location. Whether this is a form of breakdown of the secondary or not could not be determined with the present measurement techniques.

Several other conclusions were reached and are summarized below:

a) The use of the present cross wire technique, employing four spatial passes and two different probe configurations for a single survey, was satisfactory in measuring the flow conditions and establishing trends of the pre-breakdown flow. Velocity profiles obtained with the cross wires compared well with previous seven hole probe and laser doppler anemometry data taken using the same planforms.

b) The grid resolution at which experimental data is acquired must be accounted for when comparisons of data are made. This is especially so if point values are to be reported which result form discrete differentiation of the data. In the present study, the grid resolution of the cross wire data was 30% finer than the seven hole probe data and this resulted in an increase in the maximum vorticity of over 60%.

c) The circulation profiles for the present tests exhibited a logarithmic dependence on radial distance from the core axis. The slopes of the different configurations appeared to follow the form $2\dfrac{\sin(\alpha)}{\sin(\Lambda)}$ for the planforms investigated.

d) Although the axial vorticity distribution is severely altered as the breakdown region is encountered, there appears to be some maximum in the spanwise vorticity distribution that occurs in the region just preceding breakdown.

e) The majority of the positive axial vorticity is confined to the subcore region of the vortex in the pre-breakdown vortex state. The use of the maximum value of axial vorticity is deceptive in determining the local strength of the vortex structure, because it is a point property and dependent on the grid resolution.

f) The trends in the negative axial vorticity distributions, which are concentrated in the secondary vortex region, remained similar for the different configurations investigated in the present study, despite geometric and angle of attack differences. Adjustment of the flowfield to changing test conditions, such as angle of attack occurred for the most part in the positive axial

vorticity regions. In addition, the magnitude of the negative axial vorticity was similar for all three test cases.

g) Two vortex core definitions were examined using the present cross wire data: a jet core, based on the diameter of the vortex within which the axial velocity was greater than $u/U_\infty = 1.5$, and subcore, defined as the distance between the maximum and minimum tangential velocities in the core. In general, both cores gave indications of an increase in size with distance from the apex and the growths rates appeared to be scaling with the local semispan. The jet core size remained constant aft of approximately 70% of the chord to the trailing edge. Finer grid resolution data and flow visualization results suggested that the subcore maintains a constant diameter over the central regions of the planform as reported by Verhaagen and van Ransbeeck (1990).

h) The surface pressure distribution, as measured along rays underneath the vortex core, give virtually no indication of the onset or passage of breakdown.

i) The surface flow directly inboard of the leading edge and outboard of secondary attachment line indicates a flow direction inwards from the trailing edge, towards the wing centerline, and in the axial direction. If the flow is in a direction towards the leading edge, the axial component of the flow would need to be in a direction opposite to that of the oncoming stream.

j) The maximum axial velocity on the 75° sweep planform at 20° angle of incidence maintains a value between $u/U_\infty = 2.0$ to 2.5 over the majority of the wing, dropping off in the vicinity of the apex and the trailing edge . The maximum value of the axial velocity was also seen to maintain a constant value for some distance upstream of the breakdown region for the planforms exhibiting breakdown.

k) The power spectrum revealed a distinctive frequency peak between 250 and 500 Hz in all the pre-breakdown axial flow signals.

The results of this study and others, along with theoretical discussions in the literature, suggest that there are two significant conditions in the flow which will cause breakdown to occur:

the amount of local circulation present and the distribution of the external pressure field. Both of these are equally important, however it is felt that the initiation of breakdown is most sensitive to the latter. Whether this is the local adverse gradient at the trailing edge, the gradient in the external flow, or the result of an object in the downstream, this is felt to be the single most important factor for initiating breakdown, provided the vortex is near the point of criticality in terms of strength. All breakdown location versus chordwise station plots are very flat as they near the trailing edge. The breakdown rarely maintains a position at the $x/c = 1.0$ position. Instead, it will move to approximately $x/c = 0.8$ an then continue upstream. It must overcome some type of 'barrier' at the trailing edge, which is surmised to be the pressure gradient at the trailing edge as the flow recovers to freestream at the surface of the wing. This is also one of the primary reasons for the hysteresis effects in breakdown location that are seen with regard to breakdown location pitching up or pitching down. Furthermore, this sensitivity to the pressure of the flowfield is felt to be the main cause for discrepancies that appear in the literature for locating the breakdown. Models are generally constructed with great accuracy and angles of incidence are set with ± 0.1 degree in some instances. Yet locations can vary by as much as 25% of the chord as compiled by Kegelman and Roos (1989). Hall (1966) has shown that pressure gradients at the edge of the vortex core are amplified at the centerline as a result of the substantial swirl velocities. This causes the centerline flow to be very sensitive to the local environment. Hence a discrepancy in measurements could easily arise if the tunnel pressure gradients vary, especially in smaller tunnels.

The second flow condition that defines the the state of the vortex, with respect to breakdown, is its circulation at a certain chordwise location. This was especially seen to be influential for tube vortices. Increasing the circulation eventually caused breakdown. This is also the case with respect to delta wings. An increase in angle of attack, or a sweep decrease, causes the vortex to strengthen and breakdown follows, proceeding toward the apex with increasing incidence. Yet the circulation alone can not be responsible for breakdown. The breakdown location occurring on a delta wing planform at a fixed angle of attack can be easily displaced

towards the apex by the creation of an adverse pressure gradient downstream of the model itself as demonstrated by Delery, Pagan and Solignac (1987). The circulation required for breakdown to occur has now been reduced. Thus, even the presence of the trailing edge and the accompanying local pressure gradient could be crucial to the location and onset of the breakdown.

Whether the flow exists in the pre or post-breakdown state, the position of breakdown inevitably depends on some equilibrium with regard to the the forces in the vortex. The simplest explanation for the dominating factors in this balance of forces are the radial pressure gradient and the centripetal acceleration of the fluid. The state of the external environment which governs the balance of these forces determines the state of the vortex. On the pressure side, the gradient is determined by the pressure field outside the vortex and along the core. An external gradient in the chordwise direction could appreciably influence the pressure and of course the state of the vortex. A local rise in the pressure along the core axis will also initiate breakdown, whether this happens to be the effect of the trailing edge or an object placed in the path of the vortex downstream of the trailing edge. The geometry of the delta wing sets up the velocity field above the planform. Vorticity is continually being added to the vortex from the leading edge. The circulation is seen to increase with angle of attack, distance from the apex, and a decrease in the sweep angle, and the accompanying increase in the centripetal acceleration required to keep the fluid on the rotational path is second order in nature. Lambourne and Bryer noted in 1961 that an increase in the vortex strength reduced the axial pressure. The majority of correlations evaluated to date involve only the circulation or swirl of the flow but not the pressure forces directly. Recall that no evidence of the onset of breakdown is present in the Hemsch and Lucking relationship and that only the circulation is examined. The present attempt to derive a relationship incorporating both the centripetal acceleration, or strength of the vortex, and the effects of the pressure distribution only indicated that the vortex was stable at the measured locations, but did not indicate that some critical condition in the flow was imminent. Yet it is felt that this type of relationship, possibly using instantaneous values of velocity and pressure, would indicate that breakdown was forthcoming.

Many fundamental questions, arising from the simplest observations, still remain unanswered. Although some researchers may disagree, it has been shown that tracer particles introduced into the core are not centrifugally 'spun out' as seems to be indicated by upstream smoke injection techniques. Neither is smoke entrained into the subcore region if introduced about the delta wing, except at the apex. In fact there appears to be no significant mass diffusion to or from the subcore region once the vortex has been established and begins to grow. Does this imply that all the fluid in the subcore region arrives from a streamline impinging on the apex? Although the Reynolds number effects are reportedly small on the overall flow, above a certain value, there is an effect, which has not been thoroughly quantified, on the reduction of the subcore size as noted by Leibovich (1984). Since this is the region of viscous flow it might make more sense to define a Reynolds number characteristic of the flow based on the core diameter and not some fixed geometry such as the wing chord. Additional questions on the flow also need to be addressed. Why does the vortex initially assume the intense, pre-breakdown form and not the post breakdown form? How is the vorticity transported into the subcore region? Is viscous diffusion at the interface of the viscous subcore with the outer flow the sole means for vorticity transport? Regarding the last question, it has been shown that the strength of the vortex is growing as it progresses along the delta wing, indicating a definite transport of vorticity to the core region The manner in which this occurs has generally been assumed to be via the shear layer. Flow visualization indicates, however, that streamlines emanating from the leading edge shear layer never spiral directly into the core, but follow trajectories about the along a cone projecting from the apex.

Furthermore, what really occurs along a streamline path that impinges on the apex, and is subsequently redirected into the core, to cause so great a loss in the total pressure? A simple evaluation of the drop in total pressure associated with a solid body rotation yields $\Delta C_{p_t} = -(V_\phi/U_\infty)^2$. For a V_ϕ of 1.5 the $\Delta C_{p_t} = -2.25$. This is not enough to account for the measured drop in the pressure data. The drop in the total pressure implies substantial losses somewhere.

The apex seems to be the only logical location. If this is so, the importance of the geometry of the apex takes on a greater significance. If it is possible to tailor such geometry to the point where the drop in the total pressure is maximized, the static pressure in the core will drop accordingly, enabling larger lift.

With respect to further investigations, several suggestions are offered. The first pertains to the measurement procedures. The number of spatial passes required for a measurement plane must be reduced, preferably to one. Although techniques such as a three component LDV are desirable, they have their own problems and intrusive probes have indicated the ability to make comparable measurements. The size of the probe is crucial and efforts should be aimed at the smallest probe possible that can measure a completely unknown velocity vector. To incorporate these constraints may even require the design of a new form of velocity detection measurement probe.

Instantaneous measurements appear to be essential in understanding completely what is occurring in the pre and post-breakdown flow. The flow upstream of breakdown exhibits a quasi-steady nature and many investigators have used time averaged measurement techniques as a valid approach to understanding the flow. The breakdown phenomena does not appear to transmit substantial time averaged information upstream, at least based on the parameter evaluations considered here. The oscillatory nature of the breakdown zone remains unresolved. Conditional sampling and spatial correlation techniques could be used to determine the reasons for this fluctuation in breakdown location. The indication that the radial circulation distribution follows a logarithmic behavior points the way to an evaluation of the Reynolds stress field. Instantaneous pressures as well as velocities are a must to properly examine the concept of pressure acceleration ratios .

Secondly, comparative experiments should us as big a model as is possible under the circumstances to increase the resolution of the probe itself. The half span measurements of

Verhaagen and van Ransbeeck (1990) use a model 2.22 m in length compared to the present test size of under one half meter. Yet they report a subcore diameter of under 9 mm, on the same order as the present tests.

Finally, the condition of the streamwise pressure gradient bears further study in light of the possible sensitivity of this flow to this condition. A study using artificially imposed gradients would indicate the extent of influence that this parameter has on the vortex flow and help to establish bounds for actual test conditions.

APPENDIX A

DELTA WING VORTEX DATA

Anders, K., " LDV Measurements of the Velocity Field of a Leading Edge Vortex Over a Delta Wing Before and After Vortex Breakdown" Von Karman Institute for Fluid Dynamics, Technical Note 142, March 1982
- wind tunnel, Re = 170,000, U_∞ = 18 - 19.5 m/s
- flat plate, 137.5 mm chord, 1.5 mm thick, 8.5° stnd bevel
- aspect ratio = 1.6, Λ = 68.2;
- LDA core traversals:

$$\alpha = 19.3 \; ; \; x/c = 0.67, 0.74, 0.82, 0.93, 1.0$$

$$\alpha = 28.9 \; ; \; x/c = 0.55, 0.65, 0.73, 0.88, 1.0$$

Anderson, M.W., Beran, P.S., and McCann, M.K. "Vortex Breakdown Over Delta Wings" Graduate Aeronautical Laboratories, California Institute of Technology, Pasedena, CA 91125, 1983
- water tunnel, dye injection, U_∞ = 0.5 ft/s
- flat plate, 7.8 - 15" chord, 1/16 - 1/4" thick, 26.6 - 33.7° stnd bevel
- Λ = 64.8, 75, 80, 85 ; α = 20, 25, 30, 35, 40, 42, 45

Carcaillet, R., Manie, F., Pagan, D. and Solignac, J.L. "Leading Edge Vortex Flow Over a 75 Degree-Sweep Delta Wing- Experimental and Computational Results." ICAS 86.
- water tunnel, dye injection, U_∞ = 40 m/s, Rec = 4e06
- flat plate, 0.5 m, 1.45 m chord, 20° stnd bevel
- Λ = 75 ; α = 20
- LDV,five hole probe, surface pressure measurements

Chigier, Norman A., "Measurement of Vortex Breakdown Over a Delta Wing Using a Laser Anemometer" NEAR TR 62, Nielsen Engineering and Research Inc., Mountain View, Ca. June 5, 1974.
- wind tunnel, Re = unknown, U_∞ = unknown
- flat plate, 137.5 mm chord, 1.5 mm thick, symmetrical bevel
- aspect ratio = 1.46, Λ = 70; α = 20, 25, 35
- LDA core traversals:
  x/c = 0.71, 0.789, 0.868, 1.507

Earnshaw, P.B. and Lawford, J.A. "Low Speed Wind Tunnel Experiments on a Series of Sharp Edged Delta Wings" ARC R & M, No 3424, March 1964.
- wind tunnel, Re = 200,000 - 400,000, U_∞ = 80 ft/s
- plano/convex, 0.589 - 1.178 ft chord,

- $\Lambda = 45, 55, 60, 65, 70, 76$; $\alpha = 12 - 37$
- force, surface flow vis.

Elle, B. J. "An Investigation at Low Speed of the Flow near the Apex of Thin Delta Wings with Sharp Leading Edges " ARC   R & M, No 3176, January 1958.

- water tunnel, air bubbles, Re = 700,000, $U_\infty = 12$ ft/s
- flat plate, 1/16" thick, 7° stnd bevel
- $\Lambda = 70$ half span ; α = varied

Elsenaar, A., Hjelmberg, L., Bütefisch, K., and Bannik, W.J. "The International Vortex Flow Experiment" 1988 in Portugal

- water tunnel, air bubbles, Re = 700,000, $U_\infty = 12$ ft/s
- flat cropped delta w/ NACA 64A005 profile , 1/16" thick, 7° stnd bevel
- $\Lambda = 55,65$ full span ; α = varied, M= 0.4 to 4.0
- LDV,five hole probe, force, surface pressure measurements;
      surface flow vis.

Erickson, Gary E., "Vortex Flow Correlation",Technical Report AFWAL-TR-80-3143 Flight Dynamics Laboratory, Wright Patterson Air Force Base, January 1981

- water and wind tunnels, various Re, Λ,
- many different configurations

Hummel, D., and Srinivasan, P.S. "Vortex Breakdown Effects on the Low-speed Aerodynamic Characteristics of Slender Delta Wings in Symmetrical Flow" <u>Journal of the Royal Aeronautical Society</u> Vol.71 April.

- wind tunnel, Re = 1.4e06 - 1.7e06, $U_\infty = 40$m/s
- flat upper and beveled lower surfaces, triangular cross section
   0.52 and 0.625 m chord
- $\Lambda = 60, 68.2$; α = varied

Hummel D. "On the Vortex Formation Over a Slender Wing at Large Angles of Incidence" AGARD CP-247 January 1979, pp.15-1 - 15-7.

- wind tunnel, Re = 2e06
- flat upper and beveled lower surfaces, triangular cross section, 750 mm chord
- aspect ratio = 1.0, $\Lambda = 76$; $\alpha = 20.5$
- surface pressure measurements
- Five Hole Probe grid surveys:
      in 4 planes behind the wing trailing edge

Iwanski, Kenneth P., "An Investigation of the Vortex Flow over a Delta Wing With and Without External Jet Blowing" Masters Thesis, University of Notre Dame, April 1988.

- wind tunnel, Re = 150,000
- flat plate, 15.85" chord, 1.0" thick, 45° stnd bevel
- $\Lambda = 70$; $\alpha = 30$
- LDA core traversals:
      x/c = 0.15, 0.225, 0.3, 0.375, 0.411, 0.448, 0.484, 0.521, 0.557, 0.593

Kirkpatrick, D.L. "Analysis of the static Pressure Distribution on a Delta Wing in Subsonic Flow" ARC R&M 3619 1970

- wind tunnel, U_∞ = 120 ft/s, Re = 3.15e06
- symmetrical X-section, max t/c = 0.048, 50" chord

- Aspect Ratio 1.616, Λ = 68; α = -2° - 26°
- Surface Pressures

Kegelman, J.T. and Roos, F.W. "The Flowfield of Bursting Vortices over Moderately Swept Delta Wings" AIAA Paper 90-0599 Jan 8-11, 1990 Reno, NA.
Kegelman, J.T. and Roos, F.W. "An Experimental Investigation of Sweep Angle Influence on Delta Wing Flows" AIAA Paper 90-0383 Jan 8-11, 1990 Reno, NA.

- wind tunnel, Re = 0.3e06 - 2.0 e06, U_∞ = 10 m/s

- Λ =60, α = 12 - 20; 70, α = 25 - 33
- flat plates, 24" (60°) and 30" (75°), 0.5 " thick, 25° stnd bevel
- LDA, SHP, surface pressures, flow visualization

Kjelgaard, S. and Sellers, W.L. III, "Detailed Flowfield Measurements over a 75° Delta Wing For Code Validation" NASA Langley Research Center, Hampton, Virginia NASA TN 2997

- wind tunnel, Re = 0.5e06, 1.0e06, 1.5e06,U_∞ = 30 ft/s

- flat plate, 22.392" chord, 0.3" thick, 10° stnd bevel

- Λ = 75; α = 20.5;
- LDV, surface vis, total pressure, five hole probe,
      x/c = 0.7, 0.9, 1.1

Lambourne, N. C., and Bryer, D. W., "The Bursting of Leading Edge Vortices-Some Observations and Discussion of the Phenomena," Aeronautical Research Council, Reports and Memoranda, No. 3282, 1962.

- wind and water tunnel, Re = 10,000 - 4.6e06, U_∞ = 80 ft/s
- flat and cambered plates, 3.1, 8, 8.5, 47.5 " chord, 16° bevel

- Λ = 50, 65 ; α = 16 - 28

McKeman, J.F. and Nelson R.C. "An Investigation of the Breakdown of the Leading Edge Vortices on a Delta Wing at High Angles of Attack" Masters Thesis, University of Notre Dame, January 1983.

- wind tunnel, Re = 225,000
- flat plate, 16" chord, 0.75" thick

- Λ = 70 ; α = 20, 25, 30, 35, 40 ; β = 0 - 12 in 1° increments

Naarding S.H.J. and Verhaagen, N. G. "Experimental and Numerical Investigation of the Vortex Flow Over a Sharp Edged Delta Wing with and without Sideslip" Delft University Report LR-573, December 1988.

- wind tunnel, Re = 2.5e06, U_∞ = 44 m/s
- biconvex, 850 mm chord
- aspect ratio = 1.0, Λ = 75.96 ; α = 21.1 ; β = -20 - 20
- force, surface pressure, five Hole Probe, Laser light sheet, surface vis

Pagan, D. and Solignac, J.L. "Experimental Study of the Breakdown of a Vortex Generated By a Delta Wing" La Recherche Aérospatiale, No 3, May-June 1986.
- wind tunnel, Re = 580,000,U_∞ = 14.5 m/s
- flat plate, 560 mm chord
- Λ = 75; α = 19.3
- LDA and Five Hole Probe in the far wake and breakdown in wake

Payne, F. M. "The Structure of Leading Edge Vortex Flows Including Vortex Breakdown" PhD Dissertation, University of Notre Dame, May 1987.
- wind tunnel, Re = 255,000,U_∞ = 30 ft/s
- flat plate, 16" chord, 0.25" thick, 25° stnd bevel
- α = 10, 20, 30, 40
- LDA and SHP core traversals:

Λ = 70, 85, x/c = 0.5 α = 10, 20, 30, 40

Λ = 85, α = 40, x/c = 0.55, 0.6, 0.65, 0.675, 0.7, 0.75
- SHP grid surveys (normal to model):

Λ = 70, 75, 80, 85, x/c = 0.5 α = 10, 20, 30, 40

Λ = 85, α = 40, x/c = 0.55, 0.6, 0.65, 0.675, 0.7, 0.75

Peckham, D.H. "Low-Speed Wind Tunnel Tests on a Series of Uncambered Slender Pointed Wings with Sharp Edges" ARC R&M 3186 N62-10253, Report Aero 2613, December 1958.
- wind tunnel, Re = 2.3e06 - 8.6 e06,U_∞ = 80 - 300 ft/s
- flat plates, biconvex, thick wings 100" chord, 0.25" thick, 25° stnd bevel
- Λ = 76,gothic ; α = 10, 20, 30, 40
- pressure, force balance, surface flow visualization

Schrader, K. F., Reynolds, G. A., and Novak, C. J. "Effects of Mach Number and Reynolds Number on Leading-Edge Vortices at High Angle of Attack" AIAA Paper 88-0122 January 11-14, 1988.
- wind tunnel, Re = 0.25e06 - 10 e06,U_∞ = 80 - 300 ft/s
- flat plate, sharp edge, 20.3 cm chord
- Λ = 63; α = 0 to 33
- LDV, force balance, surface pressure, surface flow visualization

Sforza Data??

Thompson, D.H. "A Water Tunnel Study of Vortex Breakdown Over Wings with Highly Swept Leading Edges" Australian Defence Scientific Service Note ARL/A. 356 May 1975
- water tunnel, dye injection, Re = 9,800,U_∞ = 74 mm/s
- flat plate, 150 mm chord, 1.8 mm thick, symmetrical 30° included bevel
- Λ = 60, 65, 70, 75, 80; α = prebreakdown - 45

Verhaagen, N.G.. "An Experimental Investigation of the vortex Flow Over Delta and Double Delta Wings at Low Speed" Delft University of Technology Report LR-372 Sept 1983, Delft, The Netherlands AGARD-CP-342 Aerodynamics of Vortical Type Flows in Three Dimensions, April 1983.
- wind tunnel, Re = 1.4e06 ,U_∞ = 30 m/s

    - flat plate, sharp edge, 20.3 cm chord

    - $\Lambda = 76$; 76/60, 76/40 double delta wings, $\alpha = 5$ to 25

    - force balance, , surface oil flow visualization, laser light sheet

Vorropoulos,G. and Wendt, J.F.,"Preliminary Results of LDV surveys in the Compressible Leading Edge Vortex of a Delta Wing" Von Karman Institute for Fluid Dynamics, Technical Note 137, August 1982

    - wind tunnel, $M_\infty = 0.4, 0.62, 0.80$

    - flat plate, 150 mm chord

    - aspect ratio = 2.0, $\Lambda = 63.4$; $\alpha = 10$

    - LDA grid surveys:

            x/c = 0.8, 0.6, 1.0

Wentz, W.H. "Wind Tunnel Investigations of Vortex Breakdown on Slender Sharp Edged Wings" PhD Thesis, University of Kansas, 1968

    - wind tunnel, Re = 1e06

    - flat plate, 13 models, $15°$ stnd bevel

    - $\Lambda = 50 - 85$; α = varied

FullSpan sweep: 75   Re: 250000   Δy/s: 0.03   y/s: 0 to 1.2
          chord: 406.4 mm   Δz/s: 0.03   z/s: surface to 1

alpha	x/c	filename	u / U∞ Min	Max	v / U∞ Min	Max	w / U∞ Min	Max	Max u/U Core @ y/s	@ z/s	Axial Vorticity (spn/U∞) Min	Max	Circulation 1/U∞chord r/s = 0.6	1/U∞span r/s = 0.6	Rsby #	Rsby√2	Rsby mx.	Integrated dim spn	Convection dim crd	d subcore y/s	mm	d jetcore y/s	mm	Comments:
20	0.20	02/05.dat	0.56	2.05	-1.14	1.38	-1.38	1.21	0.72	0.38	-48.08	62.02	0.11	2.05	0.88	1.07	0.73	1677.09	31294.82	0.090	1.960	0.231	5.024	
20	0.30	20/04.dat	0.35	2.27	-1.02	1.48	-1.36	1.47	0.66	0.36	-42.92	75.48	0.16	1.97	0.87	0.78	0.67	-	-	0.090	2.940	0.222	7.246	
20	0.30	11/05.dat	0.38	2.25	-0.84	1.42	-1.24	1.17	0.66	0.36	-15.39	64.75	0.16	2.00	1.56	1.29	0.77	1693.71	21070.10	0.090	2.940	0.262	8.544	
20	0.40	12/04.dat	0.52	2.33	-0.93	1.48	-1.25	1.28	0.69	0.37	-30.88	65.67	0.20	1.91	1.60	1.18	0.79	1595.78	14888.79	0.090	3.920	0.24	10.47	
20	0.41	13/04.dat	0.41	2.28	-0.90	1.39	-1.27	1.25	0.66	0.37	-35.84	72.28	0.21	1.89	1.56	1.05	0.53			0.120	5.358	0.248	11.1	
20	0.42	14/04.dat	0.31	2.30	-0.91	1.40	-1.25	1.23	0.66	0.40	-29.40	62.90	0.24	2.10	0.94	0.89	0.49			0.150	6.860	0.268	12.27	
20	0.43	16/04.dat	0.46	2.29	-0.88	1.48	-1.34	1.29	0.66	0.36	-30.50	75.11	0.24	2.04	1.56	1.02	1.02			0.060	2.809	0.25	11.71	
20	0.43	04/05.dat	0.50	2.26	-1.09	1.44	-1.20	1.62	0.66	0.36	-42.93	51.58	0.24	2.10	1.27	0.99	0.73			0.120	5.619	0.24	11.24	
20	0.43	07/05.dat	0.41	2.29	-0.81	1.44	-1.23	1.19	0.66	0.36	-40.47	66.17	0.22	1.87	1.48	1.16	0.77			0.090	4.214	0.22	10.31	
20	0.44	17/04.dat	0.39	2.29	-1.04	1.40	-1.22	1.21	0.66		-39.79	70.10	0.23	1.99										Skewed core
20	0.45	18/04.dat	0.44	2.42	-0.81	1.45	-1.15	1.36	0.66	0.36	-32.03	68.10	0.24	1.95	0.96	0.86	0.59			0.120	5.880	0.22	10.77	
20	0.47	23/04.dat	0.51	2.47	-0.80	1.51	-1.33	1.25	0.66	0.36	-35.21	72.89	0.23	1.80	1.39	1.13	0.75			0.090	4.606	0.249	12.11	
20	0.47	17/05.dat	0.52	2.46	-0.91	1.41	-1.10	1.17	0.66	0.36	-16.62	63.37	0.25	2.02	0.96	0.88	0.86			0.090	4.606	0.249	12.77	
20	0.48	03/05.dat	0.38	2.35	-0.96	1.44	-1.36	1.30	0.66	0.39	-31.74	74.84	0.27	2.06	1.06	0.95	0.42			0.150	7.840	0.263	13.72	
20	0.49	2324.dat	0.45	2.35	-0.84	1.41	-1.16	1.20	0.66	0.36	-41.09	70.82	0.23	1.76	0.90	0.81	0.74			0.090	4.802	0.234	12.47	
20	0.50	11/04.dat	0.37	2.33	-0.92	1.38	-1.25	1.19	0.69	0.40	-27.61	69.31	0.29	2.13	1.18	0.87	0.56	1846.41	13781.78	0.120	6.534	0.213	11.58	
20	0.50	19/04.dat	0.42	2.42	-1.08	1.46	-1.43	1.37	0.69	0.39	-31.62	73.87	0.27	2.05	0.93	0.60	0.36	1719.28	12838.88	0.180	9.801	0.245	13.31	
20	0.60	24/04.dat	0.46	2.30	-0.85	1.43	-1.19	1.25	0.66	0.35	-16.08	66.95	0.31	1.92	0.87	0.81	0.76	1644.66	10229.90	0.090	5.880	0.205	13.39	
20	0.63	23/05.dat	0.44	2.50	-0.82	1.37	-1.18	1.32	0.66	0.37	-19.88	69.66			0.97	0.82	0.60			0.120	8.232	0.228	15.67	
20	0.67	24/05.dat	0.39	2.41	-0.98	1.54	-1.25	1.43	0.66	0.37	-30.17	80.48			1.01	0.84	0.40			0.150	10.944	0.228	16.64	skewed core
20	0.70	30/04.dat	0.45	2.34	-0.80	1.34	-1.18	1.26	0.66	0.37	-18.56	60.58	0.34	1.82	2.33	1.54	0.64	1553.38	8281.85	0.120	9.147	0.191	14.58	
20	0.70	21/05.dat	0.39	2.32	-0.91	1.43	-1.51	1.38	0.66	0.37	-17.98	85.79			0.96	0.80	0.36	1789.61	9541.29	0.150	11.434	0.204	15.55	
20	0.75	25/05.dat	0.28	2.33	-0.88	1.34	-1.29	1.25	0.66	0.37	-25.89	70.11			0.91	0.82	0.74			0.090	7.350	0.188	15.32	
20	0.80	01/05.dat	0.40	2.36	-0.79	1.34	-1.02	1.19	0.66	0.37	-19.00	64.33	0.38	1.76	0.96	0.85	0.61	1494.77	6973.18	0.120	10.454	0.176	15.32	
20	0.90	29/05.dat	0.24	2.26	-0.98	1.23	-1.10	1.19	0.63	0.37	-22.42	67.27			0.87	0.81	0.56	1438.05	5963.20	0.120	11.761	0.146	14.33	
20	1.10	30/05.dat	0.29	2.10	-0.75	1.27	-0.87	1.53	0.60	0.36	-13.00	69.66			1.51	1.02	1.01			0.060	7.187	0.096	11.52	
30	0.30	14/04.dat	0.39	3.38	-1.22	2.07	-1.84	1.93	0.66	0.42	-22.20	111.20			0.93	0.85	0.67	2178.10	27095.97	0.090	2.940	0.419	13.68	
30	0.40	14/05.dat2	0.44	3.49	-1.11	2.12	-2.01	1.81	0.66	0.43	-32.85	112.00			1.61	1.04	1.04	2281.44	21286.06	0.060	2.613	0.415	18.08	
30	0.50	15/05.dat	0.31	3.20	-1.17	2.00	-1.87	1.83	0.63	0.45	-22.50	98.90			0.84	0.80	0.36	2242.65	16739.37	0.180	9.801	0.391	21.27	windy
30	0.55	01/06.dat	0.25	2.82	-1.05	1.10	-1.11	1.18	0.66	0.45	-15.80	57.70			-	-78.54	1.08			0.090	5.390	0.327	19.57	breakdown
30	0.60	27/05.dat	0.23	2.32	-1.80	2.30	-1.92	1.77	0.60	0.47	-22.55	53.84			-	-	0.36	-	-	0.240	15.681	0.18	11.78	breakdown
30	0.51	1106.dat	0.00	3.22	-1.16	2.78	-1.91	3.26	0.63	0.41	-18.39	120.14			0.82	0.89	0.89	-	-	0.060	3.332	0.331	18.38	zero axial vel
30	0.49	18/06	0.34	2.87	-1.27	1.96	-1.85	2.31	0.60	0.39	-19.35	109.75			-	-	0.35	-	-	0.150	8.004	0.336	17.93	zero axial vel

FullSpan sweep: 75   Re: 250000   Δy/s: 0.015   y/s: 0.55 to 0.85
          chord: 406.4 mm   Δz/s: 0.015   z/s: 0.25 to 0.55

alpha	x/c	filename	u / U∞ Min	Max	v / U∞ Min	Max	w / U∞ Min	Max	Max u/U Core @ y/s	@ z/s	Axial Vorticity (spn/U∞) Min	Max	Circulation 1/U∞chord r/s = 0.6	1/U∞span r/s = 0.6	Rsby #	Rsby√2	Rsby mx.	Integrated dim spn	Convection dim crd	d subcore y/s	mm	d jetcore y/s	mm	Comments:
20	0.40	2208.dat	-	-	-	-	-	-	-	-	-	-								-	-			Debries in run skewed core
20	0.40	2308.dat	1.03	2.44	-0.96	1.56	-1.30	1.43	0.70	0.39	-23.60	121.12			1.34	0.91	0.54			0.08	3.27			skewed core
20	0.50	2408.dat	1.08	2.54	-0.93	1.64	-1.25	1.55	0.70	0.39	-24.18	145.90	N/A		1.26	0.95	0.39			0.09	4.90	N/A		skewed core
20	0.60	2808.dat	1.02	2.48	-1.05	1.49	-1.33	1.34	0.69	0.37	-15.60	119.88			1.06	0.94	0.55			0.08	4.90			
20	0.50	2908.dat	0.98	2.51	-0.94	1.49	-1.35	1.40	0.70	0.39	-15.90	124.10			1.12	0.75	0.34			0.12	6.53			
20	0.70	3008.dat	0.98	2.54	-0.90	1.36	-1.19	1.25	0.66	0.37	-11.83	125.98			1.06	0.99	0.45			0.09	6.86			

FullSpan sweep: 75   Re: 250000   Δy/s: 0.01   y/s: 0.55 to 0.75
          chord: 406.4 mm   Δz/s: 0.01   z/s: 0.3 to 0.5

alpha	x/c	filename	u / U∞ Min	Max	v / U∞ Min	Max	w / U∞ Min	Max	Max u/U Core @ y/s	@ z/s	Axial Vorticity (spn/U∞) Min	Max	Circulation 1/U∞chord r/s = 0.6	1/U∞span r/s = 0.6	Rsby #	Rsby√2	Rsby mx.	Integrated dim spn	Convection dim crd	d subcore y/s	mm	d jetcore y/s	mm	Comments:
20	0.60	0911.dat	1.35	2.51	-0.98	1.47	-1.29	1.36	0.69	0.37	-20.66	145.80	N/A		1.10	0.79	0.49			0.07	4.57	N/A		alignment errors
20	0.80	0911.2.dat	1.11	2.34	-0.99	1.35	-1.12	1.33	0.65	0.36	-11.10	151.60			1.08	0.79	0.31			0.10	8.71			

FullSpan sweep: 70   Re: 250000   Δy/s: 0.03   y/s: 0 to 1.2
          chord: 406.4 mm   Δz/s: 0.03   z/s: surface to 1

alpha	x/c	filename	u / U∞ Min	Max	v / U∞ Min	Max	w / U∞ Min	Max	Max u/U Core @ y/s	@ z/s	Axial Vorticity (spn/U∞) Min	Max	Circulation 1/U∞chord r/s = 0.6	1/U∞span r/s = 0.6	Rsby #	Rsby√2	Rsby mx.	Integrated dim spn	Convection dim crd	d subcore y/s	mm	d jetcore y/s	mm	Comments:
20	0.30	2006.dat	0.43	2.64	-0.96	1.70	-1.33	1.45	0.69	0.319	-18.31	80.35			1.02	0.81	0.55	1762.67	16143.02	0.120	5.325	0.276	12.23	
20	0.40	2106.dat	0.46	2.69	-0.85	1.67	-1.34	1.44	0.66	0.300	-27.12	78.07			0.93	0.83	0.76	1471.71	10108.70	0.090	5.325	0.247	14.61	
20	0.50	2206.dat	0.48	2.64	-0.95	1.63	-1.39	1.51	0.66	0.287	-21.27	86.52			1.25	1.02	1.02	1671.58	9185.28	0.060	4.438	0.232	17.18	

HalfSpan sweep: 75   Re: 250000   Δy/s: 0.03   y/s: 0.2 to 1.19
          chord: 406.4 mm   Δz/s: 0.03   z/s: surface to 0.75

alpha	x/c	filename	u / U∞ Min	Max	v / U∞ Min	Max	w / U∞ Min	Max	Max u/U Core @ y/s	@ z/s	Axial Vorticity (spn/U∞) Min	Max	Circulation 1/U∞chord r/s = 0.6	1/U∞span r/s = 0.6	Rsby #	Rsby√2	Rsby mx.	Integrated dim spn	Convection dim crd	d subcore y/s	mm	d jetcore y/s	mm	Comments:
20	0.50	1411.dat	0.44	1.98	-0.65	1.22	-1.07	1.08			-23.04	22.58										N/A		align errors

HalfSpan sweep: 75   Re: 250000   Δy/s: 0.015   y/s: 0.5 to 0.8 for 1611&1711
          chord: 406.4 mm   Δz/s: 0.015   z/s: 0.2 to 0.5 for 1611&1711

alpha	x/c	filename	u / U∞ Min	Max	v / U∞ Min	Max	w / U∞ Min	Max	Max u/U Core @ y/s	@ z/s	Axial Vorticity (spn/U∞) Min	Max	Circulation 1/U∞chord r/s = 0.6	1/U∞span r/s = 0.6	Rsby #	Rsby√2	Rsby mx.	Integrated dim spn	Convection dim crd	d subcore y/s	mm	d jetcore y/s	mm	Comments:
20	0.50	1511.1.dat	0.85	2.18	-0.82	1.27	1.05	1.42	0.66	0.33	-17.16	98.83					0.42			0.11	9.63			Off Center
20	0.50	1511.2.dat	1.16	2.28	-0.82	1.07	-1.00	1.15	0.67	0.32	-6.48	111.75	N/A				0.68			0.06	5.50	N/A		Re16" crd/oc er
20	0.50	1611.dat	1.00	2.35	-0.92	1.39	-1.09	1.13	0.65	0.32	-10.64	112.10					0.56			0.08	6.88			Re 16" chord
20	0.50	1711.dat	0.92	2.09	-0.83	1.23	-1.13	1.18	0.65	0.32	-15.85	96.20					0.58			0.08	6.88			

APPENDIX C

ASSOCIATED ERRORS

Overheat Error

Using the error of the anemometer as ± 0005 or 0.002 ohms, an estimate of the error on a required overheat ratio can be determined. For the purposes here, an overheat of 1.8 will be used. Assume that the nulling of the probe to obtain the cold wire resistance has resulted in a value of 4.000 ohms. This would then represent a range of 3.998 to 4.002 Ω. For an overheat of 1.8 the resulting operating resistance would be set to

$$(1.8 * 4.000 \, \Omega) \quad = \quad 7.200 \, \Omega.$$

but the range of this value is 7.198 Ω to 7.202 Ω. Thus the actual overheats could range from

$$\frac{7.198}{4.002} = 1.799 \quad \text{to} \quad \frac{7.202}{3.998} = 1.801$$

or

$$\pm \, 0.08\%$$

Velocity Measurement Error

The nature of the equations used to determine the velocity field data makes error analysis difficult using standard methods, such as that outlined by Kline (1985). Thus, a comparison with data obtained by other previous investigators was used to qualify the present data. An indication of

245

the sensitivity of the output of the velocity equations to changes in the measured input voltages can, however, be indicated using a sensitivity analysis.

Two spatial locations were considered. Both were examined using the data at the $x/c = 0.5$ chord station for the 75° sweep wing at 20° angle of attack. The first spatial location was on the core axis, corresponding to $y/s = 0.69$ and $z/s = 0.39$. Listed below are the measured voltages for the three wires at that location, along with the standard deviations and the resulting velocities using the equations (3.13 a-c).

$$V1 = 3.202 \text{ volts } \sigma = 0.87\% \qquad u/U\infty = 2.318$$
$$V2 = 3.114 \text{ volts } \sigma = 0.77\% \qquad v/U\infty = 0.2917$$
$$V3 = 3.211 \text{ volts } \sigma = 1.6\% \qquad w/U\infty = -0.4762$$

The input voltages were then altered, one at a time, to examine the effect on the calculated velocities. Each voltage was first changed by ± its standard deviation. Then a 2% change was applied to all the cases. The resulting change in the velocities, compared to the baseline values are listed below.

$\Delta V1$	$\Delta V2$	$\Delta V3$	$\Delta u\,\%$	$\Delta v\,\%$	$\Delta w\,\%$
+0.87%	0%	0%	+0.8	-81.8	+25.8
-0.87%	0%	0%	-2.2	+80.6	-3.3
0%	+0.77%	0%	+2.2	-7.4	-63.7
0%	-0.77%	0%	-2.5	+18.3	+39.2
0%	0%	+1.6%	-3.1	+99.4	+45.5
0%	0%	-1.6%	+0.3	-13.4	-4.9
+2.0%	0%	0%	+0.4	-53.0	+70.7
-2.0%	0%	0%	-5.6	+157.	+3.5
0%	+2.0%	0%	+2.0	+110.	-63.9
0%	-2.0%	0%	-6.3	+43.0	+84.0
0%	0%	+2.0%	-6.1	-160.	+78.1
0%	0%	-2.0%	-2.2	+76.9	+34.2

It is immediately obvious that, although the axial velocity changed by no more than about 3% for all the standard deviation perturbations, the other components demonstrated exceedingly

high differences when compared to the baseline values. The v velocity component is seen to be most sensitive to the change from V1. Less than a 1% change can cause over 80% change in the value of v. The w component shows similarly large deviations for changes in V2.

The above case consists of one large component, u/U_∞, and two smaller components, roughly an order of magnitude below the axial velocity. Therefore a second spatial location was chosen from the same survey plane where the velocities were of similar magnitude. The location selected was $y/s = 0.51$ and $z/s = 0.24$. The resulting voltages and velocities were:

$$V1 = 2.434 \text{ volts} \quad \sigma = 3.5\% \qquad u/U_\infty = 0.899$$
$$V2 = 2.488 \text{ volts} \quad \sigma = 2.3\% \qquad v/U_\infty = 0.937$$
$$V3 = 2.705 \text{ volts} \quad \sigma = 1.6\% \qquad w/U_\infty = -0.764$$

Again the input voltages were perturbed by their standard deviations, which can be seen to be larger than the previous case, and the resulting change in the output velocity was recorded. Considerably more uniform variation in the output velocities is observed. The axial component shows larger changes than before, however none of the other components show changes greater than those of u/U_∞.

ΔV1	ΔV2	ΔV3	Δu %	Δv %	Δw %
+3.5%	0%	0%	+17.4	-15.5	-1.3
-3.5%	0%	0%	-18.8	+12.2	+1.9
0%	+2.3%	0%	+11.0	+1.7	-14.4
0%	-2.3%	0%	-12.2	-0.7	+12.6
0%	0%	+1.6%	-15.4	+9.6	+14.2
0%	0%	-1.6%	+12.3	-9.6	-14.9

Vorticity Error

An estimate of the error in the axial vorticity based on the error in the spatial location can be determined using the standard method of Kline (1985). The vorticity is defined as

$$\Omega_x = \frac{\partial w}{\partial y} - \frac{\partial v}{\partial z} \tag{C1}$$

or in terms of discrete values

$$\Omega_x = \frac{\Delta w}{\Delta y} - \frac{\Delta v}{\Delta z} \tag{C2}$$

The uncertainty in Ω_x, U_{Ω_x}, is determined from

$$U_{\Omega_x} = \sqrt{\left(U_{\Delta y}\frac{\partial\Omega_x}{\partial\Delta y}\right)^2 + \left(U_{\Delta z}\frac{\partial\Omega_x}{\partial\Delta z}\right)^2 + \left(U_{\Delta w}\frac{\partial\Omega_x}{\partial\Delta w}\right)^2 + \left(U_{\Delta v}\frac{\partial\Omega_x}{\partial\Delta v}\right)^2} \tag{C3}$$

or

$$U_{\Omega_x} = \sqrt{\left(U_{\Delta y}\frac{-\Delta w}{\Delta y^2}\right)^2 + \left(U_{\Delta z}\frac{\Delta v}{\Delta z^2}\right)^2 + \left(U_{\Delta w}\frac{1}{\Delta y}\right)^2 + \left(U_{\Delta v}\frac{-1}{\Delta z}\right)^2} \tag{C4}$$

Disregarding the velocity errors for the moment, the uncertainty based only on spatial error can be determined. Hence

$$U_{\Omega_x} = \sqrt{\left(U_{\Delta y}\frac{-\Delta w}{\Delta y^2}\right)^2 + \left(U_{\Delta z}\frac{\Delta v}{\Delta z^2}\right)^2} \tag{C5}$$

If the uncertainty in the spatial location is set equal to the resolution of the system,

$$U_{\Delta y} = 0.0254 \text{ mm} \quad \text{and} \quad U_{\Delta z} = 0.0208 \text{ mm}$$

The calculated uncertainty can be expressed as a fractional uncertainty of the value of Ω_x itself by

$$\frac{U_{\Omega_x}}{\Omega_x} = \frac{\Delta y \sqrt{\left(\frac{U_{\Delta y}}{\Delta y^2}\right)^2 + \left(\frac{U_{\Delta z}}{\Delta z^2}\right)^2}}{2} \tag{C6}$$

eliminating the need to calculate an actual value of Ω_X.

Three stations were selected along the 75° sweep planform, x/c = 0.3, 0.5, and 0.8. The values of $\Delta y/s = \Delta z/s = 0.03$ for the data acquired, however in order to maintain the same spatial location for the vorticity values the spatial distance used in equation (C2) is twice this. The actual values of Δy and Δz depend on the chordwise station at which they are determined. as shown below, along with the calculated fractional uncertainties for these using equation (C6).

x/c	$\Delta y=\Delta z$ (mm)	$2\Delta y$ (mm)	U_{Ω_X}/Ω_X %	U_{Ω_X}/Ω_X % (1mm)
0.3	0.98	1.96	0.84	36.1
0.5	1.63	3.26	0.50	21.7
0.8	2.61	5.22	0.31	13.5

Payne (1987) states that the overall positional accuracy of the system is ± 1 mm. If this is interpreted as the uncertainty in Δy and Δz, the fractional uncertainty of the vorticity increases dramatically to the percentages noted in the last column.

To include the effect of the velocity error, equation (C4) must be employed. An error estimate for the velocity is required as well as some values for Δw and Δv. Using the values of $\Delta y = \Delta z = 3.26$ mm at the x/c = 0.5 station, and selecting values of $\Delta w = -\Delta v = 0.1U_{\infty}$ m/s, a value of $\Omega_X = 61.3$ U_{∞} 1/s is determined. If the error in the velocities is only taken to be 15% of the values obtained in the core, the uncertainty from (C4) is calculated to be over 80% of the value of Ω_X.

Circulation Error

The error in the calculated circulation can be calculated in a similar manner as the vorticity. The circulation, defined as

$$\Gamma \quad = \quad \int_r V \cdot dr \qquad (C7)$$

can be expressed as a summation of terms, each of which has an error associated with it.

$$\Gamma \quad = \quad \sum_{i=1}^{n} (V\Delta y)_n \qquad (C8)$$

where $\Delta y = \Delta z$. Thus, ignoring the error due to velocity, the uncertainty based on the error in the spatial location can be derived as

$$U_\Gamma = \sqrt{\left(U_{\Delta y1} \frac{\partial \Gamma}{\partial \Delta y_1}\right)^2 + \left(U_{\Delta y2} \frac{\partial \Gamma}{\partial \Delta y_2}\right)^2 + \ldots\ldots} \qquad (C9)$$

where

$$\frac{\partial \Gamma}{\partial \Delta y_1} = \frac{\partial \Gamma}{\partial \Delta y_n} = V_n$$

If the values of V_n are assumed to be the same along a path of integration, or for the worst case scenario V_n is set equal to the largest value along the:

$$U_\Gamma = V_n \sqrt{U_{\Delta y1}^2 + U_{\Delta y2}^2 + \ldots\ldots}$$

or ·

$$U_\Gamma = V_n \sqrt{\sum_{i=1}^{n} (U_{\Delta y_n})^2} \qquad (C10)$$

As an example, the station of x/c = 0.5 is used again. If the integration path is taken to be out to a radius of r/s = 0.25, the value of V_n can be set to the maximum of V_n = 1.3 U_∞ from Figure 5.15b. The circulation at this station and radius was calculated to be approximately 0.2*(cU_∞) from Figure 5.29. At this radius approximately 34 summations are required based on the local grid spacing of y/s = z/s = 0.03. Using the uncertainty in the grid spacing of 0.0254 mm for both y and z directions yields a value of

$$U_\Gamma = 0.193 \text{ e-03 } U_\infty$$

or

$$\frac{U_\Gamma}{\Gamma} = 0.24\%$$

about half that of the vorticity for the same case. If the maximum uncertainty in Δy of 1 mm is used, however, an error of 9.3% is determined, again about half that of the vorticity. This, of course, assumes a negligible error in the velocity.

APPENDIX D

FURTHER CROSS WIRE DERIVATIONS

The technique of Sherif and Pletcher (1987) uses two positions of an X-wire array with the wires are in a plane perpendicular to the probe axis. Use of this method gave success in terms of magnitudes that were comparable to other measurements of the same delta wing flowfield. These equations were rewritten for the probe configuration of the two wires parallel to the oncoming stream and at ±45° and are detailed below. The resulting equations were similar to that obtained by Sherif and Pletcher. They also consisted of a set of three nonlinear equations with three unknowns plus a fourth equation. The direction of V and W could also be determined from the voltages, as was shown earlier. Hence if these nonlinear equations could be solved, the velocity vector would be known. This derivation is now explained in more detail.

Recall the general geomertry for a single hot wire introduced in Chapter 3 and based on the figure below
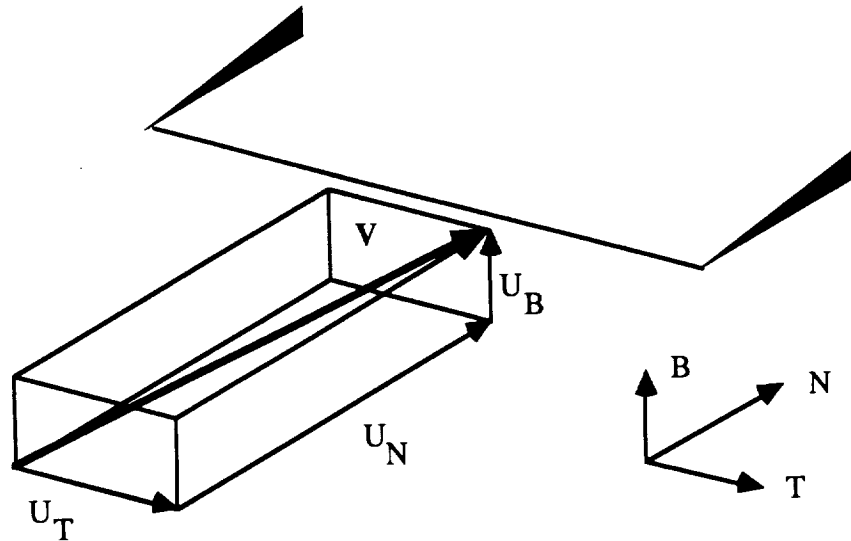
Figure D1 Single Wire Geometry

The effective velocity measured by the wire was expressed by Jørgensen (1971) as:

$$U_{eff}^2 = U_N^2 + k_1^2 U_T^2 + k_2^2 U_B^2$$

As outlined in Chapter 3, the present study required four spatial passes to uniquely determine the unknown flowfield. It was desirable to minimize the number of grid sweeps required to reduce both the data acquisition time and the potential for error. Several schemes were tried, including iterative techniques based on simplified forms of the Jørgensen equation, however none were successful. The original derivation of Sherif and Pletcher (1987) was then applied to the configuration with the wires lying in a plane parallel to the probe axis, using the geometry below.
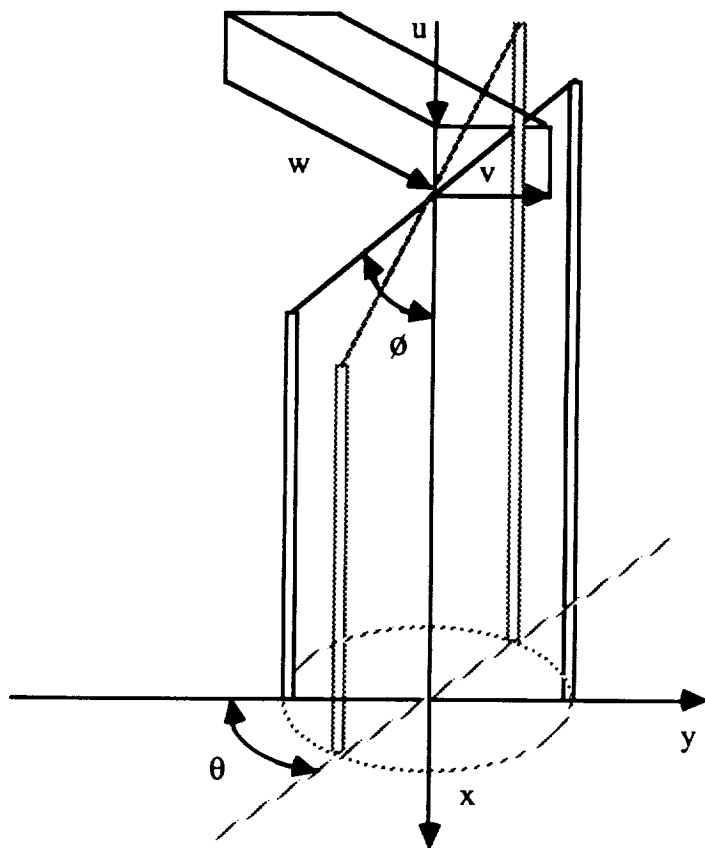
Figure D2 Single Slant Wire Geometry

The velocity is decomposed into the components below

$$U_N = u \sin\phi + v \cos\theta \cos\phi + w \sin\theta \cos\phi$$

$$U_T = -u \cos\phi + v \cos\theta \sin\phi - w \sin\theta \sin\phi$$

$$U_B = v \sin\theta + w \cos\theta$$

where ϕ is the angle of the wire relative to the x-axis and θ is the rotation angle of the probe, θ being equal to zero degrees in the x-y plane.

For an x-wire in the x-y plane, the two wires lie at $\phi = 45°$ and $\phi = 135°$ with $\theta = 0°$. This is also equivalent to $\phi = 45°$ and $\theta = 0°$ and $180°$. Hence

a) $\theta = 0°, \phi = 45°$: $\qquad U_N = \dfrac{u}{\sqrt{2}} + \dfrac{v}{\sqrt{2}} = \dfrac{\sqrt{2}}{2}(u+v)$

$$U_T = \dfrac{v}{\sqrt{2}} - \dfrac{u}{\sqrt{2}} = \dfrac{\sqrt{2}}{2}(v-u)$$

$$U_B = w$$

Therefore: $\qquad U_{eff}^2 = \dfrac{(u+v)^2}{2} + k_1^2 \dfrac{(v-u)^2}{2} + k_2^2 w^2$

Similarly

b) $\theta = 0°, \phi = 135°$: $\qquad U_{eff}^2 = \dfrac{(u-v)^2}{2} + k_1^2 \dfrac{(v+u)^2}{2} + k_2^2 w^2$

Hence: a) $\quad U_{eff}^2 = \dfrac{u^2}{2}(1+k_1^2) + \dfrac{v^2}{2}(1+k_1^2) + k_2^2 w^2 + uv(1- k_1^2) = U_a^2 \qquad$ (D1)

b) $\quad U_{eff}^2 = \dfrac{u^2}{2}(1+k_1^2) + \dfrac{v^2}{2}(1+k_1^2) + k_2^2 w^2 - uv(1- k_1^2) = U_b^2 \qquad$ (D2)

Rotation of the probe to $\theta = 90°$ yields

$\emptyset = 45°$

c) $U_{eff}^2 = \frac{(u+w)^2}{2} + k_1^2 \frac{(-u-w)^2}{2} + k_2^2 v^2$

$$U_{eff}^2 = \frac{u^2}{2}(1+k_1^2) + k_2^2 v^2 + \frac{w^2}{2}(1+k_1^2) + uw(1+k_1^2) = U_c^2 \qquad (D3)$$

$\emptyset = 135°$

d) $U_{eff}^2 = \frac{(u-w)^2}{2} + k_1^2 \frac{(u-w)^2}{2} + k_2^2 v^2$

$$U_{eff}^2 = \frac{u^2}{2}(1+k_1^2) + k_2^2 v^2 + \frac{w^2}{2}(1+k_1^2) - uw(1+k_1^2) = U_d^2 \qquad (D4)$$

Thus, four nonlinear equations in three unknowns result with the effective velocities U_a, U_b, U_c, and U_d determined from the calibration curves. The directions for v and w are simply found in the same manner as the present method. The angles are defined from the x-axis as

$$\alpha = 45 - \tan^{-1}\left(\frac{U_b}{U_a}\right) = \text{angle of the velocity component in the xy plane}$$

$$\gamma = 45 - \tan^{-1}\left(\frac{U_d}{U_c}\right) = \text{angle of the velocity component in the xz plane}$$

Further manipulation of equations 1 to 4 yields

$$U_a^2 - U_b^2 = 2uv(1 - k_1^2) \qquad (D5)$$

$$U_c^2 - U_d^2 = 2uw(1 + k_1^2) \qquad (D6)$$

$$U_a^2 + U_b^2 = u^2(1 + k_1^2) + v^2(1 + k_1^2) + 2k_2^2 w^2 \qquad (D7)$$

$$U_c^2 + U_d^2 = u^2(1 + k_1^2) + 2k_2^2 v^2 + w(1 + k_1^2) \tag{D8}$$

Subtracting (D8) from (D7) and defining the result as ζ

$$\zeta = U_a^2 + U_b^2 - U_c^2 - U_d^2 = v^2(1 + k_1^2 - 2k_2^2) + w^2(2k_2^2 - 1 - k_1^2) \tag{D9}$$

Dividing equation (D5) by (D6) and denoting this as β:

$$\frac{U_a^2 - U_b^2}{U_c^2 - U_d^2} = \frac{v(1 - k_1^2)}{w(1 + k_1^2)} = \beta$$

Rearranging

$$v = w \beta \frac{(1 + k_1^2)}{(1 - k_1^2)}$$

or

$$v^2 = w^2 \beta^2 \frac{(1 + k_1^2)^2}{(1 - k_1^2)^2} = w^2 \sigma^2 \tag{D10}$$

where σ equals β multiplied by $\dfrac{(1 + k_1^2)}{(1 - k_1^2)}$

Finally, substitution of (D10) into (D9)

$$\zeta = w^2 \sigma^2 (1 + k_1^2 - 2k_2^2) + w^2 (2k_2^2 - 1 - k_1^2)$$

or

$$\zeta = w^2(k_1^2(\sigma^2 - 1) + 2 k_2^2(1 - \sigma^2) + \sigma^2 - 1) \tag{D11}$$

and solving for w

$$w = \left(\frac{\zeta}{k_1^2(\sigma^2 - 1) + 2 k_2^2(1 - \sigma^2) + \sigma^2 - 1} \right)^{0.5} \qquad \text{(D12)}$$

Thus it would appear that w, and susequently u and v, could be solved explicitly.

Unfortunately, lines of very large or small magnitudes were observed in the velocity fields calculated from equation (D12) and the resulting expressions for u and v. In addition, the values of u determined were not representitive at all topographically, although the magnitudes were comparable. From equation (D12) it can be seen that when σ approached 1, the value of w becomes infinite. Equation (D10) indicates that for $\sigma = 1$, $w = v$, and thus it may be that a separate solution must be determined when $w = v$. To determine this, v was set equal to w in equations (D1) to (D4)

$$U_a^2 = \frac{u^2}{2}(1+k_1^2) + \frac{w^2}{2}(1+k_1^2) + k_2^2 w^2 + uw(1- k_1^2)$$

$$U_b^2 = \frac{u^2}{2}(1+k_1^2) + \frac{w^2}{2}(1+k_1^2) + k_2^2 w^2 - uw(1- k_1^2)$$

$$U_c^2 = \frac{u^2}{2}(1+k_1^2) + k_2^2 w^2 + \frac{w^2}{2}(1+k_1^2) + uw(1+ k_1^2)$$

$$U_d^2 = \frac{u^2}{2}(1+k_1^2) + k_2^2 w^2 + \frac{w^2}{2}(1+k_1^2) - uw(1+ k_1^2)$$

Now

$$U_a^2 + U_b^2 = u^2(1+ k_1^2) + w^2(1+ k_1^2 + 2k_2^2) \qquad \text{(D13)}$$

and

$$U_a^2 - U_b^2 = 2uw(1- k_1^2)$$

or

$$u = \frac{U_a^2 - U_b^2}{2w(1- k_1^2)} \qquad \text{(D14)}$$

Substituion of (D14) into (D13):

$$U_a^2 + U_b^2 = \left(\frac{U_a^2 - U_b^2}{2w(1- k_1^2)}\right)^2 (1+ k_1^2) + w^2(1+ k_1^2 + 2k_2^2)$$

or

$$w^4 - w^2 \frac{U_a^2 + U_b^2}{1+ k_1^2 + 2k_2^2} + \frac{U_a^2 - U_b^2}{4(1- k_1^2)^2} \frac{1+ k_1^2}{1+ k_1^2 + 2k_2^2} = 0 \qquad (D15)$$

Solutions to equation (D15) also failed to produce velocity fields without regions of non-convergence. Newtons iteration scheme helped, however constraints (as in $\beta \pm .2$) were required to get rid of the singularities. Thus, for the present tests, the method outlined in Chapter 3 was employed.

REFERENCES

I Vortex Flows

Delta Wing Flows

Agrawal, S., Barnett, R.M., and Robinson, B.A. "Investigation of Vortex Breakdown on Delta Wings Using Euler and Navier-Stokes Equations" AGARD Symposium on Vortex Flow Aerodynamics, October 1990, Scheveningen, The Netherlands.

Anders, K., " LDV Measurements of the Velocity Field of a Leading Edge Vortex Over a Delta Wing Before and After Vortex Breakdown" Von Karman Institute for Fluid Dynamics, Technical Note 142, March 1982

Ashenberg, J. "A Model for Vortex Breakdown on Slender Wings" AIAA Journal Vol.25 No.12 December 1987 pp. 1622-1624

Batchelor, G.K. "An INtroduction to Fluid Dynamics" © 1967 Cambridge University Press pp. 543 - 555.

Barnwell, R.W. "Extension of Hypersonic, High Incidence, Slender Body Similarity" AIAA Journal Vol. 25 No. 11 December 1987 pp. 1519-1522.

Benjamin, T.B. "Theory of Vortex Breakdown Phenomena" J. Fluid Mech., Vol.14, June 1962. pp 593 - 629

Benjamin, T.B. J. Fluid Mech., Vol.28, June 1962. pp 65 - 84

Bossel, H.H. "Vortex Breakdown Flowfield", Phys. of Fluids, Vol. 12, No. 3, March 1969.

Carcaillet, R., Manie, F., Pagan, D. and Solignac, J.L. "Leading Edge Vortex Flow Over a 75 Degree-Sweep Delta Wing- Experimental and Computational Results." ICAS 86.

Carr, M.P. "Accuracy Study of Transonic Flow Computations for Three Dimesional Wings" AGARD Symposium on Validation of Computational Fluid Dynamics Lisbon, Portugal. May 1988.

Cornelius, K. C. "3-D Analysis of Laser Measurements of Vortex Bursting on a Chined Forebody Fighter Configuration" AIAA 90-3020-CP AIAA 8th Applied Aerodynamics Conference, Portland Oregon, August 20-22, 1990.

Cunningham, Atlee M., Jr., "Vortex Flow Hysteresis", General Dynamics, Fort Worth Division >1985

Dagan, A. and Almosnino, D."Vorticity equation Solutions for Slender Wings at High Angles of Attack" 89-1989-CP

Delery, J., Pagan, D. and Solignac, J.L., "On the Breakdown of the Vortex Induced by a Delta Wing" Colloquium on Vortex Control and Breakdown Behavior, Baden, Switzerland, ONERA TP 1987-105, April 6-7, 1987.

Delery, J. "Physique des Ecoulements Tourbillonnaires" AGARD Symposium on Vortex Flow Aerodynamics, October 1990, Scheveningen, The Netherlands.

Dixon, C.J. "Theoretical and Qualitative Analysis of the Effects of Free Vortices on Lifting Surfaces" 89-2238-CP

Earnshaw, P.B. "An Experimaantal Investigation of the Structure of a Leading-Edge Vortex" ARC R & M, No 3281, March 1961.

Earnshaw, P.B. and Lawford, J.A. "Low Speed Wind Tunnel Experiments on a Series of Sharp Edged Delta Wings" ARC R & M, No 3424, March 1964.

Elle, B. J. "An Investigation at Low of the Flow near the Apex of Thin Delta Wings with Sharp Leading Edges " ARC R & M, No 3176, January 1958.

Ekaterinaris, J. and Schiff, L.B., "Vortical Flows over Delta Wings and Numerical Prediction of Vortex Breakdown" AIAA 90-0102 January 8-11, 1990 Reno, Nevada.

Elsenaar, A., Hjelmberg, L., Bütefisch, K., and Bannik, W.J. "The International Vortex Flow Experiment" AGARD Symposium on Validation of Computational Fluid Dynamics Lisbon, Portugal. May 1988.

Engler, R.H. "Vortex Breakdown - Investigations by using the Ultrasonic-Laser-Method and Laser-Sheet Technique" ICAS-88-3.11.3

Er-El, J. and Yitzhak, Z. "Experimental Examination of the Leading Edge Suction Analogy", AIAA Journal of Aircraft, Vol.25, No.3 March 1988

Erickson, Gary E., "Vortex Flow Correlation",Technical Report AFWAL-TR-80-3143 Flight Dynamics Laboratory, Wright Patterson Air Force Base, January 1981

Erickson, Gary E., "Water Tunnel Studies of Leading Edge Vortices."AIAA Journal of Aircraft, June 1982. Vol.19, No.6.

Escudier, M.P. and Keller J.J. "Vortex Breakdown: A Two Stage Transition" AGARD-CP-342, No. 25, April 1983.

Fujii, K. and Schiff, L.B. "Numerical Simulation of Flows over a Strake-Delta Wing" AIAA Journal, Vol.27, Sept 1989, pp. 1153-1162.

Gad-el-Hak, M. and Blackwelder, R.F."The discrete vortices from a delta wing" AIAA Journal, Vol.25, No.8 1985, pp.1042-1049.

Grabowski, W.J. and Berger, S. A.,"Solutions of the Navier Stokes Equations for Vortex Breakdown" Journal of Fluid Mechanics Vol 75, 1976 pp 525 - 544.

Hall, J.L. "An Introduction to Vortex Breakdown and Vortex Core Bursting" Aeronautical Note, NAE-AN-28, NRC No.24336, Ottawa, Canada, 1985

Hall, M.G. "A theory for the core of a leading edge vortex" Journal of Fluid Mechanics, Vol. 11 1961, p 209.

Hall, M.G. "Vortex Breakdown" Annual Review of Fluid Mechanics, Vol. 4 1972, p 195 - 217.

Hawk, J., Barnett, R., and O'Neil, P. "Investigation of High Angle of Attack Vortical Flow Over Delta Wings" 28th AIAA Aerospace Scences Meeting, AIAA 90-0101 January 8-11, 1990 Reno, Nevada.

Hartwich, P.M., Hsu, C., Luckring, J.M., and Liu, C.H. "Numerical Study of the Vortex Burst Phenomena for Delta Wings" AIAA Paper 88-0505, 26th Aerospace Sciences Neeting, January 1988. Reno,NV.

Hemsch, M. J. and Luckring, J. M. "Connection between Leading Edge Sweep, Vortex Lift and Vortex Strength for Delta Wings" AIAA Journal of Aircraft Vol.27, No.5 May 1990.

Hemsch, M. J. "Engineering Analysis of Slender Body Aerodynamics using the Sychev Similarity Parameter" AIAA Journal of Aircraft Vol.25, No.7 May 1988 pp. 625-631.

Hemsch, M. J. "Similarity for High-Angle-of-Attack Subsonic/Transonic Slender Body Aerodynamics" AIAA Journal of Aircraft Vol.26, No.1 May 1989 pp. 56-66

Hilgenstock, A. and Vollmers, H. "On the Simulation of Compressible Flows Past Delta Wing, Delta Wing-Body and Delta Wing-Canard" AGARD Symposium on Vortex Flow Aerodynamics, October 1990, Scheveningen, The Netherlands.

Hitzel, S. M. "Wing Vortex Flows up into Vortex Breakdown" Theoretical Aerodynamics, Dornier GmbH, Friedrichshafen, West Germany AIAA 88-2518 6th Applied Aerodynamics Conference, Williamsburg, VA. June 1988.

Hitzel, S. M., Wagner, B., and Leicher, S. "Euler Simulation of the Voretx Flow Experiment A Critical Consideration" Theoretical Aerodynamics, Dornier GmbH, Friedrichshafen, West Germany. Proceedings of the International Flow Expereiment on Euler Code Validation, Stockholm, Sweden, 1986. pp. 175-186

Hoeijmakers, H.W.M. and Rizzi, A. "Vortex Fitted Potential and Vortex Captured Euler Solution for Leading Edge Flow" AIAA Journal Vol. 23 No. 12 December 1985 pp. 1983-1985.

Houtman, E.M., and Bannik, W.J. "Experimental and Numerical Investigations of the Vortex Flow over a Delta Wing at Transonic Speed" AGARD Symposium on Vortex Flow Aerodynamics, October 1990, Scheveningen, The Netherlands.

Hummel D. "On the Vortex Formation Over a Slender Wing at Large Angles of Incdence" AGARD CP-247 January 1979, pp.15-1 - 15-7.

Hummel, D., and Srinivasan, P.S. "Vortex Breakdown Effects on the Low-speed Aerodynamic Characteristics of Slender Delta Wings in Symmetrical Flow" Journal of the Royal Aeronautical Society Vol.71 April.

Iwanski, Kenneth P. "An Investigation of the Vortex Flow Over a Delta Wing with and without External Jet Blowing" Masters Thesis, University of Notre Dame, April 1988.

Kirkpatrick, D.L. "Analysis of the static Pressure Distribution on a Delta Wing in Subsonic Flow" ARC R&M 3619 1970

Krist, S.L., Thomas, J.L., Sellers, W.L. III , and Kjelgaard, S.O. "An Embedded Grid Formulation Applied to a Delta Wing" 28th Aerospace Sciences Meeting AIAA-90-0429, January 1990. Reno, NV

Jones, J.P. "The breakdown of vortices in separated flow", Dept of Aer and Astro, Unv. of Southhampton, Rep. No. 140, 1960.

Kegelman, J.T. and Roos, F.W. "Effects of Leading Edge shape and Vortex Burst on the Flowfield of a 70-Degree-Sweep Delta Wing" AIAA Paper 89-0086 Jan 9-12, 1989 Reno, NA.

Kegelman, J.T. and Roos, F.W. "The Flowfield of Bursting Vortices ove Moderately Swept Delat Wings" AIAA Paper 90-0599 Jan 8-11, 1990 Reno, NA.

Kegelman, J.T. and Roos, F.W. "An Experimental Investigation of Sweep Angle Influence on Delta Wing Flows" AIAA Paper 90-0383 Jan 8-11, 1990 Reno, NA.

Kjelgaard, S.O. and Sellers, W.L. III, "Detailed Flowfield Measurements over a 75° Swept Delta Wing for Code Validation" AGARD Symposium on Validation of Computational Fluid Dynamics, Lisbon, Portugal, May 2-5, 1988.

Kjelgaard, S.O. and Sellers, W.L. III, "Detailed Flowfield Measurements over a 75° Swept Delta Wing" NASA TP 2997 October 1990.

Lambourne, N. C., and Bryer, D. W., "The Bursting of Leading Edge Vortices-Some Observations and Discussion of the Phenomena," Aeronautical Research Council, Reports and Memoranda, No. 3282, 1961.

Lee, M. and Ho, C-M. " 'Vortex Dynamics of Delta Wings' Frontiers in Experimental Fluid Mechanics" Lecture Notes in Engineering Vol. 46 © 1989 Springer-Verlag, Berlin.

Lowson, M.V. "The Three Dimensional Vortex Sheet Structure On Delat Wigs", AGARD Symposium onFluid Dynamics of Three Dimensional Turbulent Shear Flows and Transition. Paper 11, October 1988.

Ludweig, H. "Contribution to the Explanation of the Instability of Vortex Cores Above Lifting Delta Wings", Aero. Versuchsanstalt, Gottingen, Rep. AVA/61 A01, 1961.

Mangler, K.W. and Weber, J. "The flowfield near the centre of a rolled up vortex sheet" Journal of Fluid Mechanics Vol 30 1967 pp. 177-196.

McCune, J.E. and Tavares, T.S. "Unsteady 3-D Aerodynamics of Slender Wings in Severe Maneuver" AIAA ASME SIAM APS !st National Fluid Dynamics Congress. July 25-28, 1988 Cincinati, OH.

Naarding S.H.J. and Verhaagen, N. G. "Experimental and Numerical Investigation of the Vortex Flow Over a Sharp Edged Delta Wing with and without Sideslip" Delft University Report LR-573, December 1988.

Ng, T.T. "On Leading Edge Vortex and Its Control" AIAA Atmospheric Flight Mechanics Conference, Boston MA, August 1989

O'Neil, P.J., Barnett, R.M., and Louie, C.M., "Numerical Simulation of Leading Edge Vortex Breakdown Using an Euler Code" 89-2189-CP.

Pagan, D. and Solignac, J.L. "Experimental Study of the Breakdown of a Vortex Generated By a Delta Wing" La Recherche Aérospatiale, No 3, May-June 1986.

Parker, A.G. "Aerodynamic Characteristics of Slender Wings with Sharp Leading Edges - A Review" J. Aircraft Vol. 13, No.13, March 1976

Payne, F. M. "The Structure of Leading Edge Vortex Flows Including Vortex Breakdown" PhD Dissertation, University of Notre Dame, May 1987.

Payne, F.M., Ng, T.T.,, and Nelson, R.C. "Experimental Study of the Velocity field on a Delta Wing" 19th AIAA Fluid Dynamics, Plasma Dynamics, and Laser Conference, AIAA-87-1231, Honolulu, Hawaii, June 8-10, 1987.

Payne, F. M., Ng T.T., and Nelson, R.C. "Visalization and Flow surveys of the Leading Edge Vortex Structure on Delta Wing Planforms" AIAA-86-0330 January 6-9 1986, Reno, Nevada.

Peake, D. J. and Tobak, M. "Three Dimensional INteractions and Vortical Flows with emphasis on High Speeds" NASA TM - 81169, March 1980.

Peckham, D.H.and Atkinson, S.A. "Preliminary Results of Low-Speed Wind Tunnel Tests on a Gothic Wing of Aspect Ratio 1" ARC Cp 508.

Peckham, D.H. "Low-Speed Wind Tunnel Tests on a Series of Uncambered Slender Pointed Wings with Sharp Edges" ARC R&M 3186 N62-10253, Report Aero 2613, December 1958.

Polhamus, E. C. "Predictions of Vortex Lift Characteristics by a Leading Edge Suction Analogy" Journal of Aircraft, Vol. 8, No. 4. April 1971, pp. 193-199

Powell, K. G. and Murman, E. M. " A Model for the Core of a Viscous Vortex" AIAA 88 - 0503, January 11-14, 1988

Randall, J.D. and Leibovich, S., "The Critical State: A Trapped Wave Model of Vortex Breakdown", J. Fluid Mech., Vol.58, 1973.

Schrader, K. F., Reynolds, G. A., and Novak, C. J. "Effects of Mach Number and Reynolds Number on Leading-Edge Vortices at High Angle of Attack" AIAA Paper 88-0122 January 11-14, 1988.

Smith, J.H.B. "Calculations of the Flow over Thick, Conical, Slender Wings with Leading Edge Separation" ARC R&M 3694, March 1971

Spall, R.E., Gatski, T.B. and Ash, R.L. "The structure and dynamics of bubble-type breakdown" Proceedings of the Royal Society of London, A 429, 613-637 (1990)

Squire, L. C. "Some Effects of Thickness on the Longitudinal Characteristics of Sharp-Edged Delta Wings at Low Speeds" The Aeronautical Journal of the Royal Aeronautical Society February 1967? Vol.72

Squire, H.B. "Analysis of the 'Vortex Breakdown' Phenomenon" Part 1 Imperial College, London, Dep. of Aero. Report. No. 102, 1960.

Stewartson, K. and Hall, M.G. "The inner viscous solution for the core of a leading-edge vortex" Journal of Fluid Mechanics, Vol. 15 1963, pp 306-318.

Sychev, V.V. "Three Dimensional Hypersonic Gas Flow Past Slender Bodies at High Angles of Attack", Prikladnaia Matematika i Mechanikal, Vol.24, 1960 pp 205-212.

Thomas, J.L., Taylor, S.L. and Anderson, W.K. "Navier-Stokes Computations of Flows over Low Aspect Ratio Wings" AIAA paper 87-0317, 25th AIAA Aerospace Scences Meeting, Reno NV, January 1987.

Thomas, J.L. and Newsome R.W. "Navier-Stokes Computations of Lee-Side Flows Delta Wings" AIAA Journal Vol.27 No.12, December 1989

Thompson, D.H. "A Water Tunnel Study of Vortex Breakdown Over Wings with Highly Swept Leading Edges" Australian Defence Scientific Service Note ARL/A. 356 May 1975

Thompson, D.H. "A Flow Visualization Study of Tip Vortex Formation " Defence Science and Technolgy Organization, ARL, Melbourne, Australia ARL-AERO-Note-421, 1983

Verhaagen, N. and van Ransbeeck, P. "Experimental and Numerical Investigation of the Flow in the Core of the Leading Edge Vortex" 28th AIAA Aerospace Scences Meeting, AIAA 90-0384 January 8-11, 1990 Reno, Nevada.

Verhaagen, N. and Kruisbrink, A.C.H.. "Numerical Simulation of Leading Edge Vortex Breakdown using an Euler Code" AIAA paper 89-2189 , 1989

Verhaagen, N. G. "An Experimental Investigation of the Vortex Flow Over Delta and Double-Delta Wings at Low Speed" AGARD-CP-342 Aerodynamics of Vortical Type Flows in Three Dimensions, April 1983.

Visser, K.D. "An Investigation of the Effects of a External Jet on the Performance of a Highly Swept Delta Wing" Masters Thesis, University of Notre Dame, Notre Dame, Indiana, May 1988.

Wagner, B., Hitzel, S. M., Schmatz, M.A.,Schwarz, W., Hilgenstock, A., and Scherr, S. "Status of CFD Validation on the Vortex Flow Experiment" AGARD Fluid Dynamics Symposium on Validation of the Vortex Flow Experiment. Lisbon, Portugal, May 1988

Wedemeyer, E. "Vortex Breakdown", No.9, AGARD-LS-121, December 1982.

Wentz, W.H. "Wind Tunnel Investigations of Vortex Breakdown on Slender Sharp Edged Wings" PhD Thesis, University of Kansas, 1968

Wentz, W.H. and Kohlman D.L. "Vortex Breakdown on Slender Sharp Edged Wings." Journal of Aircraft Vol.8 #3. March 1971 (AIAA Paper 69-778 July 14-16, 1969)

Wentz, W.H. and Kohlman D.L. "Wind Tunnel Investigations of Vortex Breakdown on Slender Sharp Edged Wings" NASA CR-98737, 1969.

Wentz, W.H. and MacMahon, M.C., "Further Experimental Investigations of Delta and Double Delta Flowfields at Low Speeds", NASA CR-714, Feb 1967.

Williams, B.R., Kordulla, W., Borsi, M. and Hoeijmakers, H.W.M. "Comparison of Solution of Various Euler Solvers and One Navier Stokes Solver for the Flow About a Sharp Edged Cropped Delta Wing" AGARD Symposium on Vortex Flow Aerodynamics, October 1990, Scheveningen, The Netherlands.

Wilson, James D. "Calculation of Vortex Breakdown Location for Flow over Delta Wings." Journal of Aircraft Vol.14 #10. October 1977

Zohar, Y. and Er-El, J. "The Influence of the Aspect-Ratio on the Aerodynamics of the Delta Wing at High Angle of Attack " AIAA Journal of Aircraft, Vol.25, No.3 March 1988

Axisymmetric Tube Flows

Brown, G.L. and Lopez, J.M. "Axisymmetric Vortex Breakdown Part 1: Physical Mechanisms" Aeronautical Research Laboratories, P.O. Box 4331, Melbourne, Vic., 3001, Australia. A>R>L Aero. Rep. 174, AR-004-573 (1988).

Brown, G.L. and Lopez, J.M. "Axisymmetric Vortex Breakdown Part II: Physical Mechanisms" Aeronautical Research Laboratories, P.O. Box 4331, Melbourne, Vic., 3001, Australia. A.R.L Aero. Rep. 173, AR-004-572 (1988).

Cutler, A.D., Naaseri, M., and Bradshaw, P. "Interaction between Strong Longitudinal Vortices and Turbulent Boundry Layers" Fourth Symposium on Numerical and Physiacal Aspects of Aerodynamic Flows, January 1989, California State University, Long Beach CA

Escudier, M.P. and Zehnder, N., "Vortex Flow Regimes" Journal of Fluid Mechanics, Vol.115, 1982 pp105 - 121.

Escudier, M.P., Bornstein, J., and Maxworthy, T., "The Dynamics of Confined Vortices" Proceedings of the Royal Society of London, Vol.A382, 1982 335 - 360.

Escudier, M.P. and Keller J.J. "Vortex Breakdown: A Two Stage Transition" Brown Boveri Research Center, Ch-5405 Baden, Switzerland

Faler, J. H. and Leibovich, S. "Disrupted states of Vortex Flow and Vortex Breakdown" Physics of Fluids, Vol. 20, No. 9, September 1977.

Faler, J.H. and Leibovich, S."An Experimental Map of the Internal Structure of a Vortex Breakdown" Journal of Fluid Mechanics Vol 86, 1978 pp 313 - 335.

Gartshore, I. S., "Recent Work In Swirling Incompressible Flow", NRL (Canada), LR-343, June 1962.

Harvey, J. K., "Some Observations of the Vortex Breakdown Phenomenon" Journal of Fluid Mechanics Vol. 14 pp. 585-592, 1962

Hoffmann, E.R. and Joubert, P.N., "Turbulent Line Vortices", Journal of Fluid Mechanics, Vol. 16, Pt 3, pp 395 - 411, July 1963.

Howard, L.N. and Gupte, A.S. "On the hydrodynamic and hydromagnetic stability of swirling flows", Journal of Fluid Mechanics, Vol. 14, pp 463 - 476, 1962.

Krause, E. "A Contribution to the Problem of Vortex Breakdown" Aerodynamisches Institut der RWTH Aachen, Aachen, Germany

Leibovich, S. "The Structure of Vortex Breakdown" Annual Review of Fluid Mechanics Vol. 10, 1978 pp221 - 246.

Leibovich, S. and Stewartson, K. "A Sufficient Condition for the Instability of Columnar Vortices" Journal of Fluid Mechanics, Vol.126, 1983 pp 335 - 356.

Leibovich, S. "Vortex Stability and Breakdown: Survey and Extension" AIAA Journal Vol.22, No.9 September 1984.

Lopez, J.M. "Axisymmetric Vortex Breakdown Part 1: Confined Swirling Flow" Aeronautical Research Laboratories, P.O. Box 4331, Melbourne, Vic., 3001, Australia. A>R>L Aero. Rep. 173, AR-004-572 (1988).

Mager, A. "Dissipation and Breakdown of a Wingtip Vortex" J. Fluid Mech., Vol.55 1972.

McCormick, B.W., Tangler, J.L., and Sherrieb, H.E. "Structure of Trailing Vortices" AIAA Journal of Aircraft, Vol. 5, No.3, May-June 1968 pp.260-267.

Nakamura, Y., Leonard, A. and Spalart, P.R. "Vortex Breakdown Simulation" AIAA - 85 - 1581, January 16-18, 1985

Nakamura, Y., Leonard, A. and Spalart, P.R. "Internal Structure of a Vortex Breakdown" AIAA-86-1074, May 12-14, 1986 Atlanta , Georgia.

Rayleigh, J.W.B., "On the dynamics of revolving fluids" Proceedings of the Ryal Society of London, V0l. A93, pp148-

Sarpkaya, Turgut "Effect of the Adverse Pressure Gradient on Vortex Breakdown" AIAA Journal Vol.12 May 1974.

Sarpkaya, Turgut "On stationary and travelling vortex breakdowns" J. Fluid Mechanics (1971), vol.45, part 3, pp 545-559.

Sarpkaya, Turgut "Vortex Breakdown in Swirling Conical Flows" AIAA Journal vol. 9 Sept 1971 pp1792- 1799

Uchida, S., Nakamura, Y., and Ohsawa, M. " Experiments on the Axisymmetric Vortex Breakdown in Swirling Air Flow" Transactions of the Japan Society for Aeronautical and Space Sciences, Vol. 27, 1985 pp 206-216

Tornado Flows

Bode, L., Leslie, L.M., and Smith, R.K. "A numerical study of boundry effects on concentrated vortices with application to tornadoes and waterspouts" Quarterly Journal of the Royal Meteorlogical Society, Vol. 101, April 1975. pp. 313 - 324.

Davies-Jones, R.P. "The dependence of core radius on swirl ratio in a tornado generator"Journal of Atmospheric Sciences, Vol. 30, 1973 pp. 1427 - 1430.

Davies-Jones, R.P. "Tornado Dynamics" from Thunderstorm Morphology and Dynamics, E. Kessler ed. © 1982 Vol.2, pp.197 - 236, NOAA Pub. 603 pages.

Howells, P.A., Rotunno, R., and Smith, R.K. "A comparative study of atmospheric and laboratory analogue numerical tornado vortex models" Quarterly Journal of the Royal Meteorlogical Society, Vol. 114, . pp. 801 - 822.

Pauley, R.L. "Laboratory Measurements of Axial Pressures in Two-Celled Tornado-like Vortices", Journal of Atmospheric Sciences, Vol. 46, No. 21, November 1989 pp. 3392 - 3399.

Rotunno, R. "Numerical Simulation of a Laboratory Vortex" Journal of Atmospheric Sciences, Vol. 34, December 1977 pp. 1942 - 1954.

Rotunno, R. "A Study in Tornado-like Vortex Dynamics" Journal of Atmospheric Sciences, Vol. 36, No. 1, January 1979 pp. 140 - 155.

Staley, D.O. "Effect of Viscosity on Inertial INstability in a Tornado Vortex" Journal of Atmospheric Sciences, Vol. 43, No. 20, October 1985 pp. 2137 - 2149.

Turner J.S. "The constraints imposed on tornado-like vortices by the top and bottom boundry conditions" Journal of Fluid Mechanics VOl. 25, pp 377 - 400, 1966.

Walko, R. and Gall, R. "Some Effects of Momentum Diffusion on Axisymmetric Vortices" Journal of Atmospheric Sciences, Vol. 42, No. 3, February 1985 pp. 294 - 297.

Wilson, T. and Rotunno, R. "Numerical simulation of a laminar end-wall vortex and boundry layer" Physics of Fluids, Vol. 29, No.12, December 1986, pp.3993 - 4004.

II Flow Visualization

Freymuth, P., Bank, W., and Palmer, M. "Use of Titanium Tetrachloride for Visualization of Accelerating Flows Around Airfoils" Flow Visualization III, edited by W.J. Yang, pp. 99-105, Hemisphere, Washington D.C. 1985.

Mueller, T.J. "Smoke Visualization of Subsonic and Supersonic Flows (The Legacy of F.N.M. Brown) " AFOSR Final Contract Report TN-3412-1, June 1978.

Visser, K.D., Nelson, R.C., and Ng, T.T., "Method of Cold Smoke Generation for Vortex Core Tagging" AIAA Journal of Aircraft Vol.25, No.11 November 1988.

III Hot Wire Annemometry

Andreas, E.L. "Analysis of Crossed Hot Film Velocity Data" DISA Information No. 24 May 1978.

Bearman, P.W. "Corrections for the Effect of Ambient Temperature Drift on Hot-wire Measurements in INcompressible Flow" DISA INformation No. 11, 1971.

Browne, L.W.B., Antonia, R.A., and Chua, L.P. "Calibration of X-Probes for turbulent flow measurements" Experiments in Fluids 7, 201-208 (1989).

Brunn, H.H. "Interpretation of X-hot-wire signals" DISA Information No. 18 September 1975.

Drubka, R.E., Tan-atichat, J. and Nagib, H.M. "Analysis of Temperature Compensating Circuits for Hot-wires and Hot-films" DISA Information No. 22 December 1977.

Fabris, G. "Probe and method for simultaneous measurements of "true" instantaneous temperature and three velocity components in turbulent flow" Rev. Scientific Instruments Vol. 49, No. 5, May 1978. p.654-664.

Foss, J.F. and Wallace, J.M. "The Measurement of Vorticity in Transitional and Highly Turbulent Flows" Springer Verlaag, Lecture Notes in Engineering, Advances in Fluid Mechanics Measurements, Vol. 45, 1988.

Fremuth, P. "A Bibliography of Thermal Anemometry" © TSI Incorporated 1982.

Gaulier, C. "Measurement of Air Velocity by Means of a Triple Hot Wire Probe" DISA Information No. 21 April 1977.

Günkel, A.A., Patel, R.P., and Weber, M.E. "A Shielded Hot-wire Probe for Highly Turbulent Flows and Rapidly Reversing Flows" Ind. Eng. Chem. Fundam., Vol.10, No.4, 1971.

He, Xiong "Measurement with a Rotating Slant Sensor Probe" Dantec Information No.6, February 1988.

Horvatin, M. "A Contribution to the Calibration of Hot-wire Dual Probes " DISA Information No. 10 October 1970.

Janjua, S.I., McLaughlin, D.K., Jackson, T.W., and Lilley, D.G, "Turbulence measurements in a Confined Jet Using a Six-Orientation Hot-Wire Technique" AIAA/SA/ASME 18th Joint Propulsion Conference, Cleveland, 1982 AIAA-82-1262

Jackson, T.W. and Lilley, D. G. "Accuracy and Directional Sensitivity of the Single Wire Technique" AIAA Journal Vol.24, No.3, 1986 p451-458.

Jacobsen, R.A. "Hot Wire Annemometry for In-flight measurement of Aircraft Wake Vortices" DISA Information No. 21, April 1977

Jørgensen, F.E. "Directional Sensitivity of Wire and Fiber-film Probes *An Experimental Study*" DISA Information No.11 May 1971.

Kastrinakis, E.G., Eckelmann, H. and Willmarth, W.W. Rev. Scientific Instruments 5, 1979. p.759 .

Klatt, F. "The X Hot-wire Probe in a Plane Flow Field" DISA Information No. 8 July 1979.

Kovasznay, L.S.G. Quarterly Progress Report of Aero Dept. Contract NORD-8036-JHB-3D, The John Hopkins University, 1950.

Lekakis, I.C., Adrian, R.J., and Jones, B.G. "Measurement of velocity vectors with orthogonal and non-orthogonal triple-sensor probes" Experiments in Fluids 7 p 228-240, 1989

Löfdahl, L. "Hot-Wire Techniques for the Determination of the Reynolds Stress Tensor in Three-Dimensional Flow" Dantec Information No. 3 September 1986

Lueptow, R.M., Breuer, K.S., and Haritonidis, J.H. "Computer-aided calibration of X-probes using a Lookup Table" Experiments in Fluids 6, 115-118 (1988)

Machen, P.C. "Correction of Unlinearised Hot-Film Anamometer Measurements for Ambient Temperature Changes" Dantec Information No. 03 September 1986.

Manca, O., Mastrullo, R., and Mazzei, P. "Calibration of Hot-Wire Probes at Low Velocities in Air With Variable Temperatures" Dantec Information No,6, February 1988.

Mojola, O.O. "A Hot-wire method for Three dimensional Shaear Flows" DISA Information No. 16, July 1974.

Pailhas, G. and Cousteix, J. "Caracteristiques d'une Couche Limite en Aval d'un Tourbillon de Bord D'Attaque" AGARD Symposium on Vortex Flow Aerodynamics, October 1990, Scheveningen, The Netherlands.

Sherif, S.A. and Pletcher, R.H. " A Normal-Sensor Hot Wire/Film Probe Method for the Analysis of Highly Three Dimensional Flows" ASME Applied Mechanics Biomechanical and Fluid Engineering FED Vol 49, p19-22, Cinncinati, OH, 1987

Vukoslavevic, P. and Wallace, J.M. "Influence of velocity gradients on measurements of velocity and streamwise vorticity with hot-wire X array probes" Rev. Scientific Instruments Vol. 52, No. 6, June 1981. p.869-879.

IV Other

Brendel, M. and Huber, A.F. II. "An Experimental Investigation of the Flow Quality in an Indraft Subsonic Wind Tunnel Using a Single Hot Wire Annemometer" University of Notre Dame Internal Report 1984.

Kline, S.J., "The Perposes of Uncertainty Analysis", Journal of Fluids Engineering, June 1985, pp. 153 - 160.

Visser, K.D, "3D Traverser Code for the Mac II", Internal Document, Department of Aerospace and Mechanical Engineering, University of Notre Dame, December 1989.